

# UC San Diego

## UC San Diego Electronic Theses and Dissertations

### Title

Metal-Controlled Assembly of Peptide and Protein-based Engineered Biomaterials

### Permalink

<https://escholarship.org/uc/item/8f91s1g4>

### Author

Smith, Sarah Jane

### Publication Date

2016

Peer reviewed|Thesis/dissertation

UNIVERSITY OF CALIFORNIA, SAN DIEGO

**Metal-Controlled Assembly of Peptide and Protein-based Engineered Biomaterials**

A dissertation submitted in partial satisfaction of the requirements for the degree of

Doctor of Philosophy

in

Chemistry

by

Sarah Jane Smith

Committee in charge:

Professor F. Akif Tezcan, Chair  
Professor Timothy Baker  
Professor Stephen Howell  
Professor Elizabeth Komives  
Professor Michael Sailor

2016

Copyright

Sarah Jane Smith, 2016

All rights reserved.

The Dissertation of Sarah Jane Smith is approved, and is acceptable in quality and form for publication on microfilm and electronically:

---

---

---

---

---

Chair

University of California, San Diego

2016



## DEDICATION

To my family and friends who have supported me throughout this journey

## EPIGRAPH

“You can observe a lot just by just watching.”

“You’ve got to be very careful if you don’t know where you are going, because you might not get there.”

*Yogi Berra*

## TABLE OF CONTENTS

SIGNATURE PAGE .....	iii
DEDICATION .....	iv
EPIGRAPH .....	v
TABLE OF CONTENTS .....	vi
LIST OF TABLES .....	xii
ACKNOWLEDGEMENTS .....	xx
VITA .....	xxiii
ABSTRACT OF THE DISSERTATION .....	xxv
1. Proteins as building blocks: using metal ions to fold and assemble biological molecules .....	1
1.1 Introduction .....	1
1.2 Mimicking protein-protein interactions through designed systems .....	2
1.2.1 Peptides to target protein-protein interactions .....	2
1.2.2 Assembly of ordered protein arrays .....	3
1.3 Metal ions at protein interfaces .....	5
1.4 Metal-directed protein self-assembly .....	6
1.5 Goals of this Thesis .....	9
1.6 References .....	10
2. Functional, metal-based crosslinkers for $\alpha$ -helix induction in short peptides .....	14
2.1 Abstract .....	14
2.2 Introduction .....	15
2.3 Results and Discussion .....	17
2.3.1 Preparation of peptides containing His/Quin HCMs .....	17
2.3.2 Metal Binding Properties of His/Quin HCMs .....	19
2.3.3 Metal-induced $\alpha$ -Helicity in HCM-containing Peptides .....	25
2.3.4 Functionalization of HCMs .....	29
2.3.5 HCM-mediated helicity in non-Ala-rich peptide sequences .....	33
2.4 Conclusions .....	35
2.5 Materials and Methods .....	36
2.5.1 General Considerations .....	36
2.5.2 Synthesis of unnatural amino acids .....	37
2.5.3 Peptide Synthesis .....	45
2.5.4 Determination of metal binding affinity .....	49
2.5.5 Circular Dichroism Spectroscopy (CD) .....	50
2.5.6 Fluorescence Spectroscopy .....	51

2.6	Acknowledgements.....	53
2.7	References.....	54
3. Tunable Helicity, Stability and DNA-Binding Properties of Short Peptides with Hybrid Metal Coordination Motifs .....		
3.1	Abstract.....	60
3.2	Introduction.....	61
3.3	Results and Discussion .....	63
3.3.1	Design of HCM-peptides .....	63
3.3.2	Metal-binding properties of HCM-peptides.....	65
3.3.3	Metal-dependent $\alpha$ -helix induction in HCM peptides .....	69
3.3.4	Stability of HCM-peptides.....	72
3.3.5	HCM peptides for DNA binding and recognition.....	80
3.4	Conclusions.....	90
3.5	Materials and Methods.....	91
3.5.1	General Considerations.....	91
3.5.2	Synthesis of 5-iodoacetamido-1,10-phenanthroline .....	93
3.5.3	Peptide synthesis.....	96
3.5.4	Determination of metal binding affinity .....	101
3.5.5	Circular dichroism spectroscopy (CD) .....	102
3.5.6	Trypsin Digestion.....	103
3.5.7	Spectroscopic dimerization studies.....	104
3.5.8	Analytical Ultracentrifugation (AUC) .....	104
3.5.9	FRET dimerization studies .....	105
3.5.10	Gel shift assays with radiolabeled DNA.....	107
3.6	Acknowledgements.....	110
3.7	References.....	111
4. Designed, Helical Protein Nanotubes with Variable Diameters from a Single Building Block.....		
4.1	Abstract.....	119
4.2	Introduction.....	119
4.3	Design of protein building blocks.....	123
4.3.1	Determining protein packing by crystallography .....	124
4.4	Formation of variable diameter protein nanotubes .....	126
4.4.1	Structural analysis of $Zn_8R_4$ nanotubes.....	130
4.4.2	Mechanical properties of $Zn_8R_4$ nanotubes.....	135
4.4.3	Formation of multiwalled nanotubes .....	138
4.5	Conclusions.....	139
4.6	Materials and Methods.....	140
4.6.1	Site-directed mutagenesis and protein expression/purification .....	140
4.6.2	Macromolecular crystallography .....	140
4.6.3	Assembly of $Zn_8R_4$ nanostructures.....	141
4.6.4	Preparation of specimens and imaging of $Zn_8R_4$ nanostructures .....	141
4.6.5	Processing of TEM micrographs .....	142

4.6.6	Calculation of persistence length .....	142
4.7	Acknowledgements .....	143
4.8	References .....	143
5. Two Dimensional Crystals Self-Assembled through Three Different Types of		
Biological Interactions .....		147
5.1	Abstract .....	147
5.2	Introduction .....	147
5.3	Results and Discussion .....	149
5.3.1	Design of self-assembling, protein-DNA conjugates .....	149
5.3.2	Zinc-directed self-assembly in solution .....	151
5.3.3	Analysis of DNA interactions .....	154
5.3.4	Metal-binding interactions .....	160
5.3.5	Structural studies and modeling the protein-assembly .....	163
5.4	Conclusions .....	165
5.5	Materials and Methods .....	166
5.5.1	General considerations .....	166
5.5.2	Site-directed mutagenesis and protein expression/purification .....	166
5.5.3	Conjugation of DNA to protein .....	166
5.5.4	Characterization of DNA-protein conjugates .....	168
5.5.5	Preparation of <sup>21</sup> C-RIDC3-DNA nanostructures .....	169
5.5.6	Imaging of nanostructures .....	170
5.5.7	Testing for DNA-hybridization .....	172
5.5.8	Quantification of Zn <sup>II</sup> in assembled arrays .....	174
5.5.9	Macromolecular crystallography .....	175
5.5.10	Image analysis .....	177
5.6	Acknowledgements .....	177
5.7	References .....	177
6. Conclusions and Future Directions .....		
6.1	Introduction .....	182
6.2	Peptide-HCM based mimics of protein-protein interactions .....	182
6.3	Designing protein assemblies .....	183
6.3.1	Assembly of variable diameter protein nanotubes .....	183
6.3.2	Single point mutations cause large morphological changes .....	185
6.3.3	Applications of protein and hybrid DNA-protein materials .....	187
6.4	Conclusions .....	188
6.5	Materials and Methods .....	189
6.5.1	Negatively stained samples for transmission electron microscopy .....	189
6.5.2	Atomic Force Microscopy (AFM) .....	189
6.5.3	Macromolecular crystallography .....	190
6.6	References .....	191

## LIST OF ABBREVIATIONS

ADA	<i>N</i> -(2-acetamido)iminodiacetic acid
AFM	atomic force microscopy
Ala	alanine
Asp	aspartic acid
AUC	analytical ultracentrifugation
BH3	Bcl-2 homology domain 3
Bis-His	bis-histidine clamp
Bis-phen	bis-phenanthroline
bZIP	basic leucine zipper
CB	conjugation buffer
CCD	charge-coupled device
CD	circular dichroism
CHCA	$\alpha$ -cyano-4-hydroxycinnamic acid
Cys	cysteine
Cyt	cytochrome
DCC	dicyclohexylcarbodiimide
DCM	dichloromethane
DIPEA	Diisopropylethylamine
DMF	dimethylformamide
DNA	deoxyribonucleic acid
DTT	dithiothreitol
EDTA	ethylenediaminetetraacetic acid
EGTA	ethylene glycol tetraacetic acid
ESI	electrospray ionization
EtBr	ethidium bromide
FFT	fast Fourier transform

FPLC	fast protein liquid chromatography
FRET	Förster resonance energy transfer
Glu	glutamic acid
HCM	hybrid coordination motif
HEPES	4-(2-hydroxyethyl)-1-piperazineethanesulfonic acid
His	histidine
HPLC	high performance liquid chromatography
HOBt	N-hydroxybenzaldehyde
IA	iodoacetamide
IA-Quin	5-iodoacetamido-8-hydroxyquinoline
IR	infrared spectroscopy
$K_d$	dissociation constant
LC-MS	liquid chromatography-mass spectrometry
Lys	lysine
MALDI-TOF	matrix assisted laser desorption/ionization-time of flight
MBPC	metal binding protein complex
MDPSA	metal-directed protein self-assembly
MeOH	methanol
MES	2-(N-morpholine)ethanesulfonic acid
Met	methionine
MOPS	3-(N-morpholine)propanesulfonic acid
MS	mass spectrometry
MSED	MS end-to-end distance
NMR	nuclear magnetic resonance
PAR	4-(2-pyridylazo)resorcinol
PDB	protein database
Phen	1,10-phenanthroline

PPI	protein-protein interaction
Quin	8-hydroxyquinoline
$R_2$	dimeric, metal-free $^{H59/C96}$ RIDC3
RIDC3	Rosetta interface designed cytochrome 3
Rmsd	root mean square deviation
RPM	revolutions per minute
SDS-PAGE	sodium dodecyl sulfate polyacrylamide gel electrophoresis
SEM	scanning electron microscopy
Ser	serine
SPPS	solid phase peptide synthesis
SV	sedimentation velocity
Sulfo-SMCC	sulfosuccinimidyl-4-[N-maleimidomethyl]cyclohexane-1-carboxylate
TBE	tris borate EDTA buffer
TFA	trifluoroacetic acid
TEM	transmission electron microscopy
TFE	trifluoroethanol
TG	tris glycine buffer
$T_m$	melting temperature
Tpy	terpyridine
Tris	tris(hydroxymethyl)aminomethane
UA	uranyl acetate
UV-vis	ultraviolet-visible spectroscopy
$Zn_8R_4$	$Zn_8.^{H59/C96}$ RIDC3 <sub>4</sub>



## LIST OF TABLES

Table 2.1: Dissociation constants for various peptide-metal complexes. Numbers in parentheses correspond to standard deviation in the last reported significant figure. ....	23
Table 2.2: Percent helicities for various metal-peptide complexes calculated (top) by comparison with a sample containing 60% TFE, and (bottom) using the ratio $[\theta]_{222}/[\theta]_{\max}$ . .....	28
Table 2.3: Fluorescence quantum yields for the Zn-adducts of various peptides.....	53
Table 3.1: Dissociation constants for peptide-metal complexes and metal-mediated dimers .....	69
Table 3.2: Percent helicities for metal-peptide complexes by (top) comparison with a sample containing 60% TFE and (bottom) calculated using the ratio $[\theta]_{222}/[\theta]_{\max}$ . ....	71
Table 3.3: Calculated $T_m$ for each of the peptide-metal combinations. The signal at 222 nm was measured to observe peptide unfolding as the temperature was gradually increased. .....	75
Table 3.4: Changes in the $T_m$ for each peptide upon metal-binding. $\Delta T_m$ s were calculated by subtracting the $T_m$ for each metal-free (EDTA) sample from metal-bound peptide....	75
Table 3.5: Kinetic parameters for the tryptic digestion of <b>P3</b> under various conditions..	77
Table 3.6: Helicity and $T_m$ of metal-free and metal-bound <b>P8</b> . ....	82
Table 3.7: Quantification of helicity and melting temperature ( $T_m$ ) of DNA-bound <b>P8</b> ..	86
Table 3.8: Apparent dissociation constants for the <b>P8</b> -DNA complex in the presence of various metal ions. ....	88
Table 3.9: Dissociation constants of chelators used as competing ligands for UV-vis titrations to measure the metal binding affinity for peptide-HCMs.....	102
Table 4.1: X-ray data collection and refinement statistics for $Zn_8R_4$ .....	125
Table 4.2: Structural and Derived Mechanical Properties of the $Zn_8R_4$ Tubes .....	135
Table 5.1: Comparison of formation temperature and lattice parameters of various DNA-protein conjugates. ....	157
Table 5.2: X-ray data collection and refinement statistics for $^{21}C^{73}A$ RIDC3 .....	176
Table 6.1: X-ray data collection and refinement statistics for $^{21}C^{63}S$ RIDC3.....	190

## LIST OF FIGURES

Figure 1.1: Examples of stabilized helices to mimic protein-protein interactions (PPIs). . . . .	2
Figure 1.2: Examples of assembled protein-materials.....	4
Figure 1.3: Examples of natural, metal-mediated protein oligomers.....	6
Figure 1.4: Applications of metal-directed protein self-assembly.....	8
Figure 2.1: (a) Proposed scheme for $\alpha$ -helix induction through tridentate metal coordination by an HCM. The remaining coordination sites on the metal are likely filled by aquo ligands. (b) Chemical structures of various Quin functionalities. (c) Sequences of peptide constructs prepared in this study. ....	16
Figure 2.2: UV-vis spectral changes upon Quin-M <sup>II</sup> coordination. A solution containing 16 $\mu$ M H-EMeQuin and 45 $\mu$ M EGTA was titrated with increasing amounts of M <sup>II</sup> . ....	20
Figure 2.3: Peptide-metal binding titrations and fits. Titrations of (a) H-EMeQuin, (b) H-CQuin, and (c) H-EQuin with late first row transition metals as monitored by UV-vis spectroscopy. Two different models were used for fitting. ....	21
Figure 2.4: Dynafit scripts for describing metal-peptide binding equilibria. Two models for binding were used: (a) A 1:1 peptide:metal competitive binding model, and: (b) A 1:1 and 2:1 peptide:metal competitive binding model, taking into account the possibility for metal-induced peptide dimerization at limiting metal concentrations. ....	22
Figure 2.5: Changes in the circular dichroism spectra of HCM-bearing peptides upon binding Cu <sup>II</sup> and Zn <sup>II</sup> . Spectra were acquired at 4 °C with 10 $\mu$ M peptide and 30 $\mu$ M EDTA or metal in 5 mM sodium borate buffer at pH 7.5. Corresponding spectra for Co <sup>II</sup> and Ni <sup>II</sup> are shown in Figure 2.6 and Figure 2.7. ....	24
Figure 2.6: CD spectra of various peptides at 25 °C. Each sample was prepared with 10 $\mu$ M peptide and 30 $\mu$ M of either M <sup>II</sup> or EDTA. ....	26
Figure 2.7: CD spectra of various peptides at 4 °C. Each sample was prepared with 10 $\mu$ M peptide and 30 $\mu$ M of either M <sup>II</sup> or EDTA.. ....	27
Figure 2.8: (a) H-EMeQuin fluorescence upon metal addition ( $\lambda_{exc} = 385$ nm). (b) Normalized fluorescence intensity ( $F/F_0$ ) of each peptide when bound to Zn <sup>II</sup> as compared to the metal-free peptide. ....	30
Figure 2.9: (a) Proposed scheme for the formation of the Re(Quin)(CO) <sub>3</sub> (His) HCM upon heating and the subsequent formation of the $\alpha$ -helix upon cooling. (b) Observed changes in the CD spectrum upon heating and subsequent cooling of the Re-HCM peptide.. ....	31

Figure 2.10: UV-vis spectrum of H-CQuin(Re)(CO)<sub>3</sub>(His). The inset shows a closeup of the band at 410 nm. This band was used as the excitation wavelength for luminescence. 32

Figure 2.11: Changes in the H-CQuin(Re)(CO)<sub>3</sub>(His) luminescence spectrum upon His coordination after heating. 25 μM peptide in 2.5 mL water. The sample was excited at 410 nm. .... 33

Figure 2.12: Sequences of wild-type and HCM-modified Bax BH3 domain peptides (top). Far-UV CD spectra of Bax-HCM in the presence and absence of Cu<sup>II</sup> (blue) and Zn<sup>II</sup> (magenta) acquired at 4 °C (solid lines) or 25 °C (dashed lines).. .... 34

Figure 2.13: (a) Synthetic scheme for the synthesis of iodoacetamido-8-hydroxyquinolinate (IQuin). (b) ESI-MS (positive mode) of IQuin. Observed peak at 329.0 amu (exp.: 328.9) [M + H]<sup>+</sup>. The peak at 237.0 amu corresponds to the side product chloracetamido-8-hydroxyquinolinate (exp.: 236.7) [M + H]<sup>+</sup>..... 38

Figure 2.14: (a) Synthetic scheme for the synthesis of 5-{N-[(9H-fluoren-9-ylmethoxy(carbonyl)]-L-glutamino}-8-hydroxyquinoline (Fmoc-E(Quin)-OH). (b) ESI-MS (positive mode) of Fmoc-E(Quin)-OH. Observed peak at 512.1 amu (exp.: 512.2) [M + H]<sup>+</sup>..... 39

Figure 2.15: (a) Synthetic scheme for the synthesis of 5-Aminomethyl-8-hydroxyquinoline (NH<sub>2</sub>MeQuin). (b) ESI-MS (positive mode) of NH<sub>2</sub>MeQuin. Observed peak at 175.0 amu (exp.: 175.1) [M + H]<sup>+</sup>..... 41

Figure 2.16: (a) Synthetic scheme for the synthesis of 5-{N-[(9H-fluoren-9-ylmethoxy)carbonyl]-L-glutaminomethyl}-8-hydroxyquinoline (Fmoc-E(MeQuin)-OH). (b) ESI-MS (positive mode) of Fmoc-E(MeQuin)-OH. Observed peak at m/z = 526.3 amu (exp.: 526.2 amu) [M + H]<sup>+</sup>..... 43

Figure 2.17: (a) Synthetic scheme for the synthesis of Re(Cl)(IQuin)(CO)<sub>3</sub>. (b) ESI-MS (negative mode) of Re(Cl)(IQuin)(CO)<sub>3</sub>. Observed peak at m/z = 633.0 amu (exp.: 632.9) [M]<sup>-</sup>, 629.0 amu (exp 628.9) [M - Cl + MeOH]<sup>-</sup>, 597.0 amu (exp 596.9) [M - Cl]<sup>-</sup>, 541.1 amu (exp 540.9) [M - I + Cl]<sup>-</sup>..... 44

Figure 2.18: Analytical HPLC traces and MALDI-TOF spectra of various peptide constructs. HPLC gradient used: 1. 0 to 5 min, 95% solvent A, constant. 2. 5 to 20 min, 95% to 60% solvent A, gradient.. .... 47

Figure 2.19: UV-vis absorption spectrum of Zn-HCQuin. Inset: The absorption band at 380 nm used for fluorescence excitation. .... 52

Figure 2.20: Reversibility of Zn<sup>II</sup>-induced H-EMeQuin fluorescence..... 52

Figure 3.1: Design of peptides P1-P7. (a) Cartoon showing the proposed mode of helix induction by metal binding to the HCM. The peptides include two pairs of salt bridging

side chains (cyan), the HCM motif with His at position *i* and Cys-Phen at position *i*+7 (green), and various amino acids incorporated at the *i*+4 position (red). ..... 63

Figure 3.2: (a) CD spectra showing the induction of helicity upon addition of various metal ions. (b) Model showing an Ile residue at the *i*+3 (pink) position in contact distance with the Phen functionality in the metal-bound HCM. (c) Molar ellipticity of peptide variants (metal-free, bound to Ni<sup>II</sup>, or in the presence of TFE) monitored at 222 nm. .... 64

Figure 3.3: UV-vis spectra changes upon Phen-M<sup>II</sup> coordination. Solutions were prepared with approximately 15 μM peptide and 50 μM chelator (EGTA in the case of Ni<sup>II</sup> and Co<sup>II</sup>, and NTA in the case of Zn<sup>II</sup> and Cu<sup>II</sup>), and increasing amounts of M<sup>II</sup> were added by titration. .... 66

Figure 3.4: Peptide-metal binding titrations and fits. Example titrations of MeSH1 with Co<sup>II</sup>, Ni<sup>II</sup>, Cu<sup>II</sup>, and Zn<sup>II</sup> as monitored by UV-vis spectroscopy. .... 67

Figure 3.5: Equations used to model the metal-binding equation, where P is the peptide, M is the metal, C is the chelator, and D is a metal-mediated peptide model. Equations (1) and (2) only are used to fit data where only peptide-metal binding is accounted for, and all three equations are used to model a 1:1 and 2:1 binding equilibria..... 68

Figure 3.6: Dynafit scripts for describing metal-peptide binding equilibria. Two models for fitting were tried, as it is expected that a metal-mediated dimer will form at limiting metal concentrations. .... 68

Figure 3.7: CD spectra of peptides at 25 °C. Samples were prepared with approximately 15 μM of peptide with an excess of either M<sup>II</sup> or EDTA..... 70

Figure 3.8: Thermal unfolding curves. The raw data is shown in the left panels, while the normalized unfolding curves are shown on the right..... 73

Figure 3.9: HPLC traces of the set of data collected for the metal-free, HCM-bound peptide during the tryptic digestion experiment. The intact peptide elutes at approximately 7.5 min; that peak disappears over time and a new peak at 6.0 min, corresponding to the cleaved peptide fragment, appears. .... 76

Figure 3.10: (a) Trypsin cleavage sites and corresponding masses of P3. .... 78

Figure 3.11: Tryptic digestion of P3 at 4 or 25 °C in the presence and absence of M<sup>II</sup>. .. 79

Figure 3.12: Design of the DNA-binding peptide P8. .... 81

Figure 3.13: Induced helicity in **P8** at (a) 25 °C and (b) 4 °C. (c) No induction of helicity was observed in **P8**<sub>bare</sub>, where HCM functionality is absent. .... 83

Figure 3.14: Metal-dependent dimerization. of **P8**. .... 84

Figure 3.15: CD spectra of <b>P8</b> in the presence and absence of $M^{II}$ and DNA.....	86
Figure 3.16: Electrophoretic mobility shift assay for monitoring <b>P8</b> -CRE binding in the absence (a) and the presence (b) of 0.5 equiv. of $Ni^{II}$ .....	87
Figure 3.17: Scheme for the possible modes of <b>P8</b> binding to DNA. In this case, the DNA can act as a template for dimerization.....	89
Figure 3.18: Synthetic scheme for the synthesis of 5-iodoacetamido-1,10-phenanthroline. ....	93
Figure 3.19: ESI-MS (positive mode) of 5-nitro-1,10-phenanthroline. Observed peak at 226.0 amu (expected 226.1 amu) $[M+H]^+$ . 248.0 amu (expected 248.1 amu) $[M+Na]^+$ . 473.1 amu (expected 473.2 amu) $[M+M+Na]^+$ . ....	94
Figure 3.20: ES-MS (positive mode) of 5-amino-1,10-phenanthroline. Observed peak at 196.1 amu (expected 196.1 amu) $[M+H]^+$ . 218.1 amu (expected 218.1 amu) $[M+Na]^+$ . 413.3 amu (expected 413.2 amu) $[M+M+Na]^+$ . ....	95
Figure 3.21: ES-MS (positive mode) of 5-iodoacetamido-1,10-phenanthroline. Observed peak at 364.1 amu (expected 364.0 amu) $[M+H]^+$ .....	96
Figure 3.22: Synthetic scheme for the functionalization of a peptide cys residue with 5-iodoacetamido-1,10-phenanthroline. ....	98
Figure 3.23: Analytical HPLC traces and MALDI-TOF spectra of various peptide constructs. ....	99
Figure 3.24: UV-vis titrations without a competing chelator to determine the stoichiometry of metal binding and dimer formation. ....	105
Figure 3.25: Titrations to determine the stoichiometry of metal-binding and dimer formation as monitored by CD. ....	105
Figure 3.26: Confirmation of dimer formation by AUC. After performing FRET experiments, the samples were analyzed by AUC. The expected sedimentation coefficient for a monomer is 0.7 S and 1.2 S for a dimer. ....	106
Figure 3.27: Quantitative FRET experiments to calculate the apparent $K_d$ of peptide dimerization. Equimolar amounts of P8F and P8R are titrated into solution and the fluorescence signal is measured.....	107
Figure 3.28: Sample gel shift assay to observe DNA binding by <b>P8</b> with the SCR DNA sequence. Lane (Q) contains CRE without any added peptide; DNA concentration is kept constant at 1 nM, while P8 concentration varies. ....	109

Figure 3.29: Sample gels from electrophoretic mobility shift assays to observe CRE binding by <b>P8</b> . At some concentrations, an intermediate band is observed that may be due to a peptide monomer bound to the DNA. Lane (Q) contains CRE without any added peptide; DNA concentration is kept constant at 1 nM, while P8 concentration varies: .	110
Figure 3.29: Inclusion of salt bridges in the peptide backbone provides helical stabilization in the apo protein, but make no difference upon metal binding. ....	116
Figure 3.30: Polarity of the HCM on the peptide. (a) Sequences of peptides with Phen located at the C-terminus or more centrally. (b) Comparison of the induction of helicity upon the addition of Ni <sup>II</sup> . ....	117
Figure 4.1: Retrosynthetic analysis of a 2D helical nanotube. Individual nanotubes (left) are formed by the folding of an anisotropic 2D array (center) that is composed of individual D <sub>2</sub> symmetric synthons (right).. ....	121
Figure 4.2: Proposed Zn-mediated assembly of a disulfide-linked protein dimer (R <sub>2</sub> ) into a closed, D <sub>2</sub> symmetric tetramer (Zn <sub>8</sub> R <sub>4</sub> ), which acts as a synthon for larger supramolecular architectures upon further Zn coordination.....	122
Figure 4.3: Crystallographic characterization of Zn <sub>8</sub> R <sub>4</sub> . Motif 1 (cyan spheres) and Motif 2 (magenta spheres) coordination sites promote intertetramer assembly and the formation of higher order arrays. Protein tetramers are alternatively colored to highlight 2D arrangement.....	123
Figure 4.4: Characterization of disulfide-crosslinked R <sub>2</sub> . (a) MALDI mass spectrum of R <sub>2</sub> . (b) SDS PAGE gel of R <sub>2</sub> after denaturation in loading buffer with (right line) or without (center lane) β-mercaptoethanol (β-ME). In the presence of β-ME, the C96-C96 bond is reduced, yielding the monomeric species. ....	124
Figure 4.5: Light micrograph image of Zn <sub>8</sub> R <sub>4</sub> crystals obtained via Zn-directed assembly. ....	125
Figure 4.6: Internal Zn <sup>II</sup> coordination sites to form Zn <sub>8</sub> R <sub>4</sub> from R <sub>2</sub> . ....	126
Figure 4.7: Mechanism for stacking of 2D Zn <sub>8</sub> R <sub>4</sub> arrays into 3D crystals. (a) Cartoon depiction of a crystallographically characterized 2D Zn-mediated array. 2D arrays are stabilized by Zn ions coordinated by N-terminal and tetracarboxylate coordination motifs. ....	127
Figure 4.8: ns TEM images of Zn <sub>8</sub> R <sub>4</sub> nanotubes. ....	128
Figure 4.9: Traces of individual nanotubes used for determining the parameters listed in Table 4.2. Each tube was traced using the FiberApp program, and the initial coordinates were placed at (0,0) so that each tube extends from the center of the plot. ....	129
Figure 4.10: Contour length distributions of each class of nanotubes.....	129

Figure 4.11: ns TEM characterization of Zn <sub>8</sub> R <sub>4</sub> arrays. (a) Single Class I nanotube with tubular (bottom) and frayed (top) segments. (b,c) 2D reconstructions of tubular (b) and frayed (c) regions of a single nanotube.....	130
Figure 4.12: TEM micrograph (a), calculated Fourier transform (b) and Fourier-filtered image (c) of the planar region of a Class I nanotube. ....	131
Figure 4.13: Image processing of the tubular region of a Class I nanotube. ....	132
Figure 4.14: TEM images of a single nanotube (left), indexed Fourier transform (center) and 2D reconstruction (right) of a Class II nanotube.....	133
Figure 4.15: TEM image of a single nanotube (left), indexed Fourier transform (center), and 2D reconstructions (right) of a Class III nanotube.....	133
Figure 4.16: Representative images of nanotubes collected by cryo TEM. The plots on the right show the tracing of each nanotube starting from position (0,0). Axes are in nanometers. ....	134
Figure 4.17: Structural model for Class II nanotubes. ....	134
Figure 4.18: Width distribution of tubes as measured in cryoEM samples. ....	135
Figure 4.19: Fits used for calculating persistence length using the FiberApp module “MS End-to-end Distance”. Please refer to the corresponding section in Materials and Methods for details. ....	136
Figure 4.20: Multi-walled tubes formed under conditions that also produce Class I tubes. ....	137
Figure 4.21: Bundles of Class II tubes formed in solution. ....	137
Figure 4.22: Low magnification TEM micrographs of class I (a) and class II (b) tubes after incubation for 1 year at room temperature.....	139
Figure 5.1: Design of protein-DNA conjugate materials. (a) Model of RIDC3 2D arrays with the addition of rhodamine at cys21. (b) Predicted model of assembly for incorporation of DNA-protein conjugate. (c) Sequences and melting temperatures of incorporated DNA. ....	150
Figure 5.2: Analysis of DNA-protein 2D arrays.....	151
Figure 5.3: Analysis of material formation immediately after the addition of Zn <sup>II</sup> (t = 0, where the material at time t = 0 was deposited on the grid within 5 minutes of Zn <sup>II</sup> addition), after 1 hr and 2 hr of incubation at 4 °C.. ....	152

Figure 5.4: Analysis of the calculated fft and lattice parameters of DNA-protein material ( $^{21}\text{C}$ RIDC3-10A/B) and protein only material (RIDC3). .....	154
Figure 5.5: Temperature effects on $^{21}\text{C}$ RIDC3-10A/B material.....	155
Figure 5.6: Two additional DNA-sequences were conjugated to $^{21}\text{C}$ RIDC3 and the ability of the DNA-protein conjugate to form ordered materials was studied. ....	156
Figure 5.7: Samples were prepared where the ratio of $^{21}\text{C}$ RIDC3-10A: $^{21}\text{C}$ RIDC3-10B was varied. The samples were analyzed by TEM, and the footprint of sheet coverage was measured for at least 100 grid squares for each sample.....	158
Figure 5.8: Fluorescence analysis of DNA-protein arrays.....	160
Figure 5.9: Analysis of the ability to form hybrid, ordered materials with protein mutants. ....	162
Figure 5.10: Crystal structure of metal free $^{21}\text{C}^{73}\text{A}$ RIDC3. (a) and (b) show alternate views of the metal-free dimeric interface which may be similar to what is underlying the structure of the $^{21}\text{C}$ RIDC3-10A/B materials.....	164
Figure 5.11: (a) Electron density map of negatively stained $^{21}\text{C}$ RIDC3-10A/B materials. (b) Electron density map of $^{21}\text{C}$ RIDC3-10A/B materials obtained using cryoEM conditions. ....	165
Figure 5.12: Analysis of DNA-protein conjugate.....	168
Figure 5.13: Analysis of a dissolved crystal. The UV-vis ratio of $\text{Abs}_{415}:\text{Abs}_{260}$ was as expected, and SDS-PAGE gel electrophoresis confirmed the presence of only DNA-protein conjugate. ....	169
Figure 5.14: TEM images of grid squares set up with $^{21}\text{C}$ RIDC3-10A and $^{21}\text{C}$ RIDC3-10B at varying ratios.....	173
Figure 5.15: PAR calibration curve to detect $\text{Zn}^{\text{II}}$ concentration in solution.....	175
Figure 6.1: Analysis of $^{21}\text{C}^{63}\text{A}$ RIDC3 materials. ....	184
Figure 6.2: Analysis of $^{21}\text{C}^{73}\text{A}$ RIDC3 materials. ....	186



## ACKNOWLEDGEMENTS

I would like to thank my advisor, Professor Akif Tezcan, for his support and encouragement throughout my graduate school career. His enthusiasm for science and excitement for new ideas is never-faltering and contagious. Although it wasn't always easy getting there, I have become a much better scientist through my experiences working with Akif, and his drive to put forward the best science we possibly can is truly inspiring.

I have been fortunate to have spent the last 6 years in a department that is truly supportive and collaborative. In particular, I would like to thank Betsy Komives and her group for their assistance over the years. The peptide work in Chapters 2 and 3 would not have gotten off of the ground without Betsy's aid and insights. I would also like to thank Tim Baker and his research group for their assistance with TEM image collection and analysis. Norm Olson and James Bouwer have been wonderful resources in the TEM facility as well.

The group of students and postdocs in the Tezcan lab—and I've overlapped with every one of them—have been a pleasure to work with. They have supported me through laughter, tears, and countless trips to the coffee cart, and I couldn't have asked for a more enjoyable group of people to work with. Their passion for science is obvious—I have been inspired by those who came before me, and I look forward to seeing the new discoveries made by those who are younger. In particular, I know the materials subgroup will be in the good hands of Rohit and Rob, and I am excited to see how they push the research forward.

I would like to thank my family—my parents, my brother Matt, and my sister-in-law Hannah--for their support, even when they had no idea what I was talking about. I

have always looked forward to their visits to San Diego, and cannot thank them enough for their never-ending support and encouragement as I pursued my dreams.

The support of my husband, Doug Collins, has been incredible and unwavering. He never complained through late-night on-campus pickups and dinner drop-offs, and I am not sure I would have made it through graduate school without him.

Finally, I would like to thank the friends who have supported me from both near and far. Having dinner with Alan, Abbas, and Sam gave me something to look forward to every week—Dinner Thursday is one of the things I will miss most about San Diego. They have truly become my San Diego family.

Chapter 2 is reproduced in part with permission from the Royal Society of Chemistry. Smith, S.J.; Du, K.; Radford, R.J.; Tezcan, F.A. Functional, metal-based crosslinkers for  $\alpha$ -helix induction in short peptides. *Chemical Science*. 2013, 4, 3740.

Chapter 3 is in preparation for submission to *Chemical Science*: Smith, S.J.; Radford, R.J.; Tezcan, F.A. Tunable Helicity, Stability and DNA-Binding Properties of Short Peptides with Hybrid Metal Coordination Motifs. 2016.

Chapter 4 is reprinted with permission from Brodin, J.D.\*; Smith, S.J.\*; Carr, J.R.; Tezcan, F.A. Designed, helical protein nanotubes with variable diameters from a single building block. *Journal of the American Chemical Society*. 2015, 137, 10468. Copyright 2015 American Chemical Society.

Chapter 5 is reproduced in part from a manuscript currently being prepared for submission. Smith, S.J.; Cardone, G.; Suominen, L.; Baker, T.S.; Tezcan, F.A. Two-

dimensional crystals assembled through three different types of biological interactions.2016.

The dissertation author is primary author on all reprinted materials. She would like to thank the Molecular Biophysics Training Grant for providing funding for part of this work.

## VITA

### EDUCATION

- 2009 B.S., Chemistry, Massachusetts Institute of Technology  
2009 B.S., Biology, Massachusetts Institute of Technology  
2011 M.S., Chemistry, University of California, San Diego  
2016 Ph.D., Chemistry, University of California, San Diego

### AWARDS AND HONORS

- 2013 Teddy Traylor Award  
2010 Molecular Biophysics Training Grant (NIH)  
2010 NSF Graduate Student Fellowship Program Honorable Mention  
2009 MIT Chemistry Research Award

### PUBLICATIONS

**Smith, S.J.;** Cardone, G.; Suominen, L.; Baker, T.S.; Tezcan, F.A. Two-dimensional crystals assembled through three different types of biological interactions. *In preparation*. 2016.

**Smith, S.J.;** Radford, R.J.; Tezcan, F.A. Tunable helicity, stability and DNA-binding properties of short peptides with hybrid metal coordination motifs. *Chemical Science, in preparation*. 2016.

Brodin, J.D.\*; **Smith, S.J.\*;** Carr, J.R.; Tezcan, F.A. Designed, helical protein nanotubes with variable diameters from a single building block. *Journal of the American Chemical Society*. 2015, 137, 10468.

**Smith, S.J.;** Du, K.; Radford, R.J.; Tezcan, F.A. Functional, metal-based crosslinkers for  $\alpha$ -helix induction in short peptides. *Chemical Science*. 2013, 4, 3740.

Huang, Z.; Zhang, X. Bosch, M.; **Smith, S.J.;** Lippard, S.J. Tris(2-pyridylmethyl)amine (TPA) as a membrane-permeable chelator for interception of biological mobile zinc. *Metallomics*. 2013, 5, 648.

Zhang, X.; Hayes, D.; **Smith, S.J.;** Friedle, S.; Lippard, S.J. New Strategy for quantifying biological zinc by a modified zinpyr fluorescence sensor. *Journal of the American Chemical Society*. 2008, 130, 15788.

## FIELDS OF STUDY

Major Field: Chemistry

Studies in Bioinorganic Chemistry  
Professor F. Akif Tezcan

ABSTRACT OF THE DISSERTATION

Metal-Controlled Assembly of Peptide and Protein-based Engineered Biomaterials

by

Sarah Jane Smith

Doctor of Philosophy in Chemistry

University of California, San Diego, 2016

Professor F. Akif Tezcan, Chair

Protein-protein interactions are ubiquitous throughout nature at many length and time scales—from transient interactions between individual proteins for signaling and electron transfer to the self-assembly over large distances of bacterial S-layer protein coats. Extensive research has been undertaken to attempt to mimic, interrogate, interrupt, or design protein-protein interactions, but natural protein-protein interactions often form as a result of many accumulated weak interactions over large, heterogeneous molecular surfaces, making them challenging to design. As a way to overcome these challenges, we have previously introduced methods of synthesizing protein-protein interactions with

minimal surface design through the directional and highly controllable coordination of metal ions on protein surfaces.

The goal of this thesis work has been to expand the scope and functionality of these metal-directed protein and peptide interactions. First, we show that, like proteins, short peptides can be directed to fold and assemble in biologically relevant ways using coordination chemistry, while incorporating additional metal-based functionality on the peptide backbone. We then extend the scale of protein self-assembly to highly ordered, crystalline protein nanotubes with tunable diameters. Finally, we demonstrate the ability to assemble protein-DNA nanomaterials in a manner that, similar to what is observed in nature, relies on the sum of a number of weak interactions to form highly ordered protein-DNA arrays. Overall, we demonstrate the ability to use metal ions to coordinate interactions on scales as small as single protein-protein interactions to as large as micrometer scale arrays.

# **1. Proteins as building blocks: using metal ions to fold and assemble biological molecules**

## **1.1 Introduction**

Proteins fulfill a wide variety of roles in biological systems, from catalyzing reactions to regulating gene transcription to providing structural support; thus, proteins can be described as nature's building blocks. Much of the functionality of proteins stems from their interactions with other biological molecules. For instance, interactions between members of the Bcl-2 family of proteins help to regulate cell viability, and their misregulation is often a factor in the development of cancer.<sup>1</sup> Collagen is a protein that functions as a structural support and whose properties are the result of the assembly of 3-helix bundles that can then organize into larger fibers.<sup>2</sup> Microtubules can rapidly assemble and disassemble as necessary to provide structural support during the process of cell division.<sup>3</sup> Given the structural and functional diversity that arises from protein-protein interactions and protein self-assembly, they constitute highly exciting targets for molecular design as well as for the creation of synthetic mimics for their interrogation. Yet, many of these protein-protein interactions and protein self-assembly processes occur through weak, non-covalent, but highly specific interactions across large areas on protein surfaces,<sup>4,5</sup> which are difficult to design and engineer.<sup>6</sup> A wide variety of strategies has been employed to direct interactions between biological molecules to mimic those found ubiquitously throughout nature.<sup>7</sup>



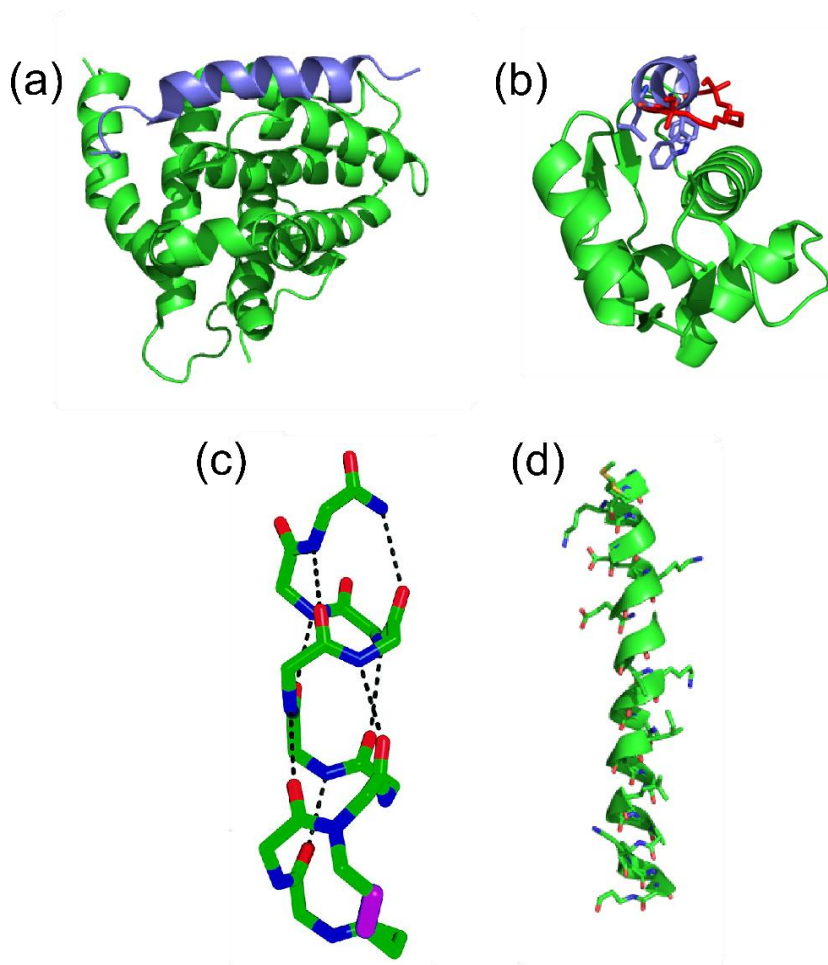


Figure 1.1: Examples of stabilized helices to mimic protein-protein interactions (PPIs). (a) Natural complex of Bcl-x1 with Bad peptide binding partner, demonstrating the extended surface area of PPIs. PDB ID: 1G5J (b) A peptide stabilized in an  $\alpha$ -helix conformation by a hydrocarbon staple bound to Mdm2, a potential target for cancer therapy. PDB ID: 3V3B (c) NMR-derived structure of a helical peptide containing a hydrogen-bond surrogate (HBS), shown in purple. Adapted from reference 25. (d) Crystal structure of a peptide containing  $\beta$ -amino acids, showing the potential of peptides consisting of a mixture of  $\alpha$ - and  $\beta$ -amino acids to mimic native helical folds. PDB ID: 3C3F.

## 1.2 Mimicking protein-protein interactions through designed systems

### 1.2.1 Peptides to target protein-protein interactions

At the smallest scale, there has been interest in mimicking protein-protein interactions for therapeutic applications.<sup>8-10</sup> Many diseases result from the misregulation

of proteins within a cell, often due to either the accumulation of mutations prohibiting native protein-protein interactions or due to the over- or under-expression of protein binding partners.<sup>11,12</sup> Protein-protein interactions are therefore an attractive therapeutic target, but until recently, one that has been thought of as “undruggable,” as it is very difficult to design small molecules to interact with an extended protein surface, and protein therapeutics are generally most useful against extracellular protein targets.<sup>13</sup> Short peptides, while the ideal size to enter cells and target protein surface interactions,<sup>14</sup> tend to be unstructured, making them susceptible to protease degradation or reducing their ability to recognize their binding targets.<sup>15</sup> Researchers have developed a number of ways to stabilize folded peptides through the use of covalent crosslinking,<sup>16-25</sup> the incorporation of hydrogen-bond surrogates<sup>26,27</sup> or  $\beta$ -amino acids,<sup>28-30</sup> or by the design of miniature peptides where residues important for protein-protein interactions are grafted onto a stably folded platform (Figure 1.1).<sup>31</sup>

### **1.2.2 Assembly of ordered protein arrays**

On much larger scales, there have been efforts to design ordered protein arrays that extend across nano- or micrometers. Inspired in part by natural, S-layer proteins that form ordered arrays on the surface of bacterial and archaeal cells and can be found in p1, p2, p3, p4, or p6 symmetry,<sup>32-34</sup> the idea of assembling crystalline protein arrays to take advantage of natural protein functionalities in ordered, high density arrays is exciting (Figure 1.2). S-layer proteins, in particular, have been investigated for potential applications in material templating<sup>35-37</sup> among other nanobiotechnological applications.<sup>38</sup> Ordered nanomaterials

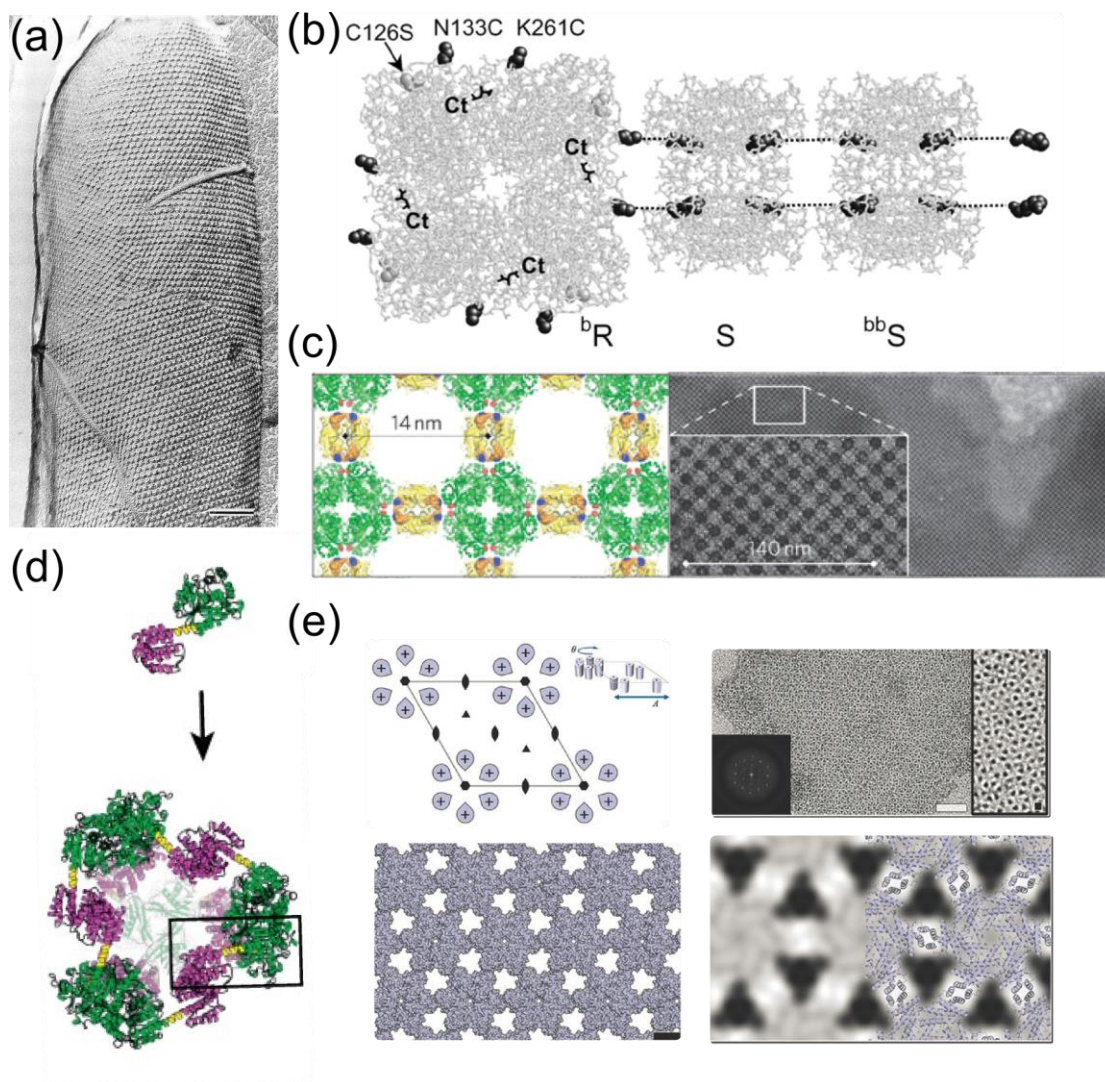


Figure 1.2: Examples of assembled protein-materials. (a) Bacterial S-layer, a natural 2-dimensional protein assembly. Adapted from reference 33. (b) Assembly scheme for 2-dimensional materials consisting of a  $C_4$ -symmetric protein assembled using biotin-streptavidin connector. Adapted from reference 40. (c) Ordered protein lattices created by fusing naturally oligomeric proteins with a linker region. Adapted from reference 43. (d) Oligomeric protein fusion to create discrete assemblies with the linker region shown in yellow. Adapted from reference 44. (e) Computationally designed proteins with inherent symmetry assemble into ordered lattices. Adapted from reference 50.

have been designed from DNA<sup>39</sup> or peptide<sup>40</sup> building blocks and the design rules for these biological molecules are relatively well understood. Proteins are significantly more complicated and have been much more difficult to use to develop ordered arrays, although

this also makes protein materials potentially more exciting than those developed from simpler building blocks.<sup>32</sup> A few strategies have been employed to successfully synthesize protein arrays, including (1) creating protein systems with attached binding molecules that will polymerize with adjacent proteins (Figure 1.2d),<sup>41-43</sup> (2) principles of matching symmetry and creating fused proteins that will oligomerize (Figure 1.2b,c),<sup>44-48</sup> or (3) *de novo* computational protein design (Figure 1.2e).<sup>49-51</sup> However, these methods are limited to use in proteins that have high symmetry or homooligomerize, or require significant computation design and have a fairly low success rate from initial computational design to protein expression and material assembly.

### 1.3 Metal ions at protein interfaces

In addition to the widely studied functional or structural roles of metal ions within a protein fold, metals are also widely utilized by nature at protein-protein interfaces. Recent analysis of the PDB has revealed that 4-5% of protein oligomers contain an interfacial transition metal ion with a structural or functional role.<sup>52</sup> For instance, a family of voltage-gated potassium channel proteins form a pore upon homotetramerization where each protein monomer contains a HX<sub>5</sub>CX<sub>20</sub>CC motif and a tetramer is formed upon Zn<sup>II</sup> coordination to the Cys<sub>3</sub>His sites between protein monomers (Figure 1.3a).<sup>53</sup> A second example is the ATPase Rad50 protein, part of the Mre11 complex that is essential for chromosomal maintenance. It was discovered that the Rad50 homodimerization domain is mediated by a Cys<sub>4</sub> dimerization domain in a Zn-hook motif (Figure 1.3b, crystallized with Hg<sup>+</sup>).<sup>54</sup> The size and orientation of the metal-induced dimer matches the expected configuration necessary to bridge homologous DNA sequences during recombination. These examples, where metals mediated protein-oligomerization through interfacial

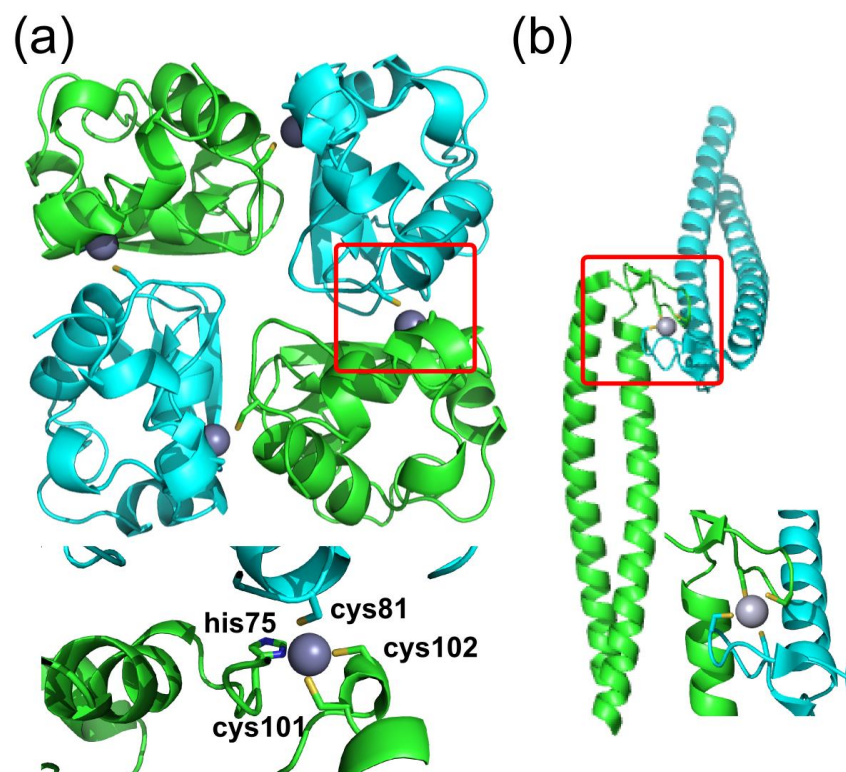


Figure 1.3: Examples of natural, metal-mediated protein oligomers. (a) A Cys<sub>3</sub>His amino acid motif binds Zn<sup>II</sup> (crystallized here with Hg<sup>+</sup>), coordinating the assembly of a tetrameric voltage-gated potassium channel. PDB ID: 3KVT (b)

binding, along with many other examples in nature, serve as the inspiration for our methods of metal-directed protein self-assembly (MDPSA).

#### 1.4 Metal-directed protein self-assembly

Inspired by the use of metal ions at protein interfaces, we have developed a method of metal-directed protein self-assembly, where only a few mutations on a protein surface enable the directed metal coordination and the assembly of protein monomers based on the metal coordination geometry.<sup>55,56</sup> Cytochrome *cb*<sub>562</sub> was chosen as a model system as it is a 4-helix bundle protein, stable, and monomeric at millimolar concentrations (Figure 1.4a).<sup>57</sup> High affinity metal-binding sites were designed to create the protein construct

Metal Binding Protein Complex 1 (MBPC-1),<sup>58</sup> containing two bis/His motifs at the  $i/i+4$  positions on one face of an  $\alpha$ -helix (Figure 1.4b). It had previously been established that the installation of bis/His motifs on peptide surfaces bind metal ions with micromolar affinity, and metal-coordination can help to stabilize the peptide in an  $\alpha$ -helical fold. Upon the addition of  $Zn^{II}$ , the formation of discrete, higher ordered species was observed in solution using analytical ultracentrifugation (AUC), and a crystal structure of a tetramer with 4 bound  $Zn^{II}$  ions, where each  $Zn^{II}$  ion was bound to a H73/H77 bis-his motif on one protein monomer, H63 from a second protein, and D74 from a third protein in a tetrahedral geometry. Further, upon the addition of metals with different coordination geometries, the addition of  $Cu^{II}$  caused the formation of a dimeric protein species with the metal bound in a square-pyramidal geometry, and the addition of  $Ni^{II}$  bound a trimer of MBPC-1 in an octahedral geometry.<sup>59</sup> These results demonstrate that it is possible to control protein assembly by directed metal-binding, where the orientation of the ligands (in this case, protein) is determined by the binding preferences of the particular metal that is used for assembly (Figure 1.4c,d).

From this initial work, multidentate chelating ligands were post-synthetically added to the protein surface at an engineered, reactive cysteine residue to create a tridentate metal-binding motif with a his residue 7 amino acids away (2 turns of an  $\alpha$ -helix) on the protein surface to further improve our control of metal-mediated assembly.<sup>60,61</sup> Metal-coordination to these tri-coordinate hybrid coordination motifs (HCMs) was shown to stabilize the fold of the protein against both thermal and chemical denaturation. In particular, upon the addition of  $Ni^{II}$  to a protein containing a his/quinn HCM, a cis-Quinn dimer was obtained that was found to align to the basic domain of a bZip homodimer with a root-mean-



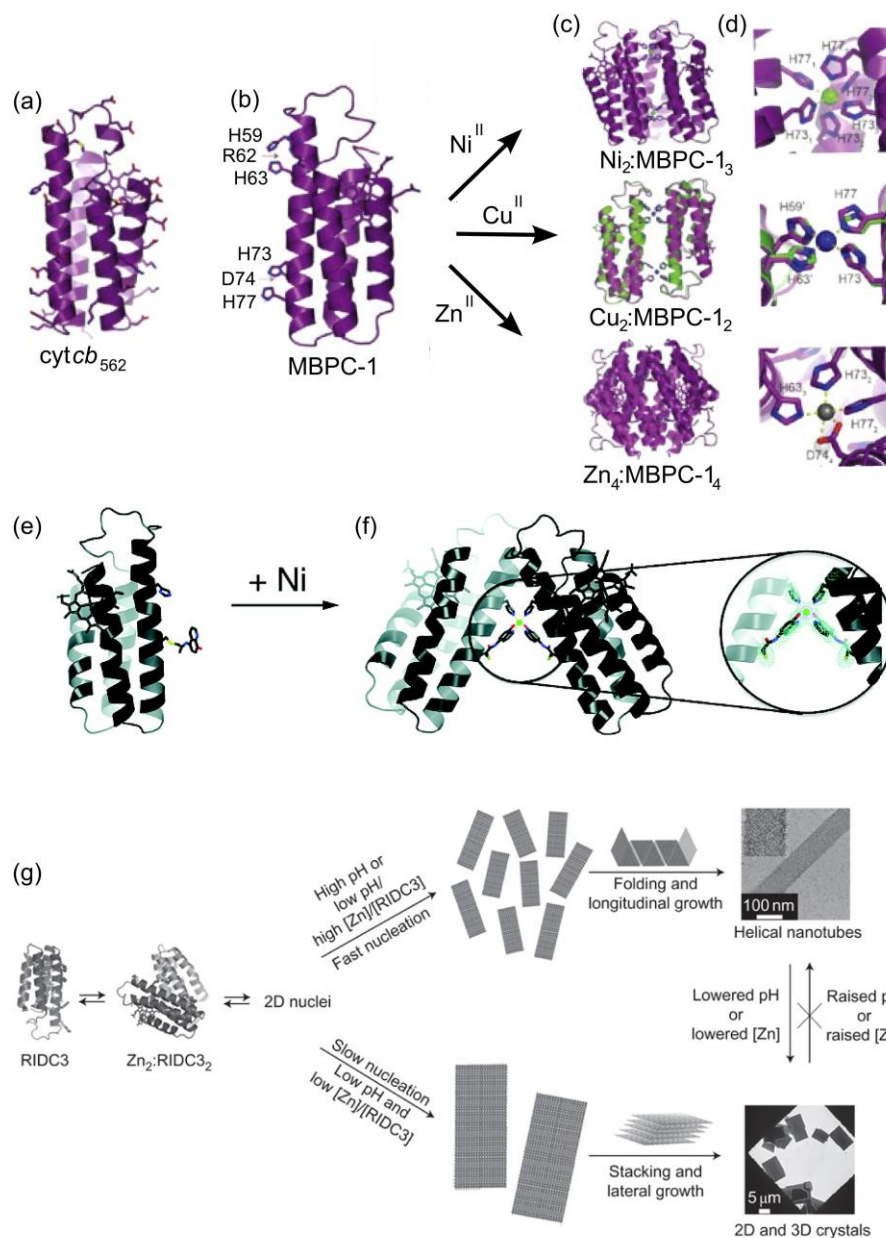


Figure 1.4: Applications of metal-directed protein self-assembly. (a) Cartoon of the building block *cyt cb<sub>562</sub>*, showing potential metal-binding residues as sticks. (b) MBPC-1 can assemble into discrete architectures (c) upon metal coordination, and the geometry of the protein oligomers depend on the binding geometry (d) of the metal ion. (e) Incorporation of the his-quin hybrid-coordination motif on the protein surface assembles protein dimers (f) upon Ni<sup>II</sup> coordination. (g) Assembly of RIDC3 monomers upon Zn<sup>II</sup> coordination, first into dimers upon binding to high affinity metal sites, and then to extended protein arrays. Panels a-d adapted from ref. 54, e-f from ref. 59, and g from ref. 61.

square deviation of 1.6 Å over the helical carbon backbone in the dimeric interface (Figure 1.4e,f).

A second application of MDPSA has been to direct the formation of ordered, 1- and 2-dimensional protein materials using a cytochrome *cb<sub>562</sub>* variant with a redesigned protein interface (RIDC3). We have shown that by incorporating both high affinity Zn<sup>II</sup> binding sites that mediate tetramer formation, and low affinity Zn<sup>II</sup> binding sites that can coordinate protein tetramers to assemble into highly ordered, crystalline 1-dimensional nanotubes or 2-dimensional protein arrays (Figure 1.4g).<sup>62</sup> Further, the assembly of these arrays protected against protein denaturation under conditions that would typically disrupt non-covalent protein assemblies and structures.<sup>63</sup>

## 1.5 Goals of this Thesis

The main goals of my research dissertation are:

- (1) *To expand the use of metal-ion coordination onto short peptide backbones to create stably-folded, helical peptide platforms that mimic biological interactions*
- (2) *To create new protein-based materials by expanding our control over their metal-directed assembly processes*

We have now established the use of MDPSA as a viable method to assemble discrete protein oligomers or large, ordered protein-assemblies. As discussed above, there has been a great deal of interest in finding methods of folding peptide  $\alpha$ -helices to mimic biological interactions. We aim to show that the use of metal-coordination to fold peptides enables us to obtain biologically relevant orientations to target protein-protein and protein-DNA interactions. Further, we have the ability to take advantage of inherent metal functionalities that are not available in other methods of helix stabilization.



We next intend to demonstrate the formation of novel nanobiomaterials. First, we show that by increasing the symmetry of the tetrameric protein building block, we are able to better control anisotropic assembly of protein nanotubes by mediating solution conditions. In this case, these effects are manifest in the observation of crystalline nanotubes with tunable diameters.

Finally, we have created a completely novel biomaterial by synthesizing DNA-protein conjugates that are then assembled into crystalline arrays by metal coordination. These materials form extended arrays in a cooperative manner, and are one of the first examples of a hybrid DNA-protein material that does not rely exclusively on programmable DNA interactions for assembly.

## 1.6 References

- (1) Adams, J. M.; Cory, S. *Science* **1998**, *281*, 1322.
- (2) van der Rest, M.; Garrone, R. *FASEB J.* **1991**, *5*, 2814.
- (3) Jordan, M. A.; Wilson, L. *Nat Rev Cancer* **2004**, *4*, 253.
- (4) Nooren, I. M. A.; Thornton, J. M. *EMBO J.* **2003**, *22*, 3486.
- (5) Bullock, B. N.; Jochim, A. L.; Arora, P. S. *J. Am. Chem. Soc.* **2011**, *133*, 14220.
- (6) Murray, J. K.; Gellman, S. H. *Biopolymers* **2007**, *88*, 657.
- (7) Yin, H.; Hamilton, A. D. *Angew. Chem. Int. Ed.* **2005**, *44*, 4130.
- (8) Azzarito, V.; Long, K.; Murphy, N. S.; Wilson, A. J. *Nat. Chem.* **2013**, *5*, 161.
- (9) Edwards, T.; Wilson, A. *Amino Acids* **2011**, *41*, 743.
- (10) Arkin, M. R.; Wells, J. A. *Nat. Rev. Drug Discov.* **2004**, *3*, 301.
- (11) Keane, H.; Ryan, B. J.; Jackson, B.; Whitmore, A.; Wade-Martins, R. *Sci. Rep.* **2015**, *5*, 17004.

- (12) Thompson, C. B. *Science* **1995**, 267, 1456.
- (13) Verdine, G. L.; Walensky, L. D. *Clin. Cancer Res.* **2007**, 13, 7264.
- (14) Whitty, A.; Kumaravel, G. *Nat Chem Biol* **2006**, 2, 112.
- (15) Estieu-Gionnet, K.; Guichard, G. *Expert Opin. Drug Discov.* **2011**, 6, 937.
- (16) Jackson, D. Y.; King, D. S.; Chmielewski, J.; Singh, S.; Schultz, P. G. *J. Am. Chem. Soc.* **1991**, 113, 9391.
- (17) Miller, S. E.; Kallenbach, N. R.; Arora, P. S. *Tetrahedron* **2012**, 68, 4434.
- (18) Walensky, L. D.; Bird, G. H. *J. Med. Chem.* **2014**, 57, 6275.
- (19) Walensky, L. D.; Kung, A. L.; Escher, I.; Malia, T. J.; Barbuto, S.; Wright, R. D.; Wagner, G.; Verdine, G. L.; Korsmeyer, S. J. *Science* **2004**, 305, 1466.
- (20) Blackwell, H. E.; Grubbs, R. H. *Angew. Chem. Int. Ed.* **1998**, 37, 3281.
- (21) Fujimoto, K.; Kajino, M.; Inouye, M. *Chem. Eur. J.* **2008**, 14, 857.
- (22) Taylor, J. W. *J. Pept. Sci.* **2002**, 66, 49.
- (23) Phelan, J. C.; Skelton, N. J.; Braisted, A. C.; McDowell, R. S. *J. Am. Chem. Soc.* **1997**, 119, 455.
- (24) Taylor, J. W. *Biopolymers* **2002**, 66, 49.
- (25) Baek, S.; Kutchukian, P. S.; Verdine, G. L.; Huber, R.; Holak, T. A.; Lee, K. W.; Popowicz, G. M. *J. Am. Chem. Soc.* **2012**, 134, 103.
- (26) Patgiri, A.; Jochim, A. L.; Arora, P. S. *Acc. Chem. Res.* **2008**, 41, 1289.
- (27) Cabezas, E.; Satterthwait, A. C. *J. Am. Chem. Soc.* **1999**, 121, 3862.
- (28) Horne, W. S.; Price, J. L.; Gellman, S. H. *Proc. Nat. Sci. Acad. U.S.A.* **2008**, 105, 9151.
- (29) Kritzer, J. A.; Stephens, O. M.; Guarracino, D. A.; Reznik, S. K.; Schepartz, A. *Bioorg. Med. Chem.* **2005**, 13, 11.
- (30) Cheng, R. P.; Gellman, S. H.; DeGrado, W. F. *Chem. Rev.* **2001**, 101, 3219.
- (31) Kritzer, J. A.; Zutshi, R.; Cheah, M.; Ran, F. A.; Webman, R.; Wongjirad, T. M.; Schepartz, A. *ChemBioChem* **2006**, 7, 29.
- (32) Baneyx, F.; Matthaei, J. F. *Curr. Opin. Biotechnol.* **2014**, 28, 39.

- (33) Pum, D.; Toca-Herrera, J. L.; Sleytr, U. B. *Int. J. Mol. Sci.* **2013**, *14*, 2484.
- (34) Sára, M.; Sleytr, U. B. *J. Bacteriol.* **2000**, *182*, 859.
- (35) Mark, S. S.; Bergkvist, M.; Yang, X.; Teixeira, L. M.; Bhatnagar, P.; Angert, E. R.; Batt, C. A. *Langmuir* **2006**, *22*, 3763.
- (36) Shenton, W.; Pum, D.; Sleytr, U. B.; Mann, S. *Nature* **1997**, *389*, 585.
- (37) Dieluweit, S.; Pum, D.; Sleytr, U. B. *Supramolecular Science* **1998**, *5*, 15.
- (38) Ilk, N.; Egelseer, E. M.; Sleytr, U. B. *Curr. Opin. Biotechnol.* **2011**, *22*, 824.
- (39) Seeman, N. C. *Annu. Rev. Biochem.* **2010**, *79*, 65.
- (40) Ulijn, R. V.; Smith, A. M. *Chem. Soc. Rev.* **2008**, *37*, 664.
- (41) Ringler, P.; Schulz, G. E. *Science* **2003**, *302*, 106.
- (42) Kitagishi, H.; Kakikura, Y.; Yamaguchi, H.; Oohora, K.; Harada, A.; Hayashi, T. *Angew. Chem. Int. Ed.* **2009**, *48*, 1271.
- (43) Oohora, K.; Onoda, A.; Hayashi, T. *Chem. Commun.* **2012**, *48*, 11714.
- (44) Sinclair, J. C.; Davies, K. M.; Venien-Bryan, C.; Noble, M. E. M. *Nat. Nanotech.* **2011**, *6*, 558.
- (45) Lai, Y.-T.; King, N. P.; Yeates, T. O. *Trends Cell Biol.* **2012**, *22*, 653.
- (46) Padilla, J. E.; Colovos, C.; Yeates, T. O. *Proc. Nat. Sci. Acad. U.S.A.* **2001**, *98*, 2217.
- (47) Dotan, N.; Arad, D.; Frolow, F.; Freeman, A. *Angew. Chem. Int. Ed.* **1999**, *38*, 2363.
- (48) Lai, Y.-T.; Cascio, D.; Yeates, T. O. *Science* **2012**, *336*, 1129.
- (49) King, N. P.; Bale, J. B.; Sheffler, W.; McNamara, D. E.; Gonen, S.; Gonen, T.; Yeates, T. O.; Baker, D. *Nature* **2014**, *510*, 103.
- (50) King, N. P.; Sheffler, W.; Sawaya, M. R.; Vollmar, B. S.; Sumida, J. P.; André, I.; Gonen, T.; Yeates, T. O.; Baker, D. *Science* **2012**, *336*, 1171.
- (51) Gonen, S.; DiMaio, F.; Gonen, T.; Baker, D. *Science* **2015**, *348*, 1365.
- (52) Song, W. J.; Sontz, P. A.; Ambroggio, X. I.; Tezcan, F. A. *Annu. Rev. Biophys.* **2014**, *43*, 409.

- (53) Bixby, K. A.; Nanao, M. H.; Shen, N. V.; Kreusch, A.; Bellamy, H.; Pfaffinger, P. J.; Choe, S. *Nat. Struct. Mol. Biol.* **1999**, *6*, 38.
- (54) Hopfner, K.-P.; Craig, L.; Moncalian, G.; Zinkel, R. A.; Usui, T.; Owen, B. A. L.; Karcher, A.; Henderson, B.; Bodmer, J.-L.; McMurray, C. T.; Carney, J. P.; Petrini, J. H. J.; Tainer, J. A. *Nature* **2002**, *418*, 562.
- (55) Radford, R. J.; Brodin, J. D.; Salgado, E. N.; Tezcan, F. A. *Coord. Chem. Rev.* **2011**, *255*, 790.
- (56) Salgado, E. N.; Radford, R. J.; Tezcan, F. A. *Acc. Chem. Res.* **2010**, *43*, 661.
- (57) Faraone-Mennella, J.; Tezcan, F. A.; Gray, H. B.; Winkler, J. R. *Biochemistry* **2006**, *45*, 10504.
- (58) Salgado, E. N.; Faraone-Mennella, J.; Tezcan, F. A. *J. Am. Chem. Soc.* **2007**, *129*, 13374.
- (59) Salgado, E. N.; Lewis, R. A.; Mossin, S.; Rheingold, A. L.; Tezcan, F. A. *Inorg. Chem.* **2009**, *48*, 2726.
- (60) Radford, R. J.; Nguyen, P. C.; Ditri, T. B.; Figueroa, J. S.; Tezcan, F. A. *Inorg. Chem.* **2010**, *49*, 4362.
- (61) Radford, R. J.; Nguyen, P. C.; Tezcan, F. A. *Inorg. Chem.* **2010**, *49*, 7106.
- (62) Brodin, J. D.; Ambroggio, X. I.; Tang, C.; Parent, K. N.; Baker, T. S.; Tezcan, F. A. *Nat. Chem.* **2012**, *4*, 375.
- (63) Brodin, J. D.; Carr, J. R.; Sontz, P. A.; Tezcan, F. A. *Proc. Nat. Sci. Acad. U.S.A.* **2014**, *111*, 2897.

## 2. Functional, metal-based crosslinkers for $\alpha$ -helix induction in short peptides

### 2.1 Abstract

Many protein-protein interactions that play a central role in cellular processes involve  $\alpha$ -helical domains. Consequently, there has been great interest in developing strategies for stabilizing short peptides in  $\alpha$ -helical conformations toward the inhibition and interrogation of protein-protein interactions. Here, we show that tridentate Hybrid-Coordination Motifs (HCMs), which consist of natural (histidine, His) and an unnatural (8-hydroxyquinoline, Quin) metal binding functionality, can bind divalent metal ions with high affinity and thereby induce/stabilize an  $\alpha$ -helical configuration in short peptide sequences. The Quin functionality is readily introduced onto peptide platforms both during or after solid-state peptide synthesis, demonstrating the preparative versatility of HCMs. A systematic study involving a series of HCM-bearing peptides has revealed the critical importance of the length of the linkage between the Quin moiety and the peptide backbone as well as the metal coordination geometry in determining the extent of  $\alpha$ -helix induction. Through  $Zn^{II}$  coordination or modification with  $Re^I(Quin)(CO)_3$ , the HCM-bearing peptides can be rendered luminescent in the visible region, thus showing that HCMs can be exploited to simultaneously introduce structure and functionality into short peptides. The general applicability of HCMs is demonstrated via metal-induced  $\alpha$ -helix formation in a peptide sequence that mimics the helical BH3 domain of the pro-apoptotic protein Bax.

## 2.2 Introduction

Many natural protein-protein interactions (PPIs) are mediated by  $\alpha$ -helical recognition and binding motifs on protein surfaces.<sup>1</sup> Because of the central involvement of PPIs in all cellular processes, considerable research activity has focused on designing non-natural,<sup>2-8</sup> protein-<sup>9,10</sup> or peptide-based platforms that structurally and chemically mimic  $\alpha$ -helical protein surface motifs.<sup>11,12</sup> A drawback of using small peptidic platforms is that they are generally unstructured and susceptible to proteolytic cleavage.<sup>13</sup> To overcome this challenge, a number of strategies have been devised to stabilize them in  $\alpha$ -helical conformations. These strategies include the incorporation of  $\alpha$ -amino acids with restricted conformation space,<sup>14,15</sup> inclusion of salt-bridging residues in  $i/i+4$  positions,<sup>16</sup> crosslinking of side chains through covalent bonds<sup>17-26</sup> or metal-coordination,<sup>27-32</sup> and utilization of hydrogen bond surrogates.<sup>33,34</sup> Each of these platforms has its own set of advantages concerning ease of preparation, the extent of protein modification and  $\alpha$ -helix induction, stability, target recognition and *in vivo* uptake, but none of them simultaneously offer all of these advantages or are universally applicable. Moreover, in most instances, these helix induction motifs solely serve a structural purpose, with little functional value added to the peptide. Therefore, it would be desirable to have access to alternative experimental platforms for helix induction that are easy to incorporate and modify, while simultaneously allowing the peptide to be functionalized and its secondary structure and other physicochemical properties to be easily modified.

Toward this goal, we present here short peptides that display Hybrid Coordination Motifs (HCMs), which are tridentate metal coordination modules consisting of a natural metal-coordinating residues such as histidine (His) at position  $I$  and an unnatural, bidentate

chelating group such as 8-hydroxyquinoline (Quin) or 1,10-phenanthroline (Phen) covalently attached to the side chain at position  $i+7$  (Figure 2.1). We first introduced HCMs as high-affinity coordination units on the surface of a folded, four-helix bundle protein (cytochrome *cb<sub>562</sub>*) to mediate protein self-assembly upon metal coordination.<sup>35,36</sup>

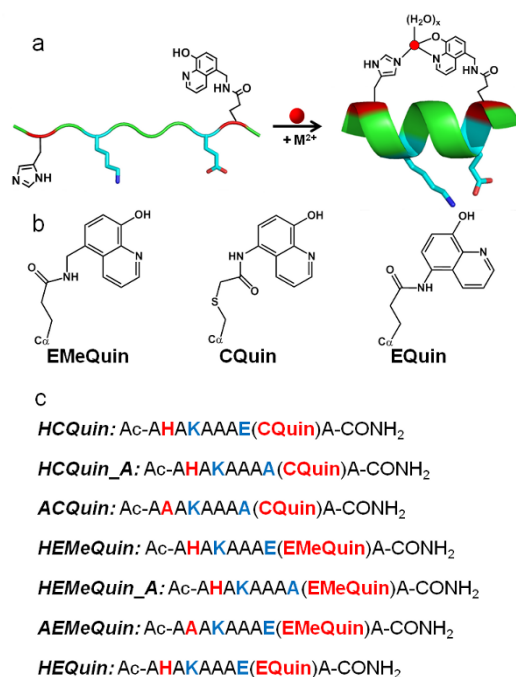


Figure 2.1: (a) Proposed scheme for  $\alpha$ -helix induction through tridentate metal coordination by an HCM. The remaining coordination sites on the metal are likely filled by aquo ligands. (b) Chemical structures of various Quin functionalities. (c) Sequences of peptide constructs prepared in this study. The coloring scheme corresponds to that in (a).

These studies revealed that the stability of the entire cyt *cb<sub>562</sub>* fold increased by up to 4 kcal/mol upon binding of various divalent transition metal ions ( $Co^{II}$ ,  $Ni^{II}$ ,  $Cu^{II}$ , and  $Zn^{II}$ ), suggesting that HCMs might also be employed toward induction of  $\alpha$ -helicity in unstructured peptides while allowing the incorporation of metal-based functionalities.

Here, we have undertaken a systematic study in which we explored the chemical and physical properties of 10-residue-long peptides decorated with  $i/i+7$  His/Quin HCMs. We describe that the Quin moiety can be readily installed onto peptides either after solid-phase peptide synthesis (SPPS) via coupling to a cysteine (Cys) side chain or in the form of an unnatural amino acid during SPPS. We have found that the induction of  $\alpha$ -helicity is critically dependent on the linker length between the Quin moiety and the peptide backbone, and that the extent of  $\alpha$ -helicity can be controlled by the choice of the coordinating metal ion. The His/Quin HCMs can be rendered luminescent through  $Zn^{II}$  binding, or alternatively, via coordination to a luminescent and substitution-inert  $Re^I(Quin)(CO)_3$  moiety following SPPS. Finally, it is shown that His/Quin HCMs can induce considerable  $\alpha$ -helicity in a peptide sequence that mimics the BH3 domain of the pro-apoptotic protein Bax. Thus, HCMs represent a versatile, easily implementable platform that allows simultaneous induction/modulation of  $\alpha$ -helicity and the introduction of metal-based functionalities into peptide sequences.

## **2.3 Results and Discussion**

### **2.3.1 Preparation of peptides containing His/Quin HCMs**

#### **2.3.1.1 General**

The sequence and basic architecture of the HCM-bearing peptide platforms we have investigated are shown in Figure 2.1. All constructs are 10-residue, alanine (Ala)-rich peptides that were synthesized with a C-terminal amide and an acylated N-terminus via SPPS using standard Fmoc protecting group chemistry. Complete details on synthesis, peptide modification, purification and chemical analysis can be found in Materials and Methods. In general, the peptide sequences contained a His residue at position 2 ( $i$ ) and a



Quin-functionalized sidechain at position 9 ( $i+7$ ), which would be two turns away in an  $\alpha$ -helical configuration. The parent sequence also contained a lysine (Lys) at position 4 and a glutamic acid (Glu) at position 8 to form a potential salt bridge on a second face of the helix to further promote  $\alpha$ -helicity and to increase the solubility of the peptide.

### 2.3.1.2 Routes for the incorporation of Quin functionality

The Quin functionality was introduced in two different ways: either during SPPS in the form of a pre-synthesized unnatural amino acid or after SPPS through covalent coupling to a Cys residue. For the former strategy, two Quin-bearing, Fmoc-protected amino acids (EQuin and EMeQuin, Figure 2.1b) were first prepared through the HATU-mediated coupling of 5-aminomethyl-8-hydroxyquinoline to Fmoc-protected L-Glu (see Materials and Methods for synthetic details). EMeQuin presents the Quin functionality one extra methylene group removed from the peptide backbone compared to EQuin. The third Quin variant, CQuin, was obtained through the covalent coupling of 5-iodoacetamido-8-hydroxyquinoline (IA-Quin) to a Cys at position 9 following SPPS, paralleling our previous strategy to place a Quin moiety on the surface of the cytochrome *cb<sub>562</sub>*. CQuin, like EMeQuin, is separated from the peptide backbone by five single bonds although two of these bonds are slightly longer thioether linkages. It is important to note that the pre-SPPS preparative route of EQuin and EMeQuin potentially affords flexibility for creating multiply-functionalized HCM-bearing peptides, and eliminates the complications associated with postsynthetic labeling of Cys residues on whole-length peptides. It should further be mentioned that Quin-functionalized L-amino acids such as Sox have been previously reported by Imperiali and colleagues,<sup>37,38</sup> who placed these functionalities within  $\beta$ -turn peptides for Zn<sup>II</sup> sensing. The short side chains of Sox derivatives, which

feature only a single methylene group between the Quin moiety and the  $\alpha$ -carbon, are ideal for placement into the interior of a folded peptide, whereas EMeQuin, EQuin, and CQuin functionalities are, by design, long enough to extend over two turns on the surface of an  $\alpha$ -helix.

### 2.3.1.3 Control peptides

In addition to H-EMeQuin, H-EQuin and H-CQuin (where H stands for the His component of the HCM in the 2 position), we prepared two further sets of peptides to investigate a) the importance of the His component of the HCM and b) the necessity of the Lys(4)-Glu(8) salt bridge in the induction of  $\alpha$ -helicity. For (a), we prepared the constructs A-CQuin and A-EMeQuin, which have His(2) replaced with a non-coordinating alanine (Ala) residue. For (b), we prepared H-CQuin-A and H-EMeQuin-A, which include an Ala in place of Glu(8).

### 2.3.2 Metal Binding Properties of His/Quin HCMs

We first studied the binding thermodynamics of  $\text{Co}^{\text{II}}$ ,  $\text{Ni}^{\text{II}}$ ,  $\text{Cu}^{\text{II}}$  and  $\text{Zn}^{\text{II}}$  to the three HCM-bearing peptides, H-EMeQuin, H-CQuin and H-EQuin, by monitoring the 20-nm red shift of the  $\pi$ - $\pi^*$  absorption band of Quin ( $\lambda_{\text{max}} = 244$  nm) upon metal coordination (Figure 2.2). As we previously observed with HCMs installed on the cytochrome *cb*<sub>562</sub> surface,<sup>35,36</sup> the binding affinities of the HCM-bearing peptides were too high to be measured by direct titrations. Therefore, EGTA (ethylene glycol tetraacetic acid) or ADA (*N*-(2-acetamido)iminodiacetic acid) was included in the titration as a competing ligand. ADA was used in cases where metal-peptide binding was not strong enough to compete

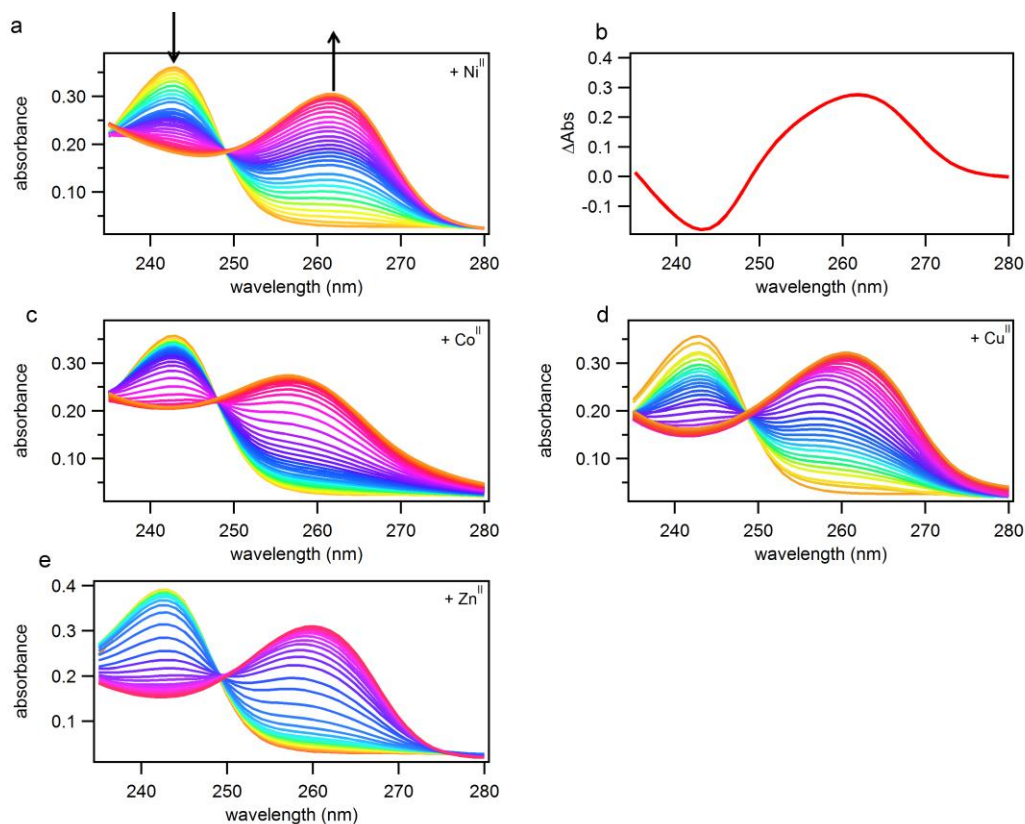


Figure 2.2: UV-vis spectral changes upon Quin-M<sup>II</sup> coordination. A solution containing 16  $\mu\text{M}$  H-EMeQuin and 45  $\mu\text{M}$  EGTA was titrated with increasing amounts of M<sup>II</sup>. (a) An approximately 20 nm red shift is observed upon Ni<sup>II</sup> binding, shifting the maximum absorbance of the  $\pi$ - $\pi^*$  transition from approximately 244 nm to 262 nm. (b) The difference spectrum between the first, completely metal-free spectrum and the last, completely Ni<sup>II</sup>-bound spectrum. (c) The spectral shift as a result of Co<sup>II</sup> binding. (d) The spectral shift as a result of Cu<sup>II</sup> binding. (e) The spectral shift as a result of Zn<sup>II</sup> binding.

with EGTA, specifically in the cases of Co<sup>II</sup> and Zn<sup>II</sup>. Under our experimental conditions, which included 10-20  $\mu\text{M}$  peptide, 30-60  $\mu\text{M}$  EGTA or ADA, and 0-60  $\mu\text{M}$  M<sup>II</sup>, all binding curves were best described using a model that simultaneously took into account a 1:1 peptide:metal binding equilibrium (P:M) and a 2:1 metal-mediated peptide dimerization

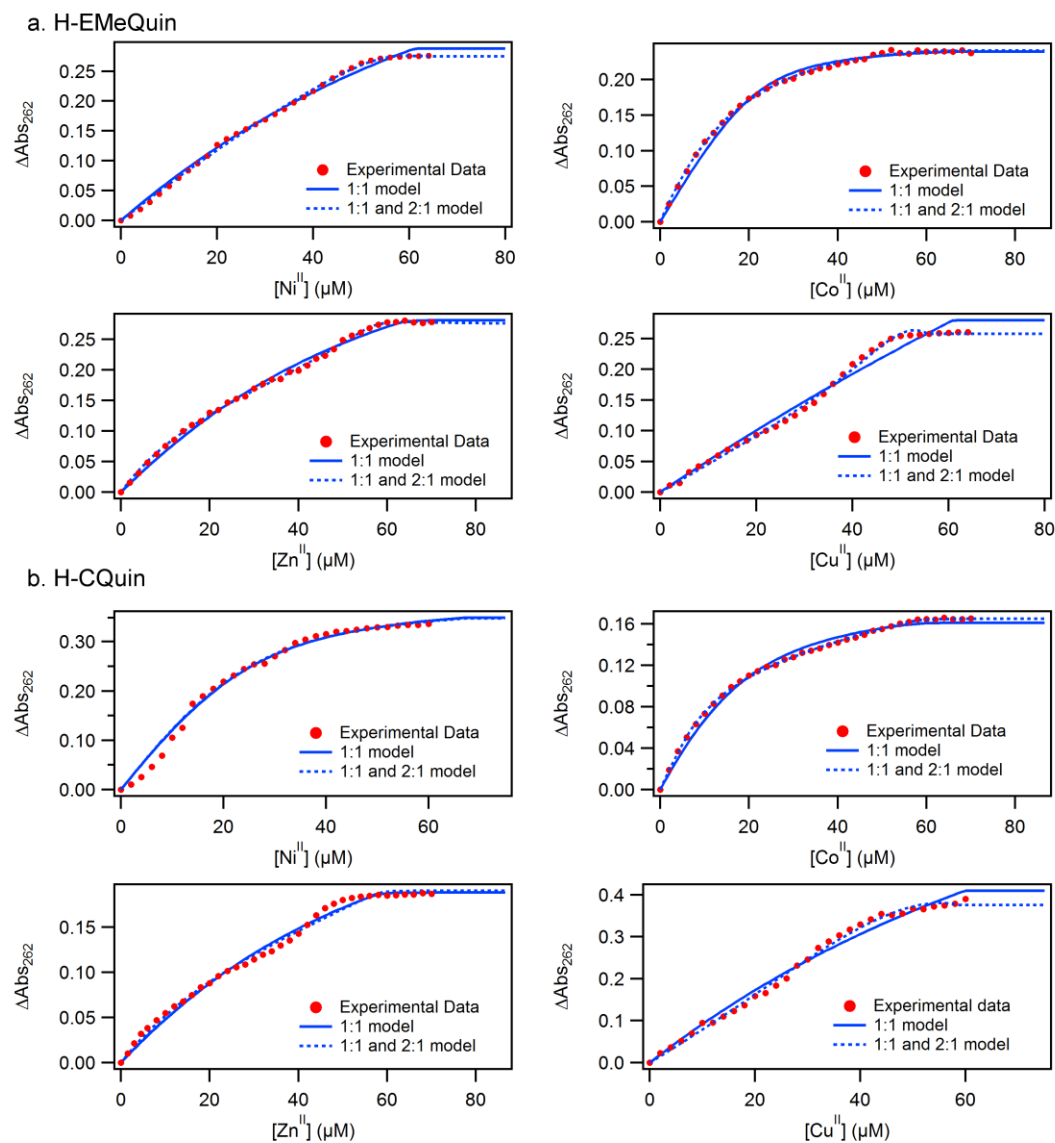


Figure 2.3: Peptide-metal binding titrations and fits. Titrations of **(a)** H-EMeQuin, **(b)** H-CQuin, and **(c)** H-EQuin with late first row transition metals as monitored by UV-vis spectroscopy. Two different models were used for fitting, one assuming a 1:1 binding stoichiometry between the peptide and metal (solid blue line), and the second accounting for the possibility of metal-induced dimerization (dotted blue line). The 1:1 and 2:1 model fit the data better, indicating that a peptide-metal dimer was likely forming at low metal concentration. In all cases, the values for metal-binding obtained through the 1:1 and 2:1 model were reported.

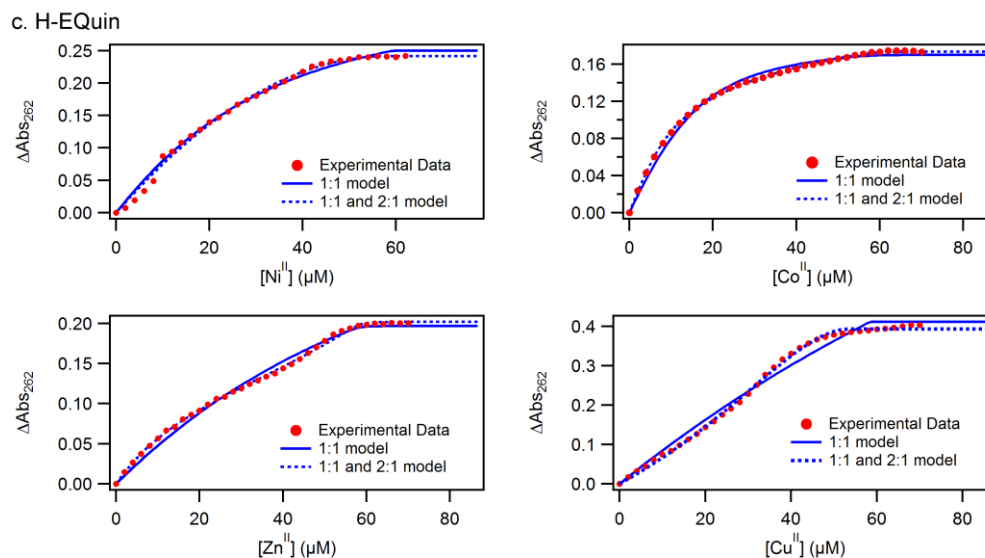


Figure 2.3: Peptide-metal binding titrations and fits, continued.

<p>a.</p> <pre>[task] task = fit data = equilibria ?  [mechanism] p + m &lt;==&gt; pm : kd1 dissoc e + m &lt;==&gt; em  : kd2 dissoc  [constants] kd1 = 5e-8 ? kd2 = 2.803e-9  [concentrations] p = 13.8e-6 e = 45e-6  [responses] p = 0 Pm = 15000</pre>	<p>b.</p> <pre>[task] task = fit data = equilibria ?  [mechanism] p + m &lt;==&gt; pm : kd1 dissoc e + m &lt;==&gt; em  : kd2 dissoc pm + p &lt;==&gt; d  : kd3 dissoc  [constants] kd1 = 1e-10 ? kd2 = 2.803e-9 kd3 = 1e-5 ?  [concentrations] p = 13.8e-6 e = 45e-6  [responses] p = 0 pm = 15000 d = 30000 ?</pre>
---	---

Figure 2.4: Dynafit scripts for describing metal-peptide binding equilibria. Two models for binding were used: (a) A 1:1 peptide:metal competitive binding model, and: (b) A 1:1 and 2:1 peptide:metal competitive binding model, taking into account the possibility for metal-induced peptide dimerization at limiting metal concentrations. Metal-chelator dissociation constants were obtained using MaxChelator and held fixed. The variables used include: peptide (p), metal (m), peptide-metal complex (pm), metal-induced peptide dimer (d), chelator (e), and metal-chelator complex (em). Parameters that were allowed to float during the fitting process are followed by “?” and all other parameters were held fixed.

event (P : M : P) (Figures Figure 2.3 and Figure 2.4). In all cases studied, the dissociation constant ( $K_d$ ) for metal-mediated peptide dimers was determined to be in the low  $\mu\text{M}$  range.

The dissociation constants of the metal-HCM complexes (P:M) range from nanomolar for  $\text{Co}^{\text{II}}$  and  $\text{Zn}^{\text{II}}$  to femtomolar for  $\text{Cu}^{\text{II}}$  (Table 2.1). These  $K_d$ s are two to three orders of magnitude lower than those for the free Quin ligand (Table 2.1),<sup>39</sup> indicating the formation of the intended tridentate coordination mode that we previously observed in the crystal structure of a cytochrome *cb562* variant with a surface H-CQuin motif.<sup>35,36</sup> Notably, the metal binding affinities of the HCM-peptides are three to seven orders of magnitude higher than those observed for similar peptides bearing *i/i+4* bis-His chelation motifs<sup>27,40</sup> highlighting the dramatic effect of increased denticity on metal affinity. In general, the metal binding affinities of H-EMeQuin, H-CQuin and H-EQuin roughly follow the Irving-Williams series ( $\text{Co}^{\text{II}} < \text{Ni}^{\text{II}} < \text{Cu}^{\text{II}} > \text{Zn}^{\text{II}}$ ). The affinity of H-EMeQuin for each metal ion is consistently lower (by one to two orders of magnitude) than those of H-CQuin and H-EQuin, which we attribute to specific interactions between the HCMs and the peptide surface. Quantum mechanics/molecular mechanics (QM/MM) calculations are currently

Table 2.1: Dissociation constants for various peptide-metal complexes. Numbers in parentheses correspond to standard deviation in the last reported significant figure.

	Dissociation constants (M)			
	H-CQuin	H-EMeQuin	H-EQuin	Quin
$\text{Co}^{\text{II}}$	$2 (1) \times 10^{-9}$	$1.2 (5) \times 10^{-8}$	$2 (1) \times 10^{-9}$	$6.5 \times 10^{-7}$
$\text{Ni}^{\text{II}}$	$2 (1) \times 10^{-11}$	$1.1 (1) \times 10^{-9}$	$2 (1) \times 10^{-10}$	$1.6 \times 10^{-7}$
$\text{Cu}^{\text{II}}$	$5.2 (1) \times 10^{-14}$	$1.4 (8) \times 10^{-13}$	$6.3 (1) \times 10^{-14}$	$2.3 \times 10^{-10}$
$\text{Zn}^{\text{II}}$	$6.2 (1) \times 10^{-9}$	$6.8 (3) \times 10^{-9}$	$3 (1) \times 10^{-9}$	$8.7 \times 10^{-7}$

underway to gain structural/energetic insights into H-EMeQuin, H-CQuin and H-EQuin and their metal complexes.

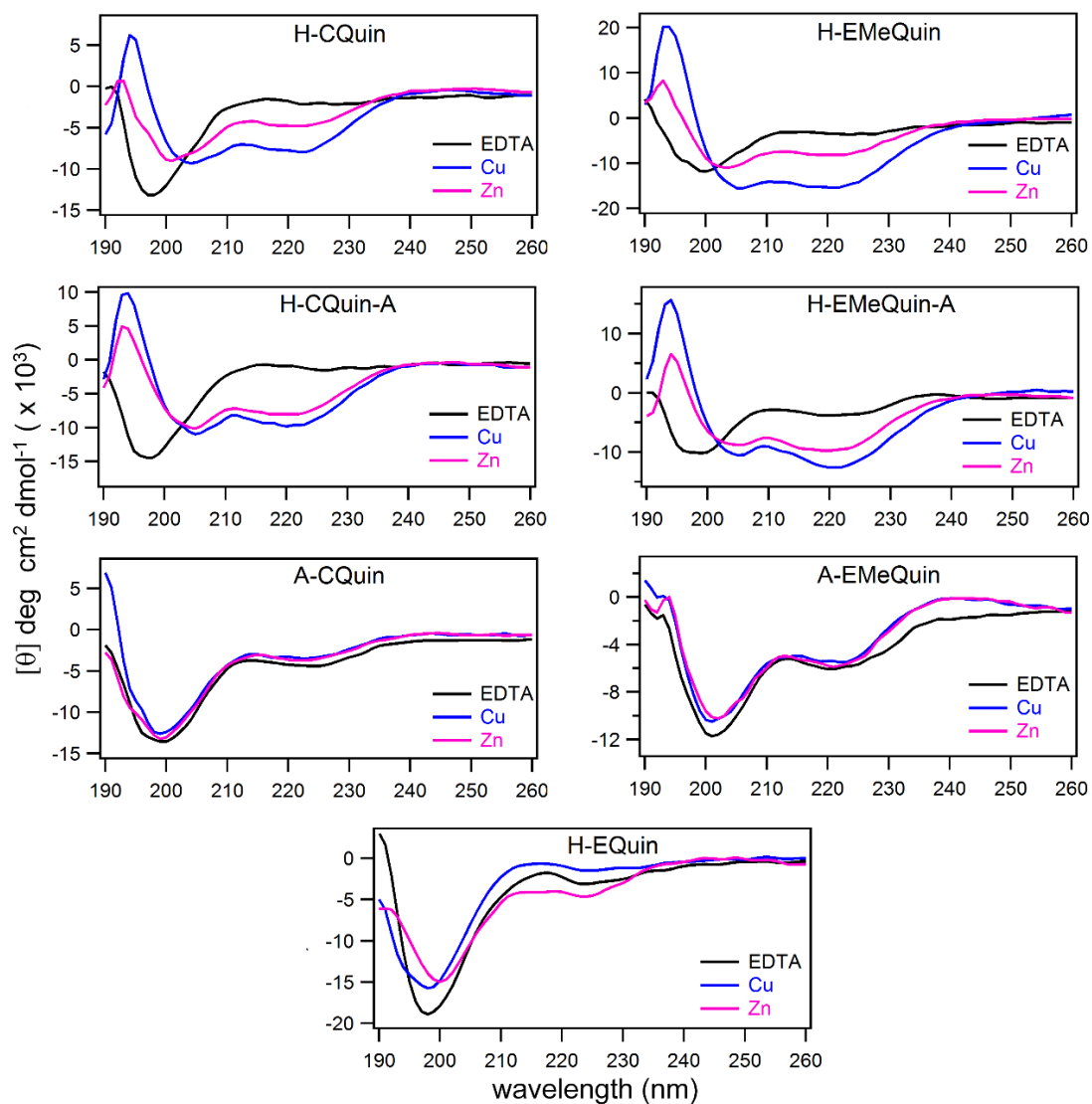


Figure 2.5: Changes in the circular dichroism spectra of HCM-bearing peptides upon binding  $\text{Cu}^{\text{II}}$  and  $\text{Zn}^{\text{II}}$ . Spectra were acquired at 4 °C with 10  $\mu\text{M}$  peptide and 30  $\mu\text{M}$  EDTA or metal in 5 mM sodium borate buffer at pH 7.5. Corresponding spectra for  $\text{Co}^{\text{II}}$  and  $\text{Ni}^{\text{II}}$  are shown in Figure 2.6 and Figure 2.7.

### 2.3.3 Metal-induced $\alpha$ -Helicity in HCM-containing Peptides

Metal-induced changes in the peptide secondary structure were monitored by circular dichroism (CD) spectroscopy (Figures Figure 2.5, Figure 2.6, and Figure 2.7), initially at 4 °C. In these experiments, a low peptide concentration (10  $\mu$ M) and a 3-fold excess of  $\text{Co}^{\text{II}}$ ,  $\text{Ni}^{\text{II}}$ ,  $\text{Cu}^{\text{II}}$ , or  $\text{Zn}^{\text{II}}$  ensured that metal-induced peptide dimerization was not a concern and that each peptide was fully bound to a metal ion. In the absence of metal binding, H-CQuin, H-EMeQuin, and H-EQuin all displayed a CD signature reflective of a random coil conformation with a minimum at 195 nm. Upon addition of metal ions, the spectrum for H-EQuin showed little to no change from the random coil conformation. In contrast, H-CQuin and H-EMeQuin, whose HCMs are one bond longer than H-EQuin, displayed a significant induction of  $\alpha$ -helicity as indicated by the emergence of two characteristic minima at  $\sim$ 206 and 222 nm.<sup>41</sup> Of all metal ions tested,  $\text{Cu}^{\text{II}}$  induced the greatest extent of helicity in H-CQuin and H-EMeQuin, followed by  $\text{Zn}^{\text{II}}$ ,  $\text{Ni}^{\text{II}}$ , and  $\text{Co}^{\text{II}}$  in descending order (Figure 2.6 and Figure 2.7). In all cases, stoichiometric metal coordination to the Quin functionality was confirmed by full red-shift of the Quin  $\pi$ - $\pi^*$  absorption band from 244 nm to 264 nm.

Upon replacement of the His component of the HCMs with an Ala to obtain A-CQuin and A-EMeQuin, metal-induced changes in the CD Spectra were abolished (Figure 2.6 and Figure 2.7). This finding confirmed that metal binding by the HCMs and the resulting cross-linking of the two-helix turn portion were responsible for  $\alpha$ -helix formation. The extent of  $\alpha$ -helicities of metal-bound H-CQuin and H-EMeQuin based on mean residue ellipticity at 222 nm are listed in Table 2.2, although such estimates have been reported to be inaccurate for short helices.<sup>42</sup> Therefore, we also obtained the CD spectra of H-CQuin



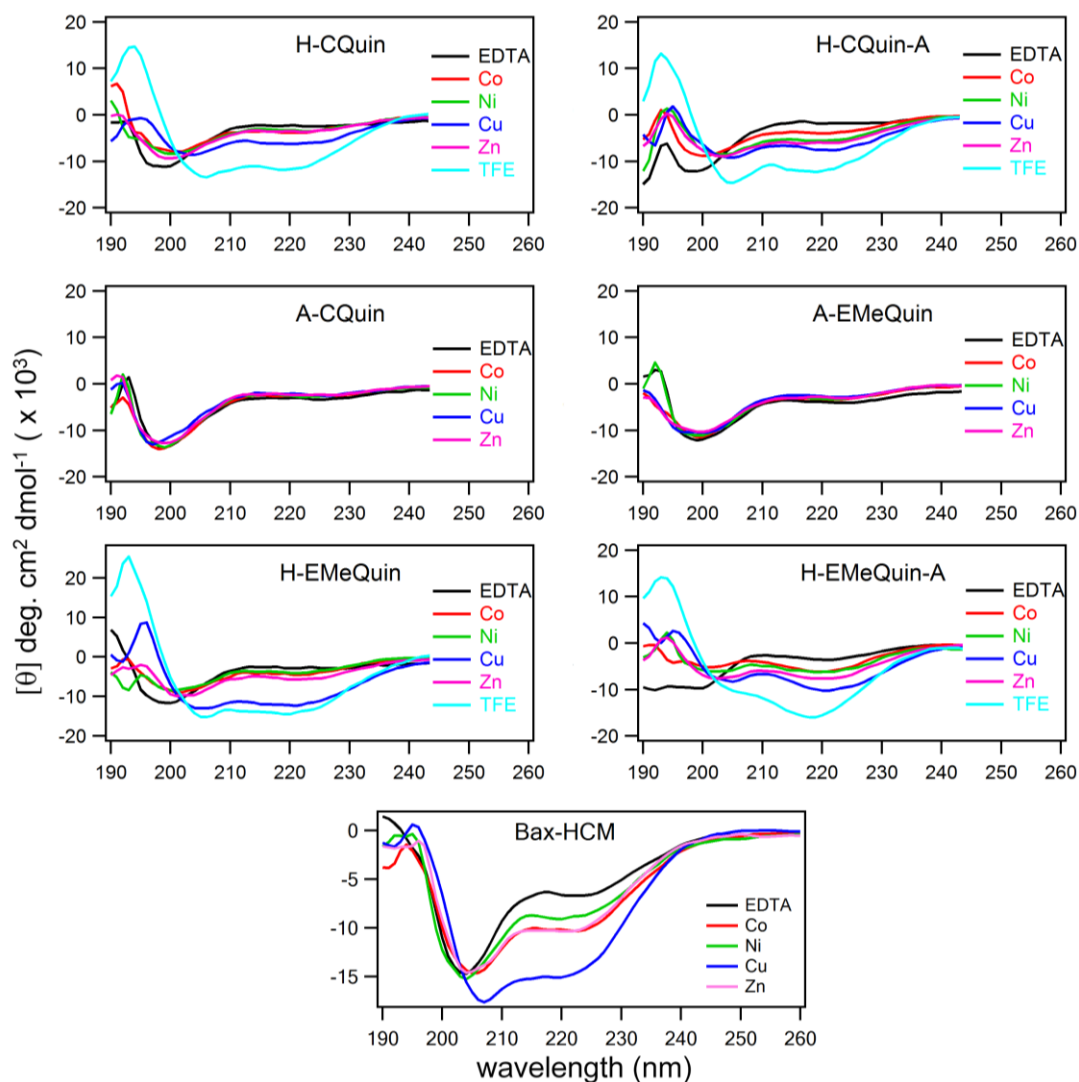


Figure 2.6: CD spectra of various peptides at 25 °C. Each sample was prepared with 10  $\mu\text{M}$  peptide and 30  $\mu\text{M}$  of either  $\text{M}^{\text{II}}$  or EDTA. For each graph, EDTA = black,  $\text{Ni}^{\text{II}}$  = green,  $\text{Co}^{\text{II}}$  = red,  $\text{Cu}^{\text{II}}$  = blue,  $\text{Zn}^{\text{II}}$  = pink, and TFE = cyan. TFE samples were prepared with metal-free peptide in 40% TFE. No further induction of helicity was observed upon the addition of metal to the TFE sample.

and H-EMeQuin in the presence of 60% trifluoroethanol (TFE), a potent helix inducer.<sup>43</sup>

Assuming that TFE produces a fully helical conformation, the  $\text{Cu}^{\text{II}}$ -complexes of H-CQuin and H-EMeQuin possess  $\sim 70\%$  and  $\sim 100\%$  helicity, respectively, at 4 °C, based on relative

CD intensities at 222 nm. At 25 °C, the Cu<sup>II</sup> complexes still retain significant secondary structure (H-CQuin, 54% helical; H-EMeQuin, 88% helical).

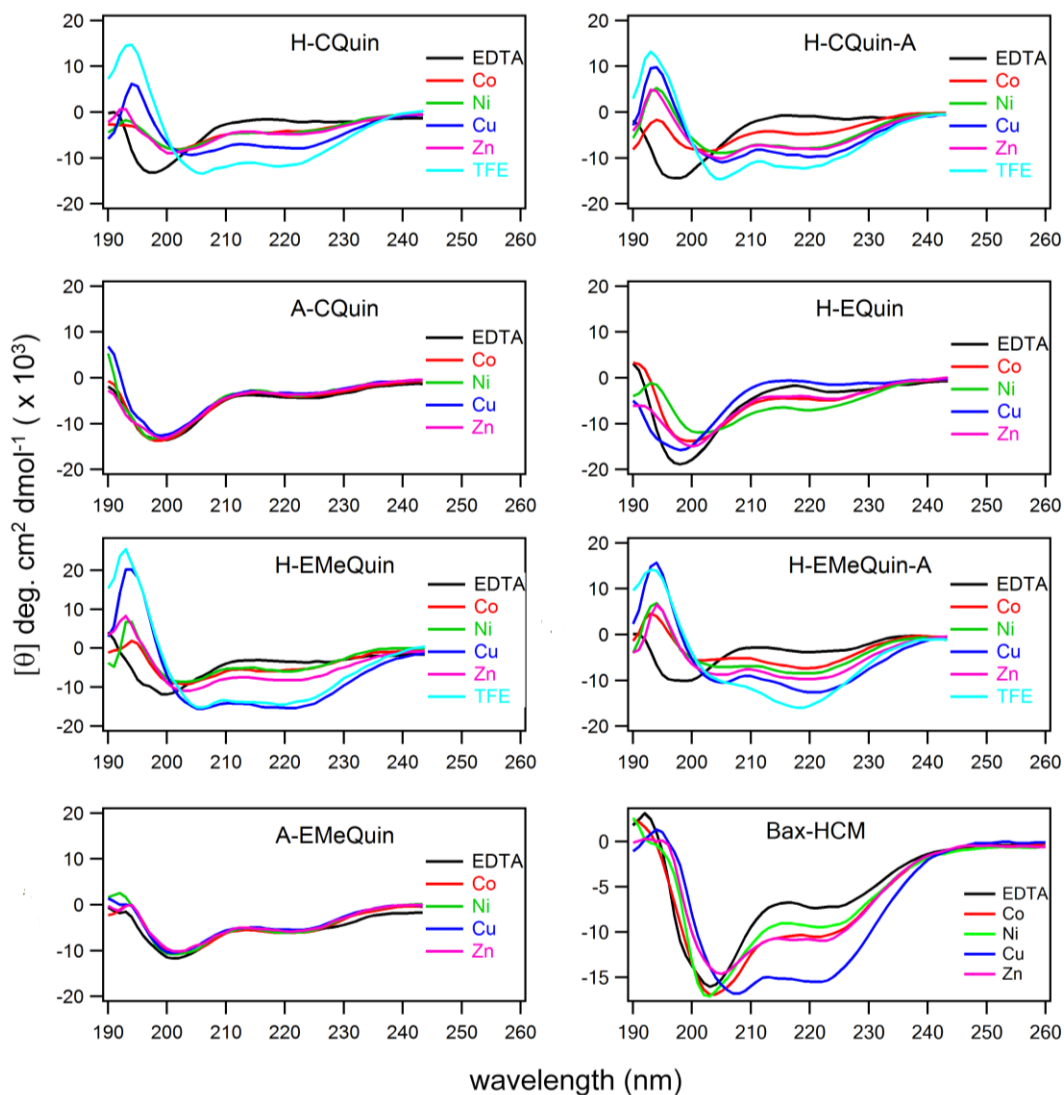


Figure 2.7: CD spectra of various peptides at 4 °C. Each sample was prepared with 10  $\mu\text{M}$  peptide and 30  $\mu\text{M}$  of either  $\text{M}^{\text{II}}$  or EDTA. For each graph, EDTA = black,  $\text{Ni}^{\text{II}}$  = green,  $\text{Co}^{\text{II}}$  = red,  $\text{Cu}^{\text{II}}$  = blue,  $\text{Zn}^{\text{II}}$  = pink, and TFE = cyan. TFE samples were prepared with metal-free peptide in 40% TFE. No further induction of helicity was observed upon the addition of metal to the TFE sample.

In order to determine whether the Lys(4)-Glu(8) salt bridge is necessary for  $\alpha$ -helix formation and the extent of its contribution to the peptide secondary structure, we examined the constructs H-EMeQuin-A and H-CQuin-A. The CD spectra of H-EMeQuin-A and H-CQuin-A showed that metal-induced helix formation was not affected by the elimination of the Lys(4)-Glu(8) salt bridge (Figure 2.6 and Figure 2.7): the helicities of both peptides ranged from ~80% in the presence of Cu<sup>II</sup> to ~40% in the presence of Co<sup>II</sup> (Table 2.2). In fact, Zn<sup>II</sup> binding induced more helicity for both peptides relative to the parent constructs containing salt bridges. Taken together, our findings clearly indicate that metal binding by the *i/i+7* HCMs alone can induce considerable  $\alpha$ -helicity in short helices. Importantly, HCMs occupy only one of the three available faces of an  $\alpha$ -helix, meaning that residues facing the other two faces can be used for the incorporation of other functionalities and for target recognition.

Table 2.2: Percent helicities for various metal-peptide complexes calculated (top) by comparison with a sample containing 60% TFE, and (bottom) using the ratio  $[\theta]_{222}/[\theta]_{\max}$ . Here  $[\theta]_{222}$  is the molar ellipticity measured at 222 nm, and  $[\theta]_{\max} = (-44000 + 250T)(1/k/n)$ , where  $k$  is a constant and equal to 4, and  $n$  is the number of amide bonds and equal to 10.

Peptide	Cu <sup>II</sup> (4 °C)	Zn <sup>II</sup> (4 °C)	EDTA(4 °C)	Cu <sup>II</sup> (25 °C)	Zn <sup>II</sup> (25 °C)
Percent Helicity, vs. TFE					
H-CQuin	69.9	42.3	18.8	53.4	32.7
H-CQuin-A	83.1	69.0	8.9	65.6	52.2
H-EMeQuin	102.2	54.7	23.3	88.3	40.9
H-EMeQuin-A	87.1	66.4	25.8	70.1	52.4
Percent Helicity, calculated					
H-CQuin	34.0	20.6	9.1	26.2	15.9
H-CQuin-A	41.2	34.2	4.4	32.5	25.9
H-EMeQuin	65.5	35.0	14.9	51.8	24.0
H-EMeQuin-A	53.4	40.7	15.8	43.0	32.1

### 2.3.4 Functionalization of HCMs

Having shown that H-CQuin and H-EMeQuin motifs tightly bind divalent transition metal ions and induce an  $\alpha$ -helical peptide conformation in doing so, we next investigated whether they can be simultaneously exploited for incorporating metal-based functionalities. In a rare previous example where this has been achieved, the Ball group has employed dirhodium complexes to induce helicity in short, unstructured peptides upon coordination to  $i/i+3$  and  $i/i+4$  Glu or Asp pairs;<sup>29</sup> the catalytic activity of these dirhodium-peptide conjugates were reported in separate studies.<sup>44,45</sup> In our case, we initially set out to take advantage of the Quin functionality, whose derivatives have long been employed in various analytical applications owing to their intense fluorescence that is activated in selective response to metal ions,<sup>46,47</sup> in particular to  $Zn^{II}$ .<sup>48-52</sup> Indeed, H-CQuin displayed a ~5-fold increase in fluorescence intensity at 540 nm upon  $Zn^{II}$  coordination, but not in the presence of  $Co^{II}$ ,  $Ni^{II}$ , or  $Cu^{II}$  (Figure 2.8a). As calculated with reference to a quinine sulfate standard, the quantum yield ( $\phi_{540nm}$ ) of  $Zn^{II}$ -H-CQuin is 0.27%, which is comparable to that of the  $Zn^{II}$  complex of free 8-hydroxy-2-methylquinoline (0.4%).<sup>50</sup> The amine group directly attached to the quinoline ring in H-CQuin likely quenches fluorescence by photoinduced electron transfer and is therefore partially responsible for the low quantum yield.<sup>53,54</sup> In accordance with this proposal, H-EMeQuin, in which the amine group is one methylene unit removed from the aromatic ring, showed a ~20-fold fluorescence enhancement upon  $Zn^{II}$  binding over background (Figure 2.8b), with an improved  $\phi_{540nm}$  of 0.64%. Further, regardless of His coordination, peptides tested containing a methylene spacer (A-EMeQuin, H-EMeQuin), consistently showed higher fluorescent intensity than

those peptides with the amine group directly attached to the quinoline ring (H-CQuin, A-CQuin, H-EQuin) (Figure 2.8b).

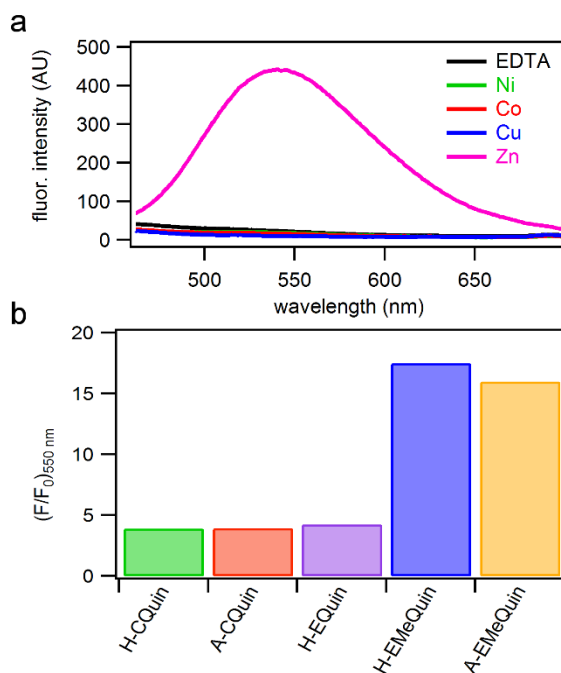


Figure 2.8: (a) H-EMeQuin fluorescence upon metal addition ( $\lambda_{\text{exc}} = 385\text{ nm}$ ). (b) Normalized fluorescence intensity ( $F/F_0$ ) of each peptide when bound to  $\text{Zn}^{\text{II}}$  as compared to the metal-free peptide.

Aside from coordinating aquated transition metal ions, the tripodal coordination motif of HCMs should also stably accommodate metal complexes that possess the appropriate geometry and could be used to endow the peptide scaffolds with additional functionalities. In particular, complexes of second- and third-row transition metals ( $\text{Re}^{\text{I}}$ ,  $\text{Ru}^{\text{II}}$ ,  $\text{Os}^{\text{II}}$ ,  $\text{Ir}^{\text{III}}$  and  $\text{Rh}^{\text{III}}$ ) display rich photophysical properties such as long lifetimes and high photostabilities<sup>55</sup> that have been exploited in biological imaging,<sup>56-61</sup> sometimes in the form of metallopeptide conjugates.<sup>62,63</sup> The direct integration of such metal complexes into a peptide crosslinking moiety would obviate the need for additional functional groups (i.e.,

fluorophores), which have been shown to influence the cellular localization of peptides.<sup>64,65</sup> Additionally, incorporation of these capped, substitution-inert metal complexes would eliminate the possibility of undesired metal-mediated peptide dimerization and yield kinetically stable conjugates that could persist in the intracellular environment, which is deprived of free metal ions.

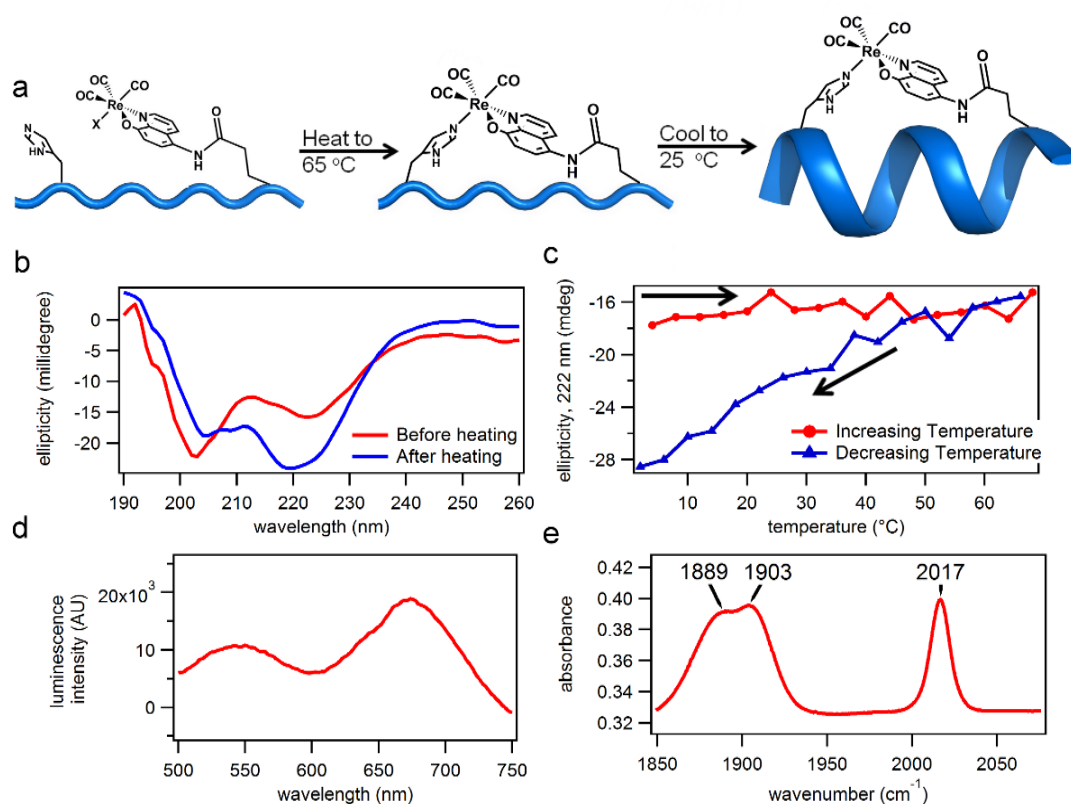


Figure 2.9: (a) Proposed scheme for the formation of the Re(Quin)(CO)<sub>3</sub>(His) HCM upon heating and the subsequent formation of the  $\alpha$ -helix upon cooling. (b) Observed changes in the CD spectrum upon heating and subsequent cooling of the Re-HCM peptide. (c) Changes in the CD signal (222 nm) during heating and cooling. (d) Emission spectrum of the Re-HCM peptide obtained after heating-cooling cycle ( $\lambda_{exc} = 410$  nm). (e) IR spectrum of the Re-HCM peptide. The peptide sample was first lyophilized and then combined with KBr to make a pellet.

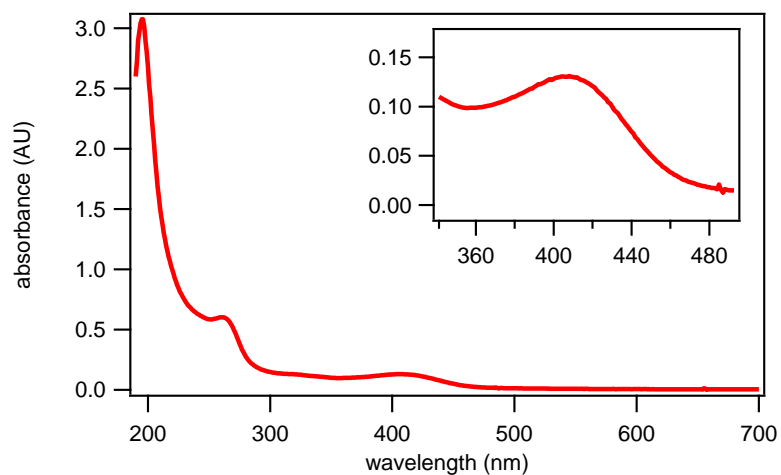


Figure 2.10: UV-vis spectrum of H-CQuin(Re)(CO)<sub>3</sub>(His). The inset shows a closeup of the band at 410 nm. This band was used as the excitation wavelength for luminescence.

To demonstrate the ability of HCMs to anchor functional metal complexes, we synthesized the luminescent  $\text{Re}^{\text{I}}(\text{IA-Quin})(\text{CO})_3\text{X}$  compound,<sup>66-68</sup> which could be directly coupled to Cys(9) following SPPS with >90% yield (Figure 2.9a). The product, purified by HPLC, had a mass of 1453.80 amu (theoretical mass = 1490.10 amu), which is consistent with the loss of the chloride ligand either during the MS experiment or earlier during purification through substitution by a solvent species. Because  $\text{Re}^{\text{I}}$  is substitution-inert, we first heated the resulting Re-peptide conjugate to 65 °C in order to promote His(2)-Re coordination, then cooled it down to room temperature, while monitoring the  $\alpha$ -helicity of the peptide by CD spectroscopy at 222 nm (Figure 2.9a). Upon the completion of the heating-cooling cycle, the  $\alpha$ -helicity of the sample significantly increased, suggesting that the  $\text{Re}^{\text{I}}$ -HCM was successfully formed (Figure 2.9b and Figure 2.9c). The product displayed a visible band at ~410 nm (Figure 2.10), whose excitation produced two luminescence bands with maxima at 550 nm and 680 nm (Figure 2.9d; see Figure 2.11 for

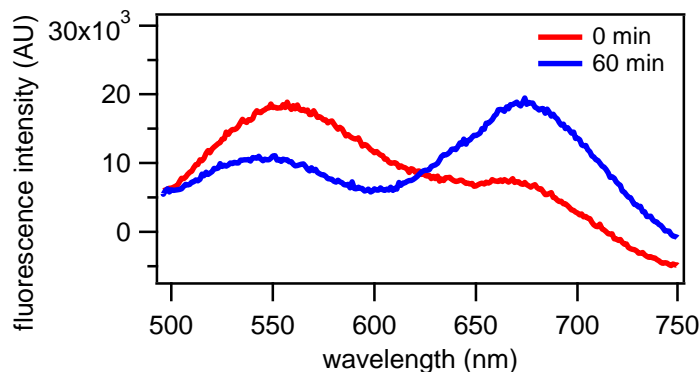


Figure 2.11: Changes in the H-CQuin(Re)(CO)<sub>3</sub>(His) luminescence spectrum upon His coordination after heating. 25  $\mu$ M peptide in 2.5 mL water. The sample was excited at 410 nm.

changes in the luminescence spectrum upon heating). These spectral features accord very well with those of the model complex, Re<sup>I</sup>(Quin)(CO)<sub>3</sub>(pyridine), which was reported to have an absorption band centered at 420-430 nm, a fluorescence band at ~530 nm and a phosphorescence band 670-690 nm.<sup>69</sup> The IR-spectrum of the Re-HCM peptide was also very similar to that of the model complex, with three maxima at 1888, 1903, and 2016 cm<sup>-1</sup> corresponding to the three carbonyl groups in a *facial* arrangement (Figure 2.9e). These results confirm the intended coordination geometry of the Re<sup>I</sup>-HCM complex and establish that His-Quin HCMs can be used to harbor functional metal complexes on an  $\alpha$ -helical peptide platform.

### 2.3.5 HCM-mediated helicity in non-Ala-rich peptide sequences

Although the HCM-peptide sequences presented thus far all display random coil signatures in the absence of metal coordination, it is well documented that Ala-rich sequences have high propensity for  $\alpha$ -helix formation.<sup>70</sup> Therefore, we sought to determine whether our HCM strategy could be employed to induce helicity in non-Ala-rich peptide sequences that may have downstream applications. To this end, we synthesized an HCM-



Bax (wt):<sup>55</sup>STKKLSECLRRIGDELDSNMELQRMI<sup>80</sup>  
 Bax-HCM: STKKLSECLRRIGDEL<sup>D</sup>HNMELQR(EMeQuin)I

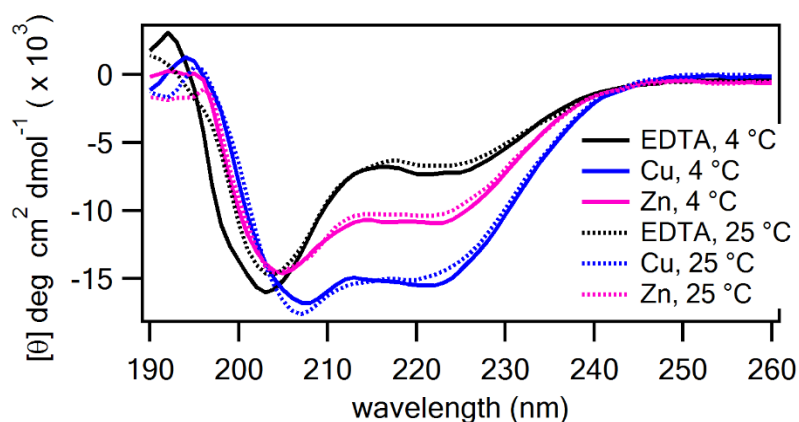


Figure 2.12: Sequences of wild-type and HCM-modified Bax BH3 domain peptides (top). Far-UV CD spectra of Bax-HCM in the presence and absence of  $\text{Cu}^{\text{II}}$  (blue) and  $\text{Zn}^{\text{II}}$  (magenta) acquired at 4 °C (solid lines) or 25 °C (dashed lines). The samples contained 10  $\mu\text{M}$  peptide and 30  $\mu\text{M}$  EDTA or metal ions in a 5 mM sodium borate buffer solution at pH 7.5.

bearing peptide sequence (Bax-HCM) based on the helical BH3 (Bcl-2 homology domain 3) motif of the pro-apoptotic protein Bax. Because BH3 domains play a central role in the interactions between Bcl-2 family proteins involved in the regulation of cell death, structural mimics of BH3 domains have received considerable attention as potential cancer therapeutics<sup>71,72</sup> and therefore constituted an interesting proof-of-principle target for our strategy. Bax-HCM, a 26-residue sequence, contained the entire helical BH3 domain (residues 55-80, Figure 2.12) of Bax which is necessary and sufficient for interaction with Bcl-2.<sup>73,74</sup> The only two variations from the wildtype protein sequence were  $\text{Ser}^{72} \rightarrow \text{His}$  and  $\text{Met}^{79} \rightarrow \text{EMeQuin}$  for the construction of the  $i/i+7$  HCM motif on the face of the BH3 helix that does not interact with the target protein. CD experiments indicated that Bax-HCM (10  $\mu\text{M}$  in concentration) displayed little-in any-helicity in the absence of metals

(Figure 2.12). Upon addition of metal ions, we observed a clear emergence of an  $\alpha$ -helical signature, the effect being largest with  $\text{Cu}^{\text{II}}$ , followed by  $\text{Zn}^{\text{II}}$ ,  $\text{Co}^{\text{II}}$  and  $\text{Ni}^{\text{II}}$  (Figure 2.6, Figure 2.7, Figure 2.12), roughly following the same trend observed with the 10-mer sequences. Notably, in contrast to these short Ala-rich peptides, Bax-HCM displayed no appreciable difference in helicity between 4 °C and 25 °C (Figure 2.12), which may be attributable to its longer length.

## 2.4 Conclusions

In summary, we have presented here the synthesis and characterization of various Quin-based HCM-bearing peptides and their metal-dependent structural and photophysical properties. There is rich and extensive literature on metal-induced  $\alpha$ -helicity peptides,<sup>27,28,31,75-79</sup> metal-peptide conjugates,<sup>63,80-83</sup> and functional metallopeptides.<sup>37,84-89</sup> Our strategy of building HCMs on peptide sequences borrows from all of these somewhat non-overlapping efforts to provide a unique combination of advantages for creating functional,  $\alpha$ -helical structures. HCM-bearing peptides are readily prepared via multiple routes with high yield in a few synthetic steps from commercially available components. HCMs are modular in the sense that they can be interchangeably (i.e., reversibly) complexed with various divalent transition metal ions or metal complexes whose different coordination properties can be utilized to control the  $\alpha$ -helicity of the peptide scaffold. Though not explored here, HCMs could also allow the control of peptide conformation through changes in solution pH or redox potential (as both of these factors can modulate inner-sphere metal coordination) so as to construct stimuli-responsive peptide platforms. Based on the two sets of peptides we studied here (the 10mer, Ala-rich sequences and the 26mer Bax BH3 domain), HCMs appear to be generally applicable for helix induction,

with the added advantage that the “helix staple” can now carry an intrinsic and useful functionality such as luminescence.

On a final note, given the tight regulation and scarcity of uncomplexed transition metal ions in the intracellular environment, the use of  $\alpha$ -helical HCM peptides containing labile metal ions (e.g.,  $\text{Co}^{\text{II}}$ ,  $\text{Ni}^{\text{II}}$ ,  $\text{Cu}^{\text{II}}$  and  $\text{Zn}^{\text{II}}$ ) may be more useful for *in vitro* experiments or for targeting extracellular proteins such as cell surface receptors. Nevertheless, as we have demonstrated with a  $\text{Re}^{\text{I}}$ -carbonyl compound, HCM peptides are readily modified with substitution-inert metal complexes, which should not only yield stable  $\alpha$ -helical peptides, but also may lend their intrinsic physical properties and chemical reactivities toward diagnostic and therapeutic *in vivo* applications.<sup>56,60</sup>

## **2.5 Materials and Methods**

### **2.5.1 General Considerations**

#### **2.5.1.1 Supplies**

Unless otherwise stated, reagents and solvents were purchased from Fisher Scientific and used without further purification. Peptide supplies (both amino acids and resin) were purchased from Aapptec and used without further purification.

#### **2.5.1.2 HPLC purification**

Reverse-phase HPLC was performed using an Agilent Technologies 1260 Infinity HPLC equipped with a preparation-scale column (Agilent preHT, 5  $\mu\text{m}$ , 21.1  $\times$  100 mm) using 0.1% trifluoroacetic acid (TFA) in water as solvent A and acetonitrile as solvent B. Peptide absorbance was monitored at 220 nm or 254 nm (the absorbance of Quin), and fractions were manually collected. After initial purification, an analytical column (Agilent

Eclipse plus C<sub>18</sub>, 3.5  $\mu$ m, 4.6  $\times$  100 mm) using the same gradient to determine purity. All peptides were purified to >90% pure and the masses were verified using MALDI-TOF mass spectrometry. Preparative scale columns were run at 8 ml/min and analytical scale columns were run at 1 mL/min.

### **2.5.1.3 Mass spectrometry**

Mass spectrometry analysis was carried out at the Molecular Mass Spectrometry Facility at UCSD. Peptide mass spectrometry was performed on a Bruker Biflex IV MALDI-TOF mass spectrometer. In a typical experiment, 3  $\mu$ L of a dilute peptide sample (1-10  $\mu$ M) was combined with 3  $\mu$ L  $\alpha$ -cyano-4-hydroxycinnamic acid (CHCA) (Agilent) as a matrix. 3  $\mu$ L of this solution was plated on a standard 288 well plate and dried completely before analysis.

Small molecule mass spectrometry was performed using electrospray ionization (ESI) on a Quattro Ultima Triple Quadrupole mass spectrometer. Samples were prepared at a concentration of 0.1-1.0 mg/mL in a 50% MeOH solution in water. Analysis was performed under both the positive and negative ion modes.

## **2.5.2 Synthesis of unnatural amino acids**

### **2.5.2.1 Synthesis of Iodoacetamido-8-hydroxyquinolate (IQuin)**

Iodoacetic anhydride was first synthesized by adding 1.19 g of iodoacetic acid (Sigma, 6.4 mmol) dissolved in 10 mL ethyl acetate to 660 mg of dicyclohexylcarbodiimide (DCC) (Sigma, 3.2 mmol) dissolved in an additional 10 mL of ethyl acetate. White precipitate formed immediately and the reaction was allowed to stir for 2 hours in the dark. The white precipitate (dicyclohexylurea) was filtered and the filtrate was evaporated to

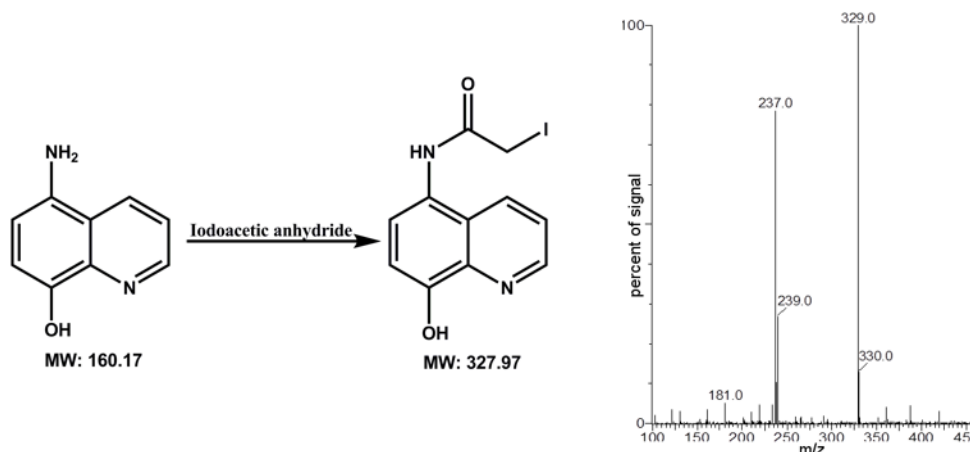


Figure 2.13: (a) Synthetic scheme for the synthesis of iodoacetamido-8-hydroxyquinolate (IQin). (b) ESI-MS (positive mode) of IQin. Observed peak at 329.0 amu (exp.: 328.9)  $[M + H]^+$ . The peak at 237.0 amu corresponds to the side product chloracetamido-8-hydroxyquinolate (exp.: 236.7)  $[M + H]^+$ .

dryness. Concurrently, 500 mg of 5-amino-8-hydroxyquinolate dihydrochloric acid (2.1 mmol) was added to 10 mL of acetonitrile with 1 mL triethylamine (7 mmol) and refluxed at 80 °C for 2 hours to dissolve, resulting in a clear, dark solution. Iodoacetic anhydride was then dissolved in 5 mL acetonitrile and added to the 5-amino-8-hydroxyquinolate dihydrochloric solution and the mixture was stirred overnight at room temperature in the dark. The product was isolated by filtration and washed with 5% sodium bicarbonate (aq). The resulting solid was dried *in vacuo* to afford the desired product in 80% crude yield (0.55 g, 1.67 mmol).  $^1\text{H}$  NMR (500 MHz, acetonitrile- $d_3$ ):  $\delta$  (ppm) 8.88 (d,  $J = 4.6$  Hz, 1H), 8.66 (s, 1H), 8.53 (d,  $J = 8.6$  Hz, 1H), 7.72 (m,  $J = 4.6, 8.6$ , 1H), 7.53 (d,  $J = 8.6$  Hz, 1H), 7.24 (d,  $J = 8.6$  Hz, 1H), 3.96 (s, 2H). ESI-MS (+):  $m/z$  calculated for  $(\text{C}_{11}\text{H}_9\text{IN}_2\text{O} + \text{H})$  328.9 amu  $[M+H]^+$ , found 329.0 amu. HPLC retention time: 4.9 min, 85%  $\text{H}_2\text{O}$  + 0.1% trifluoroacetic acid, 15% acetonitrile. As synthesized, the product was judged to be approximately 55% pure by HPLC and was used without further purification. The large

side product was chloroacetamido-8-hydroxyquinolate which would also react specifically with the cysteine on the target peptides, therefore, it was decided that it was not necessary to remove it. To better structurally characterize the desired product, a small amount was purified by prep-scale HPLC and a fraction was collected that was used for NMR analysis.

### 2.5.2.2 Synthesis of 5-{N-[(9H-fluoren-9-ylmethoxy)carbonyl]-L-glutamino}-8-hydroxyquinoline (Fmoc-E(Quin)-OH)

Fmoc-Glu-OtBu (Aapptec) (1.30 g, 3.0 mmol) was mixed with HATU (1.14 g 3.0 mmol) in a round-bottom flask. The mixture was dissolved with 5 mL of 10% 2, 4, 6-collidine in DMF with stirring. In a separate vial, 5-amino-8-hydroxyquinoline (0.70 g, 3.0 mmol) was dissolved in 10% (v/v) 2, 4, 6-collidine in DMF (15 mL), yielding a dark brown solution, which was added to the Fmoc-Glu-OtBu/HATU solution with stirring. The reaction occurred overnight at room temperature. The mixture was then filtered to give a brown solution and the filtrate was evaporated to dryness, resulting in brown oil. The oil was re-dissolved in 100 mL dichloromethane (DCM) and washed with 0.1 M HCl (3 x 30 mL) and brine (2 x 30 mL). The organic phase was dried over MgSO<sub>4</sub>, and evaporated to

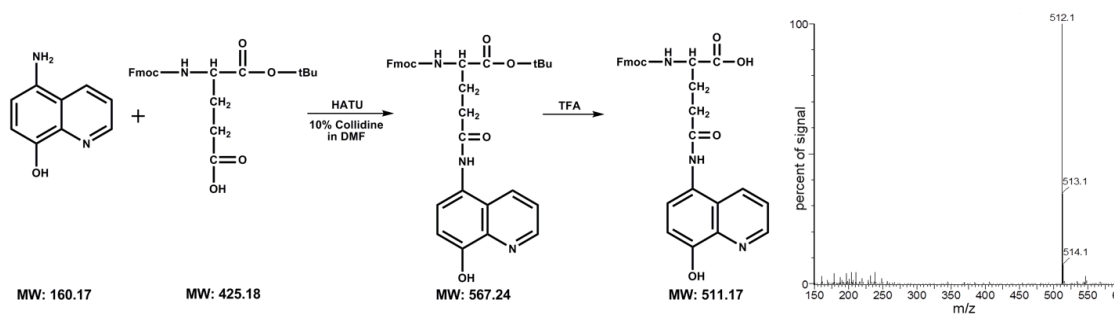


Figure 2.14: (a) Synthetic scheme for the synthesis of 5-{N-[(9H-fluoren-9-ylmethoxy)carbonyl]-L-glutamino}-8-hydroxyquinoline (Fmoc-E(Quin)-OH). (b) ESI-MS (positive mode) of Fmoc-E(Quin)-OH. Observed peak at 512.1 amu (exp.: 512.2) [M + H]<sup>+</sup>.

dryness, resulting in reddish brown oil. TFA (20 mL) was added to the oil and the mixture was stirred for 2 hours, at which time it was added to cold diethylether (500 mL). The solution was then stored at  $-80^{\circ}\text{C}$  for 2 hours to allow for complete precipitation of the amino acid. The light yellow precipitate was collected by filtration, re-dissolved by a minimal amount of acetonitrile and evaporated to dryness, yielding a brown powder.  $^1\text{H}$  NMR (400 MHz, dimethyl sulfoxide- $d_6$ ):  $\delta$  (ppm) 9.85 (s, 2H), 8.90 (d,  $J = 3.9$  Hz, 1H), 8.46 (d,  $J = 8.6$  Hz, 1H), 7.90 (d,  $J = 7.7$  Hz, 2H), 7.75 (d,  $J = 7.7$ , 2H), 7.73 (d,  $J = 8.1$ , 1H), 7.65 (q,  $J = 4.3$  Hz, 1H), 7.49 (d,  $J = 8.2$  Hz, 1H), 7.42 (t,  $J = 7.7$  Hz, 2H), 7.34 (t,  $J = 7.3$  Hz, 2H), 7.13 (d,  $J = 8.1$  Hz, 1H), 4.25 (m, 3H), 4.08 (td,  $J = 8.2, 4.7$ , 1H), 2.56 (t,  $J = 7.7$ , 2H), 2.05 (td,  $J = 7.3, 8.1$ , 2H) ESI-MS (+):  $m/z$  calculated for ( $\text{C}_{29}\text{H}_{25}\text{N}_3\text{O}_6 + \text{H}$ ) 512.2 amu  $[\text{M}+\text{H}]^+$ , found 512.1 amu. HPLC retention time: 10.3 min, 58%  $\text{H}_2\text{O}$  + 0.1% trifluoroacetic acid, 42% acetonitrile.

### 2.5.2.3 Synthesis of 5-Aminomethyl-8-hydroxyquinoline ( $\text{NH}_2\text{MeQuin}$ )

This synthesis was adapted from a previously published protocol.<sup>90</sup> 8-hydroxyquinoline (11.60 g, 80.0 mmol) was dissolved in concentrated HCl (40 mL). Formaldehyde (30% aqueous solution) (6.4 mL, 80.0 mmol, Fisher) was added to the bright yellow solution. HCl gas was generated by mixing concentrated sulfuric acid and concentrated HCl and the gas was bubbled through the 8-hydroxyquinoline solution. The reaction was held at room temperature for 30 min while a bright yellow precipitate formed. To quench the reaction, dry acetone (100 mL) was added. The precipitate was collected by filtration and washed by dry acetone (200 mL) to yield ClMeQuin in 70% yield (10.81 g, 56.0 mmol.) ClMeQuin (10.30 g, 53.0 mmol) was mixed with sodium azide (10.40 g, 159.0

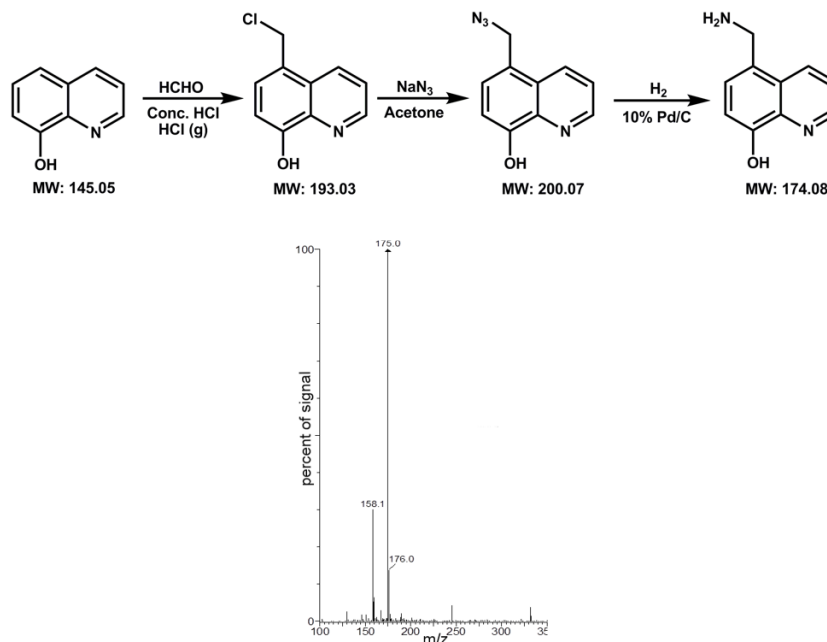


Figure 2.15: (a) Synthetic scheme for the synthesis of 5-Aminomethyl-8-hydroxyquinoline (NH<sub>2</sub>MeQuin). (b) ESI-MS (positive mode) of NH<sub>2</sub>MeQuin. Observed peak at 175.0 amu (exp.: 175.1) [M + H]<sup>+</sup>.

mmol) in dry acetone (200 mL). The mixture was refluxed at 75 °C overnight. The resulting light green mixture was cooled to room temperature, filtered and the light green filtrate was collected. After evaporating to dryness, the product was re-dissolved in a minimal amount of DMF and then added to 1 L of cold water. A large quantity of pale green precipitate formed and was collected by filtration, to afford N<sub>3</sub>MeQuin in 70% yield (7.47 g, 37.4 mmol). N<sub>3</sub>MeQuin (2.00 g, 10.0 mmol) was dissolved in a minimal amount of a solution consisting of 50% methanol and 50% dichloromethane (v/v). The solution was hydrogenated under 25 psi of hydrogen gas with a catalytic amount of dry 10% palladium on activated carbon (Fisher). After 1 hour, an additional 200 mL of 50% methanol in dichloromethane was added to ensure complete solvation of the product. The catalyst was discarded by filtration and the light brown filtrate was evaporated to dryness, affording the desired product, a light yellow powder in 69% yield (1.20 g, 6.9 mmol). <sup>1</sup>H NMR (400



MHz, dimethyl sulfoxide- $d_6$ ):  $\delta$  (ppm) 8.84 (d of d,  $J = 4.4, 1.5$  Hz, 1H), 8.38 (d of d,  $J = 8.4, 1.5$  Hz, 1H), 7.55 (q,  $J = 4.4$  Hz, 1H), 7.45 (d,  $J = 7.7$  Hz, 1H), 7.26 (s, 2H), 7.13 (d,  $J = 7.7$  Hz, 1H), 4.66 (s, 2H). ESI-MS (+):  $m/z$  calculated for ( $C_{10}H_{10}N_2O + H$ ) 175.1 amu  $[M+H]^+$ , found 175.0 amu. HPLC retention time: 6.8 min, 76%  $H_2O$  + 0.1% trifluoroacetic acid, 24% acetonitrile.

#### 2.5.2.4 Synthesis of 5-{*N*-[(9*H*-fluoren-9-ylmethoxy)carbonyl]-L-glutaminomethyl}-8-hydroxyquinoline (Fmoc-E(MeQuin)-OH)

Fmoc-Glu-OtBu (0.85 g, 2.0 mmol) and HATU (0.76 g, 2.0 mmol) were mixed and dissolved in 10% (v/v) 2,4,6-collidine in DMF (5 mL) with stirring. In a separate vial,  $NH_2MeQuin$  was suspended in 10% (v/v) 2, 4, 6-collidine in DMF (20 mL) with gentle heating to form a slurry and then transferred to the activated amino acid forming an orange, cloudy solution which cleared after 2 hours. The reaction was stirred overnight at room temperature. The resulting mixture was evaporated to dryness under constant heating and vacuum, to yield brown oil. The oil was dissolved in  $CH_2Cl_2$  (100 mL) and then washed by 0.1 M HCl (3 x 100 mL) followed by brine (2 x 50 mL). The organic phase was dried over anhydrous  $MgSO_4$ , filtered, and evaporated to dryness, yielding a light yellow solid. The crude product was purified using flash chromatography, eluting in 5% (v/v) methanol in dichloromethane ( $R_f \sim 0.6$ ). The purified product was evaporated to dryness and then re-dissolved in TFA (10 mL). After 2 hours, the mixture was transferred into cold diethylether (500 mL) and stored at  $-80^\circ C$  for 2 hours to allow for complete precipitation. The bright yellow precipitate was collected by filtration, re-dissolved in a minimal amount of acetonitrile, and evaporated to dryness, to afford the desired product, a bright yellow solid,

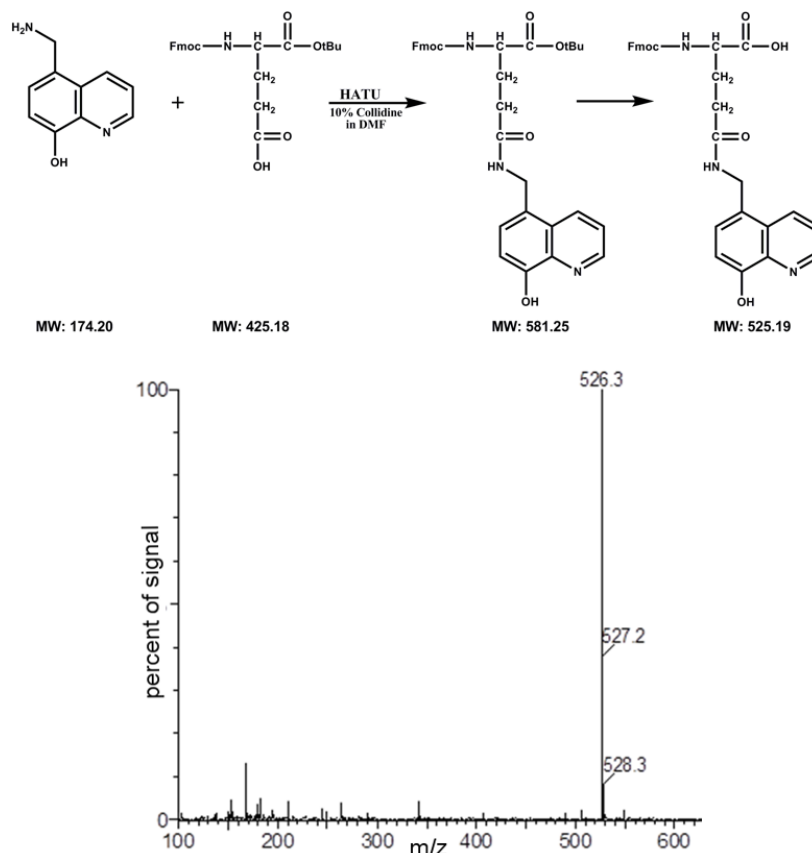


Figure 2.16: (a) Synthetic scheme for the synthesis of 5-{*N*-[(9*H*-fluoren-9-ylmethoxy)carbonyl]-*L*-glutaminomethyl}-8-hydroxyquinoline (Fmoc-E(MeQuin)-OH). (b) ESI-MS (positive mode) of Fmoc-E(MeQuin)-OH. Observed peak at  $m/z = 526.3$  amu (exp.: 526.2 amu)  $[M + H]^+$ .

in 40% yield. (0.42 g, 0.8 mmol).  $^1\text{H}$  NMR (400 MHz, dimethyl sulfoxide- $d_6$ ):  $\delta$  (ppm) 8.92 (d,  $J = 3.7$  Hz, 1H), 8.62 (d,  $J = 8.4$  Hz, 1H), 8.35 (t,  $J = 5.4$  Hz, 1H), 7.88 (d,  $J = 7.4$  Hz, 2H), 7.73 (d,  $J = 4.4$  Hz, 1H), 7.72 (d,  $J = 7.7$  Hz, 2H), 7.69 (dd,  $J = 8.1, 6.7$  Hz, 1H), 7.45 (d,  $J = 8.1$  Hz, 1H), 7.40 (t,  $J = 7.4$  Hz, 2H), 7.31 (t,  $J = 7.4$  Hz, 2H), 7.13 (d,  $J = 7.7$  Hz, 1H), 4.60 (d,  $J = 5.4$ , 2H), 4.25 (m, 3H), 3.95 (td,  $J = 8.1, 4.4$  Hz, 1H), 2.20 (t,  $J = 7.7$  Hz, 2H), 1.80 (td,  $J = 13.1, 7.7$  Hz, 2H). ESI-MS (+):  $m/z$  calculated for  $(\text{C}_{30}\text{H}_{27}\text{N}_3\text{O}_6 + \text{H})$  526.2 amu  $[M+H]^+$ , found 526.3 amu. HPLC retention time: 9.4 min, 65%  $\text{H}_2\text{O}$  + 0.1% trifluoroacetic acid, 35% acetonitrile.

### 2.5.2.5 Synthesis of $\text{Re}(\text{Cl})(\text{IQuin})(\text{CO})_3$

$\text{Re}(\text{Cl})(\text{CO})_5$  (0.03 g, 0.1 mmol) was placed in a round bottom flask. HPLC-purified IQuin (0.03 g, 0.1 mmol) was added to the flask, and the flask was degassed. Degassed, dry acetonitrile (50 mL) was then added, and the reaction was refluxed under argon overnight in the dark. The following day, the reaction was slowly cooled to room temperature and the reaction mixture was then poured into ice cold hexanes. The solvents were removed in vacuo and the product was redissolved in 50% acetonitrile and 50% water + 0.1% trifluoroacetic acid and then HPLC purified on a preparative scale column as discussed in “General Considerations,” using a gradient of 5% solvent B to 40% solvent B over 25 min. The product eluted from the column in 35% acetonitrile and was yellow in color. The HPLC fractions containing the product were dried by lyophilization. Despite presence of an impurity (ESI-MS (-):  $m/z$  511.0 amu), peptide labeling was performed (see Section III c.) and the labeled peptide was purified to homogeneity (See Figure S6h).  $^1\text{H}$  NMR (500 MHz, acetonitrile- $d_3$ ):  $\delta$  (ppm) 8.95 (d,  $J = 5.2$  Hz, 1H), 8.47 (s, 1H), 8.40 (d,  $J = 8.6$  Hz, 1H), 7.56 (m,  $J = 5.2, 8.6$ , 1H), 7.38 (d,  $J = 8.0$  Hz, 1H), 6.88 (d,  $J = 8.0$  Hz,

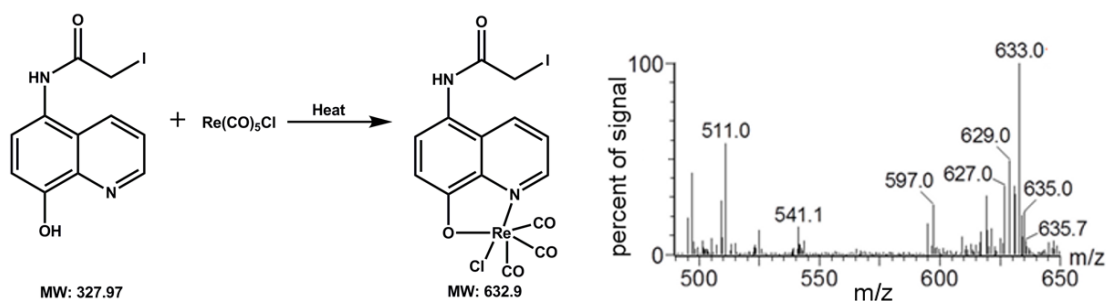


Figure 2.17: (a) Synthetic scheme for the synthesis of  $\text{Re}(\text{Cl})(\text{IQuin})(\text{CO})_3$ . (b) ESI-MS (negative mode) of  $\text{Re}(\text{Cl})(\text{IQuin})(\text{CO})_3$ . Observed peak at  $m/z = 633.0$  amu (exp.: 632.9)  $[\text{M}]^-$ , 629.0 amu (exp 628.9)  $[\text{M} - \text{Cl} + \text{MeOH}]^-$ , 597.0 amu (exp 596.9)  $[\text{M} - \text{Cl}]^-$ , 541.1 amu (exp 540.9)  $[\text{M} - \text{I} + \text{Cl}]^-$ .

1H), 3.95 (s, 2H). ESI-MS (-):  $m/z$  calculated for ( $C_{14}H_8IN_2O_5ReCl + H$ ) 632.9 amu  $[M]^-$ , found 633.0 amu, 629.0 amu  $[M - Cl + MeOH]^-$ , 597.0 amu  $[M - Cl]^-$ , 541.1 amu  $[M - I + Cl]^-$ . IR peaks: 1901, 1917, 2023  $cm^{-1}$ .

### 2.5.3 Peptide Synthesis

#### 2.5.3.1 General protocols for Solid Phase Peptide Synthesis

Peptides were synthesized using a MilliPore 9050 or an Aapptec Focus XC peptide synthesizer. All peptides were *N*-terminal acylated and *C*-terminal amidated. Standard Fmoc chemistry was used for synthesis, as glutamate-derived non-natural amino acids were incorporated in the same way as natural amino acids.

For each amino acid addition, the Fmoc protecting group on the *N*-terminus of the growing peptide chain was first removed with a solution of 20% (v/v) 4-methylpiperidine in dimethylformamide (DMF). A 4-fold excess of an Fmoc-protected amino acid containing a free *C*-terminus was then added in a solution of 4 M *N,N*-Diisopropylethylamine (DIPEA) in DMF with an equimolar amount of HATU and coupling was allowed to proceed for 40 min with shaking. The resin was then washed with DMF and the cycle was repeated until all amino acids were incorporated. Unnatural amino acids were incorporated during peptide synthesis using the same protocol as for natural amino acids. After the final step of synthesis, the *N*-terminus of each peptide was acylated with a mixture of 0.5 M acetic acid anhydride, 0.5 M *N*-hydroxybenzaldehyde (HOBt) and 10% (v/v) dichloromethane in DMF.

The peptide resin was removed from the synthesizer and dried *in vacuo*. The peptide was then cleaved from the resin using a cleavage cocktail containing 5% (v/v) thioanisole, 3% (v/v) ethane dithiol and 2% (v/v) anisole in trifluoroacetic acid (TFA) over

a period of two hours. After cleavage was complete, the peptide solution was filtered to remove the resin and the filtrate was added to a solution of cold ether and incubated at -80 °C overnight to precipitate the peptide from solution. The solution was then filtered, the peptide was collected as a precipitate, and dried *in vacuo*. The crude solid was redissolved in water, and purified via HPLC.

### **2.5.3.2 Functionalization of cysteine-containing peptides (H-CQuin, H-CQuin-A, A-CQuin)**

Under an argon atmosphere, 20 mg of each peptide [HCys, HCys-A, or ACys] was dissolved in 3 mL of degassed 10 mM HEPES buffer (pH 7.5) with constant stirring. A 3- to 5-fold excess of iodoacetamido-8-hydroxyquinolate (Iquin) was dissolved in 1 mL degassed DMF and added dropwise to the peptide solution. The mixture was stirred in the dark for 4 hours. The resulting dark brown solution was centrifuged and the supernatant was collected. The solution was then run on a PD MidiTrap G-10 desalting column (GE Healthcare) to remove excess IQuin and DMF. The resulting crude peptide solution was purified by HPLC, and the mass of the labeled peptide was verified by MALDI-TOF mass spectrometry.

### **2.5.3.3 Incorporation of $\text{Re}(\text{Cl})(\text{IQuin})(\text{CO})_3$**

Under an argon atmosphere, 5 mg of the HC peptide was dissolved in 0.1M HEPES at pH 7.4.  $\text{Re}(\text{Cl})(\text{IQuin})(\text{CO})_3$  was dissolved in acetonitrile and added to the peptide. The reaction mixture stirred at room temperature in the dark for 4 hours and the resulting product was purified twice by HPLC, and the correct product was verified by mass

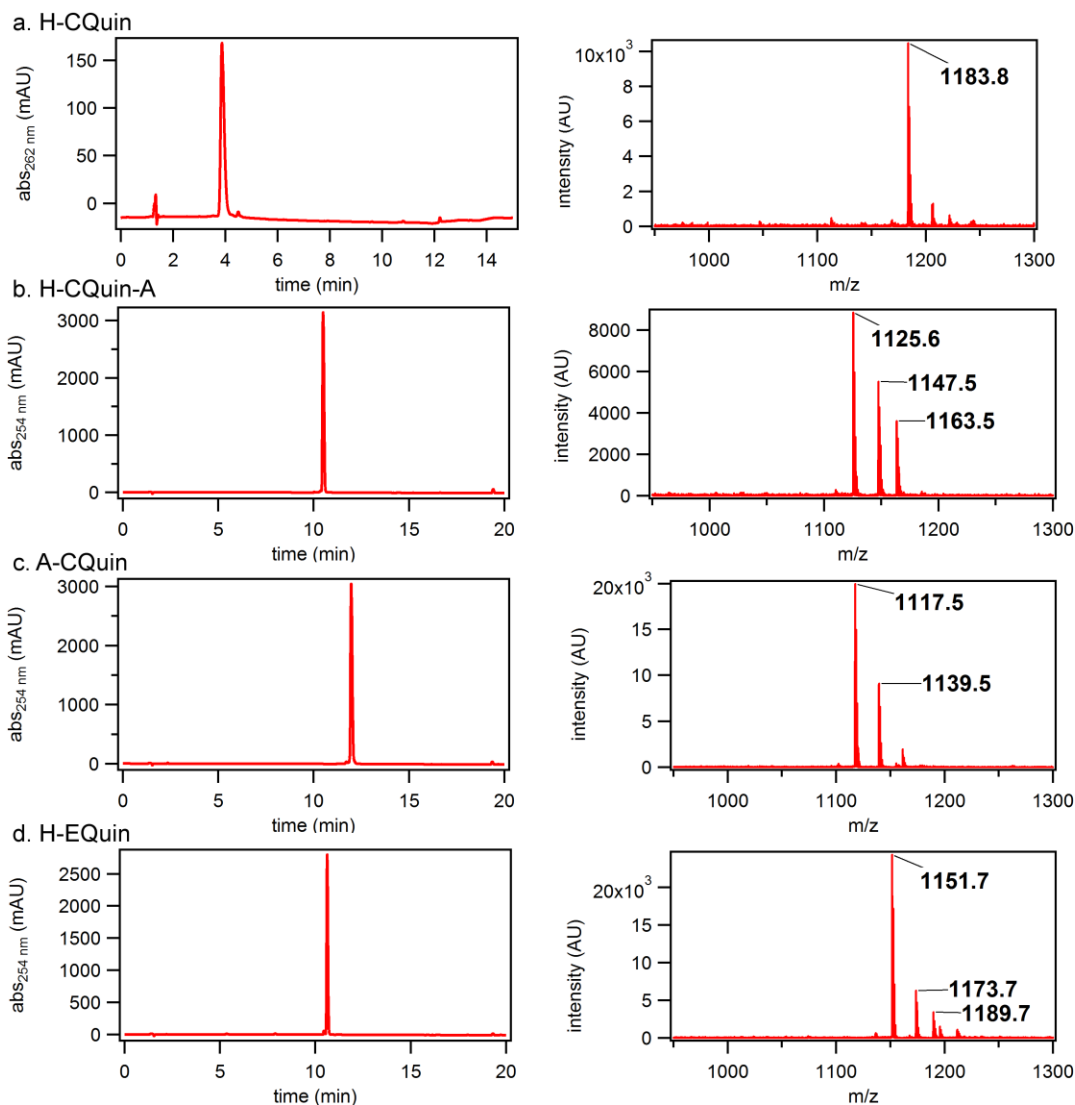


Figure 2.18: Analytical HPLC traces and MALDI-TOF spectra of various peptide constructs. HPLC gradient used: 1. 0 to 5 min, 95% solvent A, constant. 2. 5 to 20 min, 95% to 60% solvent A, gradient. except for H-CQuin and H-CQuin(Re): 1. 0 to 2 min, 90% solvent A, constant. 2. 2 to 12 min, 90% to 55% solvent A, gradient. **(a)** H-CQuin: Expected: 1185 amu. Observed: 1183.8  $[M + H]^+$ . **(b)** H-CQuin-A: Expected 1128 amu. Observed: 1125.6  $[M + H]^+$ , 1147.5  $[M + Na]^+$ , 1163.5  $[M + K]^+$ . **(c)** A-CQuin: Expected 1119 amu. Observed: 1117.5  $[M + H]^+$ , 1139.5  $[M + Na]^+$ . **(d)** H-EQuin: Expected 1153 amu. Observed: 1153.5  $[M + H]^+$ , 1176.6  $[M + Na]^+$ , 1191.9  $[M + K]^+$ . **(e)** H-EMeQuin: Expected 1167 amu. Observed: 1166.7  $[M + H]^+$ , 1187.7  $[M + Na]^+$ , 1203.7  $[M + K]^+$ . **(f)** H-EMeQuin-A: Expected 1110 amu. Observed: 1107.4  $[M + H]^+$ , 1129.4  $[M + Na]^+$ , 1145.4  $[M + K]^+$ . **(g)** A-EMeQuin: Expected 1099 amu. Observed: 1099.7  $[M + H]^+$ , 1121.6  $[M + Na]^+$ , 1137.6  $[M + K]^+$ . **(h)** H-CQuin(Re) $CO_3$ : Expected 1455 amu. Observed: 1452.7  $[M + H]^+$ . **(i)** Bax-HCM: Expected 3302 amu. Observed: 3310.2 amu  $[M + H]^+$ .

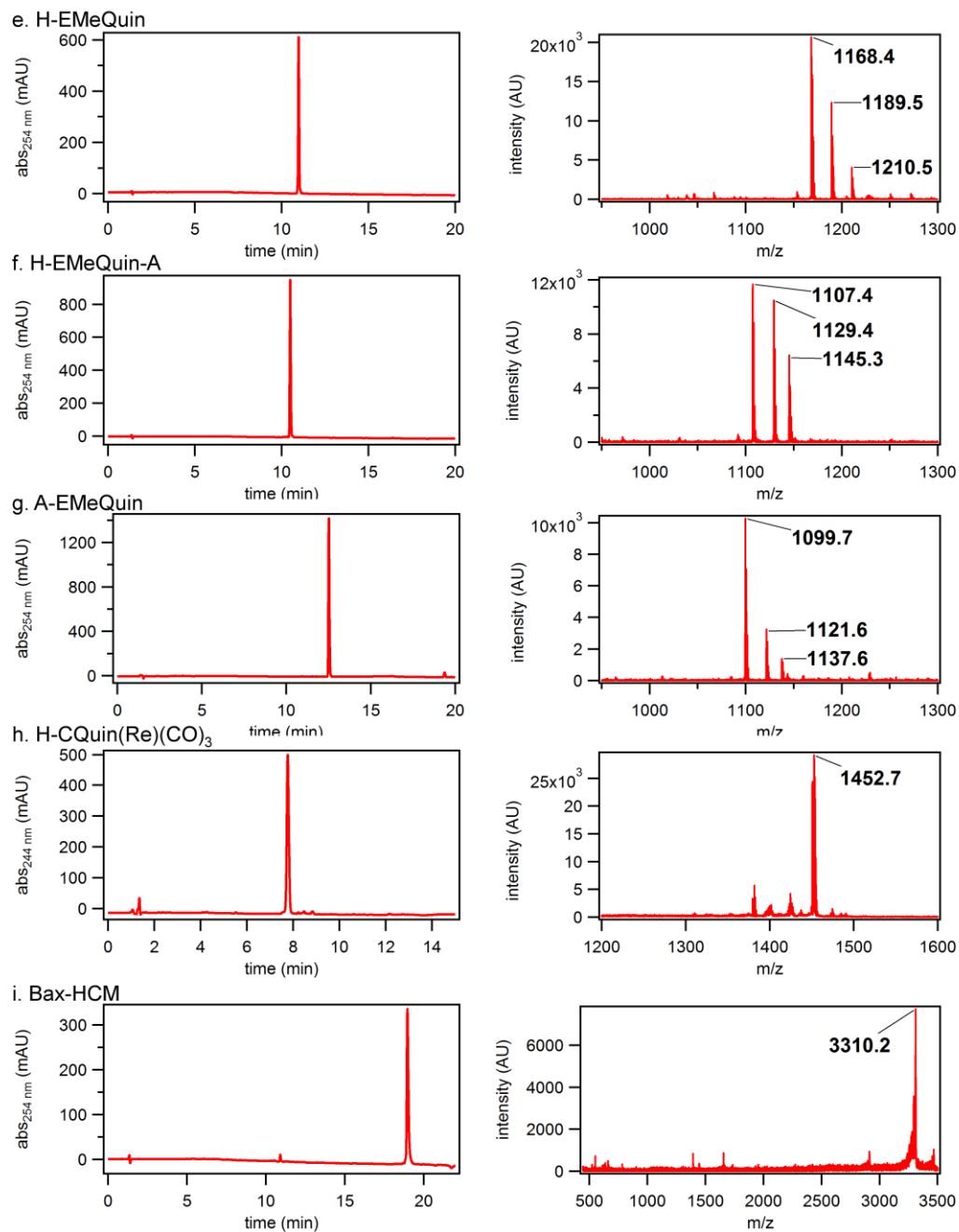


Figure 2.18: Analytical HPLC traces and MALDI-TOF spectra of various peptide constructs, continued.

spectrometry. The observed mass corresponded to the product without a chloride coordinated to the Re center. It was not determined whether this was due to replacement of the chloride ion by histidine, due to the mass spectrometry conditions themselves, or due

to replacement of the chloride ion by a solvent species. However, there were obvious spectral changes (fluorescence, CD, UV-vis) observed when the peptides were later heated which corresponded to His coordination, indicating that His had not coordinated to the Re center at that point. Finally, the peptide was heated to 65 °C for 30 min, and the coordination of the His residue was observed by CD, UV-vis, and fluorescence spectroscopy. Histidine coordination also occurred by leaving the peptide at room temperature for approximately one to two hours.

#### 2.5.4 Determination of metal binding affinity

Metal binding titrations were performed by monitoring the Quin  $\pi$ - $\pi^*$  absorption band, which shifts approximately 20 nm upon metal binding (Figure S6a). 1-mL samples were prepared containing 10-20  $\mu$ M peptide; peptide concentrations were determined using the extinction coefficient  $\epsilon_{244} = 22,000 \text{ M}^{-1}\text{cm}^{-1}$ . Each sample was prepared in 5 mM MOPS buffer at pH 7.1 pretreated with Chelex resin (BioRad) with a 3-fold excess of chelator (30-60  $\mu$ M). All pipet tips were rinsed 3 times with analytical grade 10%  $\text{HNO}_3$  (Fluka) before use. For the  $\text{Ni}^{\text{II}}$  and  $\text{Cu}^{\text{II}}$  samples, ethylene glycol tetraacetic acid (EGTA) was used as a competing chelator, and for the  $\text{Zn}^{\text{II}}$  and  $\text{Co}^{\text{II}}$  samples, N-(2-acetamido)iminodiacetic acid (ADA) was used. 2 mM metal stocks were prepared and added stepwise to the peptide solution so that the total amount never exceeded 50  $\mu$ L (5% of the total volume); each sample was equilibrated for 3 min with stirring after metal addition before the absorbance was measured. UV-vis measurements were performed on a Hewlett Packard 8452A diode array spectrophotometer. The largest changes in absorbance were measured at 262 nm upon the addition of metal, and these values were plotted as a function of  $\text{M}^{\text{II}}$  concentration



(Figure S6b). All spectra were corrected for dilution.  $M^{II}$  dissociation constants for either EGTA or ADA were calculated using MaxChelator (<http://maxchelator.stanford.edu>) and fixed during data fitting. The titration data were separately fit to two models using non-linear regression through Dynafit 3 (Biokin), where one model assumes a 1:1 peptide:metal stoichiometry while the other model takes account of the possibility of metal-induced peptide dimerization (1:1 and 2:1 peptide:metal stoichiometry) (Scheme S5, Figure S7).

### 2.5.5 Circular Dichroism Spectroscopy (CD)

Samples for circular dichroism spectroscopy (CD) analyses contained 10  $\mu\text{M}$  peptide in 5 mM sodium borate buffer at pH 7.5. The buffer had previously been treated using Chelex resin (BioRad) and all pipet tips were washed 3x with 10% analytical grade nitric acid (Fluka) before use. Peptide concentration was calculated by measuring the absorbance on a UV-vis spectrometer at 244 nm and calculating the corresponding concentration using an extinction coefficient of  $\epsilon_{244} = 22,000 \text{ cm}^{-1} \text{ M}^{-1}$  for the metal-free peptide. A 10  $\mu\text{M}$  peptide stock was first prepared, and then split into five 750  $\mu\text{L}$  samples. To each sample, a 3-fold excess of either EDTA or  $M^{II}$  was added to ensure the formation of a completely metal-free or metal-bound peptide, respectively. 5 mM metal stock solutions had previously been made using  $\text{NiCl}_2$ ,  $\text{CuSO}_4$ ,  $\text{ZnCl}_2$ , or  $\text{CoCl}_2$ . CD spectra were measured using an Aviv 215 spectrometer. The CD spectrum of each sample was measured from 190-260 nm, using a slit width of 1 nm, scanning at 1 nm intervals with a 1 s integration time. Measurements were taken at both 25  $^{\circ}\text{C}$  and 4  $^{\circ}\text{C}$  with constant stirring. Each measurement was repeated five times, averaged and smoothed with a binomial function, and corrected for any background signal from the buffer solution. For samples

containing trifluoroethanol (TFE), peptides were prepared both with a 3-fold excess of EDTA and with a 3-fold excess of Cu<sup>II</sup> in 60% TFE, but no notable difference was observed whether the peptide was metal-free or metal-bound.

### 2.5.6 Fluorescence Spectroscopy

Samples containing approximately 10  $\mu$ M of peptide were prepared in a solution of 5 mM sodium borate (pH 7.5). Each sample also contained a 3-fold excess of either Zn<sup>II</sup> or EDTA. In order to determine the quantum yield of each peptide construct when bound to Zn<sup>II</sup>, quinine sulfate in 0.1 M H<sub>2</sub>SO<sub>4</sub> was used as a standard. The absorbance of both the quinine sulfate standard and each peptide were measured at 375 nm, with initial absorption values ranging from 0.3 to 0.5. Each solution was then diluted 10-fold for fluorescence measurements. For each sample, the excitation wavelength used was 375 nm with a slit width of 2 nm, and emission was measured between 290 and 725 nm with a slit width of 2 nm and an integration time of 0.2 s; each measurement was repeated in triplicate. The following equation was used to calculate the quantum yield for each measurement (Table 2.3), where  $\Phi_F$  is the quantum yield, A is the absorption at the excitation wavelength, F is the area under the emission curve, and n is the refractive index of the solvents (in this case, the same solvent was used for each sample, so that term is equal to 1).<sup>91</sup>

$$\Phi_{F(X)} = (A_S/A_X)(F_X/F_S)(n_X/n_S)^2\Phi_{F(S)}$$

In order to determine the x-fold fluorescence turn-on for each peptide, fluorescence emission spectra were measured for both metal-free and Zn<sup>II</sup> bound peptides, and the emission value at 550 nm for the Zn<sup>II</sup> bound peptides were divided by the emission value

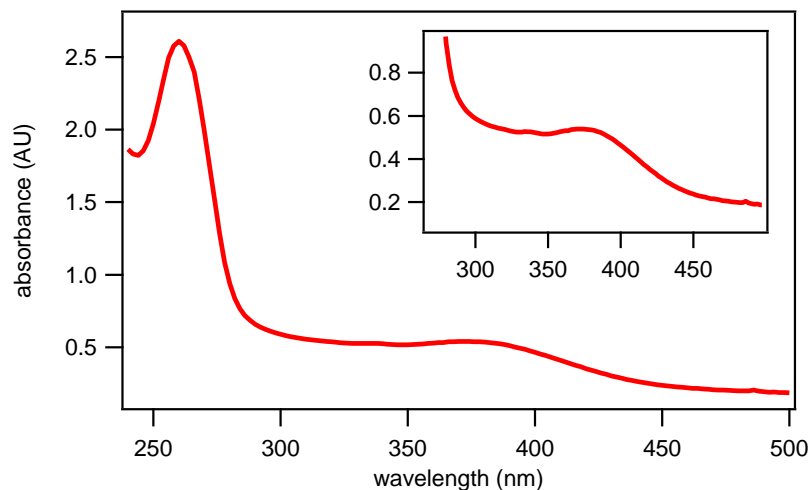


Figure 2.19: UV-vis absorption spectrum of Zn-HCQuin. Inset: The absorption band at 380 nm used for fluorescence excitation.

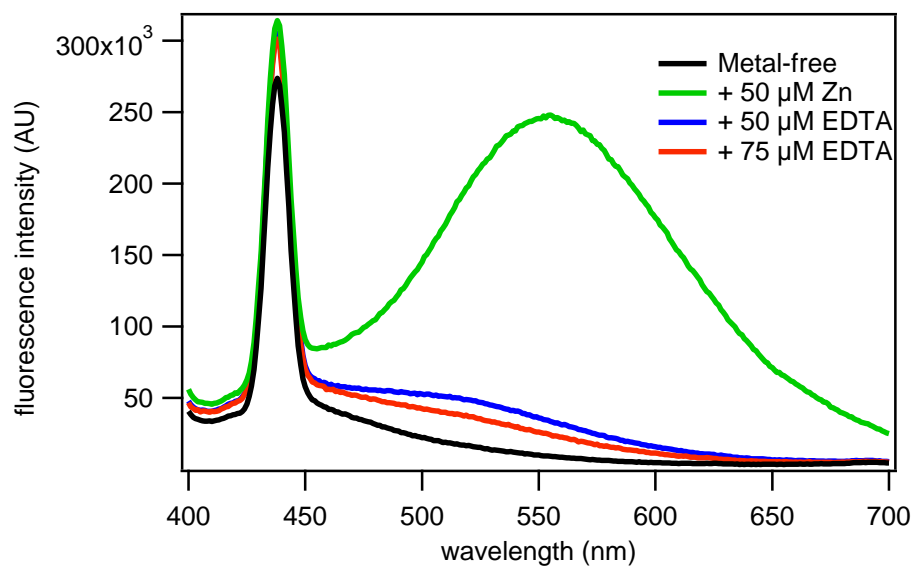


Figure 2.20: Reversibility of Zn<sup>II</sup>-induced H-EMeQuin fluorescence.

at 550 nm for the metal-free samples. H-EMeQuin samples were also prepared containing a 3-fold excess of either Co<sup>II</sup>, Ni<sup>II</sup>, or Cu<sup>II</sup>, and it was observed that no fluorescence turn-on was observed with these other metals (Figure 2.20).

Table 2.3: Fluorescence quantum yields for the Zn-adducts of various peptides.

Peptide	Quantum Yield
H-CQuin	$2.7(1) \times 10^{-3}$
H-CQuin-A	$1.9(2) \times 10^{-3}$
A-CQuin	$1.6(2) \times 10^{-3}$
H-EQuin	$3.1(1) \times 10^{-3}$
H-EMeQuin	$6.4(2) \times 10^{-3}$
H-EMeQuin-A	$8.4(1) \times 10^{-3}$
A-EMeQuin	$3.8(1) \times 10^{-3}$

The H-CQuin(Re)(CO)<sub>3</sub>(His) peptide was prepared as described previously. In all cases, the peptide was diluted to approximately 25  $\mu$ M in water in a quartz cuvette. The peptide was then heated to 65 °C, and CD, UV-vis and fluorescence spectra were taken at 30-min intervals. Any shifts observed in the measured spectra were complete by 1 hr of heating. Fluorescence spectra were measured using an excitation wavelength of 410 nm. The absorption band is shown in Figure 2.10. Samples were degassed and measured in an inert environment. Figure 2.11 shows the enhancement of emission in an oxygen-free sample.

## 2.6 Acknowledgements

We thank Professor Seth Cohen for the use of a hydrogenator, Professor Nathan Gianneschi for the use of a peptide synthesizer, Professor Elizabeth Komives for the use of a peptide synthesizer and HPLC and Dr Yongxuan Su for help with mass spectrometry and CD. We also thank Steven Chabolla for assistance with synthetic analysis and discussion. This work was supported by the US Department of Energy (DOE) (Division of Materials Sciences, Office of Basic Energy Sciences, Award DE-FG02-10ER46677 to

F.A.T., peptide synthesis), the National Science Foundation (CHE-0908115 to F.A.T.), and the National Institutes of Health (Molecular Biophysics traineeship to S.J.S.).

Chapter 2 is reproduced in part with permission from the Royal Society of Chemistry. Smith, S.J.; Du, K.; Radford, R.J.; Tezcan, F.A. Functional, metal-based crosslinkers for  $\alpha$ -helix induction in short peptides. *Chemical Science*. 2013, 4, 3740.

## 2.7 References

- (1) Bullock, B. N.; Jochim, A. L.; Arora, P. S. *J. Am. Chem. Soc.* **2011**, *133*, 14220.
- (2) Orner, B. P.; Ernst, J. T.; Hamilton, A. D. *J. Am. Chem. Soc.* **2001**, *123*, 5382.
- (3) Seebach, D.; L. Matthews, J. *Chem. Commun.* **1997**, *0*, 2015.
- (4) Gellman, S. H. *Acc. Chem. Res.* **1998**, *31*, 173.
- (5) Cheng, R. P.; DeGrado, W. F. *J. Am. Chem. Soc.* **2001**, *123*, 5162.
- (6) Kritzer, J. A.; Lear, J. D.; Hodsdon, M. E.; Schepartz, A. *J. Am. Chem. Soc.* **2004**, *126*, 9468.
- (7) Fowler, S. A.; Blackwell, H. E. *Org. Biomol. Chem.* **2009**, *7*, 1508.
- (8) Appella, D. H.; Christianson, L. A.; Klein, D. A.; Powell, D. R.; Huang, X.; Barchi, J. J.; Gellman, S. H. *Nature* **1997**, *387*, 381.
- (9) Chin, J. W.; Schepartz, A. *J. Am. Chem. Soc.* **2001**, *123*, 2929.
- (10) Zondlo, N. J.; Schepartz, A. *J. Am. Chem. Soc.* **1999**, *121*, 6938.
- (11) Azzarito, V.; Long, K.; Murphy, N. S.; Wilson, A. J. *Nat. Chem.* **2013**, *5*, 161.
- (12) Estieu-Gionnet, K.; Guichard, G. *Expert Opin. Drug Del.* **2011**, *6*, 937.
- (13) Sato, A. K.; Viswanathan, M.; Kent, R. B.; Wood, C. R. *Curr. Opin. Biotechnol.* **2006**, *17*, 638.
- (14) Toniolo, C.; Crisma, M.; Formaggio, F.; Peggion, C. *Biopolymers* **2001**, *60*, 396.

- (15) Bavoso, A.; Benedetti, E.; Di Blasio, B.; Pavone, V.; Pedone, C.; Toniolo, C.; Bonora, G. M. *Proc. Natl. Acad. Sci. U.S.A.* **1986**, *83*, 1988.
- (16) Marqusee, S.; Baldwin, R. L. *Proc. Natl. Acad. Sci. U.S.A.* **1987**, *84*, 8898.
- (17) Fujimoto, K.; Kajino, M.; Inouye, M. *Chem. Eur. J.* **2008**, *14*, 857.
- (18) Schafmeister, C. E.; Po, J.; Verdine, G. L. *J. Am. Chem. Soc.* **2000**, *122*, 5891.
- (19) Blackwell, H. E.; Grubbs, R. H. *Angew. Chem. Int. Ed.* **1998**, *37*, 3281.
- (20) Jackson, D. Y.; King, D. S.; Chmielewski, J.; Singh, S.; Schultz, P. G. *J. Am. Chem. Soc.* **1991**, *113*, 9391.
- (21) Phelan, J. C.; Skelton, N. J.; Braisted, A. C.; McDowell, R. S. *J. Am. Chem. Soc.* **1997**, *119*, 455.
- (22) Zhang, F.; Sadowski, O.; Xin, S. J.; Woolley, G. A. *J. Am. Chem. Soc.* **2007**, *129*, 14154.
- (23) Taylor, J. W. *Biopolymers* **2002**, *66*, 49.
- (24) Pellegrini, M.; Royo, M.; Chorev, M.; Mierke, D. F. *J. Pept. Res.* **1997**, *49*, 404.
- (25) Harrison, R. S.; Shepherd, N. E.; Hoang, H. N.; Ruiz-Gomez, G.; Hill, T. A.; Driver, R. W.; Desai, V. S.; Young, P. R.; Abbenante, G.; Fairlie, D. P. *Proc. Natl. Acad. Sci. U.S.A.* **2010**, *107*, 11686.
- (26) Shepherd, N. E.; Hoang, H. N.; Abbenante, G.; Fairlie, D. P. *J. Am. Chem. Soc.* **2005**, *127*, 2974.
- (27) Ghadiri, M. R.; Choi, C. *J. Am. Chem. Soc.* **1990**, *112*, 1630.
- (28) Ruan, F.; Chen, Y.; Hopkins, P. B. *J. Am. Chem. Soc.* **1990**, *1990*, 9403.
- (29) Zaykov, A. N.; Popp, B. V.; Ball, Z. T. *Chem. Eur. J.* **2010**, *16*, 6651.
- (30) Ma, M. T.; Hoang, H. N.; Scully, C. C. G.; Appleton, T. G.; Fairlie, D. P. *J. Am. Chem. Soc.* **2009**, *131*, 4505.
- (31) Kharenko, O. A.; Ogawa, M. Y. *J. Inorg. Biochem.* **2004**, *98*, 1971.
- (32) Ghadiri, M. R.; Fernholz, A. K. *J. Am. Chem. Soc.* **1990**, *112*, 9633.
- (33) Chapman, R. N.; Dimartino, G.; Arora, P. S. *J. Am. Chem. Soc.* **2004**, *126*, 12252.

- (34) Cabezas, E.; Satterthwait, A. C. *J. Am. Chem. Soc.* **1999**, *121*, 3862.
- (35) Radford, R. J.; Nguyen, P. C.; Ditri, T. B.; Figueroa, J. S.; Tezcan, F. A. *Inorg. Chem.* **2010**, *49*, 4362.
- (36) Radford, R. J.; Nguyen, P. C.; Tezcan, F. A. *Inorg. Chem.* **2010**, *2010*, 7106.
- (37) Shults, M. D.; Pearce, D. A.; Imperiali, B. *J. Am. Chem. Soc.* **2003**, *125*, 10591.
- (38) Walkup, G. K.; Imperiali, B. *J. Am. Chem. Soc.* **1997**, *119*, 3443.
- (39) Martell, A. E.; Smith, R. M. *Critical Stability Constants*; Plenum Press: New York, 1974.
- (40) Krantz, B. A.; Sosnick, T. R. *Nat. Struct. Mol. Biol.* **2001**, *8*, 1042.
- (41) Chin, D.-H.; Woody, R. W.; Rohl, C. A.; Baldwin, R. L. *Proc. Natl. Acad. Sci. U.S.A.* **2002**, *99*, 15416.
- (42) Patgiri, A.; Jochim, A. L.; Arora, P. S. *Acc. Chem. Res.* **2008**, *41*, 1289.
- (43) Luo, P.; Baldwin, R. L. *Biochemistry* **1997**, *36*, 8413.
- (44) Popp, B. V.; Ball, Z. T. *J. Am. Chem. Soc.* **2010**, *132*, 6660.
- (45) Chen, Z.; Vohidov, F.; Coughlin, J. M.; Stagg, L. J.; Arold, S. T.; Ladbury, J. E.; Ball, Z. T. *J. Am. Chem. Soc.* **2012**, *134*, 10138.
- (46) Bhatnagar, D. C.; Forster, L. S. *Spectrochim. Acta* **1965**, *21*, 1803.
- (47) Zhang, H.; Han, L.-F.; Zachariasse, K. A.; Jiang, Y.-B. *Org. Lett.* **2005**, *7*, 4217.
- (48) Fahrni, C. J.; O'Halloran, T. V. *J. Am. Chem. Soc.* **1999**, *121*, 11448.
- (49) Jotterand, N.; Pearce, D. A.; Imperiali, B. *J. Org. Chem.* **2001**, *66*, 3224.
- (50) Pearce, D. A.; Jotterand, N.; Carrico, I. S.; Imperiali, B. *J. Am. Chem. Soc.* **2001**, *123*, 5160.
- (51) Nolan, E. M.; Jaworski, J.; Okamoto, K.-I.; Hayashi, Y.; Sheng, M.; Lippard, S. J. *J. Am. Chem. Soc.* **2005**, *127*, 16812.
- (52) Jiang, P.; Guo, Z. *Coord. Chem. Rev.* **2004**, *248*, 205.
- (53) Su, J.; Xu, T.; Chen, K.; Tian, H. *Dyes Pigm.* **2000**, *44*, 87.

- (54) Bronson, R. T.; Montalti, M.; Prodi, L.; Zaccheroni, N.; Lamb, R. D.; Dalley, N. K.; Izatt, R. M.; Bradshaw, J. S.; Savage, P. B. *Tetrahedron* **2004**, *60*, 11139.
- (55) Lloyd, D.; Coogan, M.; Pope, S. A. In *Reviews in Fluorescence 2010*; Geddes, C. D., Ed.; Springer New York: 2010; Vol. 2010, p 15.
- (56) Zhao, Q.; Huang, C.; Li, F. *Chem. Soc. Rev.* **2011**, *40*, 2508.
- (57) Lo, K. K.-W.; Zhang, K. Y.; Li, S. P.-Y. *Eur. J. Inorg. Chem.* **2011**, *2011*, 3551.
- (58) Amoroso, A. J.; Coogan, M. P.; Dunne, J. E.; Fernandez-Moreira, V.; Hess, J. B.; Hayes, A. J.; Lloyd, D.; Millet, C.; Pope, S. J. A.; Williams, C. *Chem. Commun.* **2007**, *2007*, 3066.
- (59) Stephenson, K. A.; Banerjee, S. R.; Besanger, T.; Sogbein, O. O.; Levadala, M. K.; McFarlane, N.; Lemon, J. A.; Boreham, D. R.; Maresca, K. P.; Brennan, J. D.; Babich, J. W.; Zubieta, J.; Valliant, J. F. *J. Am. Chem. Soc.* **2004**, *126*, 8598.
- (60) Fernandez-Moreira, V.; Thorp-Greenwood, F. L.; Coogan, M. P. *Chem. Commun.* **2010**, *46*, 186.
- (61) Raszeja, L.; Maghnouj, A.; Hahn, S.; Metzler-Nolte, N. *ChemBioChem* **2011**, *12*, 371.
- (62) Dirscherl, G.; König, B. *Eur. J. Org. Chem.* **2008**, *2008*, 597.
- (63) Metzler-Nolte, N. *Chimia* **2007**, *61*, 736.
- (64) Szeto, H. H.; Schiller, P. W.; Zhao, K. S.; Luo, G. X. *FASEB J.* **2005**, *19*, 118.
- (65) Puckett, C. A.; Barton, J. K. *J. Am. Chem. Soc.* **2009**, *131*, 8738.
- (66) Dattelbaum, J. D.; Abugo, O. O.; Lakowicz, J. R. *Bioconjugate Chem.* **2000**, *11*, 533.
- (67) Kunkely, H.; Vogler, A. *Inorg. Chem. Commun.* **1998**, *1*, 398.
- (68) Vogler, A.; Kunkely, H. *Coord. Chem. Rev.* **2000**, *200–202*, 991.
- (69) Czerwieńec, R.; Kapturkiewicz, A.; Anulewicz-Ostrowska, R.; Nowacki, J. *J. Chem. Soc., Dalton Trans.* **2001**, 2756.
- (70) Marqusee, S.; Robbins, V. H.; Baldwin, R. L. *Proc. Natl. Acad. Sci. U.S.A.* **1989**, *86*, 5286.



- (71) Walensky, L. D.; Kung, A. L.; Escher, I.; Malia, T. J.; Barbuto, S.; Wright, R. D.; Wagner, G.; Verdine, G. L.; Korsmeyer, S. J. *Science* **2004**, *305*, 1466.
- (72) Wang, D.; Liao, W.; Arora, P. S. *Angew. Chem. Int. Ed.* **2005**, *44*, 6525.
- (73) Ku, B.; Liang, C.; Jung, J. U.; Oh, B.-H. *Cell Res.* **2011**, *21*, 627.
- (74) Shangary, S.; Johnson, D. E. *Biochemistry* **2002**, *41*, 9485.
- (75) Siedlecka, M.; Goch, G.; Ejchart, A.; Sticht, H.; Bierzyński, A. *Proc. Natl. Acad. Sci. U.S.A.* **1999**, *96*, 903.
- (76) Kelso, M. J.; Beyer, R. L.; Hoang, H. N.; Lakdawala, A. S.; Snyder, J. P.; Oliver, W. V.; Robertson, T. A.; Appleton, T. G.; Fairlie, D. P. *J. Am. Chem. Soc.* **2004**, *126*, 4828.
- (77) Nicoll, A. J.; Miller, D. J.; Fütterer, K.; Ravelli, R.; Allemann, R. K. *J. Am. Chem. Soc.* **2006**, *128*, 9187.
- (78) Kelso, M. J.; Hoang, H. N.; Appleton, T. G.; Fairlie, D. P. *J. Am. Chem. Soc.* **2000**, *122*, 10488.
- (79) Signarvic, R. S.; DeGrado, W. F. *J. Am. Chem. Soc.* **2009**, *131*, 3377.
- (80) Kozłowski, H.; Bal, W.; Dyba, M.; Kowalik-Jankowska, T. *Coord. Chem. Rev.* **1999**, *184*, 319.
- (81) Curran, T. P.; Grant, A. L.; Lucht, R. A.; Carter, J. C.; Affonso, J. *Org. Lett.* **2002**, *4*, 2917.
- (82) Vairaprakash, P.; Ueki, H.; Tashiro, K.; Yaghi, O. M. *J. Am. Chem. Soc.* **2010**, *133*, 759.
- (83) Myers, C. P.; Williams, M. E. *Coord. Chem. Rev.* **2010**, *254*, 2416.
- (84) Copeland, K. D.; Fitzsimons, M. P.; Houser, R. P.; Barton, J. K. *Biochemistry* **2001**, *41*, 343.
- (85) Ball, Z. T. *Acc. Chem. Res.* **2012**, *46*, 560.
- (86) Jain, A.; Buchko, G. W.; Reback, M. L.; O'Hagan, M.; Ginovska-Pangovska, B.; Linehan, J. C.; Shaw, W. J. *ACS Catal.* **2012**, *2*, 2114.
- (87) Ghosh, D.; Pecoraro, V. L. *Inorg. Chem.* **2004**, *43*, 7902.
- (88) Xing, G.; DeRose, V. J. *Curr. Opin. Chem. Bio.* **2001**, *5*, 196.
- (89) Franklin, S. J. *Curr. Opin. Chem. Bio.* **2001**, *5*, 201.

- (90) Li, L.; Xu, B. *Tetrahedron* **2008**, *64*, 10986.
- (91) Fery-Forgues, S.; Lavabre, D. *Journal of Chemical Education* **1999**, *76*, 1260.

### 3. Tunable Helicity, Stability and DNA-Binding Properties of Short Peptides with Hybrid Metal Coordination Motifs

#### 3.1 Abstract

Given the prevalent role of  $\alpha$ -helical motifs on protein surfaces in mediating protein-protein and protein-DNA interactions, there have been significant efforts to develop strategies to induce  $\alpha$ -helicity in short, unstructured peptides to interrogate such interactions. Toward this goal, we have recently introduced hybrid metal coordination motifs (HCMs). HCMs combine a natural metal-binding amino acid side chain with a synthetic chelating group that are appropriately positioned in a peptide sequence to stabilize an  $\alpha$ -helical conformation upon metal coordination. Here, we present a series of short peptides modified with HCMs consisting of a His and a phenanthroline group at  $i$  and  $i+7$  positions that can induce  $\alpha$ -helicity in a metal-tunable fashion as well as direct the formation of discrete dimeric architectures for recognition of biological targets. We show that the induction of  $\alpha$ -helicity can be further modulated by secondary sphere interactions between amino acids at the  $i+4$  position and the HCM. A frequently cited drawback of the use of peptides as therapeutics is their propensity to be quickly digested by proteases; here, we observe an enhancement of up to  $\sim 100$ -fold in the half-lives of the metal-bound HCM-peptides in the presence of trypsin. Finally, we show that an HCM-bearing peptide sequence, which contains the DNA-recognition domain of a bZIP protein but is devoid of the obligate dimerization domain, can dimerize with the proper geometry and in an  $\alpha$ -helical conformation to bind a cognate DNA sequence with high affinities ( $K_d \geq 65$  nM), again in a metal-tunable manner.

### 3.2 Introduction

Protein-protein<sup>2-5</sup> and protein-DNA<sup>6-9</sup> interactions are commonly mediated by  $\alpha$ -helical domains on protein surfaces.<sup>10,11</sup> Due to the prevalence of such  $\alpha$ -helical interaction motifs in nature, there has been considerable interest in designing small, synthetic systems that maintain or mimic the  $\alpha$ -helical periodicity of such motifs and therefore can recapitulate their binding and recognition properties.<sup>12-14</sup> One route toward this goal has been through the design of entirely non-biological systems such as synthetic helix mimics<sup>15,16</sup> or foldamers with incorporated  $\beta$ -amino acids.<sup>17,18</sup> Another route is to design natural peptides with a propensity to form  $\alpha$ -helical structures. Although they have the ideal size to be effective therapeutic agents and interact with an extended region on a protein or DNA surface,<sup>19</sup> short peptides are often unstructured and prone to proteolytic digestion;<sup>20</sup> these drawbacks have led to the pursuit of diverse strategies to stabilize peptides in  $\alpha$ -helical conformations such as: covalent<sup>21-29</sup> or metal-mediated<sup>30-33</sup> stapling of helical turns, utilization of hydrogen-bond surrogates,<sup>34,35</sup> incorporation of salt bridges in  $i$  and  $i+4$  positions,<sup>36</sup> or inclusion of  $\alpha$ -amino acids with restricted conformational availability.<sup>37</sup>

As an alternative approach for helix induction in peptides, we have introduced hybrid metal coordination motifs (HCMs) that consist of a natural metal-binding side chain and a non-natural metal chelating ligand, placed at the  $i$  and  $i+7$  positions.<sup>38,39</sup> Our motivation was that HCMs would not only impart  $\alpha$ -helicity through metal-mediated crosslinking across two helix turns (Figure 3.1a), but they would also provide stable coordination motifs whose metal binding properties can be modulated through the choice of metal, chelating ligand, or the solution pH. This modularity can in turn be exploited for

the incorporation of metal-based functions (e.g., luminescence and catalysis)<sup>40</sup> or metal-mediated oligomerization (as we exploit in this report).

Our early studies focused on the surface modification of a folded,  $\alpha$ -helical protein (cyt *cb*<sub>562</sub>) with *i/i+7* HCMs that consisted of a his side chain and the non-natural chelates 8-hydroxyquinoline (Quin), 1,10-phenanthroline (Phen) or 2,2':6',2''-terpyridine (Tpy).<sup>38,39</sup> These studies showed that metal binding to these HCM motifs imparted significant chemical and thermal stability to cyt *cb*<sub>562</sub> (due to helix crosslinking) in a way that could be tuned through the choice of metal ion. It was also demonstrated that the oligomerization state and geometry of HCM-modified cyt *cb*<sub>562</sub> could be controlled through the preferred coordination geometry of a metal ion. Notably, the addition of Ni<sup>II</sup> to a His-Quin HCM-modified cyt *cb*<sub>562</sub> at a 1:2 metal:protein stoichiometry led to the formation of a V-shaped protein dimer (see Figure 3.9).<sup>38</sup> This discrete protein arrangement was dictated by the octahedral-coordination geometry of the Ni:(HCM)<sub>2</sub> moiety, wherein the two Quin functionalities adopted the preferred *cis* orientation. A structural superposition of the surface helices in this dimer revealed a very close match (rmsd = 1.6 Å) with the  $\alpha$ -helical DNA-binding domains of the homo-dimeric bZIP proteins (PDB ID: 1JNM),<sup>38</sup> suggesting that HCMs could direct the formation of helical, dimeric protein/peptide scaffolds that are structurally poised to recognize biological targets without the need for engineering extensive protein surfaces or peripheral oligomerization domains.

More recently, we expanded our work from protein scaffolds to peptides and demonstrated that His-Quin HCMs could induce substantial helicity in short (10-amino acid) unstructured peptides in a metal-tunable fashion, while allowing the simultaneous generation of metal-based luminescence.<sup>40</sup> In the current report, we build further upon this

work by examining 1) whether His-Phen motifs were also capable of helix induction in small peptides, 2) the effects of secondary elements such as the identity of the  $i+4$  residue on HCM-mediated helix induction, and 3) the protection of HCM-stabilized peptides from proteolysis. Furthermore, motivated by our observations on the HCM-induced formation of discrete, V-shaped protein dimers, we investigate 4) the ability of an HCM-bearing peptide scaffold to form  $\alpha$ -helical dimers for selective DNA recognition and binding. Our findings highlight the remarkable modularity and versatility of HCMs in controlling the architecture and the biological recognition properties of small peptides.

### 3.3 Results and Discussion

#### 3.3.1 Design of HCM-peptides

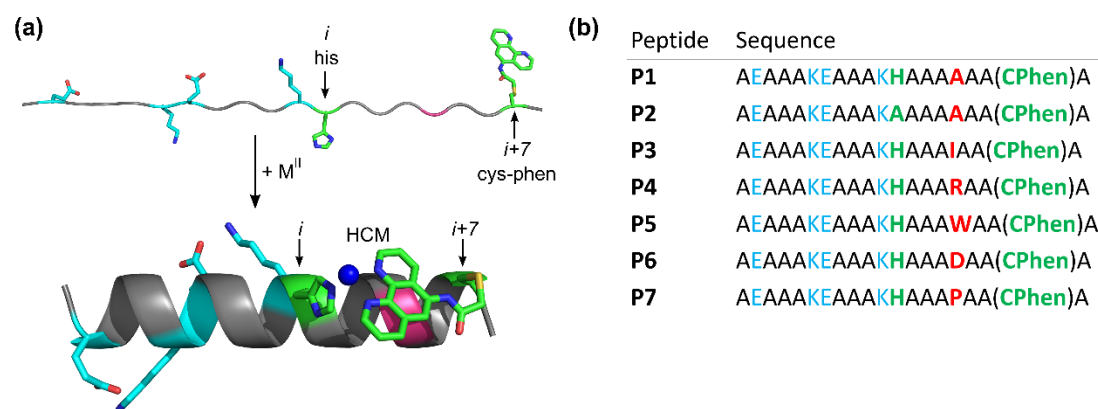


Figure 3.1: Design of peptides P1-P7. (a) Cartoon showing the proposed mode of helix induction by metal binding to the HCM. The peptides include two pairs of salt bridging side chains (cyan), the HCM motif with His at position  $i$  and Cys-Phen at position  $i+7$  (green), and various amino acids incorporated at the  $i+4$  position (red). (b) Sequences of P1-P7.

A family of 20 amino acid peptides (**P1-P7**, Figure 3.1) were synthesized to test the ability of the His-Phen HCMs to induce metal-dependent  $\alpha$ -helicity and examine the structural effects of secondary interactions between the HCM moiety and the side chain at

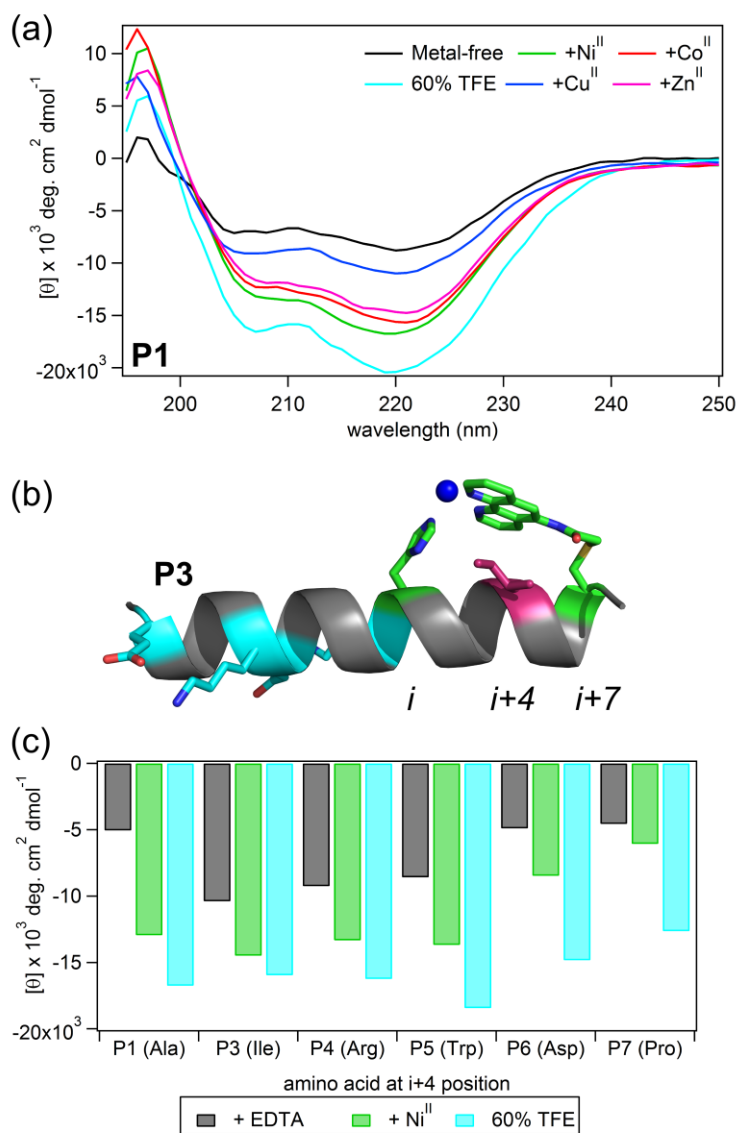


Figure 3.2: (a) CD spectra showing the induction of helicity upon addition of various metal ions. (b) Model showing an Ile residue at the *i+3* (pink) position in contact distance with the Phen functionality in the metal-bound HCM. (c) Molar ellipticity of peptide variants (metal-free, bound to Ni<sup>II</sup>, or in the presence of TFE) monitored at 222 nm.

position *i+4* (Figure 3.1). These ala-rich peptides were obtained by solid-phase peptide synthesis and contained an amidated C-terminus and an acylated N-terminus. A His and a Cys residue were placed at positions 12 (*i*) and 19 (*i+7*), respectively, and Cys19 was post-

synthetically modified with 5-iodoacetamido-1,10-phenanthroline (I-Phen) to form the desired tridentate His-Phen HCM. In this arrangement, the large aromatic Phen moiety spans directly over the side chain at the  $i+4$  position (position 16), suggesting that metal binding and helix induction by the HCM could be modulated through the interactions between Phen and the  $i+4$  residue. Thus, peptides **P1** and **P3-P7** were varied in terms of the amino acid functionalities at the  $i+4$  position (Figure 3.2). In P2, His was replaced with Ala to generate a control peptide lacking a complete HCM. All sequences contained two Glu/Lys pairs to render helix formation more favorable through additional salt bridging interactions and to increase peptide solubility.

### 3.3.2 Metal-binding properties of HCM-peptides

Employing the parent peptide **P1**, we first determined the binding affinity of the His-Phen HCM for the late first-row transition metal ions  $\text{Ni}^{\text{II}}$ ,  $\text{Co}^{\text{II}}$ ,  $\text{Cu}^{\text{II}}$ , and  $\text{Zn}^{\text{II}}$ . Due to the expected high metal binding affinities, we used ethylene glycol tetraacetic acid (EGTA) and nitrilotriacetic acid (NTA) as competing ligands in our titrations (See Materials and Methods). Metal binding was monitored by the shift of the Phen  $\pi$ - $\pi^*$  absorption band from 268 nm to 274 nm (Figure 3.3). In the case of all metal ions, metal binding curves were best fit with a two-step equilibrium model that takes into account 1:1 HCM:metal (H:M) binding as well as the subsequent metal-mediated peptide dimerization (H:M:H) event (see Figure 3.4, Figure 3.5, Figure 3.6). The dissociation constants of the metal-HCM complexes ( $K_{\text{d,M}}$ ) range from 30 nM for  $\text{Co}^{\text{II}}$  to 600 fM for  $\text{Cu}^{\text{II}}$  (Table 3.1), the affinities roughly following the Irving-Williams series:  $\text{Co}^{\text{II}} < \text{Ni}^{\text{II}} < \text{Cu}^{\text{II}} >> \text{Zn}^{\text{II}}$ , which was also observed in the case of His-Phen HCMs placed on the cyt  $cb_{562}$  surface and His-Quin HCMs (also tridentate) incorporated into 10-residue long peptides.<sup>38-40</sup> The dissociation



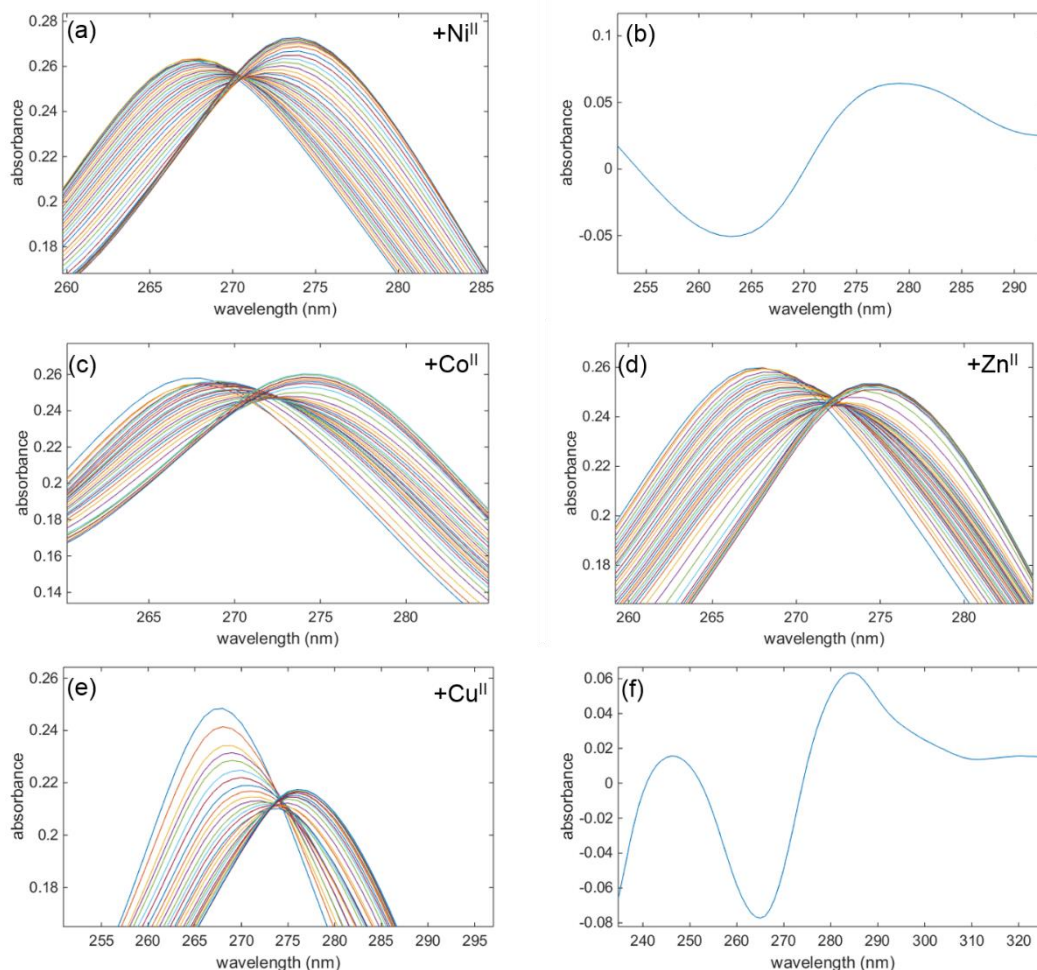


Figure 3.3: UV-vis spectra changes upon Phen- $M^{II}$  coordination. Solutions were prepared with approximately  $15 \mu\text{M}$  peptide and  $50 \mu\text{M}$  chelator (EGTA in the case of  $\text{Ni}^{II}$  and  $\text{Co}^{II}$ , and NTA in the case of  $\text{Zn}^{II}$  and  $\text{Cu}^{II}$ ), and increasing amounts of  $M^{II}$  were added by titration. A red shift of the phen  $\pi-\pi^*$  transition occurs, shifting the absorbance maximum approximately  $8 \text{ nm}$  from  $268 \text{ nm}$  to  $276 \text{ nm}$ . For  $\text{Ni}^{II}$ ,  $\text{Co}^{II}$ , and  $\text{Zn}^{II}$ , the increase in signal at  $280 \text{ nm}$  was used for fitting. For  $\text{Cu}^{II}$ , a larger transition was observed for the decrease at  $268 \text{ nm}$ , so this data was used for fitting. (a) The spectral shift as a result of  $\text{Ni}^{II}$  binding. (b) The difference spectrum between the metal-free peptide and the final spectrum of the  $\text{Ni}^{II}$  titration, showing the increase in the signal at  $280 \text{ nm}$ . (c) The spectral shift as a result of  $\text{Co}^{II}$  binding. (d) The spectral shift as a result of  $\text{Zn}^{II}$  binding. (e) The spectral shift as a result of  $\text{Cu}^{II}$  binding. (f) The difference spectrum for the  $\text{Cu}^{II}$  titration showing the greater change at  $268 \text{ nm}$ .

constants corresponding to the metal-mediated dimerization event ( $K_{d,dimer}$ ) are all in the micromolar regime ( $1\text{-}200 \mu\text{M}$ ), again similar to the dimerization constants of His-Phen

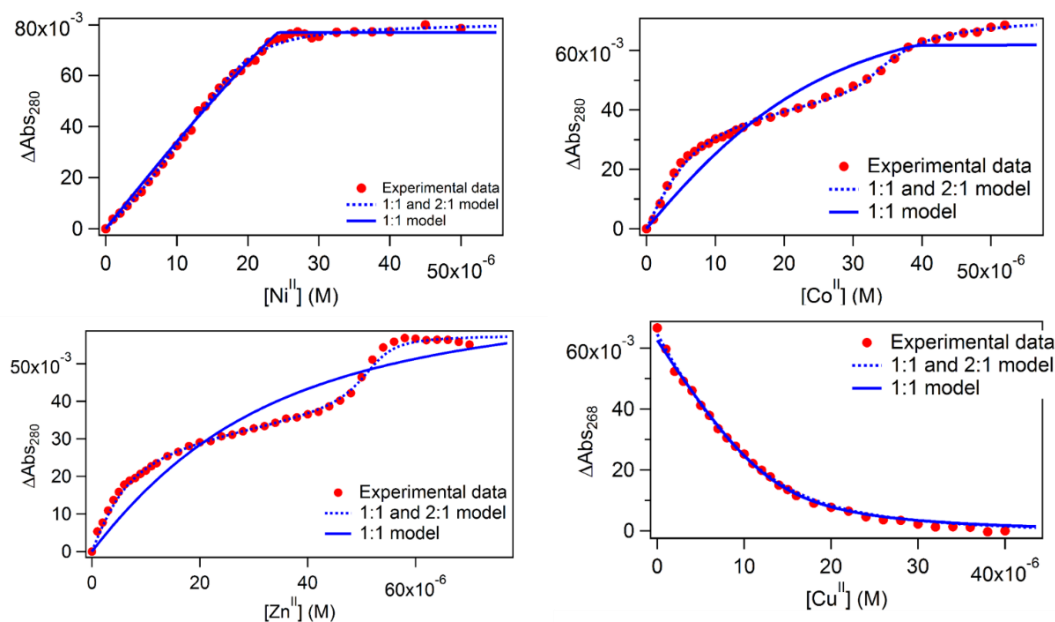


Figure 3.4: Peptide-metal binding titrations and fits. Example titrations of MeSH1 with  $\text{Co}^{\text{II}}$ ,  $\text{Ni}^{\text{II}}$ ,  $\text{Cu}^{\text{II}}$ , and  $\text{Zn}^{\text{II}}$  as monitored by UV-vis spectroscopy. Two different models were used for fitting, taking into account either a 1:1 peptide:metal binding stoichiometry (solid blue line) or both a 1:1 and 2:1 peptide:metal binding stoichiometry (dotted blue line), accounting for the possibility of a metal-induced peptide dimer. Overall, the 1:1 and 2:1 model fit the data better, indicating that a peptide dimer is likely forming in solution at limiting metal concentrations. In the case of  $\text{Cu}^{\text{II}}$ , the decrease in absorbance at 268 nm was fit to determine the binding affinity, while the increase in absorbance at 280 nm was used to fit the other three metals.

modified cyt *cb*<sub>562</sub> and His-Quin modified peptides.<sup>38-40</sup> Importantly, the  $K_{d,M}$  values are ~3-fold (for  $\text{Co}^{\text{II}}$ ) to >3 orders of magnitude (for  $\text{Cu}^{\text{II}}$ ) higher than those determined for the free Phen ligand,<sup>1</sup> and up to 6 orders of magnitude higher than those for *i/i+4* bis-His motifs incorporated into short peptides.<sup>33,41</sup> These observations confirm the formation of the desired His-Phen tridentate HCM and its ability to anchor various transition metal ions with high affinities.

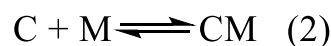
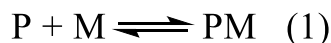


Figure 3.5: Equations used to model the metal-binding equation, where P is the peptide, M is the metal, C is the chelator, and D is a metal-mediated peptide model. Equations (1) and (2) only are used to fit data where only peptide-metal binding is accounted for, and all three equations are used to model a 1:1 and 2:1 binding equilibria.

<pre>(a) [task] task = fit data = equilibria  [mechanism] p + m &lt;==&gt; pm      kd1 dissoc e + m &lt;==&gt; em      kd2 dissoc  [constants] kd1 = 9e-10 ? kd2 = 7.789e-9  [concentrations] p = 15e-6 ?        ; M e = 50e-6          ; M  [responses] pm = .5e4 ?  [data] variable m</pre>	<pre>(b) [task] task = fit data = equilibria  [mechanism] p + m &lt;==&gt; pm      kd1 dissoc e + m &lt;==&gt; em      kd2 dissoc pm + p &lt;==&gt; d      kd3 dissoc  [constants] kd1 = 1e-11 ? kd2 = 7.789e-9 kd3 = 1e-4 ?  [concentrations] p = 19.3e-6 ?     ; M e = 50e-6         ; M  [responses] pm = .35e4 d = 2 * pm  [data] variable m</pre>
---	--

Figure 3.6: Dynafit scripts for describing metal-peptide binding equilibria. Two models for fitting were tried, as it is expected that a metal-mediated dimer will form at limiting metal concentrations. Metal-chelator dissociation constants were obtained via MaxChelator at pH 7.0, 25 °C, and 0.02 ionic strength and held fixed. The peptide concentration was calculated using an extinction coefficient of  $16,000 \text{ cm}^{-1} \text{ M}^{-1}$ . The variables used include: peptide (p), metal (m), peptide-metal complex (pm), metal-induced peptide dimer (d), chelator (e), and metal-chelator complex (em). Parameters allowed to float during the fitting process are followed by “?” and all other parameters were held fixed. In the scripts below, (a) accounts for a 1:1 peptide:metal competitive binding model, and (b) takes into account metal-induced peptide dimerization with a 1:1 and 2:1 peptide:metal competitive binding model.

### 3.3.3 Metal-dependent $\alpha$ -helix induction in HCM peptides

Circular dichroism (CD) spectroscopy was used to examine the secondary structure of **P1-P7**, to determine the extent of metal-mediated  $\alpha$ -helix induction and the structural influence of the  $i+4$  sidechain (Figure 3.1b, Figure 3.2, Table 3.1). In these experiments, we used a low concentration of peptide ( $\sim 15 \mu\text{M}$ ) and a molar excess of at least 3-fold  $\text{Co}^{\text{II}}$ ,  $\text{Ni}^{\text{II}}$ ,  $\text{Cu}^{\text{II}}$ , and  $\text{Zn}^{\text{II}}$  so as to ensure the formation of monomeric, fully metalated peptides and to prevent metal-induced dimerization. The CD signal was measured between 190-260 nm at 4 and 25 °C, with attention to the emergence of double minima at 208 and 222 nm indicative of an  $\alpha$ -helical structure.<sup>42</sup> Methods of calculating helix percentages of short peptides can be unreliable.<sup>34</sup> Therefore, we also measured the CD spectra of the peptides in 60% trifluoroethanol (TFE), a known  $\alpha$ -helix inducer,<sup>43</sup> and used these spectra as being representative of maximal helicity that could be attained for each peptide (Figure 3.7, Table 3.2).

Several pertinent observations were made: 1) Metal-mediated helix induction was observed in all peptides except the control peptide **P2**, indicating that the metal-bound His-Phen HCM indeed stabilizes an  $\alpha$ -helical structure by crosslinking two turns of the helix.

Table 3.1: Dissociation constants for peptide-metal complexes and metal-mediated dimers

Metal	His-phen HCM	Dimerization	Phen <sup>1</sup>
$\text{Co}^{\text{II}}$	$3(2) \times 10^{-8}$	$1(2) \times 10^{-6}$	$8.0 \times 10^{-8}$
$\text{Ni}^{\text{II}}$	$3(2) \times 10^{-11}$	$2(4) \times 10^{-4}$	$3.9 \times 10^{-8}$
$\text{Cu}^{\text{II}}$	$6(5) \times 10^{-13}$	$3(3) \times 10^{-5}$	$2.5 \times 10^{-9}$
$\text{Zn}^{\text{II}}$	$1.7(7) \times 10^{-8}$	$1.6(7) \times 10^{-6}$	$3.7 \times 10^{-7}$

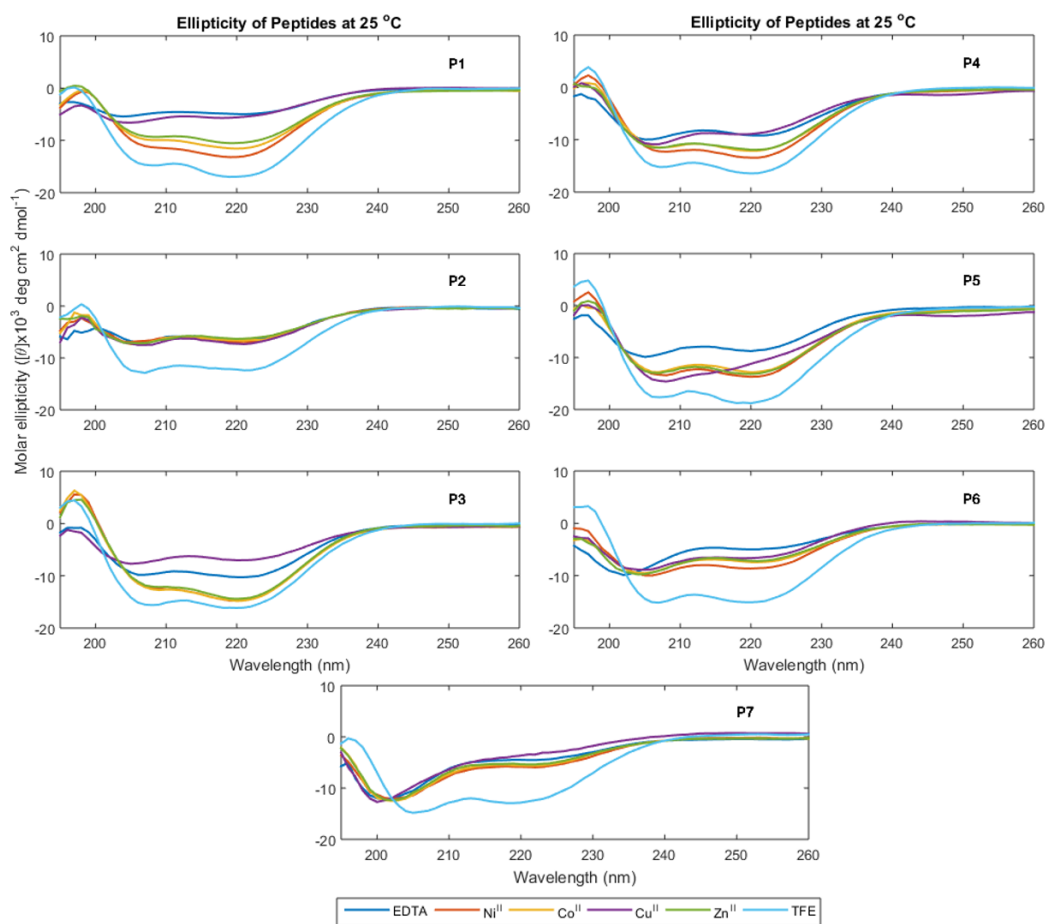


Figure 3.7: CD spectra of peptides at 25 °C. Samples were prepared with approximately 15  $\mu\text{M}$  of peptide with an excess of either  $\text{M}^{\text{II}}$  or EDTA. For each graph, EDTA = blue,  $\text{Ni}^{\text{II}}$  = red,  $\text{Co}^{\text{II}}$  = yellow,  $\text{Cu}^{\text{II}}$  = purple,  $\text{Zn}^{\text{II}}$  = green, and 60% TFE = cyan. The samples in 60% TFE were metal free; no further induction of helicity was observed upon the addition of metal.

2) In all HCM-containing peptides,  $\text{Ni}^{\text{II}}$  binding induced the most helicity,  $\text{Cu}^{\text{II}}$  the least,  $\text{Co}^{\text{II}}$  and  $\text{Zn}^{\text{II}}$  to intermediate extents. Interestingly, this trend is quite distinct from that observed for the peptides bearing His-Quin HCMs, where  $\text{Cu}^{\text{II}}$  binding yielded the most helicity and  $\text{Ni}^{\text{II}}$  frequently the least.<sup>40</sup> These differences stem from the Phen and Quin ligands directing the formation of alternate crosslinking geometries and lengths across  $i$  and  $i+7$  positions, and thereby modulating the structure of the metal-bound peptide. Since

Table 3.2: Percent helicities for metal-peptide complexes by (top) comparison with a sample containing 60% TFE and (bottom) calculated using the ratio  $[\theta]_{222}/[\theta]_{\max}$ . Here,  $[\theta]_{222}$  is the molar ellipticity measured at 222 nm, and  $[\theta]_{\max} = (-44000 + 250T) \cdot (1/(k-n))$ , where  $k$  is a constant and equal to 4, and  $n$  is the number of amide bonds and equal to 21.

Peptide	EDTA	Ni <sup>II</sup>	Co <sup>II</sup>	Cu <sup>II</sup>	Zn <sup>II</sup>
<b>Percent helicity, vs. TFE (25 °C)</b>					
<b>P1</b>	30.1	77.3	68.5	32.3	62.0
<b>P2</b>	49.8	53.6	52.9	57.5	48.6
<b>P3</b>	65.0	90.1	92.3	54.8	89.3
<b>P4</b>	56.9	82.1	73.9	52.7	73.3
<b>P5</b>	46.5	74.1	69.1	56.1	72.2
<b>P6</b>	33.0	57.1	50.8	43.3	48.7
<b>P7</b>	36.1	48.0	44.9	25.6	43.2
<b>Percent helicity, vs. TFE (4 °C)</b>					
<b>P1</b>	42.8	81.8	78.3	54.2	73.8
<b>P2</b>	75.2	76.7	75.5	77.9	74.5
<b>P3</b>	80.6	93.5	95.0	68.7	93.3
<b>P4</b>	76.1	93.3	88.9	57.9	89.7
<b>P5</b>	68.8	78.5	77.6	64.2	82.1
<b>P6</b>	47.4	72.7	68.7	69.9	69.6
<b>P7</b>	46.7	60.8	58.9	34.4	54.8
<b>Percent helicity, calculated (25 °C)</b>					
<b>P1</b>	16.7	42.9	38.0	17.9	34.3
<b>P2</b>	21.8	23.4	23.1	25.1	21.2
<b>P3</b>	34.3	48.0	48.8	29.0	47.2
<b>P4</b>	30.6	44.2	39.8	28.4	39.4
<b>P5</b>	28.4	45.3	42.2	34.2	44.0
<b>P6</b>	16.2	28.0	25.0	21.3	24.0
<b>P7</b>	15.1	20.1	18.8	10.7	18.1
<b>Percent helicity, calculated (4 °C)</b>					
<b>P1</b>	24.7	47.1	45.1	31.2	42.6
<b>P2</b>	31.6	32.2	31.7	32.7	31.3
<b>P3</b>	43.6	50.5	41.3	37.1	50.4
<b>P4</b>	42.6	52.2	49.7	32.3	50.2
<b>P5</b>	45.0	51.3	50.7	42.0	53.7
<b>P6</b>	26.2	40.2	38.0	38.6	38.4
<b>P7</b>	20.9	26.4	27.3	15.4	24.5

Phen and Quin are nearly identical in terms of the inner-sphere coordination geometry, but differ only in terms of the chelate composition (N/N vs N/O) and the size of the aromatic moiety, we conclude that even subtle differences in HCM coordination can have substantial effects on peptide structure. 3) Peptides **P3**, **P4**, and **P5**, which bear bulky, hydrophobic

side chains (Ile, Arg and Trp) in the  $i+4$  position, display considerable helicity (47-65% at 25 °C with respect to TFE-containing samples) even in the absence of metal binding (Figure 3.2, Table 3.2). Baldwin and others have previously documented the  $\alpha$ -helix stabilizing effect of hydrophobic interactions between side chains in  $i$  and  $i+4$  as well as in  $i$  and  $i+3$  positions.<sup>44-46</sup> It appears that this effect is amplified in the case of HCM-peptides due to the extensive Phen aromatic system and large hydrophobic side chains at  $i+4$  ( $i-3$  with respect to Phen). In contrast, peptide **P1** with the small Ala side chain, **P6** with the negatively charged Asp or **P7** with the Pro residue, a known helix breaker,<sup>47</sup> possess considerably less helicities (30-36% at 25 °C with respect to TFE-containing samples, (Table 3.2). 4) The increase in  $\alpha$ -helicity upon Ni<sup>II</sup> addition is sizeable in all cases (except P2), ranging from +47% (from 30% to 77% vs. TFE) for **P1** to +12% (from 36% to 48% vs. TFE) for **P7**. The highest absolute helicity, ~90%, is observed in the case of **P3**. In contrast, Cu<sup>II</sup> coordination can actually lead to  $\alpha$ -helix destabilization in some cases, for example, by as much as -10% in **P3** and **P7** (Figure 3.7, Table 3.2).

Taken together with our previous studies on His-Quin systems,<sup>40</sup> these observations on His-Phen peptides highlight the modularity of HCMs in controlling peptide structure through the choice of the metal ion and the metal chelating functionality as well as through the amino acid side chains that make secondary contacts with the HCM motif.

### 3.3.4 Stability of HCM-peptides

#### 3.3.4.1 Thermal stability of HCM peptides

We next examined whether His-Phen HCMs confer stability onto the peptide scaffolds upon metal coordination. Thermal unfolding of **P1-P7** was monitored by the

disappearance of the CD signal at 222 nm as the temperature was raised from 10-90 °C (Figure 3.8). As expected from their short sequences, all peptides display relatively low thermal denaturation points ( $T_m$ )<sup>48</sup> and shallow denaturation transitions, indicative of low cooperativity.<sup>49</sup> In general, the trends seen in the metal-mediated  $\alpha$ -helix induction are also observed in the thermal stabilities of the peptides, with Ni<sup>II</sup> binding providing the greatest

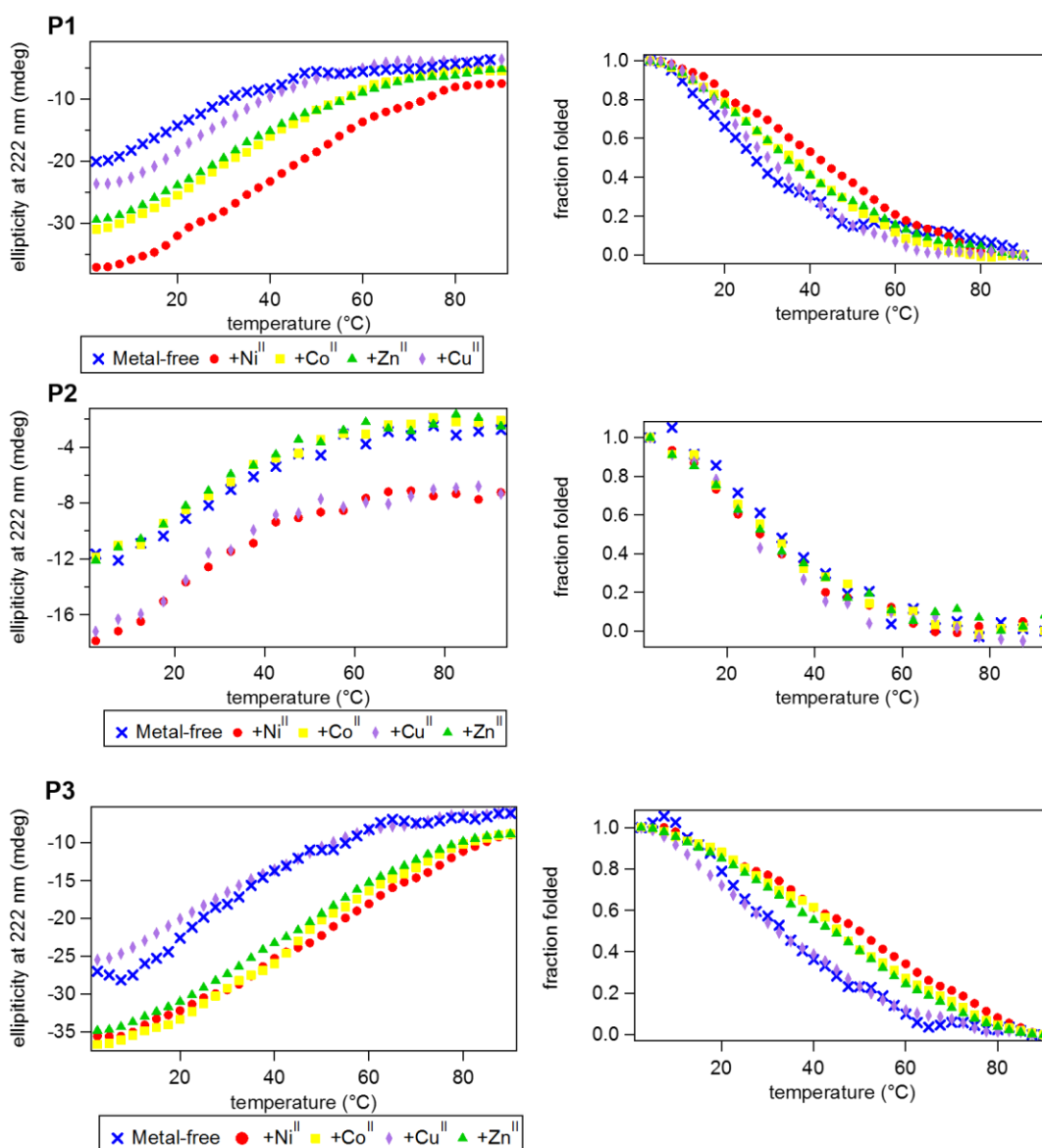


Figure 3.8: Thermal unfolding curves. The raw data is shown in the left panels, while the normalized unfolding curves are shown on the right.



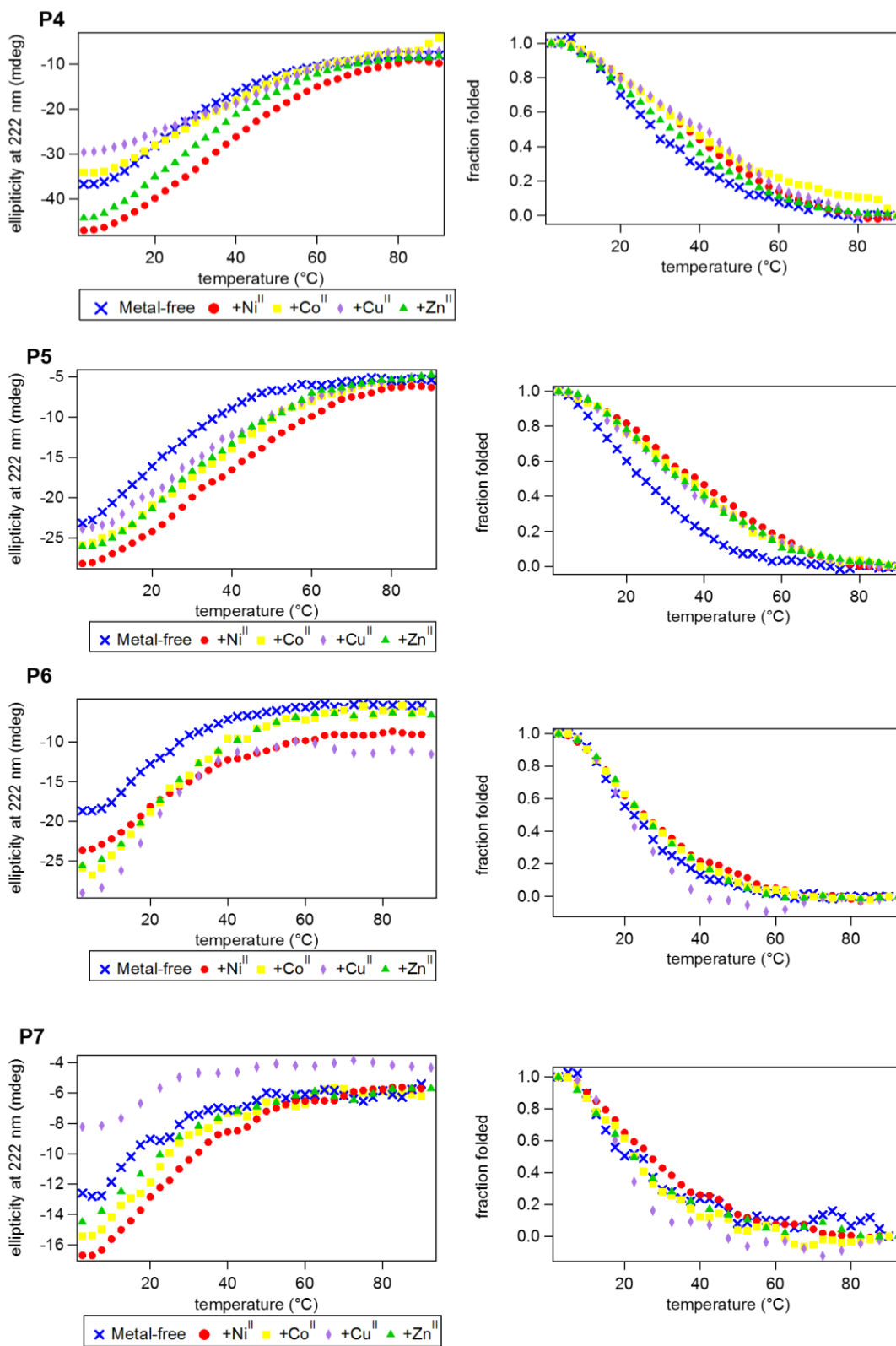


Figure 3.8: Thermal unfolding curves, continued.

Table 3.3: Calculated  $T_m$  for each of the peptide-metal combinations. The signal at 222 nm was measured to observe peptide unfolding as the temperature was gradually increased. Wavelength scans from 260-190 nm were measured for each sample before and after the thermal unfolding experiment was performed in order to verify the reversibility of the unfolding.

Peptide	EDTA	Ni <sup>II</sup>	Co <sup>II</sup>	Cu <sup>II</sup>	Zn <sup>II</sup>
P1	16.3 ± 1.9	31.6 ± 2.9	26.5 ± 0.9	22.9 ± 0.7	23.8 ± 1.0
P2	23.6 ± 0.5	20.1 ± 1.1	22.1 ± 0.8	21.5 ± 0.9	21.6 ± 0.9
P3	23.8 ± 2.0	38.7 ± 2.4	37.2 ± 1.6	18.8 ± 1.7	33.7 ± 1.0
P4	20.2 ± 0.8	28.5 ± 0.7	24.6 ± 1.9	29.4 ± 2.1	23.0 ± 0.7
P5	15.8 ± 0.8	28.4 ± 1.2	26.0 ± 1.3	22.3 ± 1.6	24.3 ± 1.9
P6	16.2 ± 0.6	17.0 ± 1.0	17.8 ± 0.5	15.9 ± 0.5	16.6 ± 1.3
P7	10.5 ± 3.3	17.0 ± 1.4	16.7 ± 1.4	9.2 ± 1.5	8.5 ± 1.0

Table 3.4: Changes in the  $T_m$  for each peptide upon metal-binding.  $\Delta T_m$ s were calculated by subtracting the  $T_m$  for each metal-free (EDTA) sample from metal-bound peptide.

Peptide	Ni <sup>II</sup>	Co <sup>II</sup>	Cu <sup>II</sup>	Zn <sup>II</sup>
P1	15.3	10.2	6.6	7.5
P2	-3.5	-1.5	-2.1	-2.0
P3	14.9	13.4	-5.0	9.9
P4	8.3	4.4	9.2	2.8
P5	12.6	10.2	6.5	7.5
P6	0.8	1.6	-0.3	0.4
P7	6.5	6.2	-1.3	-2.0

stabilization and Cu<sup>II</sup> the least. In accordance with their highest helical contents, Ni<sup>II</sup>-bound **P1**, **P3**, **P4** and **P5** possess the highest  $T_m$  values, ranging from 28 °C for **P4** and **P5** to 39 °C for **P3**. The largest metal-induced increases in  $T_m$  is seen for **P1** (up to +15 °C), which is consistent with the greatest induction of helicity for this peptide. The control peptide **P2** does not display any metal-dependent changes in stability, consistent with the lack of an HCM (Figure 3.8, Table 3.3, Table 3.4).

### 3.3.4.2 Proteolytic stability of HCM peptides

Perhaps a more practically relevant form of peptide stability is resistance to proteolytic cleavage. A commonly cited drawback to using peptides for biological targeting is their propensity to be quickly digested in the presence of proteases.<sup>50</sup> Since it has been established that proteases bind their substrates in an unfolded, extended fashion, one way of protecting the peptide backbone is by promoting a stable, folded peptide structure.<sup>50</sup> In order to measure the ability of the HCM to confer protease resistance, we chose **P3** as a test case because it possessed the highest extent of helicity in the presence of Ni<sup>II</sup> among

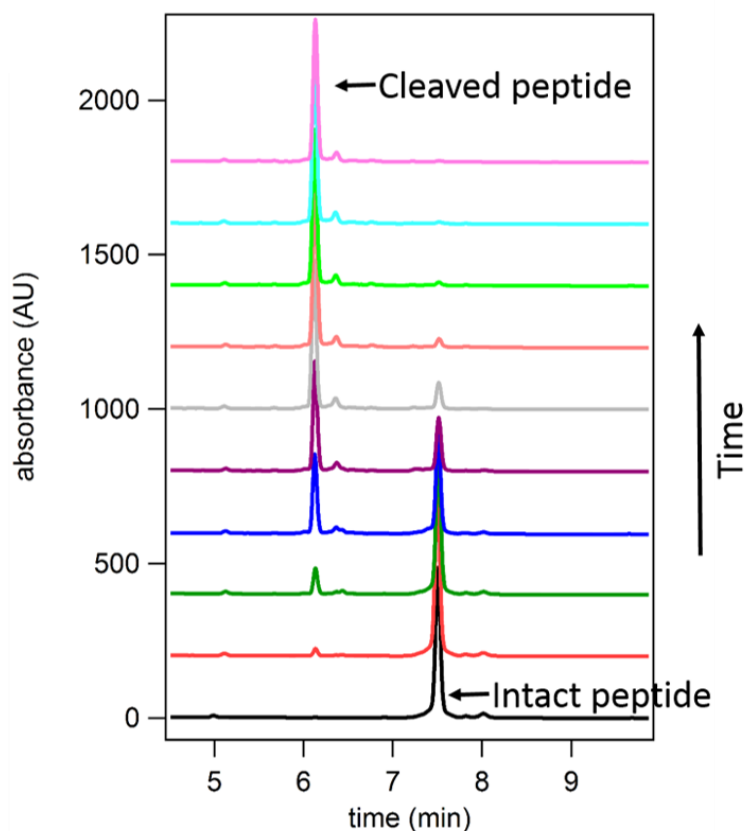


Figure 3.9: HPLC traces of the set of data collected for the metal-free, HCM-bound peptide during the tryptic digestion experiment. The intact peptide elutes at approximately 7.5 min; that peak disappears over time and a new peak at 6.0 min, corresponding to the cleaved peptide fragment, appears.

Table 3.5: Kinetic parameters for the tryptic digestion of **P3** under various conditions.

Metal	Rate (sec <sup>-1</sup> )	Half-life (min)	Enhancement over metal-free HCM
4 °C			
Metal-free: <b>P3</b> <sub>bare</sub>	$2.0 \times 10^{-3} \pm 1 \times 10^{-4}$	6	0.8
Ni <sup>II</sup> : <b>P3</b> <sub>bare</sub>	$1.7 \times 10^{-3} \pm 3 \times 10^{-4}$	7	0.9
Metal-free	$1.6 \times 10^{-3} \pm 2 \times 10^{-4}$	7	1
Ni <sup>II</sup>	$1.7 \times 10^{-5} \pm 2 \times 10^{-6}$	700	96.7
Cu <sup>II</sup>	$1.9 \times 10^{-4} \pm 2 \times 10^{-5}$	60	8.4
Zn <sup>II</sup>	$4.1 \times 10^{-5} \pm 6 \times 10^{-6}$	280	38.8
25 °C			
Metal-free	$5.0 \times 10^{-3} \pm 6 \times 10^{-4}$	2	1
Ni <sup>II</sup>	$1.1 \times 10^{-4} \pm 5 \times 10^{-6}$	106	53
Cu <sup>II</sup>	$2.3 \times 10^{-3} \pm 2 \times 10^{-4}$	5	2.5

all peptides. We incubated both metal-bound and metal-free **P3** (1.5 mM) with trypsin (0.3 mg/mL or 12.9 μM), which specifically cleaves peptides on the carboxy end of Lys or Arg residues,<sup>51</sup> of which there are two in **P3** (Lys6 and Lys11). The extent of digestion at 4 °C was determined at various time points by HPLC (Figure 3.9, Table 3.5) through monitoring the decrease in the intensity of the intact peptide peak. The cleavage products were identified by additional LC-MS experiments (Figure 3.10). Under pseudo-first order reaction rate kinetics, apo-**P3** was efficiently digested by trypsin with a  $k_{\text{digest}} = 1.6 \times 10^{-3} \text{ s}^{-1}$ , and reaching completion by approximately 1 h. Upon metal binding, **P3** becomes considerably more resistant to digestion, following the same trend (Ni<sup>II</sup> > Co<sup>II</sup> ≈ Zn<sup>II</sup> > Cu<sup>II</sup>) observed for helix induction (Figure 3.11, Table 3.5). Ni<sup>II</sup>-bound **P3** is cleaved by only 15% at 150 min, with  $k_{\text{digest}} = 1.7 \times 10^{-5}$ , nearly 100-fold slower than the apo peptide. As a comparison, a half-life enhancement of 82-fold was reported for the chymotryptic digestion of a 36-residue peptide that was stabilized through two *i/i+4* covalent staples near its N- and C-termini.<sup>52</sup> At 25 °C, the digestion rates are uniformly faster for all species and follow

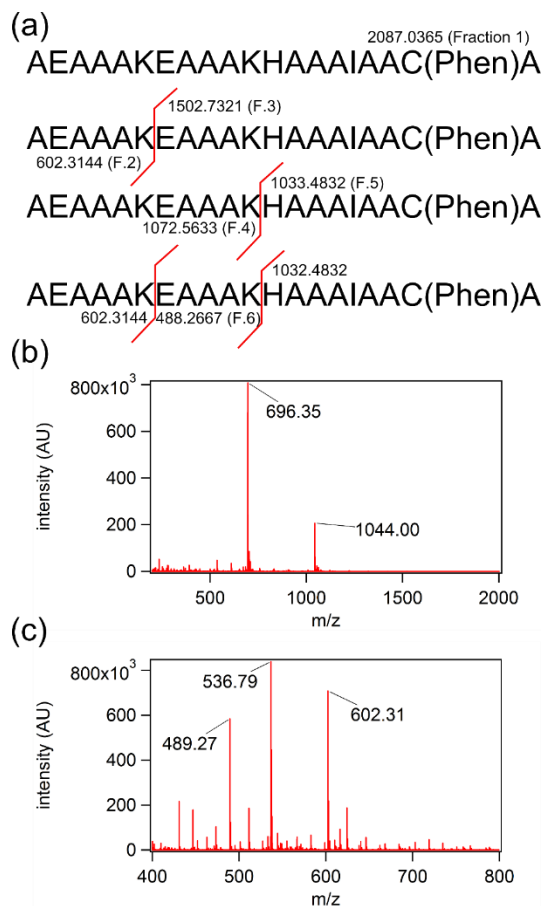


Figure 3.10: (a) Trypsin cleavage sites and corresponding masses of P3. (b) Masses of intact peptide. Expected molecular weight: 2086.03. Observed:  $[M+2H]^{2+}$ : 1044.00, expected 1044.02.  $[M+3H]^{3+}$ : 696.35, expected 696.35. (c) Masses of cleaved peptides. Expected molecular weights:  $[M+H]^+$ : 602.31, observed 602.31. Expected  $[M+H]^+$ : 489.27, observed 489.27. Expected  $[M+2H]^{2+}$ : 536.79, observed 536.79.

the same trends (Table 3.5), but the overall stabilization effect of metal binding is dampened as expected from lower absolute helicities combined with elevated enzymatic activity at this temperature. Stabilization by  $Ni^{II}$  coordination at 25 °C is now 45-fold over the apo-peptide and that by  $Cu^{II}$  binding only 2-fold. As a control, we used a variant of **P3** (**P3<sub>bare</sub>**) that was not labelled with Phen at Cys19, and therefore is devoid of the HCM and incapable of metal-mediated  $\alpha$ -helix induction. In the absence of any metal or in the presence of  $Ni^{II}$ , **P3<sub>bare</sub>** was cleaved by trypsin with essentially the same kinetics as apo-

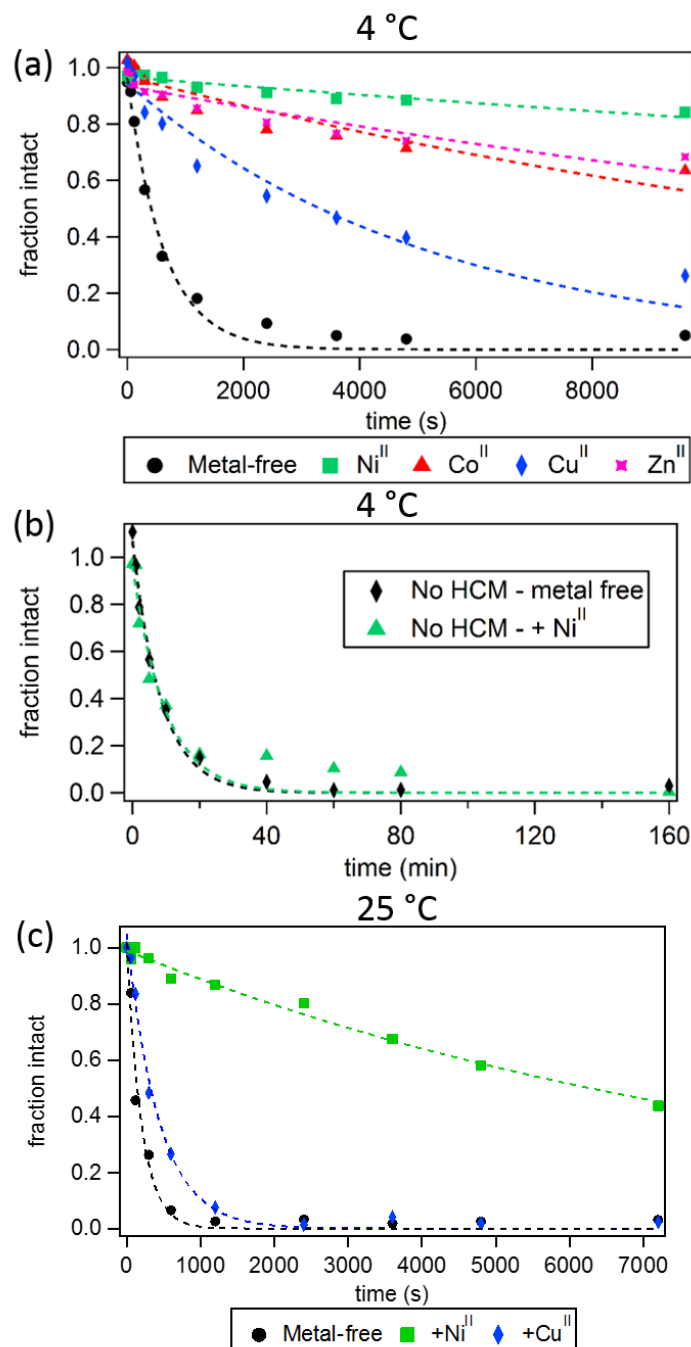


Figure 3.11: Tryptic digestion of P3 at 4 or 25 °C in the presence and absence of  $M^{II}$ . (a) Kinetics of trypsin digestion when P3 was metal-free (black circles), or bound to  $Cu^{II}$  (blue diamonds),  $Co^{II}$  (red triangles),  $Zn^{II}$  (pink squares), or  $Ni^{II}$  (green squares). (b) Kinetics of trypsin digestion of  $P3_{bare}$  in the presence or absence of  $Ni^{II}$ . (c) Kinetics of trypsin digestion of metal-free or metal-bound P3 at 25 °C.

**P3** (Figure 3.11, Table 3.5). These observations confirm that the metal-bound HCM is necessary for increased resistance to digestion and that the observed stabilization effects are not due to a possible inhibition of trypsin due to free metal ions.

It is interesting to note that at 4 °C, Cu<sup>II</sup> is able to confer tryptic stability to **P3** despite the lack of  $\alpha$ -helix induction. The observed 8-fold enhancement of peptide half-life is small compared to that observed in the case of Ni<sup>II</sup> binding, it is likely that some amount of structural confinement of the peptide backbone is caused by Cu<sup>II</sup> binding, reducing the ability of trypsin to cleave the backbone. The metal-binding affinity indicates that Cu<sup>II</sup> binds the HCM in the intended tri-coordinate motif, but it is likely that the coordination geometry preferences of Cu<sup>II</sup> do not accommodate  $\alpha$ -helical structure in the peptide backbone.

### **3.3.5 HCM peptides for DNA binding and recognition**

#### **3.3.5.1 Design of DNA-binding peptides with HCM functionality**

Having established the metal coordination and tunable  $\alpha$ -helix induction properties of HCM-peptides, we next investigated whether they could be leveraged for binding and recognition of biomolecular targets, specifically DNA. As a model, we chose basic leucine zipper (bZIP) proteins which are dimeric gene transcription factors that consist of a dimerization domain characterized by a heptad repeat of leucine residues and a DNA binding domain (basic domain) containing basic and hydrophobic residues.<sup>7</sup> Extensive structural and biochemical studies have revealed that in the DNA-bound, dimeric form of bZIP proteins, the basic domains assume an  $\alpha$ -helical conformation and adopt a distinct scissor-shaped geometry, which allows them to form extensive interactions with two adjacent DNA major grooves.<sup>7</sup> The  $\alpha$ -helix induction in the basic domains (which are not

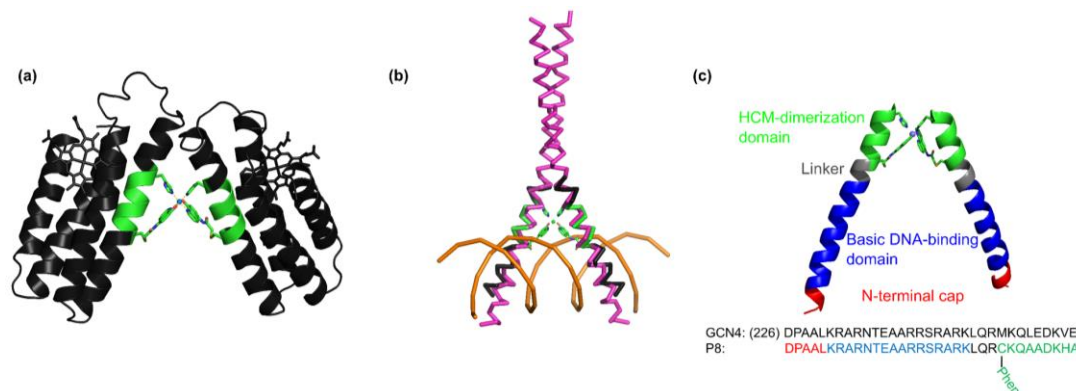


Figure 3.12: Design of the DNA-binding peptide P8. (a) The V-shaped *cyt cb<sub>562</sub>* dimer dictated by Ni<sup>II</sup> coordination to the His/Quin HCMs (green) (PDB ID: 3L1M). Adapted from reference 39. (b) Backbone superposition of the Helix3 domains of HCM-modified *cyt cb<sub>562</sub>* (black) onto the basic domain of Jun bZip homodimer (magenta) complexed with cAMP responsive element (CRE) (brown) (PDB ID = 1JNM). (c) Overall architecture and structural components of P8, and its proposed Ni-induced dimerization geometry based on the structural model in (b).

appreciably helical in isolation),<sup>53</sup> their dimerization<sup>54</sup> and their proper orientation<sup>55</sup> were found to be crucial for efficient and specific DNA binding.<sup>56</sup> Several groups have previously shown that the “zipper” domain of bZIP proteins could be replaced with an alternative method of dimerization,<sup>55,57-63</sup> i.e. disulfide binding.<sup>54</sup> Of particular interest is the work done by the Peacock<sup>64</sup> and Schepartz<sup>65,66</sup> groups, where metal ions were used to promote the correct orientation of a single peptide chain for DNA binding. The Mascareñas group has also designed peptides that can form alternate dimer orientations through either metal binding or disulphide binding, and can recognize distinct DNA sequences based on the external stimuli.<sup>67</sup>

In earlier studies, we observed that Ni<sup>II</sup> coordination by His-Quin HCMs can direct the formation of protein dimers with a discrete, rigid V-shaped architecture that closely resembles the orientation of the basic, DNA-binding domains of bZIP proteins (Figure



3.12). We thus reasoned that HCMs could provide a means to regulate DNA binding by peptide sequences simultaneously through metal-tunable  $\alpha$ -helix induction and through metal-directed dimerization and orientation.

We designed the 33-residue peptide **P8** based on GCN4, a bZIP protein that specifically binds the CRE DNA sequence.<sup>68</sup> The **P8** sequence contains the N-terminal cap of GCN4 (Asp1 to Lys5, in our numbering) and the entire 16-residue long basic domain of GCN4 (Lys6 to Lys21) without alteration. It also contains the 4-residue long linker region and an 8-residue portion of the dimerization domain, which provides an extension of sufficient length for the insertion of an  $i/i+7$  His-Phen HCM. To install the HCM, the last residue of the linker region (Met25) was converted into a Cys for the attachment of Phen and Val32 into His. Additionally, Leu28 and Asp29 in the  $i+3$  and  $i+4$  positions were converted into Ala to prevent any clashes of the side chains with the HCM motif.

### 3.3.5.2 Induced helicity in the GCN4-based peptide

Using CD spectroscopy, we first confirmed that **P8** undergoes a metal-induced increase in helicity, following the same trend ( $\text{Ni}^{\text{II}} > \text{Zn}^{\text{II}} > \text{Cu}^{\text{II}}$ ) observed in **P1-P7** (Figure

Table 3.6: Helicity and  $T_m$  of metal-free and metal-bound **P8**.

<b>P8</b> + ...	Percent Helicity, calculated		Percent Helicity, compared to sample in 60% TFE		$T_m$ (°C)
	4 °C	25 °C	4 °C	25 °C	
Metal free	9.8	2.0	42.5	29.6	$10.9 \pm 1.2$
$\text{Ni}^{\text{II}}$	16.2	6.3	56.8	41.1	$15.5 \pm 0.9$
$\text{Cu}^{\text{II}}$	10.1	4.5	43.1	31.1	$9.9 \pm 1.1$

3.13, Table 3.6). As before, this effect is eliminated in **P8**<sub>bare</sub>, which lacks the Phen functionality (Figure 3.13, Table 3.6). The induction of helicity was not as dramatic as observed on the shorter peptides, and this is likely due to the fact that the HCM was located on the C-terminal end of a much longer peptide, so the ability of the HCM to induce helicity throughout the entire peptide was limited. Overall, we calculated that the peptide was 16.2% helical when bound to Ni<sup>II</sup>, although this value was significantly higher (56.8%) when compared to a peptide in 60% TFE.

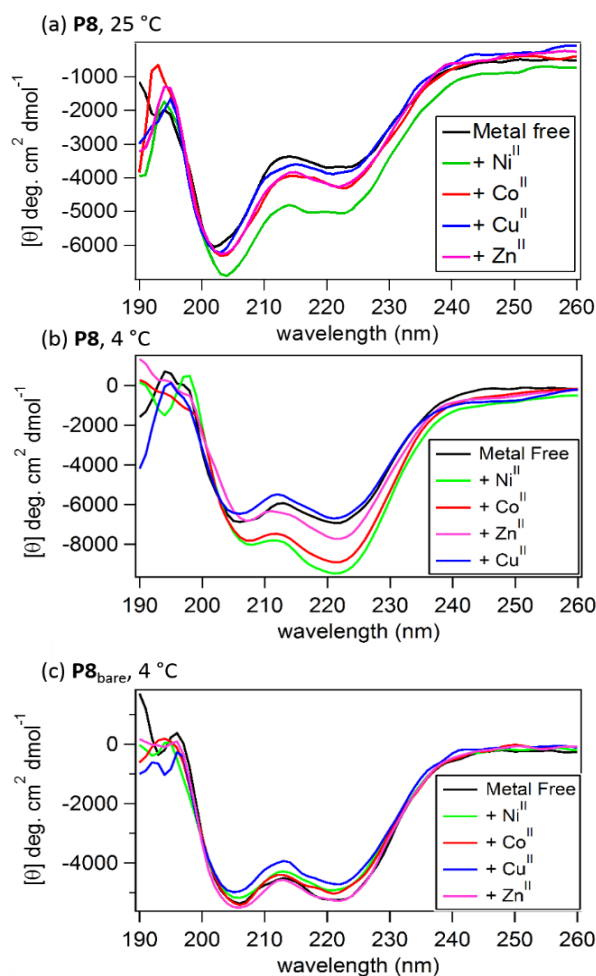


Figure 3.13: Induced helicity in **P8** at (a) 25 °C and (b) 4 °C. (c) No induction of helicity was observed in **P8**<sub>bare</sub>, where HCM functionality is absent.

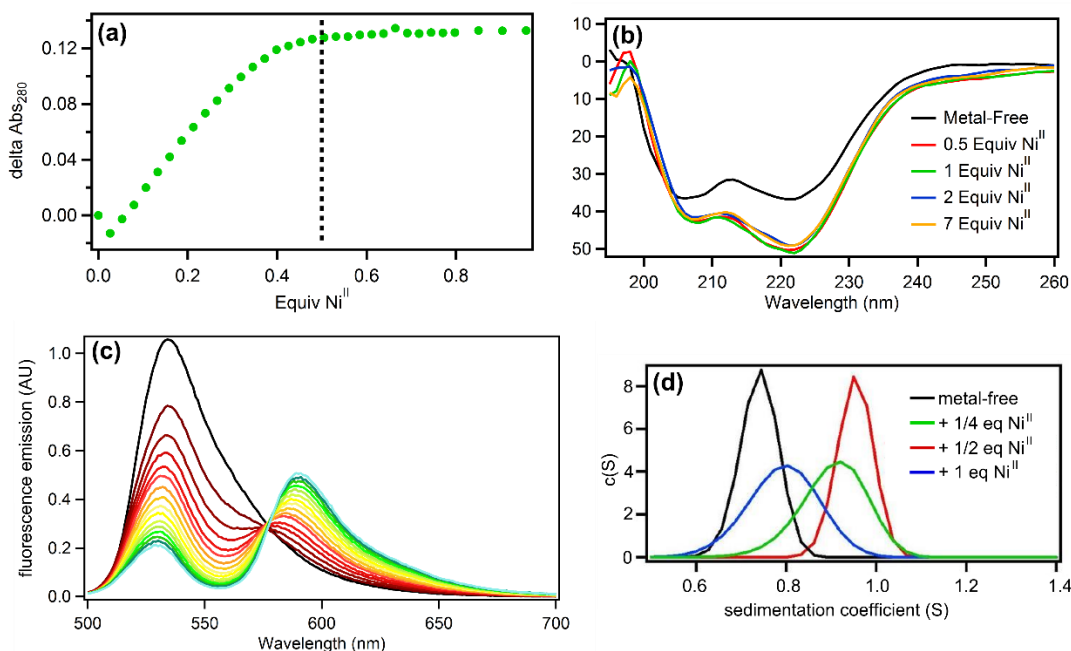


Figure 3.14: Metal-dependent dimerization. (a) Ni-binding titration of **P8** monitored by changes in the absorption spectrum of Phen at 280 nm. The dotted black line indicates saturation of binding at 0.5 equiv. of Ni<sup>II</sup> per **P8**. (b) CD titrations to determine the stoichiometry of metal-binding and dimer formation as monitored by CD. Upon the addition of Ni<sup>II</sup> no further change in secondary structure is observed after 0.5 equivalents of M<sup>II</sup> are added. (c) FRET data—the decrease in signal at 530 nm corresponds to the quenching of the fluorescein signal as the dimer forms and rhodamine is excited by FRET, which is observed in the increasing signal at 600 nm. (d) Sedimentation velocity data for **P8** in the presence of different amounts of Ni<sup>II</sup> determined by AUC.

### 3.3.5.3 Metal-based peptide dimerization

Titration of metal ions into a 15  $\mu\text{M}$  solution of **P8** indicated that the maximal helicity (measured by CD at 222 nm) and the formation of fully metallated HCM (measured by UV-vis,  $\lambda_{\text{max}}$  at 276 nm) is achieved at a ratio of 1:2 M<sup>II</sup>:**P8**, indicating the formation of the desired metal-directed peptide dimers (M:**P8**<sub>2</sub>) (Figure 3.14a, b). In order to more directly measure the formation of the metal-directed **P8** dimers, we conducted analytical ultracentrifugation (AUC) experiments. Metal-free **P8** exhibits a maximal sedimentation

coefficient at 0.75 S. The sedimentation peak shifts to 0.8 S upon addition of 0.25 equiv. of Ni<sup>II</sup> and reaches a maximum of 0.95 S at 0.5 equiv. Ni<sup>II</sup>, again consistent with the Ni<sup>II</sup>:**P8**<sub>2</sub> stoichiometry. Addition of any further Ni<sup>II</sup> leads to the enrichment of the solution with fully metallated **P8** species (Ni<sup>II</sup>:**P8**) which does not dimerize, leading to the shift of the sedimentation peak to lower values. The formation of a peptide dimer was also observed through FRET experiments (Figure 3.14). Based on the values calculated for the K<sub>d</sub> of dimerization from the UV-vis titrations of P1, we estimate that a peptide dimer forms with low μM affinity (Table 3.1).

#### 3.3.5.4 DNA binding by HCM peptides

In order to probe interactions of **P8** with the CRE DNA sequence, which should lead to increased helicity in the basic domain through structural templating, we carried out CD experiments. As we hypothesized above, induction of helicity upon metal-binding to the HCM occurs at the C-terminus and results in an overall helicity of approximately 20% for Ni<sup>II</sup> bound **P8**, and it has previously been established that helicity can be induced in the basic region of GCN4 upon DNA binding.<sup>56</sup> Thus, we expected to see a significant increase in helicity in peptides that were both metal- and DNA-bound. These experiments were conducted with sufficiently high **P8** concentrations (5 μM) to ensure the formation of the metal-mediated P8 dimer. The addition of an equimolar amount of double-stranded (ds) CRE led to a significant increase in the helicity of apo-**P8** (at both 4 and 25 °C) (Figure 3.15). These experiments were conducted with a peptide concentration of 5 μM, approximately 2 orders of magnitude above the apparent K<sub>d</sub> of DNA-binding, which may cause a transient interaction with the metal-free peptide as well, explaining the increase in

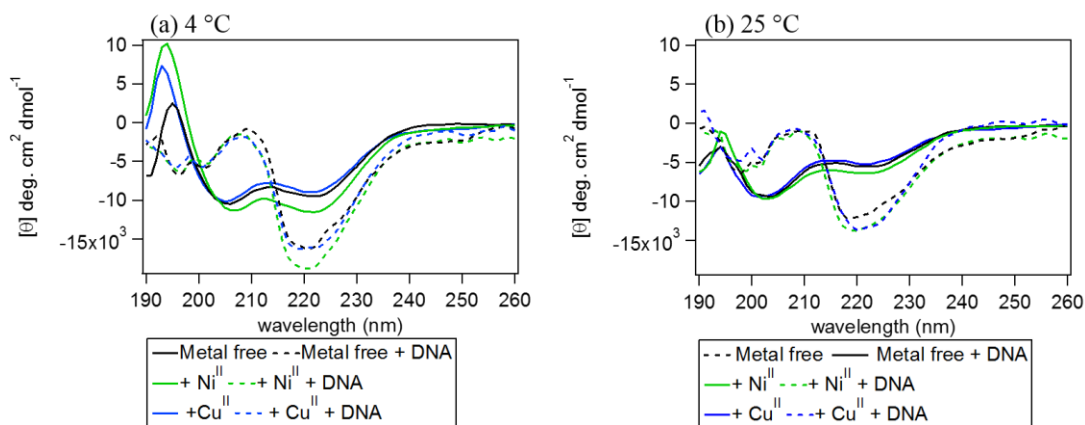


Figure 3.15: CD spectra of **P8** in the presence and absence of M<sup>II</sup> and DNA.

Table 3.7: Quantification of helicity and melting temperature ( $T_m$ ) of DNA-bound **P8**.

P8 + ...	Percent Helicity, calculated		$T_m$ (°C)	$\Delta T_m$ (compared to DNA free peptide, °C)
	4 °C	25 °C		
Metal free + DNA	39.5	26.0	$31.7 \pm 1.7$	20.8
Ni <sup>II</sup> + DNA	47.3	30.9	$36.6 \pm 0.8$	21.1
Cu <sup>II</sup> + DNA	39.9	31.2	$30.8 \pm 2.5$	20.9

helicity observed in the metal-free sample. The addition of 0.5 equiv. of Ni<sup>II</sup> or Cu<sup>II</sup> to the peptide-DNA solution led to a further increase in helicity, indicative of the formation of quaternary M:**P8**<sub>2</sub>:CRE complex. At 4 °C, the Ni<sup>II</sup>-bound **P8**-DNA adduct displayed a higher helicity compared to the Cu<sup>II</sup>-bound form, although at 25 °C, this difference became minimized. While this observation is surprising in the light of our previous finding that Ni<sup>II</sup> is a considerably better helix inducer than Cu<sup>II</sup> for peptides with His/Phen HCMs, it suggests that there is indeed an interplay between DNA-binding interactions and metal-

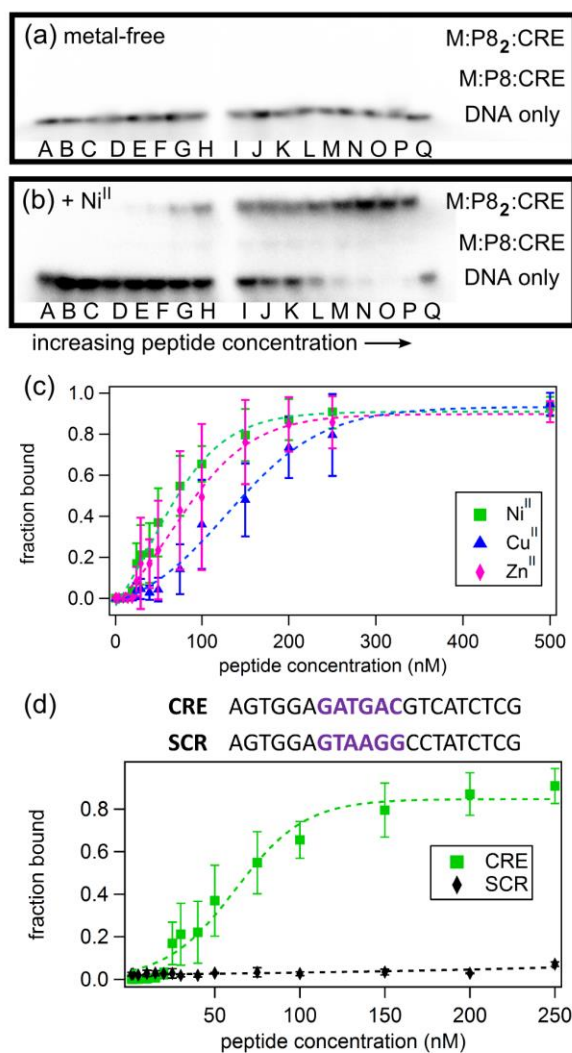


Figure 3.16: Electrophoretic mobility shift assay for monitoring **P8**-CRE binding in the absence (a) and the presence (b) of 0.5 equiv. of Ni<sup>II</sup>. Lane Q contains CRE without any added peptide; DNA concentration is kept constant at 1 nM while the **P8** concentrations varies: (A) 1 nM, (B) 2 nM, (C) 5 nM, (D) 10 nM, (E) 15 nM, (F) 20 nM, (G) 25 nM, (H) 30 nM, (I) 40 nM, (J) 50 nM, (K) 75 nM, (L) 100 nM, (M) 150 nM, (N) 200 nM, (O) 250 nM, (P) 500 nM. The intensities of the radioactively labelled CRE bands were measured by phosphorimaging. (c) Effects of different metal ions (0.5 equiv.) on CRE binding by **P8**, determined by electrophoretic mobility shift assays. (d) DNA sequence specificity of **P8** binding.

mediated peptide dimerization/helix induction. Thermal unfolding experiments were conducted to determine the  $T_m$  of DNA-bound and DNA-free peptides, and in all cases,

Table 3.8: Apparent dissociation constants for the **P8**-DNA complex in the presence of various metal ions.

Metal	DNA Sequence	$K_d$ apparent
Ni <sup>II</sup>	SCR	> 350 nM
Ni <sup>II</sup>	CRE	65 ± 4 nM
Cu <sup>II</sup>	CRE	139 ± 7 nM
Zn <sup>II</sup>	CRE	84 ± 5 nM

there was an approximately 20 °C shift in the  $T_m$  (Table 3.7).

In order to quantitatively characterize **P8**-DNA interactions and to determine their specificity and metal-dependence, we conducted gel-shift assays with radiolabeled DNA sequences. Due to the expected dissociation constants of basic domain-CRE interactions in the nM range,<sup>53</sup> we used low concentrations of ds-DNA (2 nM) and **P8** (1-500 nM), in addition to 0.5 equiv. of  $M^{II}$  (with respect to **P8** concentration). Based on the affinities of the His/Phen HCM's for various metal ions (in the nM range) and the metal-mediated dimerization constants (in the  $\mu$ M range), we would expect the **P8** peptides to be mostly metal-bound, but in a monomeric state in the absence of DNA interactions.

As shown in Figure 3.16, the binding of **P8** to CRE occurs in a metal-dependent fashion, whereby the final product has the desired  $M:P8_2:CRE$  stoichiometry (Materials and Methods). Interestingly, small amounts of monomeric  $M:P8:CRE$  species are also observed (Figure 3.16), which is consistent with a model where the monomeric, metal-bound **P8** also interacts with CRE, likely as an intermediate en route to the dimeric **P8**-DNA complex (Figure 3.17). These observations agree with previous findings that the

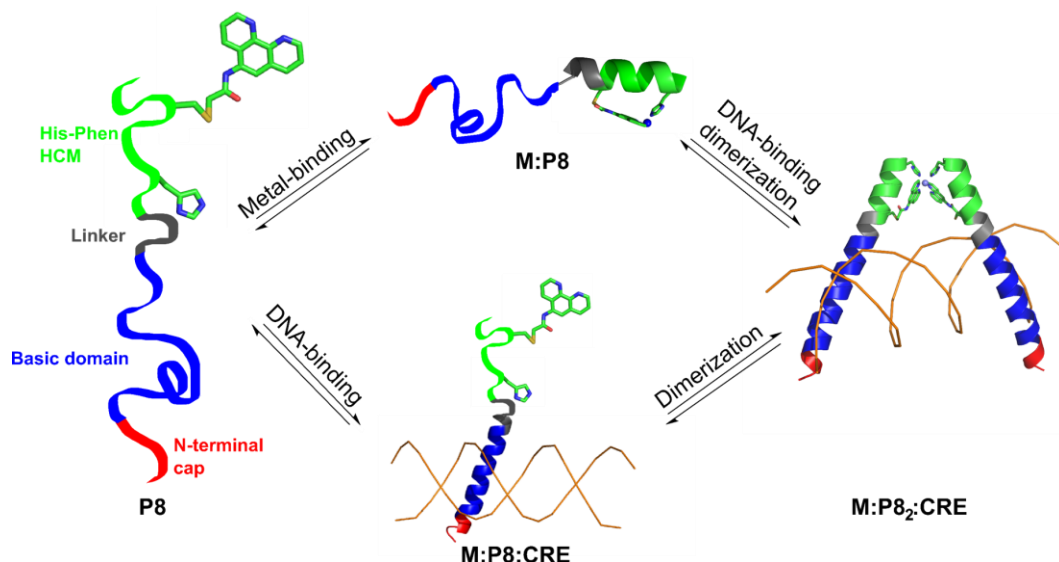


Figure 3.17: Scheme for the possible modes of **P8** binding to DNA. In this case, the DNA can act as a template for dimerization.

dimerization of certain bZIP peptides occurs on the target DNA, rather than DNA binding by preformed dimers.<sup>69-72</sup> As expected from our structural model, Ni<sup>II</sup> coordination yields the highest affinity ( $K_{d, \text{DNA}} = 65 \text{ nM}$ ) for CRE, followed by Zn<sup>II</sup> ( $K_{d, \text{DNA}} = 84 \text{ nM}$ ) and Cu<sup>II</sup> ( $K_{d, \text{DNA}} = 139 \text{ nM}$ ) (Table 3.8); this range of affinities compare well with those obtained for other synthetically dimerized bZIP-peptide constructs.<sup>54</sup> In the absence of metal ions, no DNA binding by P8 is observed. It is notable that the geometric preferences of the metal still play a role in DNA-binding, indicating that the HCM, and not simply a bis-phen dimer, is mediating the DNA-peptide interaction. It has not yet been determined whether the increased binding affinity for Ni<sup>II</sup>-bound peptides is due to the enhanced helicity, or if there is competition between metal coordination and DNA-binding when the metal-binding geometry does not orient the peptides in the proper orientation for DNA binding, decreasing the affinity of the HCM peptides. Further, there is literature precedence for both possibilities, as it has previously been demonstrated that it is possible to control peptide



binding to DNA either by stabilizing an  $\alpha$ -helix to promote binding,<sup>73</sup> or by destabilizing a helix to prohibit DNA binding.<sup>74-76</sup> Importantly, our results show that peptide-DNA interactions can be finely-tuned in a way that is dependent on the choice of the metal ion. Finally, in the presence of Ni<sup>II</sup>, no binding by P8 to the non-cognate DNA sequence SCR is observed, confirming the sequence specificity of metal-directed P8-DNA interactions.

### 3.4 Conclusions

Our results demonstrate the versatility of HCMs in tuning the structural and biochemical properties of peptides in a metal-dependent fashion. First, the HCMs offer a readily accessible and functionally flexible alternative to other types of peptide-crosslinking or helix induction strategies<sup>20</sup> in that they are reversible and the extent of helix induction is easily tuned through the choice of metal identity. Helix induction on peptide-HCM platforms is further augmented by exploiting secondary interactions of appropriately positioned amino acid sidechains with the organic component of the HCM. Second, the resulting increase in stability with respect to chemical or thermal denaturation or enzymatic hydrolysis is comparable to that which is achieved by covalent stapling approaches.<sup>52</sup> Third, under proper experimental conditions, HCMs enable the dimerization of peptides with distinct geometries that are dictated by the inner-sphere coordination preferences of the metal ions. In this study, we exploited this feature to demonstrate the ability of HCM-bearing peptides to recognize and bind a biological target. Starting with the pioneering work by Kim,<sup>54,63</sup> several synthetic strategies have been developed for the dimerization of bZIP peptides,<sup>55,58,59,62</sup> including disulfide bonding,<sup>54</sup> metal coordination,<sup>60,64-66</sup> and crosslinking with metal-tunable<sup>67</sup> or photo-switchable linkers.<sup>57,61,74</sup> These studies have collectively shown the importance of the dimeric organization of the basic domains as well

as their proper orientation for DNA binding and recognition. The HCM-based approach that we have described here is complementary to these previously described strategies. Yet, it is also distinct in the sense that the HCM motif is an integral part of the peptide scaffold due to its two-point attachment to the backbone, while in all other strategies the dimerization units are attached to the peptide chains through a single point. As a result, HCMs can simultaneously induce peptide helicity through metal coordination and lead to the formation of discrete peptide dimerization geometries, which can be modulated in combination to optimize DNA binding and recognition.

### **3.5 Materials and Methods**

#### **3.5.1 General Considerations**

##### **3.5.1.1 Supplies**

Unless otherwise stated, reagents and solvents were purchased from Fisher Scientific and used as received. Peptide supplies (amino acids and resins) were purchased from Aapptec and used without further purification.

##### **3.5.1.2 HPLC Purification**

Reverse-phase HPLC was performed using 0.1% trifluoroacetic acid (TFA) in water as buffer A and acetonitrile as buffer B. Newly synthesized peptides were purified on a preparative-scale column (Agilent preHT, 5  $\mu$ m, 21.1 x 100 mm) on an Agilent Technologies 1260 Infinity HPLC instrument; chromatograms were monitored at 220 nm to detect absorbance of the peptide backbone and fractions were collected manually. Preparative scale purifications were run at a flowrate of 6 mL/min using a gradient of 0 to 60% buffer B over 40 min. Phen-conjugated peptides were purified using the same column

and methods, monitoring the absorbance at 268 nm. After initial purification, an analytical column (Agilent Eclipse plus C<sub>18</sub>, 3.5  $\mu$ m, 4.6 x 100 mm) was run using the same gradient at a flow rate of 1 mL/min to determine purity. All peptides were isolated to >90% purity and the masses were verified using MALDI-TOF mass spectrometry.

### 3.5.1.3 Mass Spectrometry

Mass spectrometry analysis was carried out at the Molecular Mass Spectrometry Facility at UC San Diego. Peptide mass spectrometry was performed on a Bruker Bioflex IV MALDI-TOF mass spectrometer. Typically, peptides were diluted to 1-10  $\mu$ M in water, and combined with 50% by volume  $\alpha$ -cyano-4-hydroxycinnamic acid (CHCA) (Agilent) as a matrix. 3  $\mu$ L of the peptide-matrix solution was then spotted on a standard 288 well plate and the sample was dried before analysis.

Small molecule mass spectrometry was performed using electrospray ionization (ESI) on a Quattro Ultima Triple Quadrupole mass spectrometer. Samples were diluted to a concentration of 0.1-1.0 mg/mL using a solution of 50% methanol in water. Analysis was performed using both positive and negative ion modes.

Liquid chromatograph-mass spectrometry (LC-MS) was performed on Thermo Scientific Ultimate 3000 HPLC with a flow rate of 0.4 mL/min, with subsequent introduction into an Orbitrap Elite mass spectrometer with electrospray ionization. Buffer A was water with 0.1% TFA and Buffer B was acetonitrile, and both buffers had 10 mM ammonium acetate. Analysis was performed using the Xcalibur software. It was observed that the cleaved peptide products eluted at the same time by HPLC.

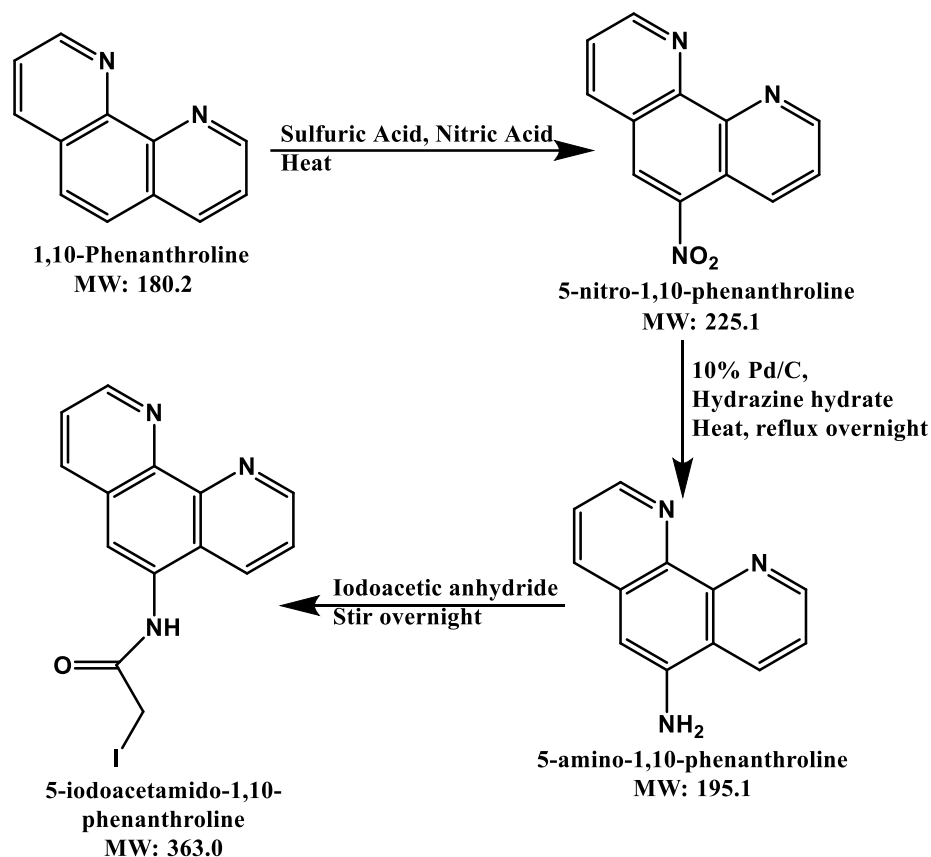


Figure 3.18: Synthetic scheme for the synthesis of 5-iodoacetamido-1,10-phenanthroline.

### 3.5.2 Synthesis of 5-iodoacetamido-1,10-phenanthroline

#### 3.5.2.1 Synthesis of 5-nitro-1,10-phenanthroline

Approximately 0.05 mol of 1,10-phenanthroline (9 g) was weighed and heated to 160 °C in 60 mL sulfuric acid until the solid dissolved. 27 mL nitric acid was then added dropwise and the reaction proceeded at 160 °C for 2 hr. After 2 hr, the reaction mixture was poured into approximately 200 mL of distilled water cooled in an ice bath. 250 mL of 10N NaOH was then added to reach a pH of approximately 3, and the reaction was filtered using Büchner filter. The solid was dried *in vacuo* overnight, and 11.6 g of product were

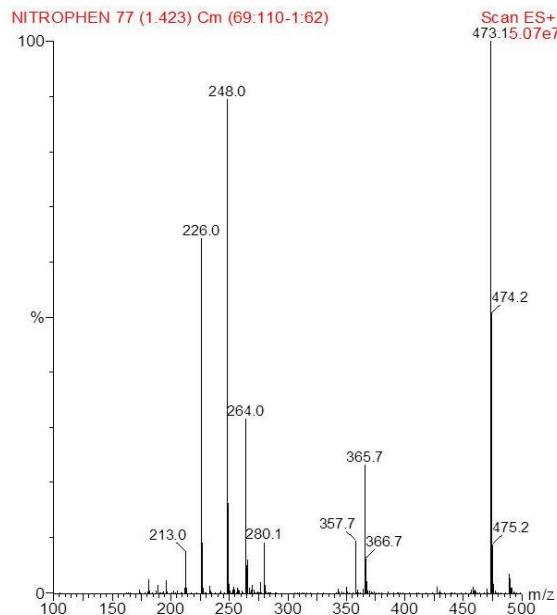


Figure 3.19: ESI-MS (positive mode) of 5-nitro-1,10-phenanthroline. Observed peak at 226.0 amu (expected 226.1 amu)  $[M+H]^+$ . 248.0 amu (expected 248.1 amu)  $[M+Na]^+$ . 473.1 amu (expected 473.2 amu)  $[M+M+Na]^+$ .

obtained for a 90% yield. ESI-MS (+):  $m/z$  calculated for  $(C_{12}H_7N_3O_2 + H)$  226.1 amu  $[M+H]^+$ , observed 226.1 amu. (Figure 3.19)

### 3.5.2.2 Synthesis of 5-amino-1,10-phenanthroline

In a 3-neck round bottom flask, 1 g of 10% Palladium on carbon (Pd/C) was added to 11.6 g of 5-nitro-1,10-phenanthroline. 500 mL of degassed ethanol was transferred to the reaction vessel by cannula, and 40 mL of hydrazine hydrate was added. The reaction mixture was sonicated for 1 hr and then refluxed overnight at 80 °C. The following day, the reaction was cooled to room temperature, filtered to remove Pd/C, and the solvent was removed by rotary evaporation. ESI-MS (+):  $m/z$  calculated for  $(C_{12}H_9N_3 + H)$  196.1 amu  $[M+H]^+$ , observed 196.1 amu. (Figure 3.20)

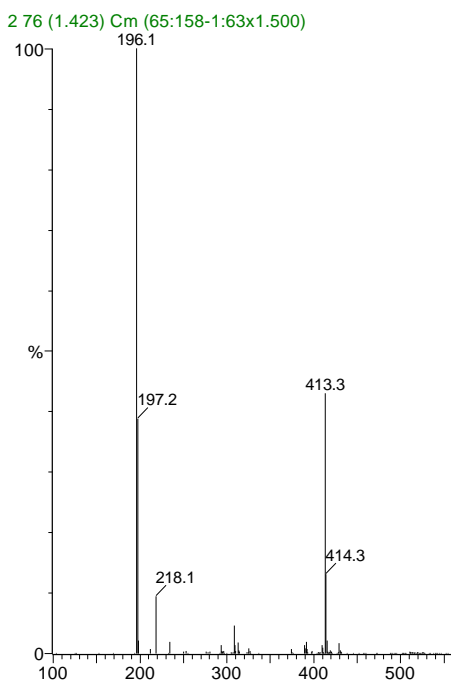


Figure 3.20: ES-MS (positive mode) of 5-amino-1,10-phenanthroline. Observed peak at 196.1 amu (expected 196.1 amu)  $[M+H]^+$ . 218.1 amu (expected 218.1 amu)  $[M+Na]^+$ . 413.3 amu (expected 413.2 amu)  $[M+M+Na]^+$ .

### 3.5.2.3 Synthesis of 5-iodoacetamido-1,10-phenanthroline

Methods were adapted as previously described.<sup>77</sup> Iodoacetic anhydride was freshly prepared by combining 1.67 g  $N,N'$ -Dicyclohexylcarbodiimide (DCC) with 3.33 g iodoacetic acid in 50 mL ethyl acetate and stirred. After 2 hr, the reaction was filtered to remove waste and evaporated to dryness using a rotary evaporator.

500 mg of 5-amino-1,10-phenanthroline was dissolved in 67 mL acetonitrile and heated to dissolve. Once dissolved, the solution was cooled to room temperature. The newly synthesized iodoacetic anhydride was dissolved in 25 mL acetonitrile and added to 5-amino-1,10-phenanthroline. These solutions were combined and reacted overnight at room temperature.<sup>77</sup>

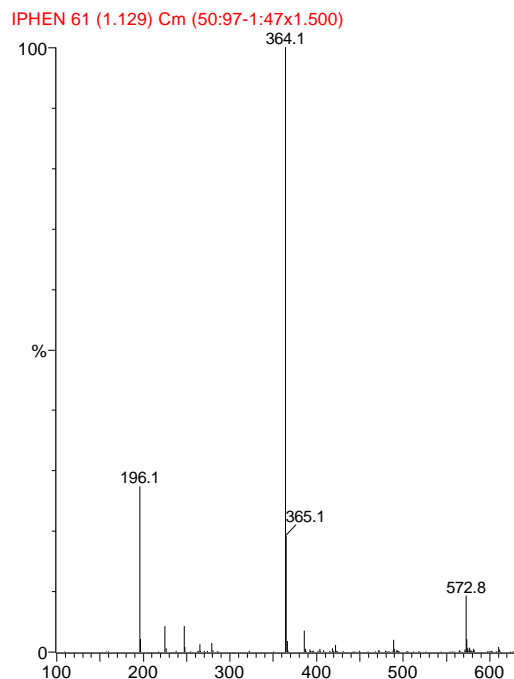


Figure 3.21: ES-MS (positive mode) of 5-iodoacetamido-1,10-phenanthroline. Observed peak at 364.1 amu (expected 364.0 amu)  $[M+H]^+$ .

The following day, the supernatant was removed using a Büchner filter and filter paper. The precipitate was washed with cold 5% sodium bicarbonate in water, followed by cold water. The solid was dried *in vacuo*, and 5-iodoacetamido-1,10-phenanthroline was obtained with a 36% yield. ESI-MS (+):  $m/z$  calculated for  $(C_{14}H_{10}IN_3O + H)$  196.1 amu  $[M+H]^+$ , observed 196.1 amu. (Figure 3.21)

### 3.5.3 Peptide synthesis

#### 3.5.3.1 General protocols for solid phase peptide synthesis

Peptides were synthesized using an Aapptec Focus XC peptide synthesizer and standard Fmoc chemistry, as previously described.<sup>40</sup> All peptides were *N*-terminal acylated and *C*-terminal amidated.

For each amino acid addition, the Fmoc protecting group on the N-terminus of the growing peptide chain was first removed with a solution of 20% (v/v) 4-methylpiperidine in dimethylformamide (DMF). A 4-fold excess of an Fmoc-protected amino acid containing a free C-terminus was then added in a solution of 4 M *N,N*-Diisopropylethylamine (DIPEA) in DMF with an equimolar amount of HATU and coupling was allowed to proceed for 40 min with shaking. The resin was then washed with DMF and the cycle was repeated until all amino acids were incorporated. After the final step of synthesis, the *N*-terminus of each peptide was acylated with a mixture of 0.5 M acetic acid anhydride, 0.5 M *N*-hydroxybenzaldehyde (HOBt) and 10% (v/v) dichloromethane in DMF.

The peptide resin was removed from the synthesizer and dried *in vacuo*. The peptide was then cleaved from the resin using a cleavage cocktail containing 5% (v/v) thioanisole, 3% (v/v) ethane dithiol and 2% (v/v) anisole in trifluoroacetic acid (TFA) over a period of two hours. After cleavage was complete, the peptide solution was filtered to remove the resin and the filtrate was added to a solution of cold ether and incubated at -80 °C overnight to precipitate the peptide from solution. The solution was then filtered, the peptide was collected as a precipitate, and dried *in vacuo*. The crude solid was redissolved in water, and purified via HPLC.

In order to incorporate fluorescein or rhodamine in the peptide, the resin of the synthesized peptide was deprotected and dried. A 2-fold excess (based on resin capacity) of either 5,6-carboxytetramethylrhodamine or 5(6)-carboxyfluorescein was dissolved in 10% 2,4,6-collidine in dimethylformamide (DMF) with an equimolar amount of HATU and added to the peptide resin. The reaction proceeded for 30 min at room temperature in



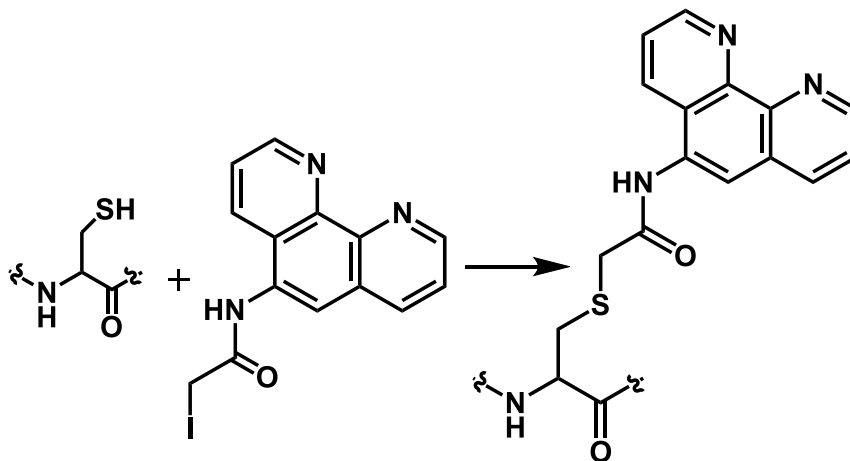


Figure 3.22: Synthetic scheme for the functionalization of a peptide cys residue with 5-iodoacetamido-1,10-phenanthroline.

the dark and was then rinsed with DMF to remove excess fluorophore. Standard peptide cleavage and purification then proceeded as previously described.

### 3.5.3.2 Functionalization of peptides with 5-iodoacetamido-1,10-phenanthroline

Under an argon atmosphere, 20 mg of each peptide was dissolved in 3 mL of degassed 10 mM HEPES buffer (pH 7.5) with constant stirring. A 3- to 5- fold excess of 5-iodoacetamido-1,10-phenanthroline (IPhen) was dissolved in 1 mL degassed DMF and added dropwise to the peptide solution. The mixture was stirred in the dark for approximately 4 hr at room temperature. Any precipitant was removed by centrifugation, and a PD MidiTrap G-10 desalting column (GE Healthcare) was used to remove excess IPhen and DMF. The crude peptide solution was purified by preparative scale HPLC as previously described, and the mass of the labeled peptide was verified by MALDI-TOF mass spectrometry (Figure 3.22, Figure 3.23)

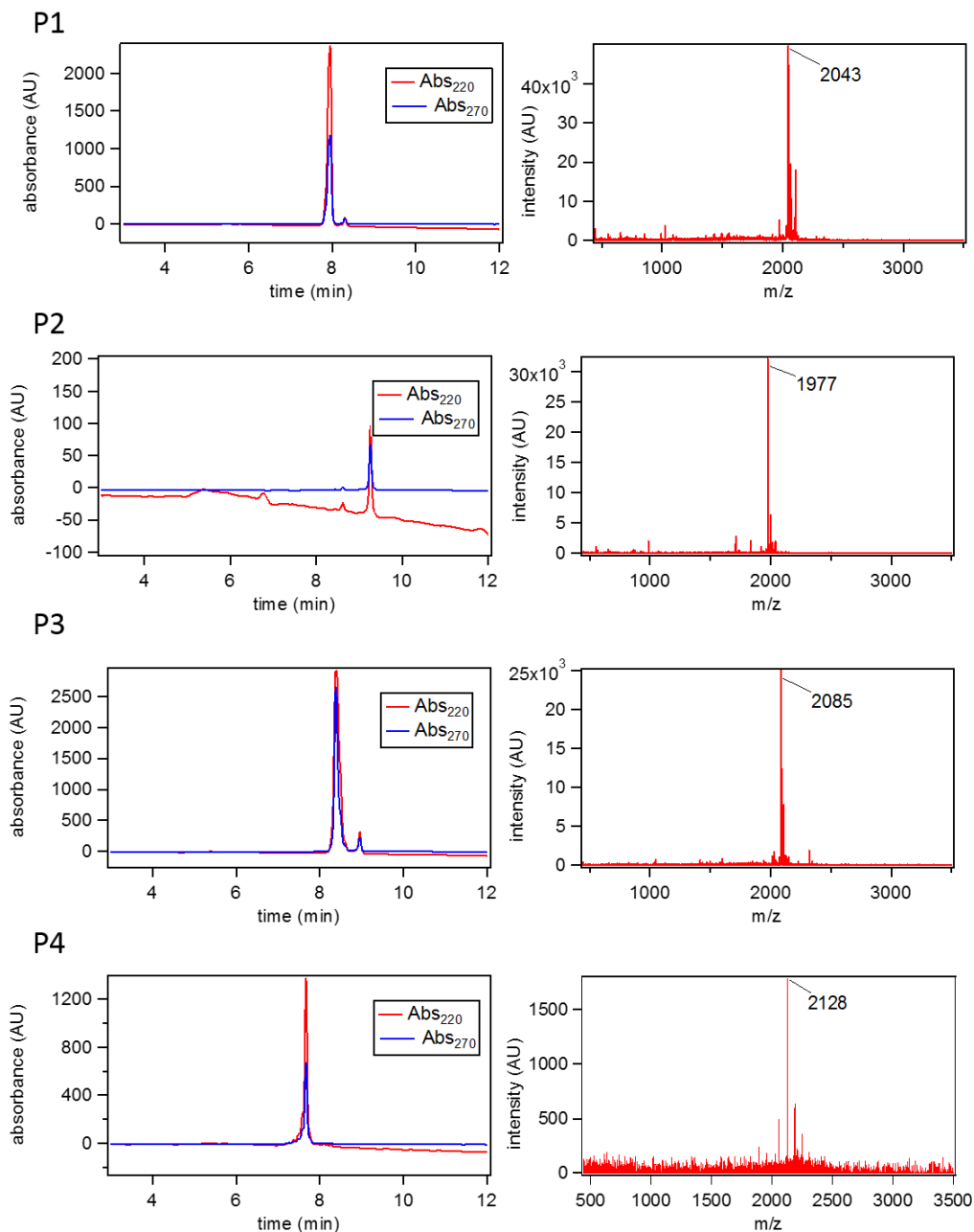


Figure 3.23: Analytical HPLC traces and MALDI-TOF spectra of various peptide constructs. HPLC gradient used: 1. 0 to 5 min, 90% solvent A, constant. 2. 5 to 20 min, 95% to 60% solvent A, gradient. P1: expected 2043 amu, observed 2043  $[M+H]^+$ . P2: expected 1977 amu, observed 1977  $[M+H]^+$ . P3: expected 2085 amu, observed 2085  $[M+H]^+$ . P4: expected 2128 amu, observed 2128  $[M+H]^+$ . P5: expected 2158 amu, observed 2159  $[M+H]^+$ . P6: expected 2087, observed 2086  $[M+H]^+$ . P7: Expected 2069, observed 2070  $[M+H]^+$ . P8: Expected 4020, observed 4022  $[M+H]^+$ .

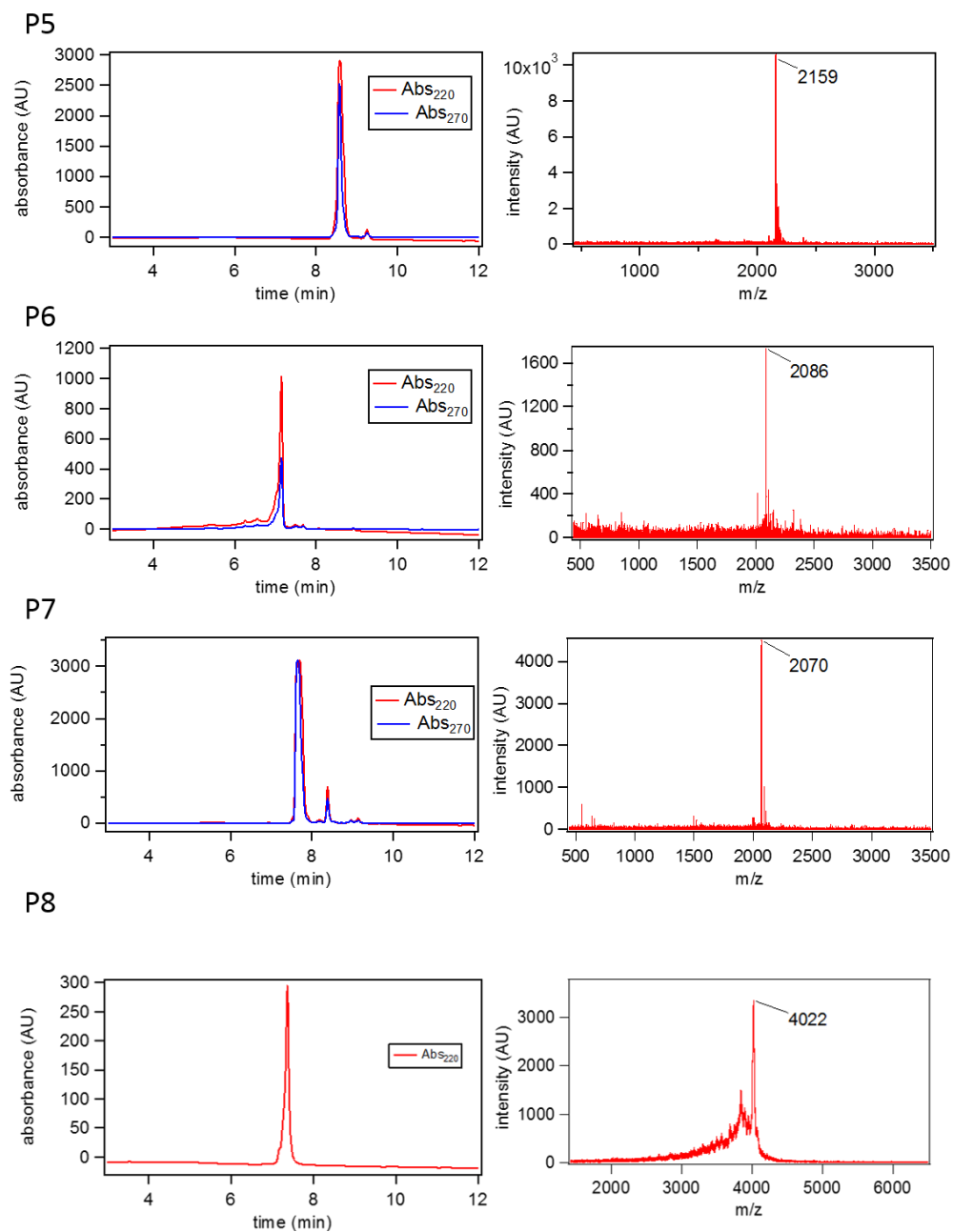


Figure 3.23: Analytical HPLC traces and MALDI-TOF spectra of various peptide constructs, continued.

### 3.5.4 Determination of metal binding affinity

Metal binding titrations were performed by monitoring the Phen  $\pi$ - $\pi^*$  absorption band, which shifts approximately 6 nm from 268 nm when metal-free to 274 nm when metal bound. 1 mL samples were prepared containing 10-20  $\mu$ M peptide; peptide concentrations were determined more precisely using the extinction coefficient  $\epsilon_{268} = 16,000 \text{ M}^{-1} \text{ cm}^{-1}$ . Each sample was prepared in 50 mM 3-(N-morpholino)propanesulfonic acid (MOPs) buffer, pH 7.0 pretreated with Chelex resin (BioRad) with a 3-fold excess of chelator (30-60  $\mu$ M). All pipet tips were rinsed 3 times with analytical grade 10% nitric acid (Fluka) before use. The chelator used as a competing ligand depended on the binding affinity of the peptide; ethylene glycol tetraacetic acid (EGTA) was used as a competitor for  $\text{Ni}^{\text{II}}$  and  $\text{Co}^{\text{II}}$  samples, while N-(2-acetamido)iminodiacetic acid (ADA) was used for the  $\text{Zn}^{\text{II}}$  and  $\text{Cu}^{\text{II}}$  titrations (Table 3.9). Metal stocks (2 mM) were prepared and added stepwise to the peptide solution so that the total amount never exceeded 5% of the total volume (50  $\mu$ L). After each metal addition, the sample was incubated for at least 3 min with constant stirring. UV-vis measurements were performed on a Hewlett Packard 8452A diode array spectrophotometer, or an Agilent 8453 UV-visible spectroscopy system. The largest changes in absorbance were measured at 280 nm, and these values were plotted as a function of  $\text{M}^{\text{II}}$  concentration after the spectra were background and dilution corrected.  $\text{M}^{\text{II}}$  dissociation constants for either EGTA or ADA were calculated using MaxChelator (<http://maxchelator.stanford.edu>) (Table 3.9) and fixed during data fitting. The titration data were separately fit to two models using non-linear regression through Dynafit 4 (Biokin),<sup>78</sup> where one model assumes a 1:1 peptide:metal stoichiometry while the other

Table 3.9: Dissociation constants of chelators used as competing ligands for UV-vis titrations to measure the metal binding affinity for peptide-HCMs.

Chelator	Metal	$K_d$ (M)
EGTA	Ni <sup>II</sup>	$4.548 \times 10^{-10}$
EGTA	Co <sup>II</sup>	$7.789 \times 10^{-9}$
ADA	Zn <sup>II</sup>	$6.8 \times 10^{-9}$
ADA	Cu <sup>II</sup>	$2.18 \times 10^{-11}$

model takes account of the possibility of metal-induced peptide dimerization (1:1 and 2:1 peptide:metal stoichiometry). (Figure 3.6)

### 3.5.5 Circular dichroism spectroscopy (CD)

15  $\mu$ M peptide stock solutions were prepared in 10 mM sodium borate buffer (NaB) at pH 7.1. The buffer had previously been treated using Chelex resin (BioRad) and all pipet tips were washed 3x with 10% analytical grade nitric acid (Fluka) before use. The stock solution was divided to prepare each of the metal-free or metal-bound samples at equal concentrations, and the concentration was verified by measuring the absorbance of the metal-free sample in a UV-vis spectrometer at 268 nm. A 3-6 fold excess of EDTA, NiCl<sub>2</sub>, CuSO<sub>4</sub>, ZnCl<sub>2</sub>, or CoCl<sub>2</sub> was added to the sample and incubated for at least one hour before analysis. Peptide samples were also prepared in 60% trifluoroethanol (TFE), and no notable difference was observed in the CD spectra for apo or metal-bound peptides dissolved in TFE.

CD measurements were recorded in a 1 cm square quartz cuvette (Starna Cells) on an Aviv 215 spectrometer. The CD spectrum of each sample was measured from 260-190 nm using a slit width of 1 nm, scanning at 1 nm intervals with a 1 s integration time.

Measurements were taken at 25 °C and 4 °C with constant stirring. Each measurement was repeated 3-5 times, averaged and smoothed with a binomial function, and corrected for any background signal from the buffer solution.

The thermal stability of the peptides was measured by monitoring the signal of each peptide as the temperature was increased from 4 °C to 90°C with a step size of either 2.5 or 5 °C. The sample was incubated for at least 5 min after a stable temperature had been reached at each point, and the measurement was integrated for 10 s. In order to obtain the  $T_m$ , the data was smoothed using a binomial function, and the first derivative of the data was taken. This data was plotted, and was fit using the KaleidaGraph program as previously described.<sup>48</sup>

### 3.5.6 Trypsin Digestion

Peptide samples were prepared at approximately 1.5 mM concentration with a three-fold excess of either EDTA for metal free samples or  $M^{II}$  in 100 mM Tris(hydroxymethyl)aminomethane (Tris) buffer, pH 8 with 10 mM  $CaCl_2$ . Samples were equilibrated at 4 °C for 15 min before trypsin was added to a final concentration of 0.3 mg/mL. At each time point, 5  $\mu$ L of the reaction solution was removed and added to 45  $\mu$ L 1% trifluoroacetic acid. Each sample was run on the analytical HPLC as previously described, and the absorbance at 268 nm was observed.

To confirm the masses of the cleaved peptides, samples were prepared in the same way and run on an LC-MS using the same conditions for separation. (See section 0 for details.)

In order to determine the fraction of intact peptide, the peaks corresponding to the intact peptide and cleaved peptide were integrated. Fraction intact = intact peptide peak

area/(intact peptide peak area + cleaved peptide peak area). The rate constants and peptide half-lives were calculated using the following equation:

$$fraction\ intact = e^{-kt}$$

where k is the rate of cleavage and t is time. Data was plotted as the fraction of peptide intact vs time.

### 3.5.7 Spectroscopic dimerization studies

15  $\mu$ M peptide solutions were prepared in 20 mM MOPs buffer, pH 7.0. 2  $\mu$ L aliquots of metal were added, and the samples were monitored either by UV-vis or CD, allowing for at least 3 min of mixing after each addition. (Figure 3.24, Figure 3.25)

### 3.5.8 Analytical Ultracentrifugation (AUC)

450  $\mu$ L samples for AUC were prepared with 40  $\mu$ M peptide in 50 mM MOPs, pH 7. EDTA was used to ensure samples were metal-free, or Ni<sup>II</sup> was added at either 0.25, 0.5, or 1 equiv. concentration. Measurements were made on a Beckman XL-I Analytical Ultracentrifuge (Beckman-Coulter Instruments) using an An-60 Ti rotor at 60,000 rpm. 400 scans were measured per sample at 25 °C by detection at 270 nm. The data were processed using Sedfit.<sup>79</sup> Buffer viscosity (0.00894 poise), density (0.99764), and protein partial specific volume (0.7132 mL/g) were calculated at 25 °C with SEDNTERP (<http://www.jphilo.mailway.com>).

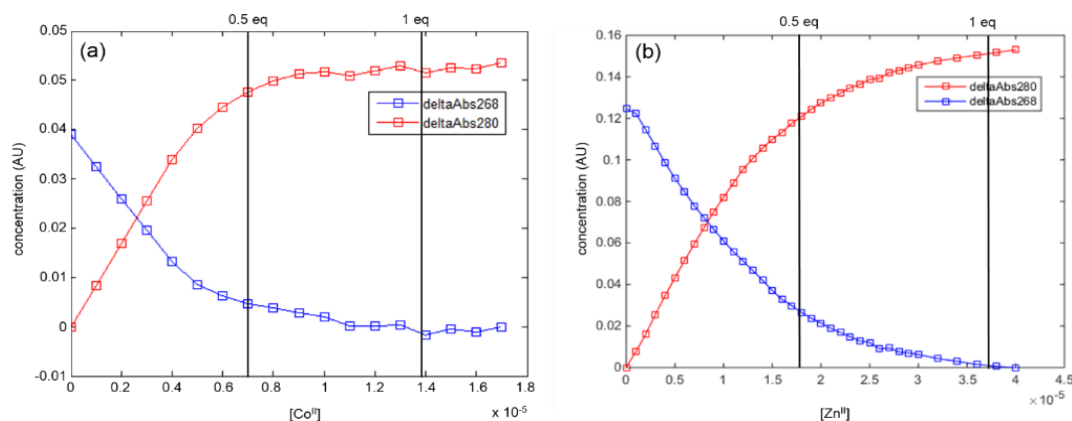


Figure 3.24: UV-vis titrations without a competing chelator to determine the stoichiometry of metal binding and dimer formation. (a) The titration with  $\text{Co}^{\text{II}}$  indicates that the peptide is almost fully dimerized at 0.5 equiv. metal. This is expected given the preference of  $\text{Co}^{\text{II}}$  for octahedral geometry. (b) The titration with  $\text{Zn}^{\text{II}}$  shows some dimer formation, but not to the same extent as  $\text{Ni}^{\text{II}}$  and  $\text{Co}^{\text{II}}$ .

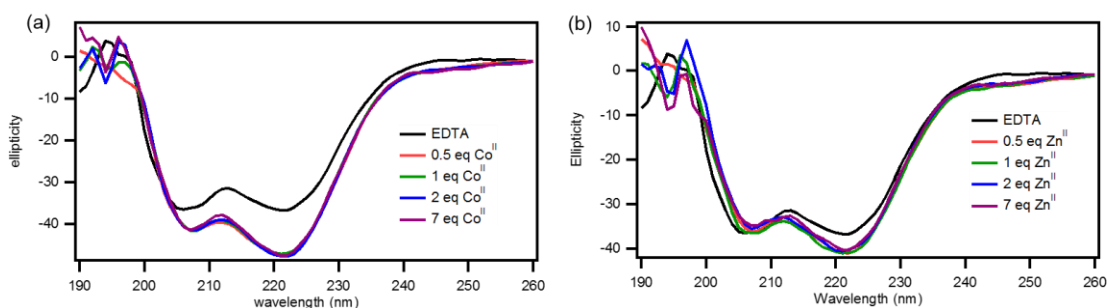


Figure 3.25: Titrations to determine the stoichiometry of metal-binding and dimer formation as monitored by CD. Upon the addition of (b)  $\text{Co}^{\text{II}}$  and (c)  $\text{Zn}^{\text{II}}$ , no further change in secondary structure is observed 0.5 equivalents of  $\text{M}^{\text{II}}$  are added, indicating that these metals are inducing dimer formation in addition to an enhancement of  $\alpha$ -helicity.

### 3.5.9 FRET dimerization studies

Two sets of FRET experiments were performed. In all cases,  $\text{Zn}^{\text{II}}$  was used for FRET experiments as it was observed that the addition of  $\text{Ni}^{\text{II}}$  caused metal-based fluorescence quenching.



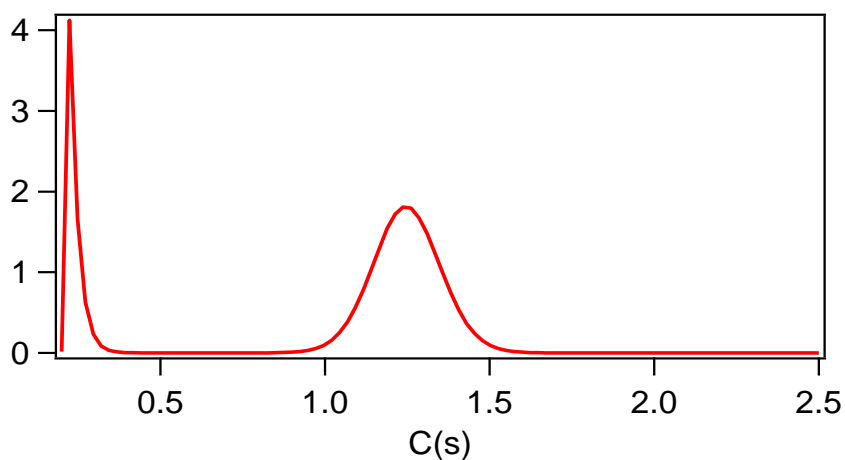


Figure 3.26: Confirmation of dimer formation by AUC. After performing FRET experiments, the samples were analyzed by AUC. The expected sedimentation coefficient for a monomer is 0.7 S and 1.2 S for a dimer.

First, a 25  $\mu\text{M}$  solution of P8-fluorescein (P8F) with 12.5  $\mu\text{M}$   $\text{Zn}^{\text{II}}$  in 50 mM Tris buffer, pH 8.5 with 10 mM NaCl and 10 mM  $\text{MgCl}_2$  was incubated at 10  $^{\circ}\text{C}$ . The fluorescence spectrum was measured using an excitation wavelength of 490 nm and the emission was measured from 500-700 nm using slit widths of 1 nm. P8-rhodamine (P8R) with 0.5 equiv.  $\text{Zn}^{\text{II}}$  was gradually titrated into the solution for final concentrations ranging from 10  $\mu\text{M}$  to 150  $\mu\text{M}$ . After each addition, the solution was stirred for 3 min before the fluorescence spectrum was measured. The formation of a dimer was also confirmed by AUC. (Figure 3.14c, Figure 3.26)

Second, a stock solution was prepared with 500  $\mu\text{M}$  P3F, 500  $\mu\text{M}$  P3R, and 500  $\mu\text{M}$   $\text{Zn}^{\text{II}}$  in 50 mM Tris buffer at pH 8.5 containing 10 mM NaCl and 10 mM  $\text{MgCl}_2$ . The stock solution was gradually titrated into a cuvette at 10  $^{\circ}\text{C}$ , increasing the total peptide concentration by 5  $\mu\text{M}$  at each addition. The sample was stirred for 3 min before the fluorescence emission spectrum was measured from 500-700 nm with excitation at 490 nm

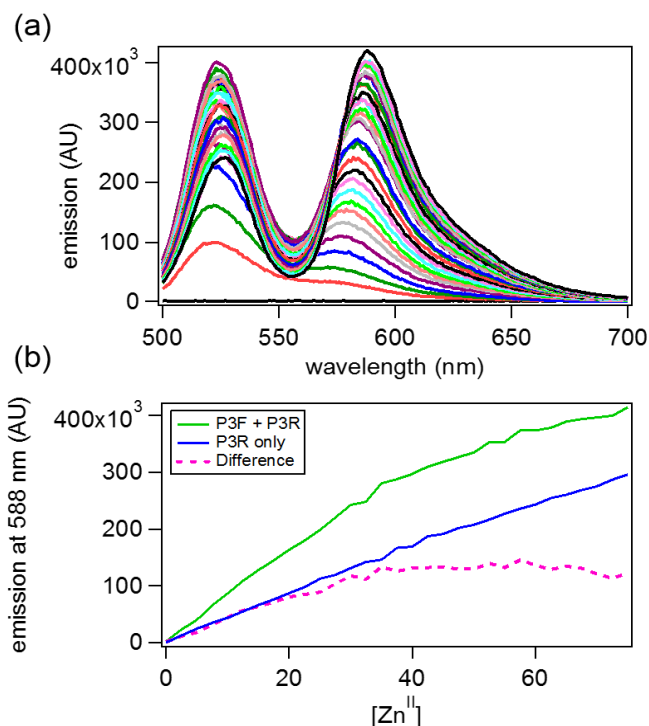


Figure 3.27: Quantitative FRET experiments to calculate the apparent  $K_d$  of peptide dimerization. Equimolar amounts of P8F and P8R are titrated into solution and the fluorescence signal is measured. (a) Raw fluorescence spectra. (b) The emission at 590 nm in the presence (green) and absence (blue) of P8F. The difference spectrum (pink, dotted) is also shown, and this is the signal that can be attributed to the formation of a P8F-P8R dimer, resulting in FRET-based rhodamine emission.

and slit widths of 1 nm. The titration was repeated with only P3R present, and the difference in the emission at 590 was calculated for each concentration of P3R. The difference in emission corresponds to the FRET-based emission when P3F is also present.

### 3.5.10 Gel shift assays with radiolabeled DNA

#### 3.5.10.1 Radiolabeling DNA

1  $\mu\text{L}$  of 20  $\mu\text{M}$  DNA was combined with 2  $\mu\text{L}$   $^{32}\text{P}$  ATP, 1  $\mu\text{L}$  10x PNK buffer (New England BioLabs), and 5  $\mu\text{L}$  of water in a 0.5 mL Eppendorf tube. 1  $\mu\text{L}$  PNK enzyme (New England BioLabs) was then added and the reaction was incubated at 37  $^{\circ}\text{C}$  for 30 min. At the same time, a 20 x 50 cm 15% polyacrylamide gel, 0.4 mm thick was poured with one

large well. After polymerization, the gel was pre-run with 0.5x TBE buffer (44.5 mM Tris base, 44.5 mM boric acid, 1 mM EDTA) at 55 watts for at least 10 min. 30  $\mu$ L of loading buffer (80% formaldehyde, 20% v/v 5x TBE, bromophenol blue) was added to the DNA reaction mixture and the solution as heated at 80 °C for 2 min. The DNA solution was then loaded into the gel at run at 55 watts for approximately 2 hr, or until the loading dye had run approximately 2/3 the length of the gel.

The location of the radiolabeled DNA was determined using a phosphorimaging plate. The DNA eluted from the gel overnight in water and the supernatant was removed. 30  $\mu$ L of 3 M sodium acetate, pH 4.9, was added to the supernatant followed by 1.2 mL of ethanol. The solution was incubated at -20 °C for at least 20 min to precipitate DNA. The DNA was then pelleted by centrifugation at 13,200 rpm at 3 °C for 1 hr, and the supernatant was removed. The DNA was then redissolved in 50  $\mu$ L of water. All waste was disposed of in radioactive waste containers.

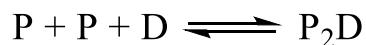
#### **3.5.10.2 Electrophoretic Mobility Shift Assays**

20-well 8% polyacrylamide gels were made using tris glycine buffer (TG). Samples were prepared with 10  $\mu$ L binding buffer (20% glycerol, 20 mM Tris, pH 7.5, containing 4 mM MgCl<sub>2</sub>, 8 mM KCl, 2% NP-40). 18  $\mu$ L of each sample was loaded and the gel was run for approximately 1.5 hours at 220 milliamps with 1X TG (25 mM Tris-HCl, 250 mM glycine with 0.1% sodium dodecyl sulfate) buffer. In general, the DNA concentration was kept constant at 1 nM while the peptide concentration was varied from 1-500 nM. The metal concentration was maintained at 0.5 equiv. peptide.

Gels were dried under vacuum and imaged using a phosphoimaging plate with overnight exposure. The band intensity was quantified, and the fraction of bound DNA was calculated using the following equation:

Fraction bound = intensity of DNA-peptide band / (intensity of DNA-peptide band + intensity of DNA band)

Dissociation constants were approximated using the following equilibrium equation using Igor Pro for nonlinear least squares regression fitting where P is the peptide, D is the DNA, P<sub>2</sub>D is the complex, and P<sub>tot</sub> is the total peptide added (Figure 3.29, Figure 3.28).



$$fraction\ bound = \frac{1}{1 + \left(\frac{K_{app}}{P_{tot}}\right)^2}$$

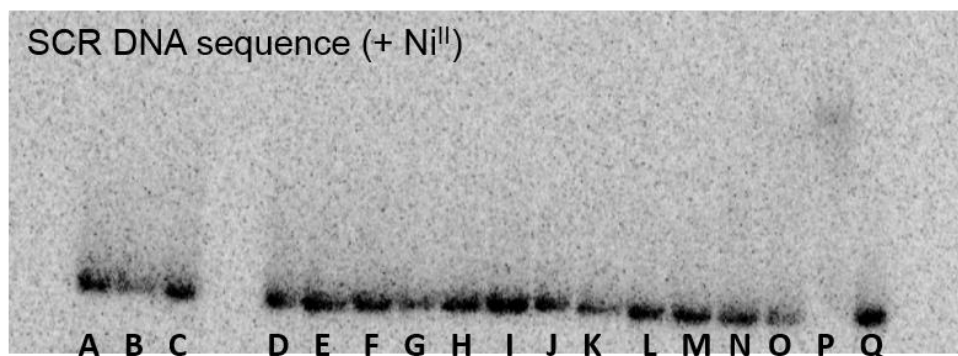


Figure 3.28: Sample gel shift assay to observe DNA binding by **P8** with the SCR DNA sequence. Lane (Q) contains CRE without any added peptide; DNA concentration is kept constant at 1 nM, while P8 concentration varies: (A) 1 nM, (B) 2 nM, (C) 5 nM, (D) 10 nM, (E) 15 nM, (F) 20 nM, (G) 25 nM, (H) 30 nM, (I) 40 nM, (J) 50 nM, (K) 75 nM, (L) 100 nM, (M) 150 nM, (N) 200 nM, (O) 250 nM, (P) 500 nM.

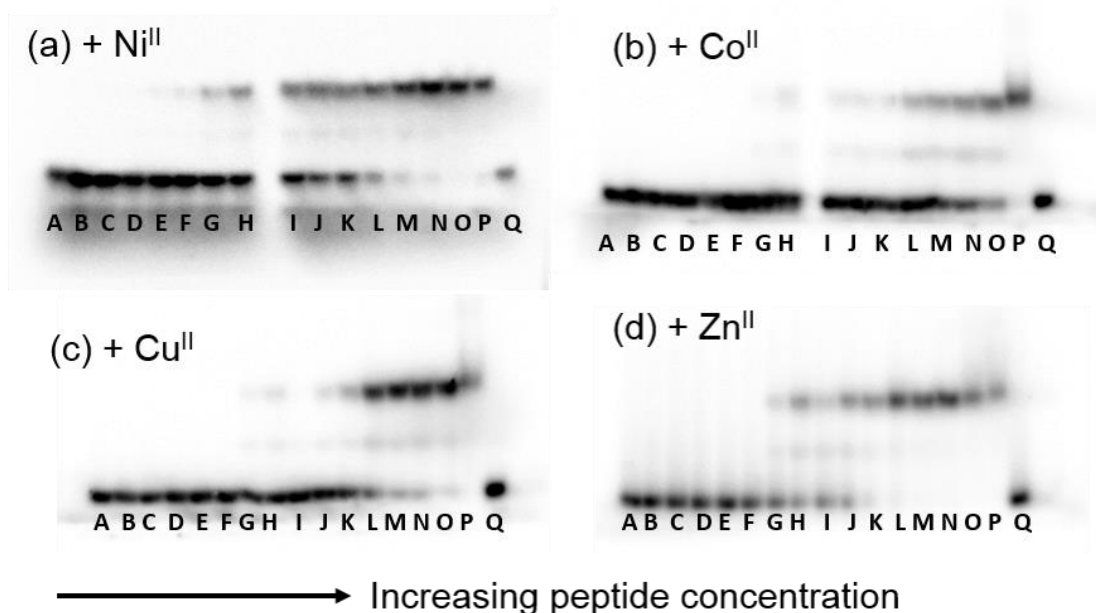


Figure 3.29: Sample gels from electrophoretic mobility shift assays to observe CRE binding by **P8**. At some concentrations, an intermediate band is observed that may be due to a peptide monomer bound to the DNA. Lane (Q) contains CRE without any added peptide; DNA concentration is kept constant at 1 nM, while P8 concentration varies: (A) 1 nM, (B) 2 nM, (C) 5 nM, (D) 10 nM, (E) 15 nM, (F) 20 nM, (G) 25 nM, (H) 30 nM, (I) 40 nM, (J) 50 nM, (K) 75 nM, (L) 100 nM, (M) 150 nM, (N) 200 nM, (O) 250 nM, (P) 500 nM.

### 3.6 Acknowledgements

The authors would like to thank Professor Nathan Gianneschi for the use of a peptide synthesizer, Professor Elizabeth Komives for the use of a peptide synthesizer and HPLC, Dr. Yongxuan Su for assistance with mass spectrometry and CD, Professor Daniel Donoghue for help with gel shift assays, Professor Ulrich Muller for help with radiolabeling DNA, and Dr. Richard Cochran for assistance with LC-MS. This work was supported by the US Department of Energy (DOE) (Division of Materials Sciences, Office of Basic Energy Sciences, Award DE-FG02-10ER46677, materials synthesis and

characterization), the National Science Foundation (CHE1306646, data analysis) and the National Institutes of Health (Molecular Biophysics traineeship to S.J.S.).

Chapter 3 is in preparation for submission to *Chemical Science*: Smith, S.J.; Radford, R.J.; Tezcan, F.A. Tunable Helicity, Stability and DNA-Binding Properties of Short Peptides with Hybrid Metal Coordination Motifs. 2016.

### 3.7 References

- (1) Martell, A. E.; Smith, R. M. *Critical Stability Constants*; Plenum Press: New York, 1974.
- (2) Burkhard, P.; Stetefeld, J.; Strelkov, S. V. *Trends Cell Biol.* **2001**, *11*, 82.
- (3) Lupas, A. N.; Gruber, M. In *Advances in Protein Chemistry*; Academic Press: 2005; Vol. Volume 70, p 37.
- (4) Youle, R. J.; Strasser, A. *Nat. Rev. Mol. Cell Biol.* **2008**, *9*, 47.
- (5) Kussie, P. H.; Gorina, S.; Marechal, V.; Elenbaas, B.; Moreau, J.; Levine, A. J.; Pavletich, N. P. *Science* **1996**, *274*, 948.
- (6) Busch, S. J.; Sassone-Corsi, P. *Trends Genet.* **1990**, *6*, 36.
- (7) Ellenberger, T. E.; Brandl, C. J.; Struhl, K.; Harrison, S. C. *Cell* **1992**, *71*, 1223.
- (8) Miller, J.; McLachlan, A. D.; Klug, A. *EMBO J.* **1985**, *4*, 1609.
- (9) Pabo, C. O.; Peisach, E.; Grant, R. A. *Annu. Rev. Biochem.* **2001**, *70*, 313.
- (10) Stites, W. E. *Chem. Rev.* **1997**, *97*, 1233.
- (11) Bullock, B. N.; Jochim, A. L.; Arora, P. S. *J. Am. Chem. Soc.* **2011**, *133*, 14220.
- (12) Azzarito, V.; Long, K.; Murphy, N. S.; Wilson, A. J. *Nat. Chem.* **2013**, *5*, 161.
- (13) Edwards, T.; Wilson, A. *Amino Acids* **2011**, *41*, 743.
- (14) Arkin, M. R.; Wells, J. A. *Nat. Rev. Drug Discov.* **2004**, *3*, 301.

- (15) Orner, B. P.; Ernst, J. T.; Hamilton, A. D. *J. Am. Chem. Soc.* **2001**, *123*, 5382.
- (16) Davis, J. M.; Tsou, L. K.; Hamilton, A. D. *Chem. Soc. Rev.* **2007**, *36*, 326.
- (17) Horne, W. S.; Gellman, S. H. *Acc. Chem. Res.* **2008**, *41*, 1399.
- (18) Cheng, R. P.; Gellman, S. H.; DeGrado, W. F. *Chem. Rev.* **2001**, *101*, 3219.
- (19) Whitty, A.; Kumaravel, G. *Nat. Chem. Biol.* **2006**, *2*, 112.
- (20) Estieu-Gionnet, K.; Guichard, G. *Expert Opin. Drug Discov.* **2011**, *6*, 937.
- (21) Jackson, D. Y.; King, D. S.; Chmielewski, J.; Singh, S.; Schultz, P. G. *J. Am. Chem. Soc.* **1991**, *113*, 9391.
- (22) Miller, S. E.; Kallenbach, N. R.; Arora, P. S. *Tetrahedron* **2012**, *68*, 4434.
- (23) Walensky, L. D.; Bird, G. H. *J. Med. Chem.* **2014**, *57*, 6275.
- (24) Walensky, L. D.; Kung, A. L.; Escher, I.; Malia, T. J.; Barbuto, S.; Wright, R. D.; Wagner, G.; Verdine, G. L.; Korsmeyer, S. J. *Science* **2004**, *305*, 1466.
- (25) Blackwell, H. E.; Grubbs, R. H. *Angew. Chem. Int. Ed.* **1998**, *37*, 3281.
- (26) Fujimoto, K.; Kajino, M.; Inouye, M. *Chem. Eur. J.* **2008**, *14*, 857.
- (27) Taylor, J. W. *Biopolymers* **2002**, *66*, 49.
- (28) Phelan, J. C.; Skelton, N. J.; Braisted, A. C.; McDowell, R. S. *J. Am. Chem. Soc.* **1997**, *119*, 455.
- (29) Taylor, J. W. *Biopolymers* **2002**, *66*, 49.
- (30) Ruan, F.; Chen, Y.; Hopkins, P. B. *J. Am. Chem. Soc.* **1990**, *112*, 9403.
- (31) Ma, M. T.; Hoang, H. N.; Scully, C. C. G.; Appleton, T. G.; Fairlie, D. P. *J. Am. Chem. Soc.* **2009**, *131*, 4505.
- (32) Zaykov, A. N.; Popp, B. V.; Ball, Z. T. *Chem. Eur. J.* **2010**, *16*, 6651.
- (33) Ghadiri, M. R.; Choi, C. *J. Am. Chem. Soc.* **1990**, *112*, 1630.
- (34) Patgiri, A.; Jochim, A. L.; Arora, P. S. *Acc. Chem. Res.* **2008**, *41*, 1289.
- (35) Cabezas, E.; Satterthwait, A. C. *J. Am. Chem. Soc.* **1999**, *121*, 3862.
- (36) Marqusee, S.; Baldwin, R. L. *Proc. Nat. Acad. Sci. U.S.A.* **1987**, *84*, 8898.

- (37) Toniolo, C.; Crisma, M.; Formaggio, F.; Peggion, C. *Biopolymers* **2001**, *60*, 396.
- (38) Radford, R. J.; Nguyen, P. C.; Ditri, T. B.; Figueroa, J. S.; Tezcan, F. A. *Inorg. Chem.* **2010**, *49*, 4362.
- (39) Radford, R. J.; Nguyen, P. C.; Tezcan, F. A. *Inorg. Chem.* **2010**, *2010*, 7106.
- (40) Smith, S. J.; Du, K.; Radford, R. J.; Tezcan, F. A. *Chem. Sci.* **2013**, *4*, 3740.
- (41) Krantz, B. A.; Sosnick, T. R. *Nat. Struct. Mol. Biol.* **2001**, *8*, 1042.
- (42) Chin, D.-H.; Woody, R. W.; Rohl, C. A.; Baldwin, R. L. *Proc. Natl. Acad. Sci. U.S.A.* **2002**, *99*, 15416.
- (43) Luo, P.; Baldwin, R. L. *Biochemistry* **1997**, *36*, 8413.
- (44) Padmanabhan, S.; Baldwin, R. L. *J. Mol. Biol.* **1994**, *241*, 706.
- (45) Padmanabhan, S.; Baldwin, R. L. *Protein Sci.* **1994**, *2*, 1992.
- (46) Creamer, T. P.; Rose, G. D. *Protein Sci.* **1995**, *4*, 1305.
- (47) Chou, P. Y.; Fasman, G. D. *Biochemistry* **1974**, *13*, 211.
- (48) John, D. M.; Weeks, K. M. *Protein Science* **2000**, *9*, 1416.
- (49) Chan, H. S.; Bromberg, S.; Dill, K. A. *Phil. Trans. R. Soc. Lond. B* **1995**, *348*, 61.
- (50) Schafmeister, C. E.; Po, J.; Verdine, G. L. *J. Am. Chem. Soc.* **2000**, *122*, 5891.
- (51) Olsen, J. V.; Ong, S.-E.; Mann, M. *Mol. Cell. Proteomics* **2004**, *3*, 608.
- (52) Bird, G. H.; Madani, N.; Perry, A. F.; Princiotta, A. M.; Supko, J. G.; He, X.; Gavathiotis, E.; Sodroski, J. G.; Walensky, L. D. *Proc. Natl. Acad. Sci. U.S.A.* **2010**, *107*, 14093.
- (53) Weiss, M. A.; Ellenberger, T.; Wobbe, C. R.; Lee, J. P.; Harrison, S. C.; Struhl, K. *Nature* **1990**, *347*, 575.
- (54) Talanian, R.; McKnight, C.; Kim, P. *Science* **1990**, *249*, 769.
- (55) Morii, T.; Simomura, M.; Morimoto, S.; Saito, I. *J. Am. Chem. Soc.* **1993**, *115*, 1150.



- (56) Hollenbeck, J. J.; McClain, D. L.; Oakley, M. G. *Protein Science* **2002**, *11*, 2740.
- (57) Bullen, G. A.; Tucker, J. H. R.; Peacock, A. F. A. *Chem. Commun.* **2015**, *51*, 8130.
- (58) Ueno, M.; Murakami, A.; Makino, K.; Morii, T. *J. Am. Chem. Soc.* **1993**, *115*, 12575.
- (59) Aizawa, Y.; Sugiura, Y.; Morii, T. *Biochemistry* **1999**, *38*, 1626.
- (60) Palmer, C. R.; Sloan, L. S.; Adrian, J. C.; Cuenoud, B.; Paoletta, D. N.; Schepartz, A. *J. Am. Chem. Soc.* **1995**, *117*, 8899.
- (61) Caamaño, A. M.; Vázquez, M. E.; Martínez-Costas, J.; Castedo, L.; Mascareñas, J. L. *Angew. Chem. Int. Ed.* **2000**, *39*, 3104.
- (62) Pellegrini, M.; Ebright, R. H. *J. Am. Chem. Soc.* **1996**, *118*, 5831.
- (63) Talanian, R. V.; McKnight, C. J.; Rutkowski, R.; Kim, P. S. *Biochemistry* **1992**, *31*, 6871.
- (64) Oheix, E.; Peacock, A. F. A. *Chem. Eur. J.* **2014**, *20*, 2829.
- (65) Cuenoud, B.; Schepartz, A. *Science* **1993**, *259*, 510.
- (66) Cuenoud, B.; Schepartz, A. *Proc. Natl. Acad. Sci. U.S.A.* **1993**, *90*, 1154.
- (67) Mosquera, J.; Jiménez-Balsa, A.; Doderó, V. I.; Vázquez, M. E.; Mascareñas, J. L. *Nat. Commun.* **2013**, *4*, 1874.
- (68) Hope, I. A.; Struhl, K. *Cell* **1986**, *46*, 885.
- (69) Cranz, S.; Berger, C.; Baici, A.; Jelesarov, I.; Bosshard, H. R. *Biochemistry* **2004**, *43*, 718.
- (70) Metallo, S. J.; Schepartz, A. *Nat. Struct. Mol. Biol.* **1997**, *4*, 115.
- (71) Kohler, J. J.; Metallo, S. J.; Schneider, T. L.; Schepartz, A. *Proc. Natl. Acad. Sci. U.S.A.* **1999**, *96*, 11735.
- (72) Kohler, J. J.; Metallo, S. J.; Schneider, T. L.; Schepartz, A. *Proc. Nat. Acad. Sci. U.S.A.* **1999**, *96*, 11735.
- (73) Kajino, M.; Fujimoto, K.; Inouye, M. *J. Am. Chem. Soc.* **2011**, *133*, 656.
- (74) Woolley, G. A.; Jaikaran, A. S. I.; Berezovski, M.; Calarco, J. P.; Krylov, S. N.; Smart, O. S.; Kumita, J. R. *Biochemistry* **2006**, *45*, 6075.

- (75) Azuma, Y.; Imanishi, M.; Yoshimura, T.; Kawabata, T.; Futaki, S. *Angew. Chem.* **2009**, *121*, 6985.
- (76) Futaki, S.; Kiwada, T.; Sugiura, Y. *J. Am. Chem. Soc.* **2004**, *126*, 15762.
- (77) Castellano, F. N.; Dattelbaum, J. D.; Lakowicz, J. R. *Anal. Biochem.* **1998**, *255*, 165.
- (78) Kuzmic, P. *Anal. Biochem.* **1996**, *237*, 260.
- (79) Schuck, P. *Biophys. J.* **2000**, *78*, 1606.
- (80) Hummer, G.; Garcia Ae Fau - Garde, S.; Garde, S. *Proteins* **2001**, *42*, 77.

## Appendix 1: Additional factors to be considered in the incorporation of HCMs to induce $\alpha$ -helicity

A second set of peptides where the position of the HCM was varied in order to determine the effect of the location and polarity of the HCM on helix-induction, and the salt bridges were removed to test whether the presence of the HCM was sufficient to induce  $\alpha$ -helicity.

### Inclusion of salt bridges for additional stabilization

A second set of peptides (**SP1-SP4**) was synthesized with the HCM in the center of the peptide and two Glu/Lys salt bridges on the opposite face of the helix. In order to

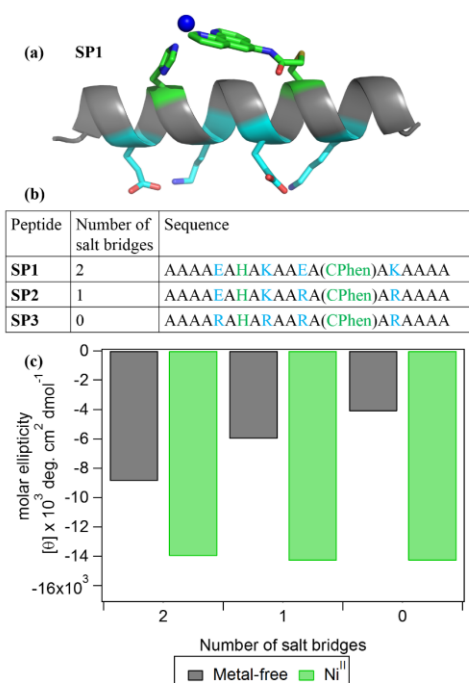


Figure 3.30: Inclusion of salt bridges in the peptide backbone provides helical stabilization in the apo protein, but make no difference upon metal binding. (a) Model of peptide containing 2 salt bridges and an HCM centered on the opposite face. (b) Sequences of the peptides. (c) Comparison of the helicity in the presence and absence of salt bridges in the presence and absence of Ni<sup>II</sup>. (Gray: metal-free, green: Ni<sup>II</sup> bound)

test the necessity of these salt bridges for helix induction, peptides were synthesized with Glu-to-Lys mutations. Without metal binding, the peptides with two salt bridges had the greatest  $\alpha$ -helical signal, followed by the peptide with a single salt bridge, and the peptide lacking salt bridges was the least helical when metal free. However, upon the addition of metal ions, there was very little difference between the three peptides, especially in the case of Ni<sup>II</sup> (Figure 3.30). These results demonstrate that the HCM is sufficient to induce helicity in short peptides.

### Placement in peptide sequence

A preference was observed for the Phen component of the HCM to be placed on the C-terminal side. It is likely that the tighter metal chelation of the Phen as compared to metal coordination to the His residue is better able to stabilize the terminus of the peptide in an  $\alpha$ -helix (Figure 3.31), and that there is more fraying of the helix when the his residue is on the terminal side.<sup>80</sup>

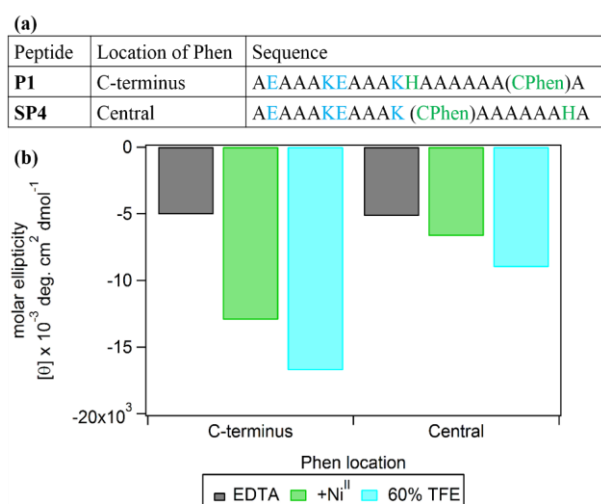


Figure 3.31: Polarity of the HCM on the peptide. (a) Sequences of peptides with Phen located at the C-terminus or more centrally. (b) Comparison of the induction of helicity upon the addition of Ni<sup>II</sup>.

Taken together with our previous studies on His-Quin HCM systems, these observations on his-Phen peptides highlight the remarkable modularity of HCMs in controlling peptide structure through the choice of the metal ion and the metal chelating functionality as well as through the amino acid side chains that make secondary contacts with the chelating functionality.

## **4. Designed, Helical Protein Nanotubes with Variable Diameters from a Single Building Block**

### **4.1 Abstract**

Due to their structural and mechanical properties, 1D helical protein assemblies represent highly attractive design targets for biomolecular engineering and protein design. Here we present a designed, tetrameric protein building block,  $Zn_8R_4$ , which assembles via Zn coordination interactions into a series of kinetically stable, crystalline, helical nanotubes whose widths can be controlled by solution conditions. X-ray crystallography and transmission electron microscopy (TEM) measurements indicate that all three classes of protein nanotubes are constructed through the same 2D arrangement of  $Zn_8R_4$  tetramers held together by Zn coordination. The mechanical properties of these nanotubes are correlated with their widths. All  $Zn_8R_4$  nanotubes are found to be highly flexible despite possessing crystalline order, owing to their small inter-building-block interaction surfaces that are mediated solely by metal coordination.

### **4.2 Introduction**

A major goal in nanotechnology is the bottom-up design and construction of self-assembled materials that combine the structural order, dynamicity, and functional properties of natural protein assemblies.<sup>1,2</sup> Of particular interest are one-dimensional, helical architectures with hollow interiors, which in nature fulfill a large number of biomechanical roles such as the formation of the cytoskeleton,<sup>3</sup> molecular transport and cell division (microtubules),<sup>4,5</sup> cell motility (bacterial flagella),<sup>6</sup> infection (type III secretion needles),<sup>7,8</sup> endocytosis (dynamin),<sup>9,10</sup> and compartmentalization (tubular virus

capsids).<sup>11</sup> Invariably, all of these biological architectures are assembled from small (<10 nm) protein building blocks that polymerize through non-covalent interactions in a helical symmetry. This mode of assembly—as opposed to, for example, linear stacking of larger, ring-like components—endows natural, 1D protein architectures with the ability to rapidly polymerize or depolymerize and to adapt their structures in response to external stimuli while retaining high mechanical/chemical stability. These properties of biological nanotubes, along with their inherent directionality, chirality, long-range and short-range periodicity, and high surface area-to-volume ratios, render them as highly attractive molecular templates and design targets.<sup>12,13</sup>

While peptide-based building blocks have shown promise for constructing helical superstructures,<sup>3,12,14-19</sup> successes in the design of tubular assemblies from protein synthons have been limited to the use of physical methods (*e.g.*, layer-by-layer assembly on solid templates),<sup>20-23</sup> assembly under harsh conditions that alter the structure of the protein subunits,<sup>24</sup> or to the use of natively ring-shaped proteins which can be manipulated to stack into tubes.<sup>25</sup> We recently established that the simultaneous strength, directionality and reversibility of metal coordination interactions can be exploited to direct the formation of small protein building blocks into discrete oligomers or highly ordered 1-, 2- and 3D architectures.<sup>26-31</sup> These assemblies are distinguished from many other designed supramolecular protein architectures by their stimuli-responsiveness. Because metal-protein interactions are inherently tunable (through metal concentration, identity, oxidation state or solution pH), it follows that the structures and assembly states of metal-directed protein architectures can also be modulated by external stimuli. Accordingly, we present here the metal-directed assembly of a designed protein building block into a series of

crystalline, helical nanotubes, whose diameters and structure-dependent mechanical properties can be varied through solution conditions that modulate metal-protein interactions.

From a retrosynthetic perspective, a 1D helical tube can be considered as an anisotropic (*i.e.*, rectangular, not square) 2D sheet wrapped around a cylinder with longitudinal and lateral growth axes (Figure 4.1). Such an anisotropic 2D sheet can be constructed from self-assembling  $D_2$  symmetric building blocks that similarly possess bi-directional symmetry in the 2D plane. If the interactions between these building blocks can be controlled (thermodynamically or kinetically) through external means, it should in principle be possible to modulate the magnitude of anisotropy between the longitudinal

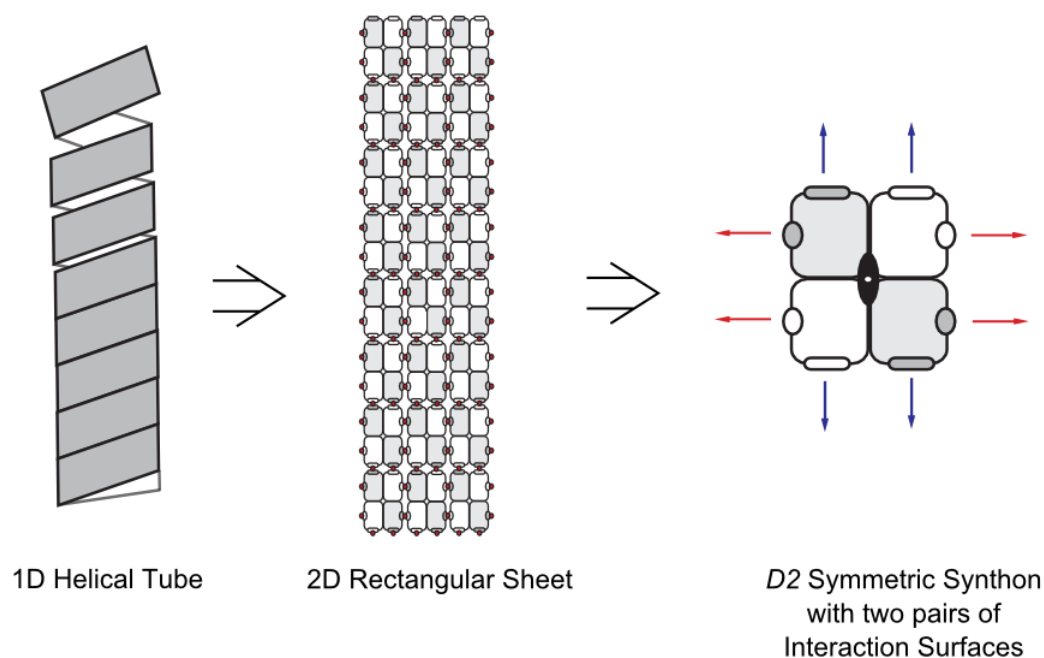


Figure 4.1: Retrosynthetic analysis of a 2D helical nanotube. Individual nanotubes (left) are formed by the folding of an anisotropic 2D array (center) that is composed of individual  $D_2$  symmetric synthons (right). The formation of an anisotropic array is driven by the presence of bidirectional interaction motifs that have differential binding strengths.



and lateral growth directions, thereby controlling the widths or the aspect ratios of the resulting tubes. Previously, we reported on the construction of  $D_2$  symmetric assemblies of the monomeric protein cytochrome  $cb_{562}$  through  $Zn^{II}$  coordination.<sup>32,33</sup> Here, we considered that these tetrameric scaffolds themselves can be used as building blocks for assembling anisotropic 2D sheets (and thereby 1D nanotubes), as they feature two sets of weakly metal chelating motifs on their external surfaces to promote bidirectional growth:

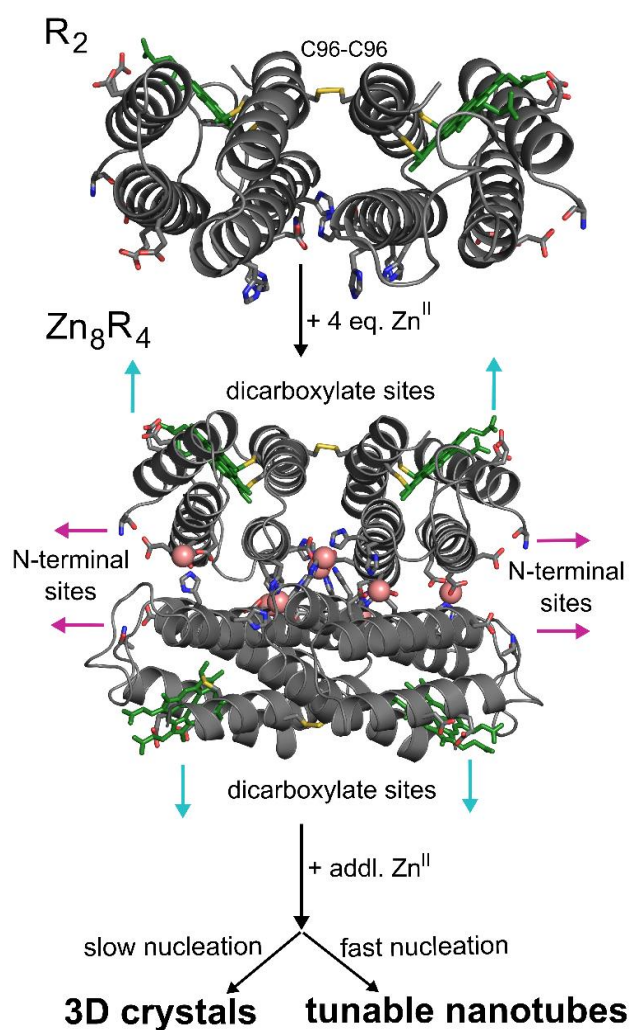


Figure 4.2: Proposed Zn-mediated assembly of a disulfide-linked protein dimer ( $R_2$ ) into a closed,  $D_2$  symmetric tetramer ( $Zn_8R_4$ ), which acts as a synthon for larger supramolecular architectures upon further Zn coordination. Heme cofactors are shown as green sticks; they have been omitted in later figures for clarity.

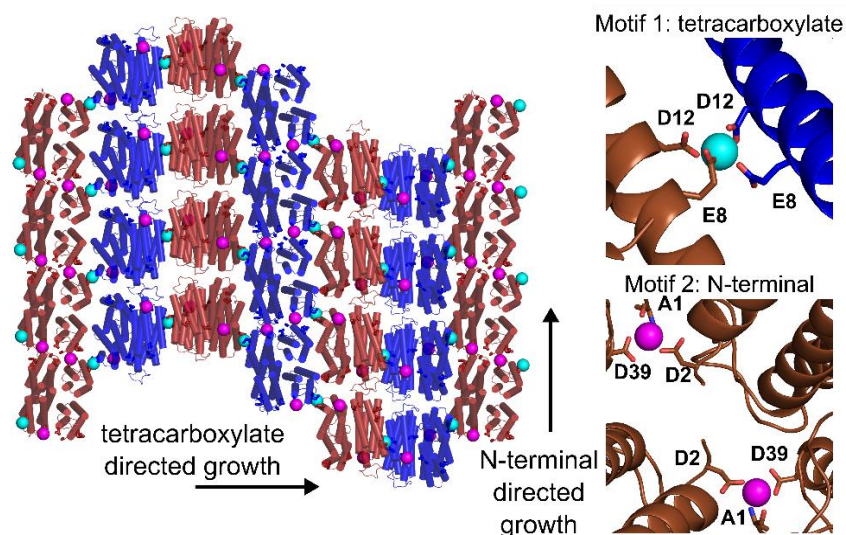


Figure 4.3: Crystallographic characterization of Zn<sub>8</sub>R<sub>4</sub>. Motif 1 (cyan spheres) and Motif 2 (magenta spheres) coordination sites promote intertetramer assembly and the formation of higher order arrays. Protein tetramers are alternatively colored to highlight 2D arrangement. See Figure 4.7 for a detailed view of an individual Zn<sub>8</sub>R<sub>4</sub> tetramer.

Motif 1) the bidentate combination of Glu8 and Asp12 carboxylates; Motif 2) the tridentate combination of Ala1 N-terminal amine and carbonyl oxygen and Glu39 carboxylate. (Figure 4.2 and Figure 4.3) Both motifs were observed in several crystal structures to be capable of mediating lattice packing interactions through Zn<sup>II</sup> coordination (PDB IDs 4JEB, 3TOM, 3QVY, 3M4B, 3M4C).

### 4.3 Design of protein building blocks

As a starting point for building a stable  $D_2$  symmetric building block, we used a cyt *cb*<sub>562</sub> variant (RIDC3) which was previously designed to form weak Zn-mediated dimers that further assembled into 1-, 2- and 3D arrays.<sup>26,27</sup> RIDC3 was engineered with a Cys residue at position 96 (informed by earlier work),<sup>33</sup> such that it could be prepared as a covalent C96-C96 linked dimer (Figure 4.2a and Figure 4.4). A His residue was then incorporated in position 59 in addition to pre-existing metal-coordinating residues on

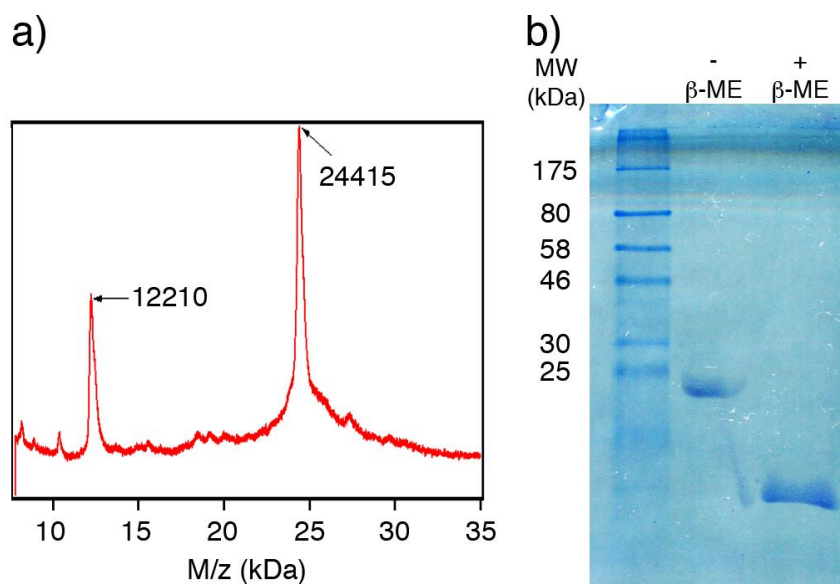


Figure 4.4: Characterization of disulfide-crosslinked  $R_2$ . (a) MALDI mass spectrum of  $R_2$ . (b) SDS PAGE gel of  $R_2$  after denaturation in loading buffer with (right line) or without (center lane)  $\beta$ -mercaptoethanol ( $\beta$ -ME). In the presence of  $\beta$ -ME, the C96-C96 bond is reduced, yielding the monomeric species.

RIDC3, such that the disulfide-linked dimers would lock into the desired  $D_2$  tetramer via coordination by a total of 8  $Zn^{II}$  ions ( $Zn_8^{H59/C96}RIDC3_4$ , Figure 4.2b). The dimeric, metal-free dimer is hereafter referred to as  $R_2$  and the metal-bound tetramer as  $Zn_8R_4$ .

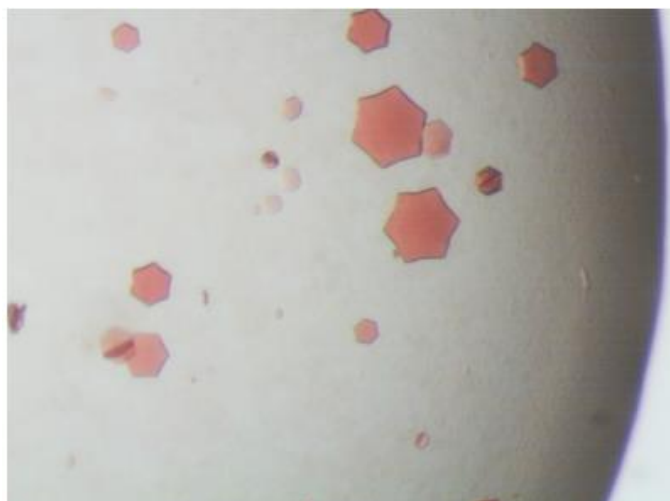
#### 4.3.1 Determining protein packing by crystallography

To probe whether  $Zn_8R_4$  properly forms and can self-assemble into planar sheets, we first set out to produce single 3D crystals by Zn-directed self-assembly. Our work with RIDC3 had shown that the growth of large Zn-directed 2D sheets and their subsequent stacking into 3D crystal lattices can be promoted by the inclusion of high concentrations of the weakly metal-coordinating buffer TRIS, which lowers the effective free Zn concentration and slows the nucleation rate.<sup>26</sup> Accordingly, we were able to obtain hexagonal, diffraction-quality crystals of  $Zn_8R_4$  from bulk solutions that contained 50  $\mu$ M  $Zn_8R_4$ , 2.5 mM  $Zn^{II}$  and 100 mM TRIS (Figure 4.5). The 2.3-Å resolution crystal structure

Table 4.1: X-ray data collection and refinement statistics for  $Zn_8R_4$ .

\*denotes highest resolution shell

Data collection location	SSRL BL 12-2
Unit cell dimensions (Å)	$52.9 \times 52.9 \times 257.1$ $\alpha=\gamma=90^\circ, \beta=120^\circ$
Space group	$P6_122$
Resolution (Å)	85.69 – 2.46
X-ray Energy (keV)	12,657
Number unique reflections	8104
Redundancy	3.5
Completeness (%)*	95.1 (87.7)
$\langle I/\sigma I \rangle$ *	6.7 (3.4)
$R_{\text{sym}}$ (%)*	8.6 (21.9)
$R_{\text{work}}/R_{\text{free}}$ (%)	22.5/29.2
R.m.s. deviations	
Bond lengths (Å)	0.011
Bond angles ( $^\circ$ )	1.385
Ramachandran plot (%)	
Most favored	99
Allowed	1
Disallowed	0.0

Figure 4.5: Light micrograph image of  $Zn_8R_4$  crystals obtained via Zn-directed assembly.

(Table 4.1,  $P6_122$ ,  $52.9 \times 52.9 \times 257.1$  Å, PDB ID 5BU7) confirmed the formation of the desired  $D_2$  symmetric tetramers, the pair of C96-C96 disulfide bonds and the two sets

of four, internal Zn-coordination sites (Figure 4.3 and Figure 4.6). The examination of the lattice revealed that the  $Zn_8R_4$  units could indeed form 2D arrays through Zn coordination by Motif1 and Motif2 (Figure 4.3). While these 2D arrays are not flat (owing to the  $6_1$  screw axis that runs along the 2D  $bc$  plane) and not every tetramer has its external Zn-coordination motifs occupied, the sheets are contiguously linked by  $Zn^{II}$  ions and the two motifs propagate self-assembly in orthogonal directions as intended. Further growth of these 2D arrays into 3D crystals is directed by  $Zn^{II}$  ions oriented perpendicular to their surfaces (Figure 4.7). Whereas the metal-mediated assembly of large 3D crystalline arrays is promoted under slow nucleation/growth conditions (low pH, low effective metal concentration), the formation of 1D nanotubes are expected to be favored when the nucleation is rapid (high pH, high effective metal concentration).<sup>26</sup>

#### 4.4 Formation of variable diameter protein nanotubes

In initial experiments for forming 1D nanotubes, we first incubated  $R_2$  dimers with a 5 fold molar excess of  $Zn^{II}$  at pH 7.5 in a non-metal chelating buffer (MOPS) to pre-form the  $Zn_8R_4$  tetramers, which was followed by the addition of another 5-fold excess of  $Zn^{II}$ . This treatment resulted in the rapid formation of uniform, helical protein nanotubes that

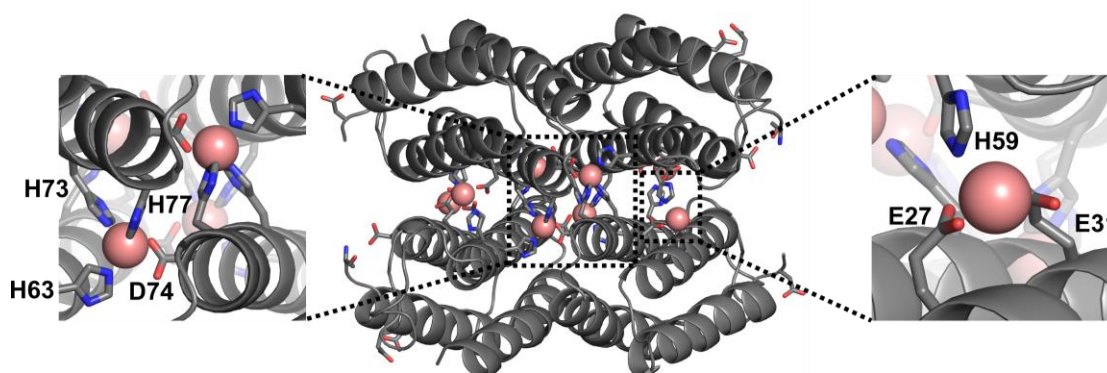


Figure 4.6: Internal  $Zn^{II}$  coordination sites to form  $Zn_8R_4$  from  $R_2$ .



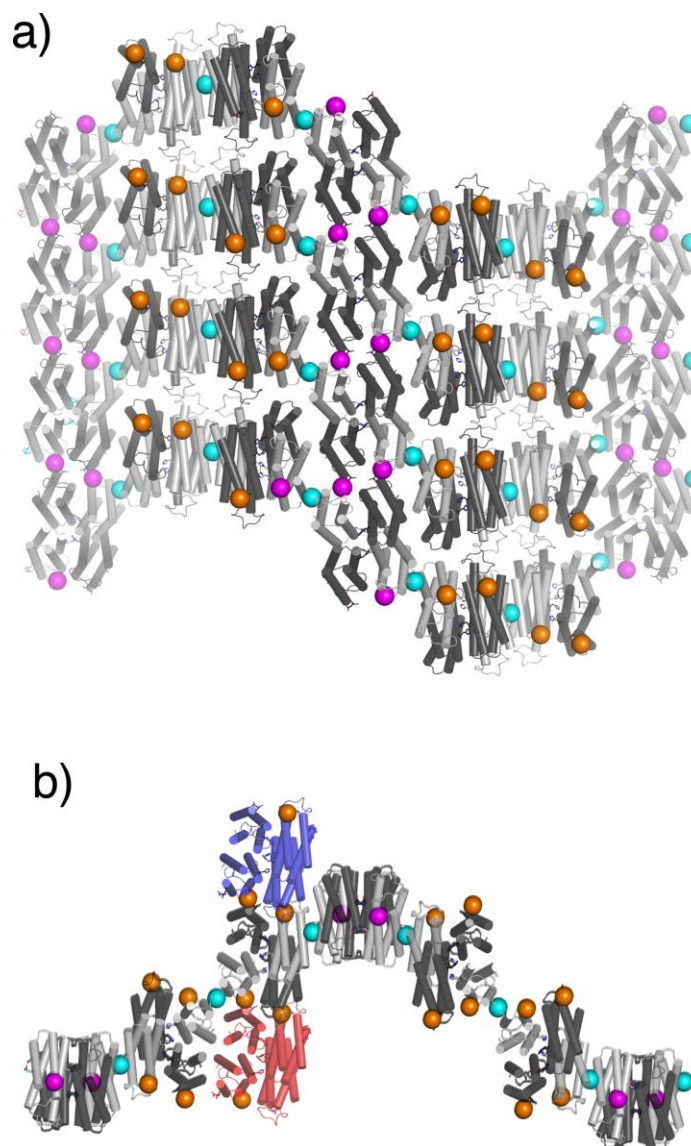


Figure 4.7: Mechanism for stacking of 2D Zn<sub>8</sub>R<sub>4</sub> arrays into 3D crystals. (a) Cartoon depiction of a crystallographically characterized 2D Zn-mediated array. 2D arrays are stabilized by Zn ions coordinated by N-terminal and tetracarboxylate coordination motifs, which are shown as magenta and cyan spheres, respectively. N-terminal coordination sites that are oriented perpendicular to the 2D array (orange spheres) allow for the growth of 3D crystals or multi-walled nanotubes. (b) Front view of a Zn-mediated 2D array. The blue and red tetramers are coordinated to Zn<sup>II</sup> sites in front of and behind the 2D array, respectively.

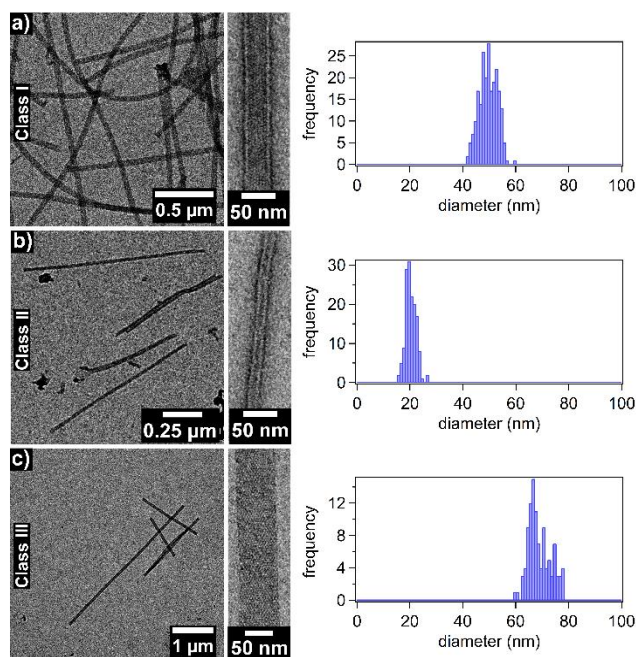


Figure 4.8: ns TEM images of  $Zn_8R_4$  nanotubes.

were  $48 \pm 3$  nm wide (Class I) based on negative-stain TEM (Figure 4.8, Figure 4.9, and Figure 4.10). In contrast, the addition of 10-fold excess  $Zn^{II}$  in the second step produced significantly thinner, monodisperse nanotubes (Class II) with a diameter of  $20 \pm 2$  nm. Stepwise  $Zn^{II}$  addition was critical for forming monodisperse populations of nanotubes. When 10-fold excess of  $Zn^{II}$  was directly added to the  $R_2$  dimer solution without the preincubation step, we observed the formation of amorphous aggregates in addition to Type I nanotubes. When a larger excess of  $Zn^{II}$  was added without the preincubation step, only amorphous aggregates were observed. The formation of these disordered species is likely due to presence of multiple possible Zn-mediated assembly modes of the  $R_2$  dimers and the formation of kinetically trapped amorphous aggregates. The above experiments were repeated at pH 6.5 (in non-coordinating, MES buffer), where the metal-protein coordination interactions (particularly that by the N-terminal amine of Motif2) would be

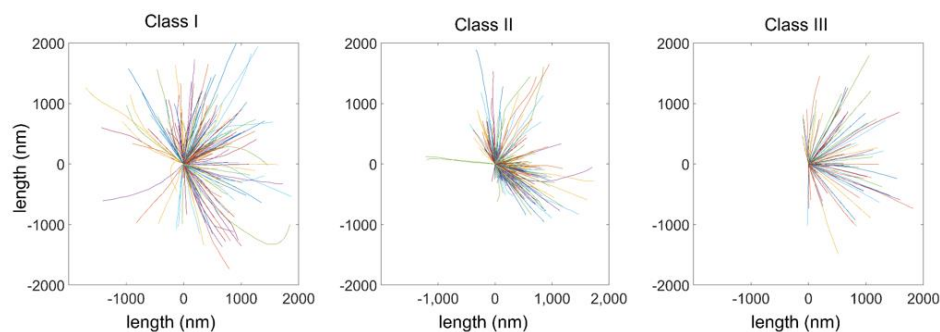


Figure 4.9: Traces of individual nanotubes used for determining the parameters listed in Table 4.2. Each tube was traced using the FiberApp program, and the initial coordinates were placed at (0,0) so that each tube extends from the center of the plot.

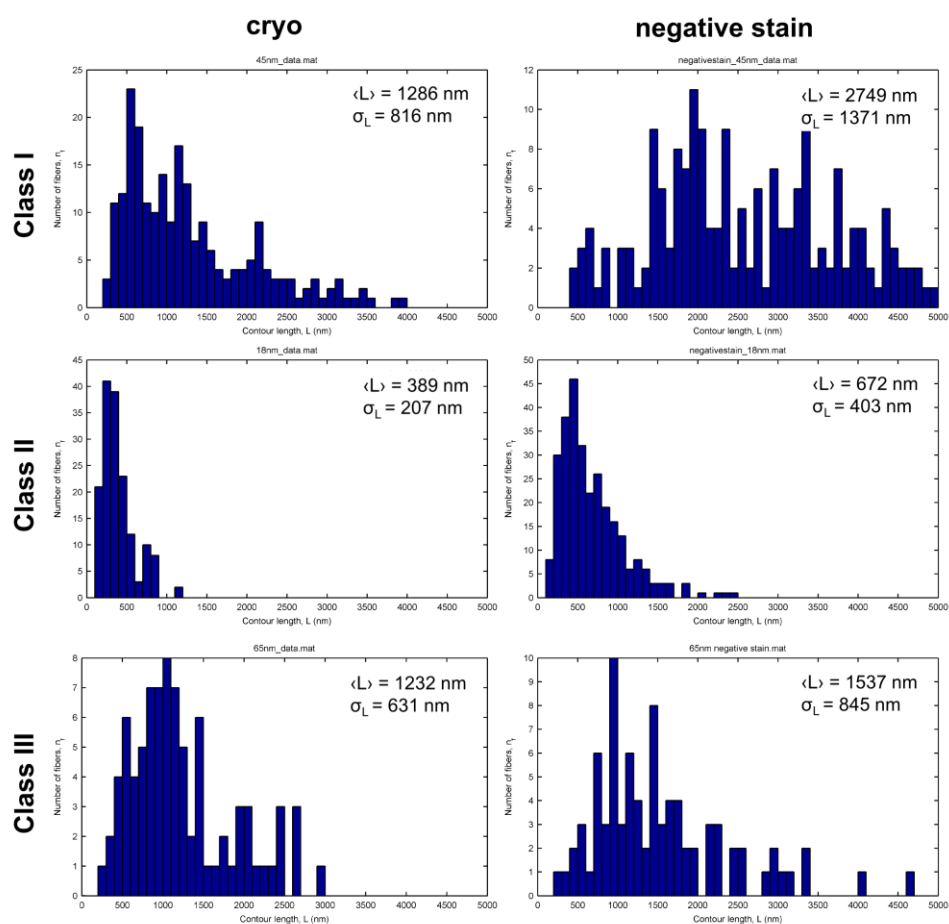


Figure 4.10: Contour length distributions of each class of nanotubes.



expected to be weaker. As at pH 7.5, the stepwise addition of 5+5-fold excess of  $\text{Zn}^{\text{II}}$  to the  $R_2$  solution yielded the Class I nanotubes and the direct addition of 20-fold excess  $\text{Zn}^{\text{II}}$  resulted in heterogeneous aggregates. In contrast, the direct addition of 10-fold excess  $\text{Zn}^{\text{II}}$  led to the formation of yet another class (Class III) of highly ordered, helical nanotubes that were  $68 \pm 4$  nm wide. The observation that the structural outcome of self-assembly is dependent on the sequence of Zn addition indicates that the formation of different classes of  $\text{Zn}_8\text{R}_4$  nanotubes is kinetically governed. We postulate that the decisive, structural-determining steps occur during initial nucleation/growth stages.

#### 4.4.1 Structural analysis of $\text{Zn}_8\text{R}_4$ nanotubes

For structural analysis of  $\text{Zn}_8\text{R}_4$  nanotubes, we first took advantage of the fact that some Class I nanotubes presented frayed ends that possessed a flat, single-layered 2D

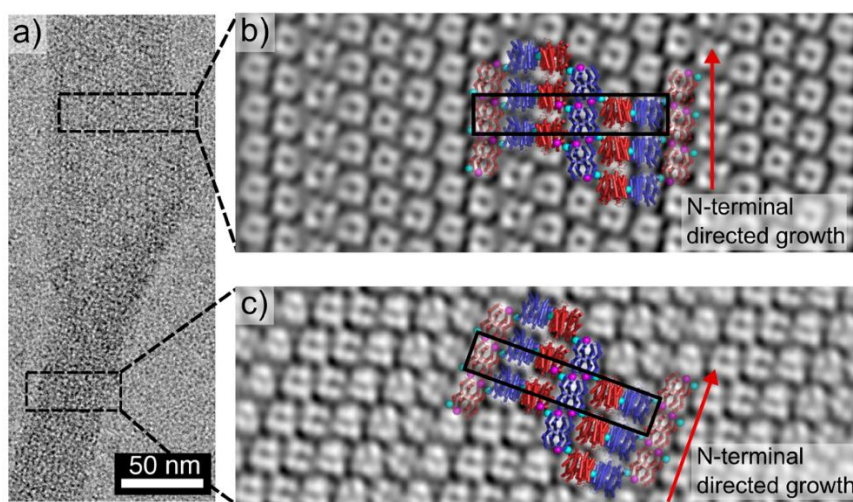


Figure 4.11: ns TEM characterization of  $\text{Zn}_8\text{R}_4$  arrays. (a) Single Class I nanotube with tubular (bottom) and frayed (top) segments. (b,c) 2D reconstructions of tubular (b) and frayed (c) regions of a single nanotube. The crystallographically characterized 2D pattern of  $\text{Zn}_8\text{R}_4$  molecules is superimposed onto the TEM reconstructions. The slight mismatch between the crystallographic model and TEM reconstruction in (b) is likely due to the curved nature of the 2D arrays, which is accounted for by the curvature of the tubes.

morphology (Figure 4.11). The reconstructed TEM images from both the tubular and the flat regions of the Class I nanotubes revealed compact structures with dimensions similar to the  $Zn_8R_4$  tetramers (Figure 4.12 and Figure 4.13) and that are clearly distinct from those that are observed in reconstructions of RIDC3 nanotubes. These tetramers are arranged into unit cells, each of which consists of six subunits, with dimensions ( $52 \text{ \AA} \times 270 \text{ \AA}$ , black boxes in Figure 4.11b and c) that are very similar to those seen in the 3D crystals. Indeed, the 2D packing arrangement of  $Zn_8R_4$  tetramers observed in the X-ray crystal structure fits reasonably well in the TEM-derived molecular pattern. An analysis of the Class II and Class III nanotubes indicates that they also contain the same arrangement (Figure 4.15 and Figure 4.16). These results strongly suggest that the Zn coordination interactions that mediate the formation of the three classes of  $Zn_8R_4$  nanotubes are the same as those present in the 3D crystal lattice. To provide further evidence that the nanotubes have a similar arrangement of tetramers as in 3D crystals, we constructed a structural model of the thinnest (Class II) tubes. This model indicates that it is possible to build a contiguous, well-

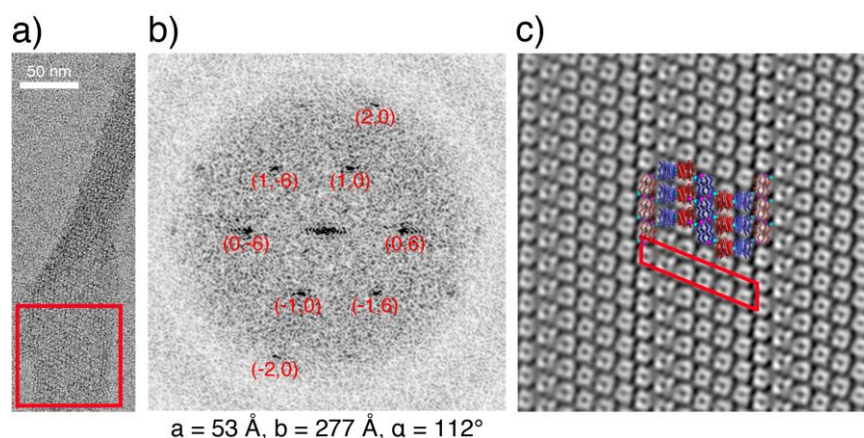


Figure 4.12: TEM micrograph (a), calculated Fourier transform (b) and Fourier-filtered image (c) of the planar region of a Class I nanotube.

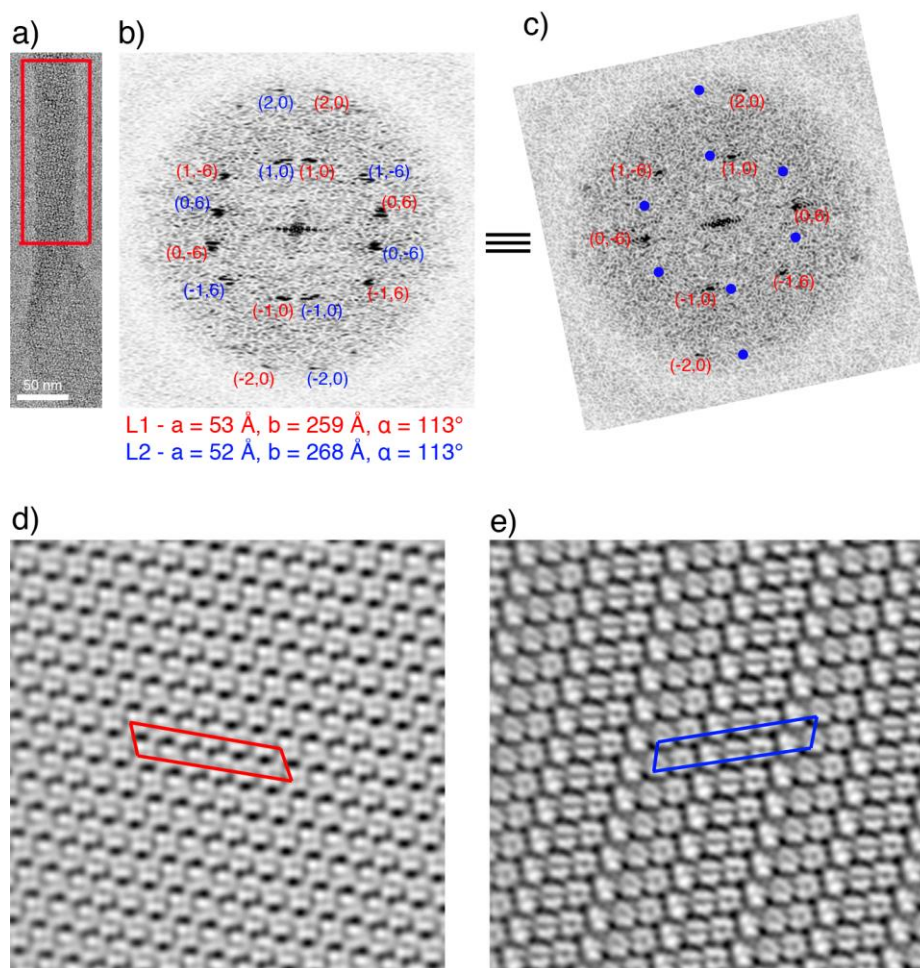


Figure 4.13: Image processing of the tubular region of a Class I nanotube. (a) Image of single  $Zn_8R_4$  nanotube. (b) Fourier transform of boxed region of the nanotube highlighting the lattices from the top and bottom of a flattened tube. (c) Fourier transform of the flattened region of a single tube rotated  $7^\circ$  to account for the angle each tube makes with the meridian. Blue dots represent a theoretical lattice generated by inserting a mirror plane along the tube meridian. (d) and (e) 2D reconstructions of each lattice in (b).

packed, helical tube with the expected 15-nm diameter using the crystallographically observed inter-tetramer interaction modalities (Figure 4.17). According to this model, the Zn-Motif1 interactions point along the lateral tube axis, whereas the Zn-Motif2 interactions are oriented longitudinally, suggesting that the width/aspect ratios of the  $Zn_8R_4$  nanotubes must be influenced by the differential Zn coordination thermodynamics/kinetics of Motif1-



and Motif2- mediated interactions. Specifically, deprotonation of the N-terminal amine of Motif2 at higher pH values apparently results in a larger difference between the interaction strengths of the coordination motifs and correspondingly thinner nanotubes.

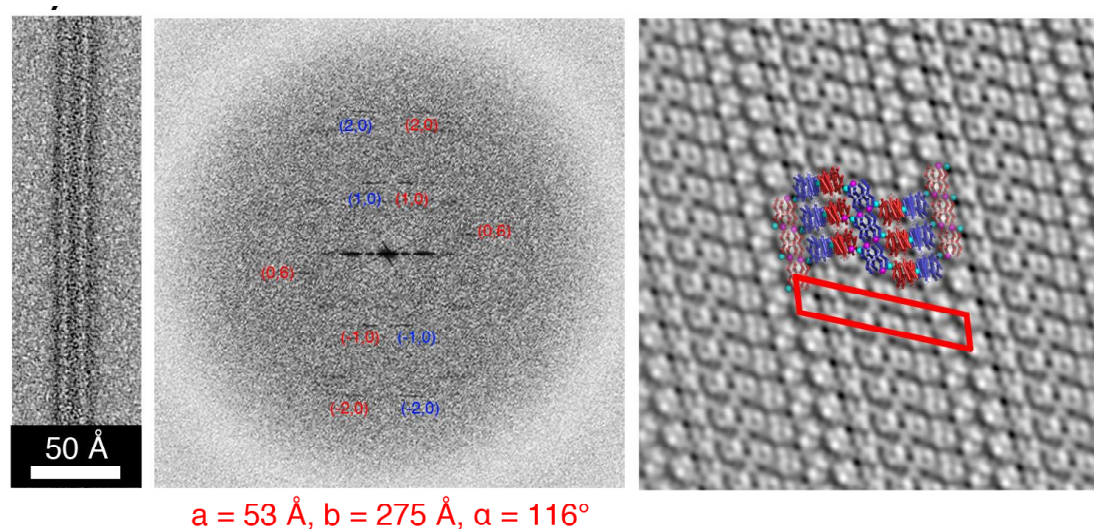


Figure 4.14: TEM images of a single nanotube (left), indexed Fourier transform (center) and 2D reconstruction (right) of a Class II nanotube.

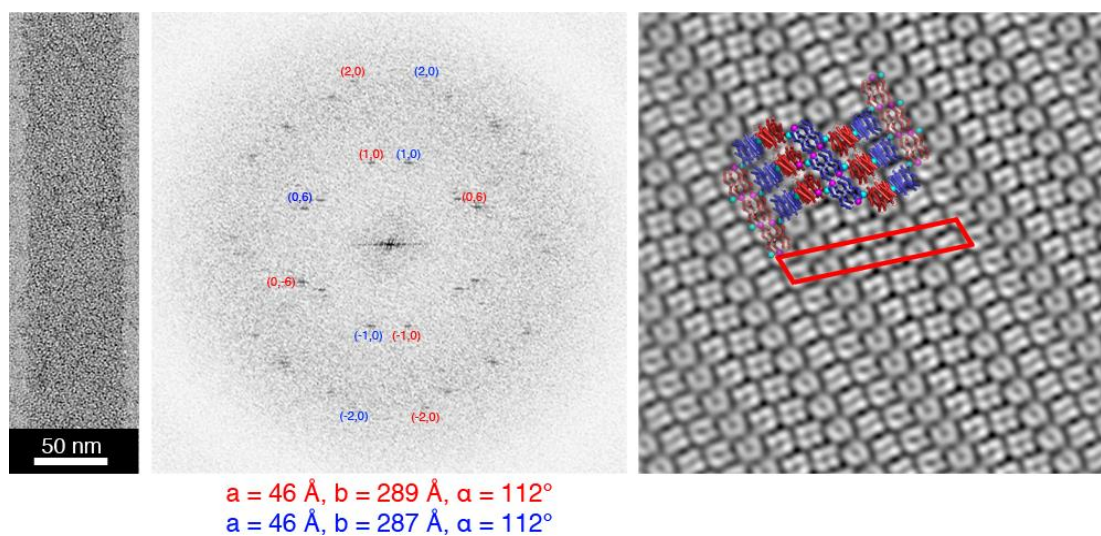


Figure 4.15: TEM image of a single nanotube (left), indexed Fourier transform

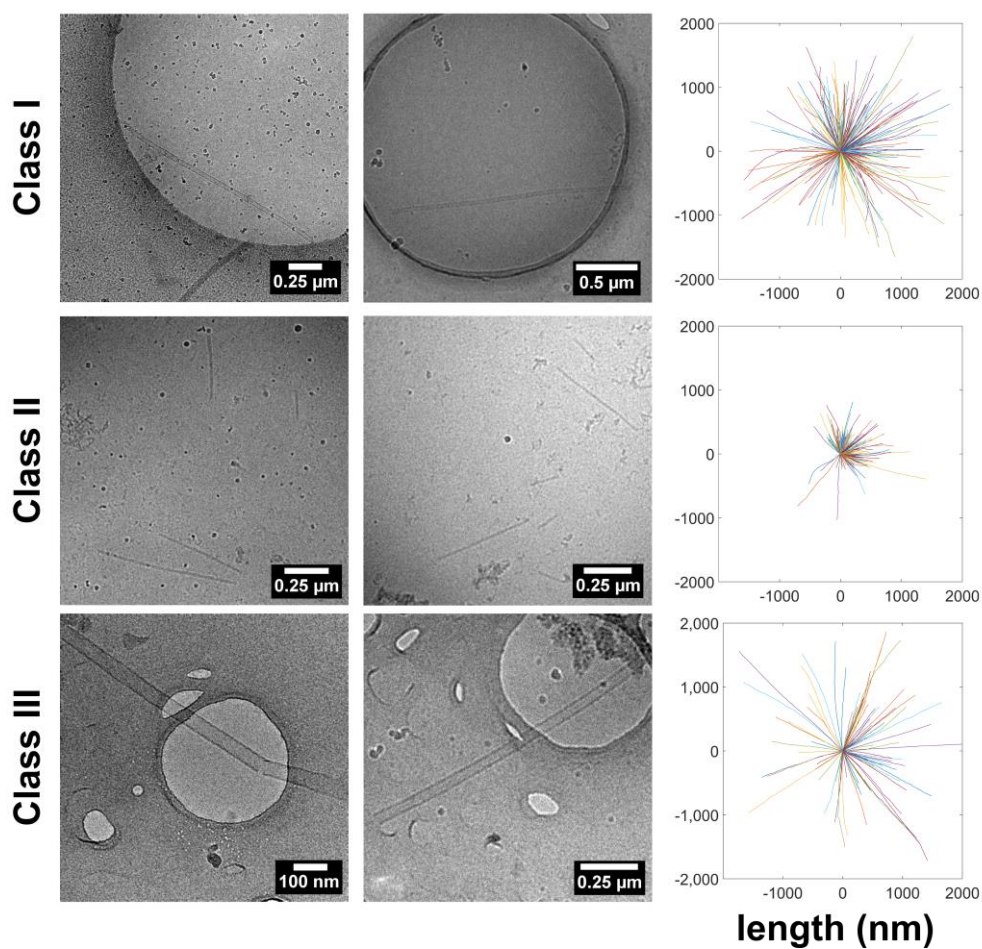


Figure 4.16: Representative images of nanotubes collected by cryo TEM. The plots on the right show the tracing of each nanotube starting from position (0,0). Axes are in nanometers.

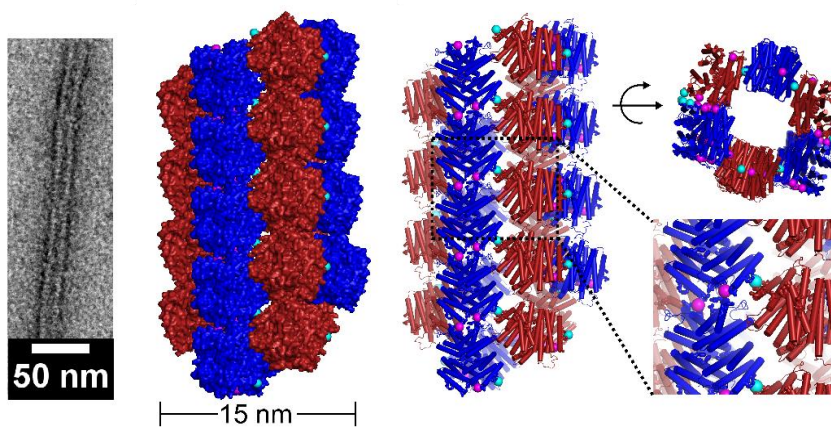


Figure 4.17: Structural model for Class II nanotubes.

#### 4.4.2 Mechanical properties of $Zn_8R_4$ nanotubes

Various structural and derived mechanical properties of the  $Zn_8R_4$  nanotubes are summarized in Table 4.2. A comparison of the cryoEM and negative-stain TEM (Figure 4.18 and Figure 4.19) analyses indicates that the wide Class III tubes undergo significant flattening by uranyl-acetate staining/drying. In contrast, the thin Class II nanotubes were not greatly affected by this treatment, which can be ascribed to their higher density of protein packing that affords resistance to lateral compression. The persistence lengths of the nanotubes were calculated using the recently published program FiberApp (Figure

Table 4.2: Structural and Derived Mechanical Properties of the  $Zn_8R_4$  Tubes

	Class I	Class II	Class III
Width (ns) [nm]	$48 \pm 3$	$20 \pm 2$	$68 \pm 4$
Width (cryo) [nm]	$25 \pm 2$	$15 \pm 1$	$46 \pm 3$
Persistence length (ns) [ $\mu\text{m}$ ]	$28.2 \pm 0.3$	$15.1 \pm 0.3$	$64.5 \pm 1.1$
Persistence length (cryo) [ $\mu\text{m}$ ]	$16.4 \pm 0.2$	$8.8 \pm 0.4$	$17.8 \pm 0.4$
Estim. Young's modulus (ns) [MPa]	1.4	15	1.1
Estim. Young's modulus (cryo) [MPa]	0.8	25	0.3

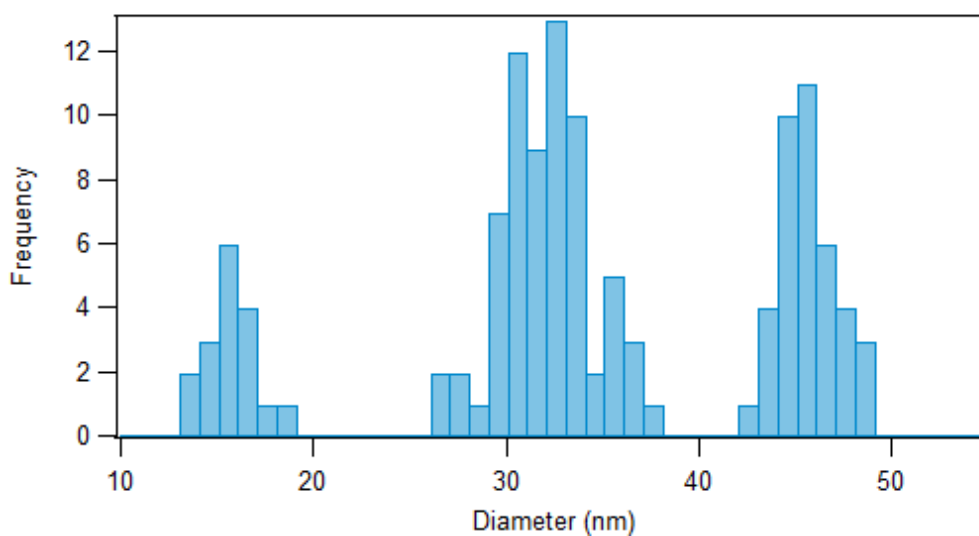


Figure 4.18: Width distribution of tubes as measured in cryoEM samples.

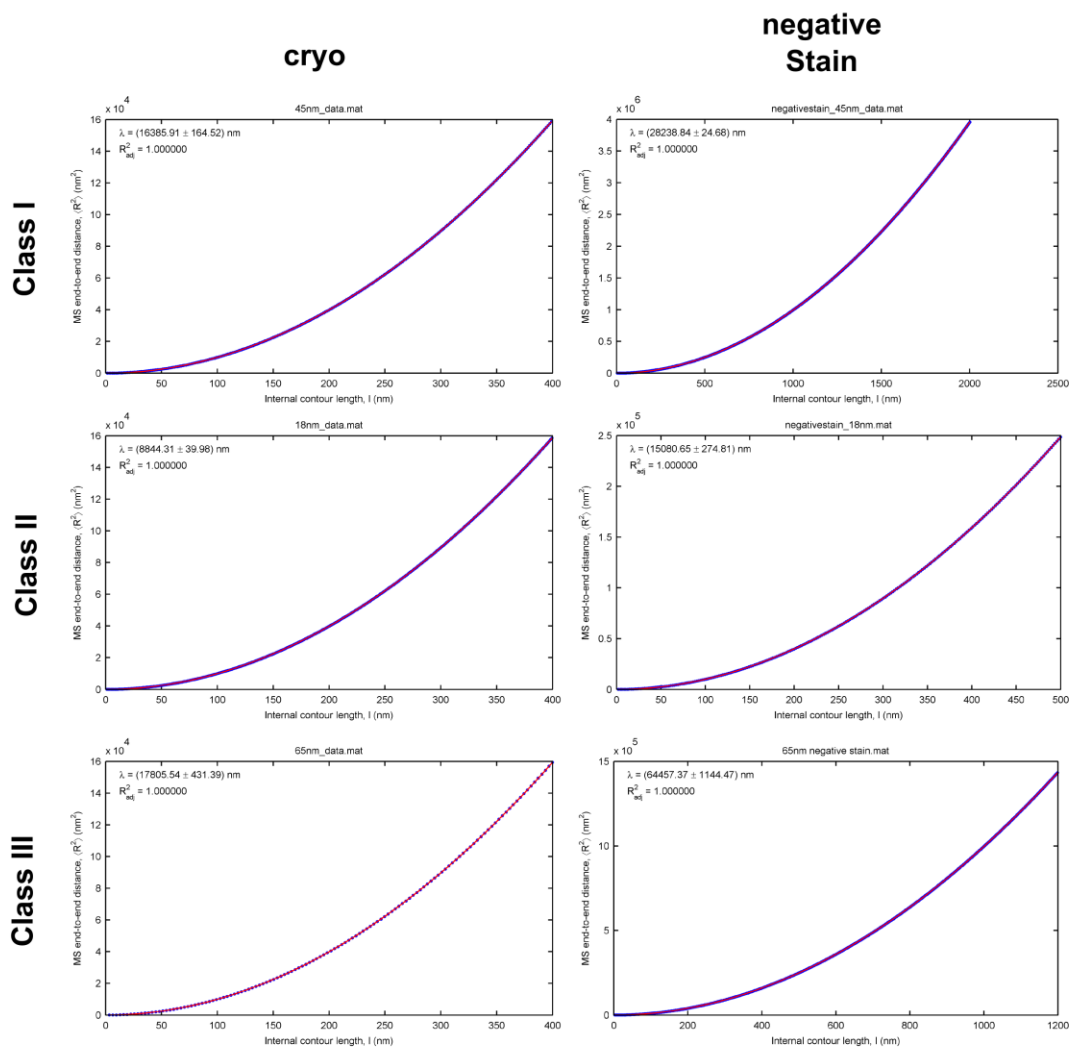


Figure 4.19: Fits used for calculating persistence length using the FiberApp module “MS End-to-end Distance”. Please refer to the corresponding section in Materials and Methods for details.

4.19),<sup>34</sup> and found to be consistently higher for uranyl-stained samples compared to cryoEM samples (Figure 4.20 and Figure 4.21), indicating that the tubes may stiffen due to staining/drying. As judged by cryoEM data, the thinnest Class II tubes are also the most flexible with a persistence length (9  $\mu\text{m}$ ) that is approximately half that of the widest Class III tubes (18  $\mu\text{m}$ ). These values are similar to the persistence lengths of actin filaments (17.7  $\mu\text{m}$ )<sup>35</sup> and significantly higher than that of double-stranded DNA (50 nm),<sup>36</sup> but



considerably lower than that of microtubules (5.2 nm).<sup>35</sup> It is notable that the  $Zn_8R_4$  nanotubes are similar to microtubules (24-nm outer and 12-nm inner diameter) in terms of their dimensions. We posit that the higher stiffness of microtubules arises from their considerably more extensive, highly evolved inter-monomer interfaces ( $\sim 3000 \text{ \AA}^2$  buried

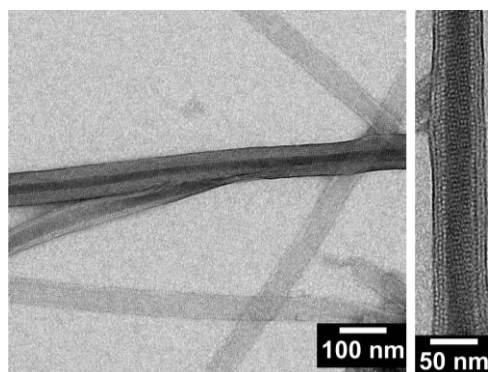


Figure 4.20: Multi-walled tubes formed under conditions that also produce Class I tubes.

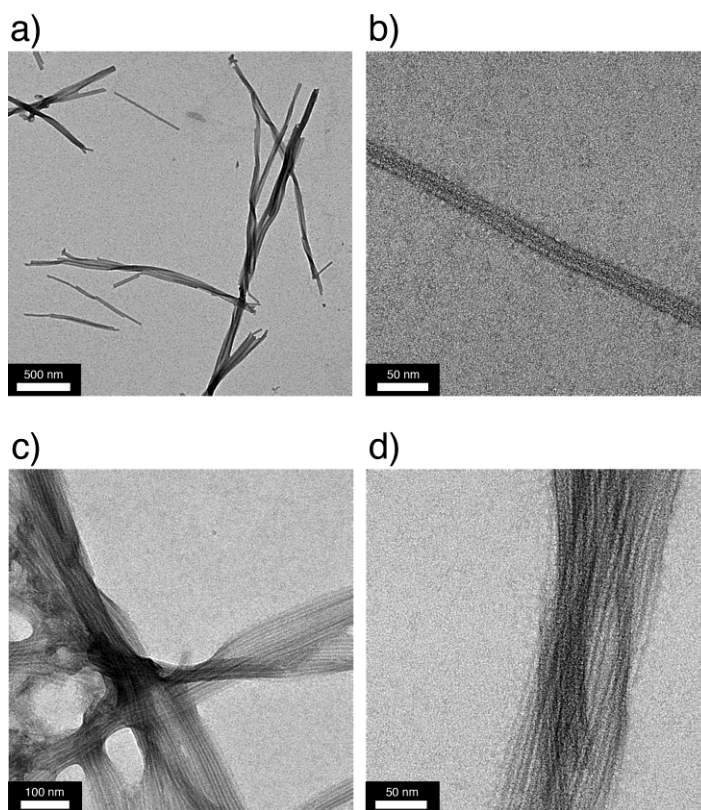


Figure 4.21: Bundles of Class II tubes formed in solution.



surface area)<sup>37</sup> compared to those in the  $Zn_8R_4$  nanotubes that are mediated solely by metal coordination with no complementary non-covalent interactions. The Young's moduli of the  $Zn_8R_4$  nanotubes can be estimated from the persistence lengths using the Equation 1.<sup>38,39</sup>

$$E = (4 \cdot k_B \cdot T \cdot P) / (\pi \cdot a^4) \quad [1]$$

where  $k_B$  is the Boltzmann constant,  $T$  is temperature,  $P$  is persistence length, and  $a$  is the radius of the tubes. The estimated Young's modulus was calculated in order to understand roughly how these novel nanotubes compare to those found in nature; additional experiments will need to be performed to directly measure this value. The range of values obtained (from 0.3 MPa for Class III to 25 MPa for Class II) are comparable to values determined for soft protein fibers such as fibrin (1-10 MPa) or elastin (1 MPa) and much less stiff than microtubules (1000-1500 MPa).<sup>38</sup> These data again indicate that the  $Zn_8R_4$  nanotubes are highly flexible, yet simultaneously possess crystalline order.

#### 4.4.3 Formation of multiwalled nanotubes

Under certain conditions, we observed the formation of unique, multi-walled nanotubes alongside Class I nanotubes (Figure 4.20). Additionally, after incubations of >1 month in solution, we observed the bundling of the Class II nanotubes, reminiscent of actin filament aggregates (Figure 4.22).<sup>40</sup> The formation of both of these superstructures is likely promoted by the presence of unsaturated Zn sites on the surfaces of the nanotubes, and may provide a means to increase their mechanical stiffness. Regardless of their flexibility,  $Zn_8R_4$  nanotubes are highly stable and persist in solution at room temperature for at least one year (Figure 4.22).

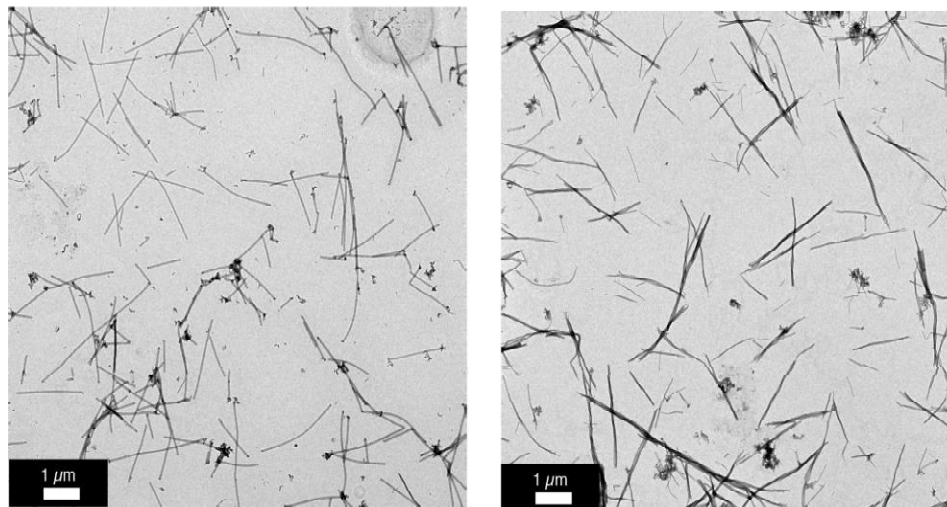


Figure 4.22: Low magnification TEM micrographs of class I (a) and class II (b) tubes after incubation for 1 year at room temperature.

#### 4.5 Conclusions

In conclusion, we have demonstrated the implementation of metal coordination chemistry to generate multiple well-defined, nanoscale architectures with different structural/mechanical properties from a single, designed protein building block. Typically, protein design approaches have aimed to construct singular structural targets that represent the thermodynamically most favored molecular arrangement formed under equilibrium conditions. This scenario contrasts with many biological self-assembly processes that proceed under non-equilibrium conditions and may yield different structural outcomes based on the environmental conditions or energy input.<sup>2</sup> In analogy to such natural, non-equilibrium processes, our study shows that it is possible to kinetically dictate protein self-assembly through the use of externally tunable intermolecular interactions such as metal coordination. Importantly, the diameters and molecular arrangements of the structures discussed here are distinct from those reported in our previous studies.<sup>27</sup> We believe that these differences result from the relative metal binding affinities of the surface-exposed

chelation motifs and that by further tuning these interactions we will be able to vastly expand the structural space accessible by metal directed protein assembly.

## **4.6 Materials and Methods**

### **4.6.1 Site-directed mutagenesis and protein expression/purification**

The R59H and T96C amino acid substitutions were introduced into the pET-ridc3<sup>26</sup> expression vector using QuikChange (Stratagene) site-directed mutagenesis and primers obtained from Integrated DNA technologies. The resulting plasmid, pET-<sup>H59C96</sup>ridc3, was transformed into chemically competent E. Coli cells and expressed and purified as previously reported.<sup>32</sup> The molecular weight of the purified protein was determined by matrix assisted laser desorption/ionization time of flight mass spectrometry (MALDI-TOF MS) to verify the incorporation of the R59H and T96C amino acid substitutions (calculated mass = 24410 Da, observed mass = 24415 Da; Figure 4.4). The purity of <sup>H59C96</sup>RIDC3 and formation of the disulfide-linked dimer, <sup>H59C96</sup>RIDC3<sub>2</sub> (*R*<sub>2</sub>), were confirmed by SDS-PAGE (Figure 4.4).

### **4.6.2 Macromolecular crystallography**

Single crystals of *Zn<sub>8</sub>R<sub>4</sub>* were obtained via Zn-directed assembly in bulk solutions containing 50 μM *R*<sub>2</sub>, 100 mM TRIS (pH 7.5) and 2.5 mM ZnCl<sub>2</sub>. After the addition of ZnCl<sub>2</sub>, the solutions immediately became turbid and a red precipitate collected at the bottom of the solution over the course of ~ 1 wk. A 20-μL aliquot of the resuspended precipitate was deposited onto a glass slide and imaged by light microscopy, which revealed the presence of hexagonal crystals (Figure 4.5).

Crystals suitable for diffraction experiments were transferred to a solution of mother liquor containing 20% glycerol as the cryoprotectant and flash-frozen in liquid nitrogen. X-ray diffraction data were collected at 100 K at SSRL BL12-2 and subsequently integrated using MOSFLM and scaled with SCALA.<sup>41</sup> Structures were then determined by molecular replacement using PHASER<sup>42</sup> and subjected to rigid-body, positional and thermal refinement in REFMAC,<sup>43</sup> along with manual rebuilding in COOT.<sup>44</sup> Crystallographic data collection and refinement statistics are listed in Table 4.1. All figures of the resulting structures were produced using PYMOL.<sup>45</sup>

#### **4.6.3 Assembly of $Zn_8R_4$ nanostructures**

$Zn_8R_4$  nanostructures were assembled in 200  $\mu$ L solutions containing 50  $\mu$ M  $R_2$  and the indicated buffer.  $ZnCl_2$  was added to these solutions from a 40 mM stock solution to obtain the indicated  $R_2:Zn^{II}$  ratios. After the addition of  $ZnCl_2$ , the solutions rapidly became turbid and the protein gradually sedimented over the course of  $\sim$ 1 wk. Small aliquots of the resuspended precipitate were removed at the indicated time points and analyzed by negative stain or cryoEM.

#### **4.6.4 Preparation of specimens and imaging of $Zn_8R_4$ nanostructures**

A 2- $\mu$ L aliquot of a solution containing the indicated  $Zn_8R_4$  nanostructures was drop cast onto a carbon coated Cu-mesh grid that had been made hydrophilic by glow discharge. After allowing the sample to adhere to the carbon support for 1 min., excess fluid was removed by blotting with Whatman filter paper. The sample was then washed with deionized water (18 m $\Omega$ ) and stained with 2% uranyl acetate. Grids were imaged on an FEI Sphera transmission electron microscope equipped with an LaB<sub>6</sub> electron gun operated at

200 keV. Images of the negatively stained specimens were recorded on a Gatan 2K2 CCD using objective-lens underfocus settings that ranged from 800 to 1200 nm.

Samples were prepared for cryo-EM samples by drop casting a 3.5- $\mu$ l aliquot of the indicated sample onto a homemade lacey carbon grid that had been made hydrophilic by glow discharge. The sample was incubated on the grid for approximately 1 min and was then blotted for 8 s using Whatman filter paper before being plunged into liquid ethane. The samples were then stored under liquid nitrogen until analysis on a FEI 200 Sphera electron microscope operated at an accelerating voltage of 200 keV. Images were recorded on a Gatan 2K2 CCD using objective-lens underfocus settings that ranged from 1 to 3  $\mu$ m.

#### **4.6.5 Processing of TEM micrographs**

All image processing was performed using the 2DX software package.<sup>46</sup> A mask was applied around individual nanostructures (planar arrays or 1D nanotubes) using the “mask crystal from polygon” function. Fast Fourier transforms (FFTs) of the masked regions were then generated using the “calculate FFT” function. Individual reflections visible in calculated FFTs were selected and served as the basis for determining lattice parameters for each nanostructure using the “evaluate lattice” function. Images were then Fourier-filtered and unbent using the “Unbend 1” and “Unbend 2” functions.

#### **4.6.6 Calculation of persistence length**

The persistence lengths of Type I, II and II nanotubes were calculated using FiberApp.<sup>34</sup> Tubes were selected for analysis if they did not cross other tubes and if their entire length was visible in a single image. The persistence length of at least 75 individual tubes from each class and method of analysis (negative stained or cryoEM) were calculated using the MS End-to-end Distance (MSED) module. FiberApp was used to trace each fiber

selected for analysis. MSED fitting analysis was performed over the full range of length values using the equation

$$\langle R^2 \rangle = 4\lambda[l - 2\lambda(1 - e^{-l/2\lambda})]$$

where  $\lambda$  is the persistence length,  $R$  is the end to end distance between two points, and  $l$  is the contour length of the nanotube. A processing length was chosen by determining where the error in fitting was lowest, and this value was used for each of the calculations (fits are shown in Figure 4.19). The persistence length was then used to calculate Young's modulus using equation 1.

#### 4.7 Acknowledgements

This work was supported by the US Department of Energy (DOE) (Division of Materials Sciences, Office of Basic Energy Sciences, Award DE-FG02-10ER46677 to F.A.T.). Use of the Stanford Synchrotron Radiation Lightsource, SLAC National Accelerator Laboratory, is supported by the US DOE, Office of Science, Office of Basic Energy Sciences under Contract No. DE-AC0276F00515.

Chapter 4 is reprinted with permission from Brodin, J.D.\*; Smith, S.J.\*; Carr, J.R.; Tezcan, F.A. Designed, helical protein nanotubes with variable diameters from a single building block. *Journal of the American Chemical Society*. 2015, 137, 10468. Copyright 2015 American Chemical Society.

#### 4.8 References

- (1) Whitesides, G. M.; Mathias, J. P.; Seto, C. T. *Science* **1991**, 254, 1312.
- (2) Mann, S. *Angew. Chem. Int. Ed.* **2008**, 47, 5306.
- (3) Dominguez, R.; Holmes, K. C. *Annu. Rev. Biophys.* **2011**, 40, 169.
- (4) Nogales, E. *Annu. Rev. Biophys. Biomol. Struct.* **2001**, 30, 397.

- (5) Wade, R. H.; Chretien, D.; Job, D. *J. Mol. Biol.* **1990**, *212*, 775.
- (6) Terashima, H.; Kojima, S.; Homma, M. *Int. Rev. Cell Mol. Biol.* **2008**, *270*, 39.
- (7) Loquet, A.; Sgourakis, N. G.; Gupta, R.; Giller, K.; Riedel, D.; Goosmann, C.; Griesinger, C.; Kolbe, M.; Baker, D.; Becker, S.; Lange, A. *Nature* **2012**, *486*, 276.
- (8) Basler, M.; Pilhofer, M.; Henderson, G. P.; Jensen, G. J.; Mekalanos, J. J. *Nature* **2012**, *483*, 182.
- (9) Stowell, M. H.; Marks, B.; Wigge, P.; McMahon, H. T. *Nat. Cell Biol.* **1999**, *1*, 27.
- (10) Mears, J. A.; Ray, P.; Hinshaw, J. E. *Structure* **2007**, *15*, 1190.
- (11) Stubbs, G.; Kendall, A. *Adv. Exp. Med. Biol.* **2012**, *726*, 631.
- (12) Reches, M.; Gazit, E. *Science* **2003**, *300*, 625.
- (13) Zhang, S. *Nat. Biotech.* **2003**, *21*, 1171.
- (14) Egelman, E. H.; Xu, C.; DiMaio, F.; Magnotti, E.; Modlin, C.; Yu, X.; Wright, E.; Baker, D.; Conticello, V. P. *Structure* **2015**, *23*, 280.
- (15) Ghadiri, M. R.; Choi, C. *J. Am. Chem. Soc.* **1990**, *112*, 1630.
- (16) Hamley, I. W. *Angew. Chem., Int. Ed.* **2007**, *46*, 8128.
- (17) O'Leary, L. E. R.; Fallas, J. A.; Bakota, E. L.; Kang, M. K.; Hartgerink, J. D. *Nat. Chem.* **2011**, *3*, 821.
- (18) Sharp, T. H.; Bruning, M.; Mantell, J.; Sessions, R. B.; Thomson, A. R.; Zaccai, N. R.; Brady, R. L.; Verkade, P.; Woolfson, D. N. *Proc. Natl. Acad. Sci. U.S.A.* **2012**, *109*, 13266.
- (19) Tarabout, C.; Roux, S.; Gobeaux, F.; Fay, N.; Pouget, E.; Meriadec, C.; Ligeti, M.; Thomas, D.; Ijsselstijn, M.; Besselievre, F.; Buisson, D. A.; Verbavatz, J. M.; Petitjean, M.; Valery, C.; Perrin, L.; Rousseau, B.; Artzner, F.; Paternostre, M.; Cintrat, J. C. *Proc. Natl. Acad. Sci. U.S.A.* **2011**, *108*, 7679.
- (20) Hou, S.; Wang, J.; Martin, C. R. *Nano Lett.* **2005**, *5*, 231.
- (21) Lu, G.; Ai, S.; Li, J. *Langmuir* **2005**, *21*, 1679.
- (22) Lu, G.; Komatsu, T.; Tsuchida, E. *Chem. Commun.* **2007**, 2980.

- (23) Qu, X.; Komatsu, T. *ACS Nano* **2010**, *4*, 563.
- (24) Lara, C.; Handschin, S.; Mezzenga, R. *Nanoscale* **2013**, *5*, 7197.
- (25) Ballister, E. R.; Lai, A. H.; Zuckermann, R. N.; Cheng, Y.; Mougous, J. D. *Proc. Natl. Acad. Sci. U.S.A.* **2008**, *105*, 3733.
- (26) Brodin, J. D.; Ambroggio, X. I.; Tang, C.; Parent, K. N.; Baker, T. S.; Tezcan, F. A. *Nat. Chem.* **2012**, *4*, 375.
- (27) Brodin, J. D.; Carr, J. R.; Sontz, P. A.; Tezcan, F. A. *Proc. Natl. Acad. Sci. U.S.A.* **2014**, *111*, 2897.
- (28) Salgado, E. N.; Ambroggio, X. I.; Brodin, J. D.; Lewis, R. A.; Kuhlman, B.; Tezcan, F. A. *Proc. Natl. Acad. Sci. USA* **2010**, *107*, 1827.
- (29) Radford, R. J.; Brodin, J. D.; Salgado, E. N.; Tezcan, F. A. *Coord. Chem. Rev.* **2011**, *255*, 790.
- (30) Radford, R. J.; Tezcan, F. A. *J. Am. Chem. Soc.* **2009**, *131*, 9136.
- (31) Song, W. J.; Tezcan, F. A. *Science* **2014**, *346*, 1525.
- (32) Salgado, E. N.; Faraone-Mennella, J.; Tezcan, F. A. *J. Am. Chem. Soc.* **2007**, *129*, 13374.
- (33) Brodin, J. D.; Medina-Morales, A.; Ni, T.; Salgado, E. N.; Ambroggio, X. I.; Tezcan, F. A. *J. Am. Chem. Soc.* **2010**, *132*, 8610.
- (34) Usov, I.; Mezzenga, R. *Macromolecules* **2015**, *48*, 1269.
- (35) Gittes, F.; Mickey, B.; Nettleton, J.; Howard, J. *J. Cell. Biol.* **1993**, *120*, 923.
- (36) Bloom, K. S. *Chromosoma* **2008**, *117*, 103.
- (37) Löwe, J.; Li, H.; Downing, K. H.; Nogales, E. *J. Mol. Biol.* **2001**, *313*, 1045.
- (38) Guthold, M.; Liu, W.; Sparks, E. A.; Jawerth, L. M.; Peng, L.; Falvo, M.; Superfine, R.; Hantgan, R. R.; Lord, S. T. *Cell. Biochem. Biophys.* **2007**, *49*, 165.
- (39) Trachtenberg, S. H., I. In *Microscopy: Science, Technology, Applications and Education*; Mendez-Villas, A. D., J., Ed.; Formatex Research Center: 2010; Vol. 3.
- (40) Bremer, A.; Aebi, U. *Curr. Opin. Cell Biol.* **1992**, *4*, 20.



- (41) Winn, M. D.; Ballard, C. C.; Cowtan, K. D.; Dodson, E. J.; Emsley, P.; Evans, P. R.; Keegan, R. M.; Krissinel, E. B.; Leslie, A. G. W.; McCoy, A.; McNicholas, S. J.; Murshudov, G. N.; Pannu, N. S.; Potterton, E. A.; Powell, H. R.; Read, R. J.; Vagin, A.; Wilson, K. S. *Acta Crystallogr. Sect. D-Biol. Crystallogr.* **2011**, *67*, 235.
- (42) McCoy, A. J.; Grosse-Kunstleve, R. W.; Adams, P. D.; Winn, M. D.; Storoni, L. C.; Read, R. J. *Journal of Appl. Crystallogr.* **2007**, *40*, 658.
- (43) Murshudov, G.; Vagin, A.; Dodson, E. *Acta Cryst.* **1996**, *D53*, 240.
- (44) Emsley, P.; Cowtan, K. *Acta Crystallogr. Sect. D-Biol. Crystallogr.* **2004**, *D60*, 2126.
- (45) DeLano, W. L. *The PYMOL Molecular Graphics System* (<http://www.pymol.org>), 2003.
- (46) Gipson, B.; Zeng, X.; Zhang, Z. Y.; Stahlberg, H. *J. of Struct. Biol.* **2007**, *157*, 64.

## 5. Two Dimensional Crystals Self-Assembled through Three Different Types of Biological Interactions

### 5.1 Abstract

The ability to design hybrid, 2-dimensional arrays would allow for the incorporation of the functionality of multiple types of biological molecules in an ordered material. Here, we present a DNA-protein conjugate that assembles to form crystalline, 2-dimensional materials. This is one of the first examples of an engineered, hybrid array where the interactions of all of the components are essential for the material assembly.

### 5.2 Introduction

Inspired by the ability of nature to create 0-,<sup>1</sup> 1-,<sup>2, 3</sup> and 2-dimensional<sup>4, 5</sup> ordered materials, efforts have been made to mimic the long range order of molecular assemblies such as actin filaments<sup>6, 7</sup> or S-layers.<sup>8-12</sup> These natural assemblies consist of protein building blocks where the interaction surfaces are non-covalent, but highly specific; these types of interactions are extremely difficult to design *de novo*.<sup>13</sup> The most successful approaches have involved the design of DNA-<sup>14-17</sup> or peptide-based nanomaterials,<sup>18-25</sup> as these building blocks are more readily programmable with predictable interactions. More recently, there has been a focus on designing protein-based nanomaterials with more extensive functionalities than those that use simpler building blocks.<sup>10</sup> For instance, the design of materials with symmetry to enable extendable interactions,<sup>26-30</sup> the incorporation of linker molecules,<sup>31-33</sup> or the computational design of *de novo*, symmetric protein interfaces<sup>34-36</sup> have allowed for the formation of ordered, extended protein assemblies. However, these approaches are not readily generalizable and extensive computational

design is required to engineer symmetric protein monomers to assemble into order arrays, and the success rate from computational design to ordered material is quite low. Further, the majority of the developed assemblies are made of single components, which limits the functionality of designed materials. Therefore, the design of hybrid materials is of great interest to expand the programmability and functionality of engineered, biological nanomaterials. Until recently, the only examples of hybrid DNA-protein materials were designed based on principles of DNA assembly, with proteins simply attached at specific positions within the DNA arrays.<sup>37-45</sup> Recently, the Mayo group designed a DNA-binding protein dimer from a previously monomeric protein.<sup>46</sup> As each protein bound DNA, the assembly was extended into a 1-dimensional (1D) nanowire exclusively through non-covalent interactions.<sup>47</sup> This is the first example of a material where both DNA-DNA interactions and protein-protein interactions are crucial for material assembly.

Our work, and that of others,<sup>48-51</sup> has been inspired by the use of metal ions at protein interfaces in natural protein assemblies.<sup>52</sup> Previously, we have assembled the monomeric protein *cb*<sub>562</sub> in discrete oligomeric architectures through the coordination of metal ions to engineered bis-histidine clamps on the protein surface.<sup>53, 54</sup> We have since expanded the use of metal-directed protein self-assembly (MDPSA) to create 1-, 2-, or 3-dimensional crystalline arrays.<sup>55-57</sup> Primarily, the *cb*<sub>562</sub> variant RIDC3, a 4-helix bundle protein that assembles into a C<sub>2</sub>-symmetric dimer upon the addition of Zn<sup>II</sup>, has been used as a building block to create 1D nanotubes and 2D, highly ordered, protein sheets. A second variant of RIDC3, <sup>H59/C96</sup>RIDC3 has been assembled into nanotubes of discrete, variable diameters, as described in Chapter 4.<sup>55</sup> The key properties in our previous work creating protein arrays include: (1) exploiting both high and low affinity Zn<sup>II</sup> binding sites to allow

for control over anisotropic growth by modulating solution conditions, and (2) open metal-coordination sites on surface-bound  $Zn^{II}$  ions enabling the addition of coordinating proteins. Additionally, we found that the site-specific addition of rhodamine at position C21 on the RIDC3 surface caused sheet stacking and the formation of multilayer arrays through the ability of rhodamine to dimerize at millimolar concentrations (Figure 5.1a). Here, we expand our control over the assembly of 2D biological nanomaterials and present a DNA-protein conjugate that can be assembled into highly ordered, 2D crystalline protein arrays through collaborative DNA-DNA, protein-protein, and metal-directed protein interactions.

### **5.3 Results and Discussion**

#### **5.3.1 Design of self-assembling, protein-DNA conjugates**

In order to further explore the assembly properties of these metal-directed, crystalline, 2D protein arrays, we conjugated complementary DNA strands site-specifically at the reactive cys on the protein  $^{21}C$ RIDC3 (Figure 5.1b). DNA strands were ordered with a 6-carbon linker between the end of the DNA strand and a 5' amide that could be modified for attachment as previously described.<sup>58</sup> The 6-carbon linker was selected to avoid steric clashes between the protein and the DNA surface; long linkers would be more flexible and make the formation of a crystalline material more difficult. We chose DNA strands with low melting temperatures (Figure 5.1c) with the expectation that the DNA interactions would act in a cooperative fashion with metal-protein interactions to form ordered materials. The DNA sequences are shown in Figure 1c, where the 10mer sequence has a predicted  $T_m$  of 7.1 °C and the 12mer has a predicted  $T_m$  of 24.5 °C. The DNA was

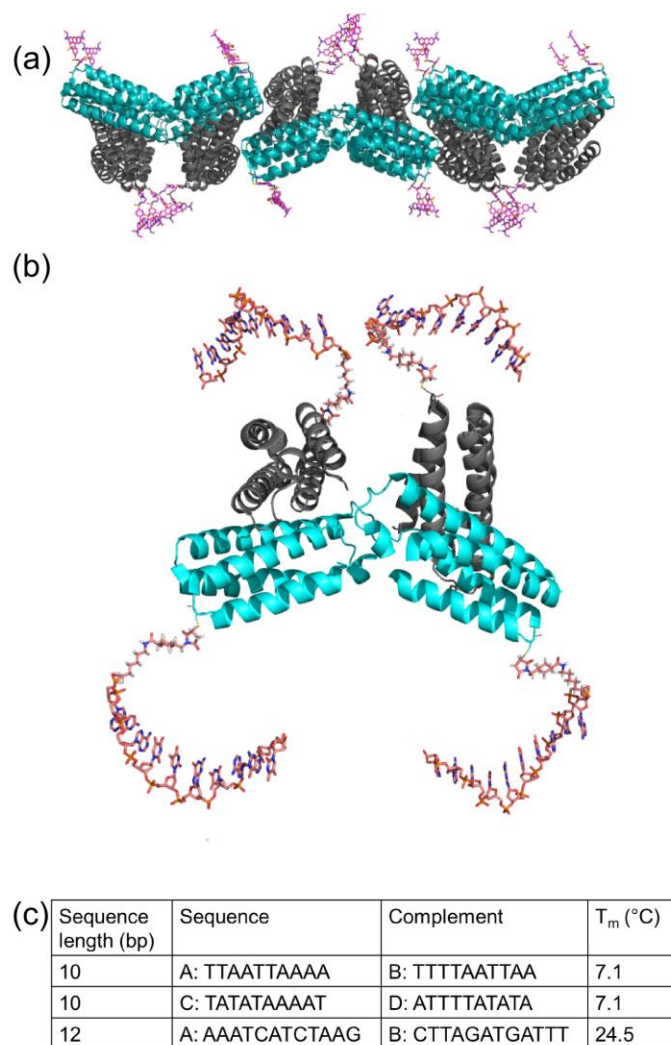


Figure 5.1: Design of protein-DNA conjugate materials. (a) Model of RIDC3 2D arrays with the addition of rhodamine at cys21. (b) Predicted model of assembly for incorporation of DNA-protein conjugate. (c) Sequences and melting temperatures of incorporated DNA.

conjugated to the protein as previously described, and each DNA-protein conjugate was purified separately. The presence of pure starting materials was verified by UV-vis, gel electrophoresis, and mass spectrometry (See Materials and Methods, Figure 5.12).

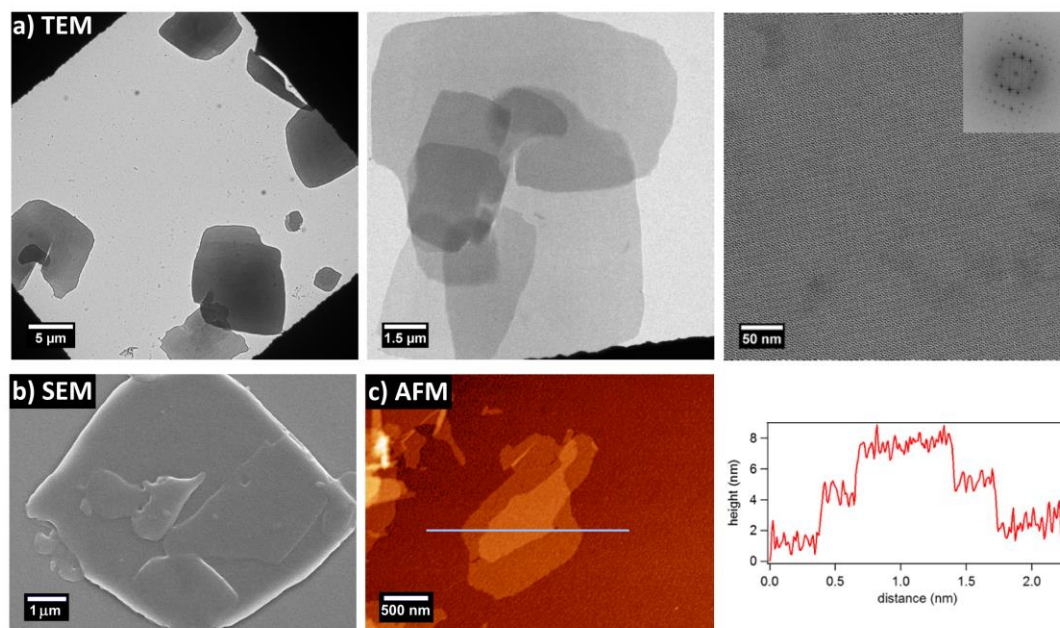


Figure 5.2: Analysis of DNA-protein 2D arrays. (a) TEM images showing the negatively stained material, including the calculated fft. (b) SEM analysis confirms the presence of nanomaterials. (c) AFM analysis to measure the height of the sheets. A single layer of sheets measures approximately 3 nm in height, which corresponds to a single protein layer thickness.

### 5.3.2 Zinc-directed self-assembly in solution

A variety of solution conditions were tested, including those that enabled the formation of RIDC3 materials, without observing the formation of ordered DNA-protein hybrid materials. However, we found that when 25 μM  $^{21}\text{C}$ RIDC3-10A and 25 μM  $^{21}\text{C}$ RIDC3-10B were combined in 20 mM 2-(N-morpholine)ethanesulfonic acid (MES) buffer at pH 4.75 with 4 equivalents of  $\text{Zn}^{\text{II}}$ , a precipitate forms within 10 min at 4 °C. When the precipitate was observed by transmission electron microscopy, we found that highly ordered, 2D arrays formed in roughly square shapes with dimensions of up to 5 μm per side. The presence of these 2D sheets was confirmed by scanning electron microscopy (SEM). The material was also determined to be single layer, one unit cell, thick by atomic

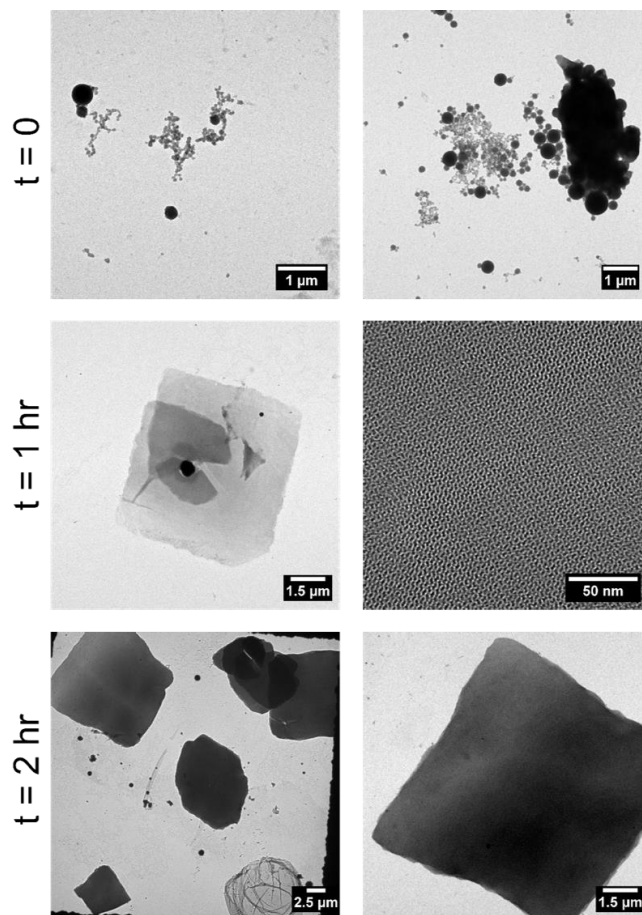


Figure 5.3: Analysis of material formation immediately after the addition of  $\text{Zn}^{\text{II}}$  ( $t = 0$ , where the material at time  $t = 0$  was deposited on the grid within 5 minutes of  $\text{Zn}^{\text{II}}$  addition), after 1 hr and 2 hr of incubation at  $4\text{ }^{\circ}\text{C}$ . No further morphological changes were observed after 2 hr.

force microscopy (AFM), where a height of approximately 3 nm, corresponding to a single protein layer, was measured. As shown in Figure 5.2, some areas appear to be multi-layered, but we believe that this is more likely the result of stacking upon deposition on a solid support as opposed to growth in the  $z$ -dimension. Based on TEM imaging and electron diffraction analysis, there does not appear to be order in the  $z$ -direction.

Grids were prepared for analysis by TEM immediately after metal was added to the  $^{21}\text{C}$ RIDC3-10A/ $^{21}\text{C}$ RIDC3-10B solution and at various time points to observe the rate of

material formation in solution (Figure 5.3). We had previously observed that, for RIDC3 sheets, precipitate formed within a few hours, but ordered arrays were not detected by TEM for approximately one week. In this case, only disordered aggregate was observed when TEM grids were prepared within 5 min of the addition of metal to the DNA-protein solution. However, within one hour, crystalline arrays were present. At 2 hr after metal addition, the sheets appeared to be more prevalent and larger. No further morphological changes were observed after overnight incubation at 4 °C. Over the same period of time, the precipitate sediments to the bottom of the solution and TEM analysis indicates that there is little disordered aggregate present. The supernatant can be removed after centrifuging the sample for 1 min at 13,300 rpm, and the material redissolved upon the addition of the chelator, ethylenediaminetetraacetic acid (EDTA). The re-dissolved material was analyzed to confirm the presence of DNA-protein conjugate only as the building block for array formation (Figure 5.13, See Materials and Methods).

TEM images of samples negatively stained with 1% uranyl acetate were analyzed in order to better understand the underlying structure of the hybrid material. Images were obtained at approximately 85,000x magnification from which Fourier transforms were computed to obtain the lattice parameters, which are distinct from those of the RIDC3 protein-only material (Figure 5.4). From this, it was inferred that the DNA-protein conjugates are forming a new material where the protein-protein and protein-metal interactions differ from those observed previously. When comparing the conditions at which these distinct materials can be formed, DNA-protein conjugates only form ordered material at pH 4.75, a condition at which no material formation is observed with RIDC3 alone. In fact, at pH 5.5, where RIDC3 materials form robustly, only disordered aggregate



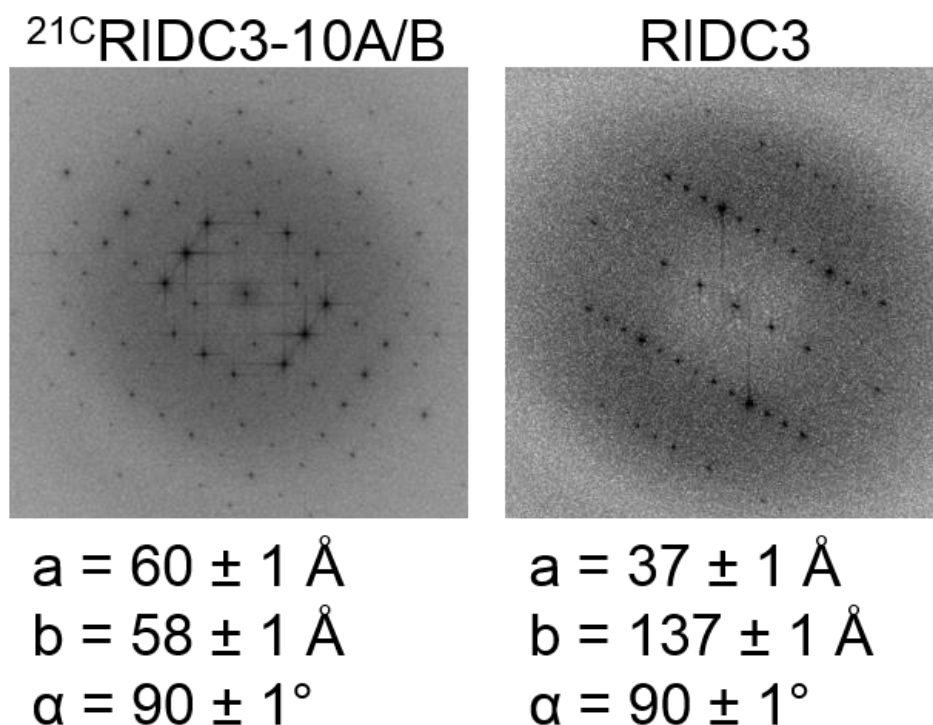


Figure 5.4: Analysis of the calculated fft and lattice parameters of DNA-protein material ( $^{21}\text{C}$ RIDC3-10A/B) and protein only material (RIDC3).

is observed via TEM with  $^{21}\text{C}$ RIDC3-10A/B. RIDC3 materials contain a high affinity metal binding site that forms a dimeric interface through metal coordination at a tris-his motif. The pKa of his is approximately 6, and is therefore expected to be protonated so it is not able to bind metal at the low pH conditions in which we are forming the DNA-protein hybrid material. We hypothesize that the high affinity  $\text{Zn}^{\text{II}}$  binding sites are not compatible with the protein orientation needed for DNA hybridization.

### 5.3.3 Analysis of DNA interactions

After heating  $^{21}\text{C}$ RIDC3-10A/B assemblies to 45 °C for 1 hr, no precipitate was visible, nor could any arrays be observed by TEM. We attribute this temperature dependence to DNA melting, as RIDC3 materials were stable at temperatures as high as

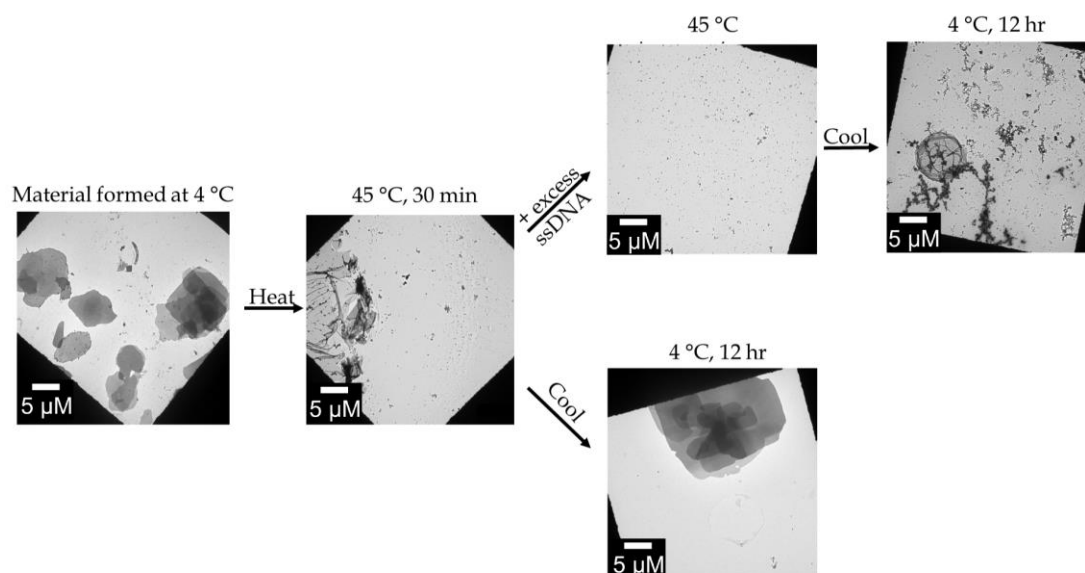


Figure 5.5: Temperature effects on  $^{21}\text{C}$ RIDC3-10A/B material. The material is initially formed at 4 °C. After heating to 45 °C, no ordered material is observed. If the solution is then cooled overnight, ordered materials are again observed. If complementary ssDNA is added to the solution while the material has been dissolved, no materials are observed even upon cooling. If ssDNA is added to the solution after ordered arrays have formed, no morphological changes are observed (not shown).

90 °C. The sample was then cooled to 4 °C and incubated overnight, after which crystalline 2D arrays were again observed by TEM (Figure 5.5). An excess of complementary single-stranded DNA was added to a second sample at 45 °C, when the material had dissolved. No ordered arrays were observed even after overnight incubation at 4 °C. If the same amount of single-stranded, complementary DNA was added to preformed sheets, no changes in the morphology or crystallinity of the material was observed, indicating the presence of excess complementary DNA prohibits 2D crystal formation. Furthermore, when 4 equiv. of  $\text{Zn}^{\text{II}}$  were added to a solution containing only  $^{21}\text{C}$ RIDC3-10A or  $^{21}\text{C}$ RIDC3-10B, no material formation was observed. Taken together, these observations

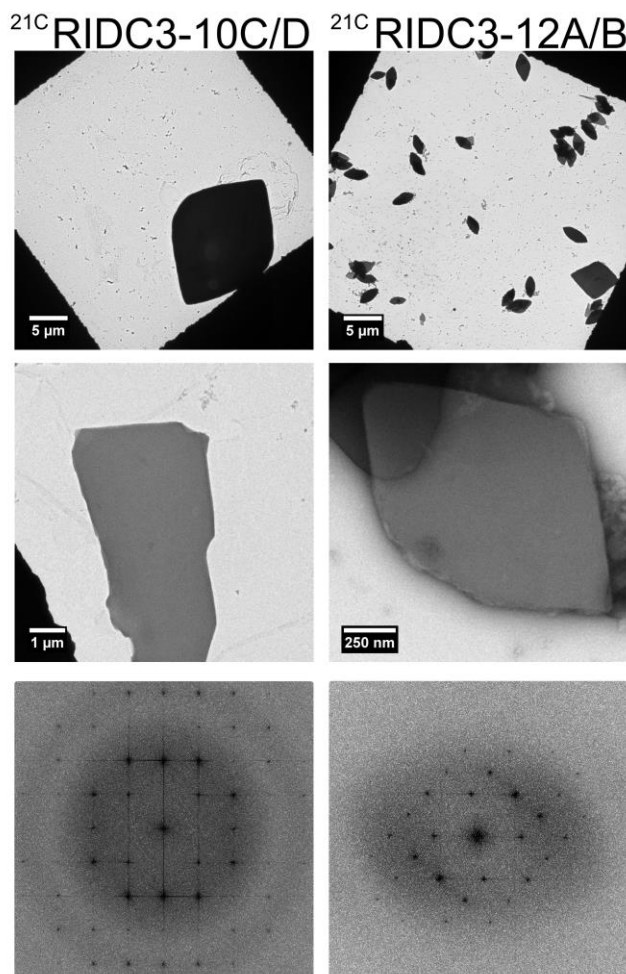


Figure 5.6: Two additional DNA-sequences were conjugated to  $^{21}\text{C}$ RIDC3 and the ability of the DNA-protein conjugate to form ordered materials was studied. The 10C/D sequence has the same length and A/T composition as the sequence previously described, and no changes in material formation were observed. 12A/B has a higher G/C content and a longer sequence, and material was observed to form much more robustly at 25 °C than at 4 °C.

imply that duplex formation between complementary DNA strands is crucial to material formation.

Two other DNA sequences were conjugated to  $^{21}\text{C}$ RIDC3 as previously described (Figure 5.6). 10C/D is a 10-base pair DNA sequence with the same A/T content as 10A/B, and therefore has the same expected size and the same predicted melting temperature.

Table 5.1: Comparison of formation temperature and lattice parameters of various DNA-protein conjugates.

DNA sequence	Predicted $T_m$ (°C)	Temp. for material formation (°C)	Lattice parameters
10A/B	7.1	4	$a = 60 \pm 1 \text{ \AA}$ , $b = 58 \pm 1 \text{ \AA}$ $\alpha = 90 \pm 1^\circ$
10C/D	7.1	4	$a = 59 \pm 1 \text{ \AA}$ , $b = 56 \pm 1 \text{ \AA}$ $\alpha = 93 \pm 1^\circ$
12A/B	24.5	25	$a = 65 \pm 1 \text{ \AA}$ , $b = 55 \pm 1 \text{ \AA}$ $\alpha = 90 \pm 0.5^\circ$

12A/B is a 12-base pair DNA sequence with a much higher predicted melting temperature, 24.5 °C compared to 7.1 °C for 10A/B and 10C/D (Figure 5.1c).  $^{21}\text{C}$ RIDC3-10C/D was found to form materials under identical conditions to  $^{21}\text{C}$ RIDC3-10A/B, and the lattice parameters of the observed materials were identical for the two assemblies (Table 5.1: Comparison of formation temperature and lattice parameters of various DNA-protein conjugates.

DNA sequence	Predicted $T_m$ (°C)	Temp. for material formation (°C)	Lattice parameters
10A/B	7.1	4	$a = 60 \pm 1 \text{ \AA}$ , $b = 58 \pm 1 \text{ \AA}$ $\alpha = 90 \pm 1^\circ$
10C/D	7.1	4	$a = 59 \pm 1 \text{ \AA}$ , $b = 56 \pm 1 \text{ \AA}$ $\alpha = 93 \pm 1^\circ$
12A/B	24.5	25	$a = 65 \pm 1 \text{ \AA}$ , $b = 55 \pm 1 \text{ \AA}$ $\alpha = 90 \pm 0.5^\circ$

). When samples of  $^{21}\text{C}$ RIDC3-12A/B were incubated at 4 °C, some ordered material was observed, but material formation was much more robust at 25 °C based on the density of ordered arrays and presence of disordered aggregate on the TEM grids, although the remainder of the solution conditions were identical to those used for  $^{21}\text{C}$ RIDC3-10A/B

(20 mM MES buffer at pH 4.75 with 4 equiv. ZnII). Additionally, the lattice parameters for 21CRIDC3-12A/B were calculated to be slightly larger than those of the 10 base-pair DNA sequences. It is expected that the longer DNA sequence would correspond to an increase in the unit cell dimension of approximately 7 Å, assuming the DNA interaction is directed along the x- or y-axis.

Further analyses of the necessity of complementary DNA interactions were designed by varying the ratio of 10A:10B present in solution.  $^{21}\text{C}$ RIDC3-10A/B samples were prepared containing various ratios of DNA strands while maintaining constant protein and  $\text{Zn}^{\text{II}}$  concentrations (50 and 200  $\mu\text{M}$ , respectively) (See materials and methods). Samples

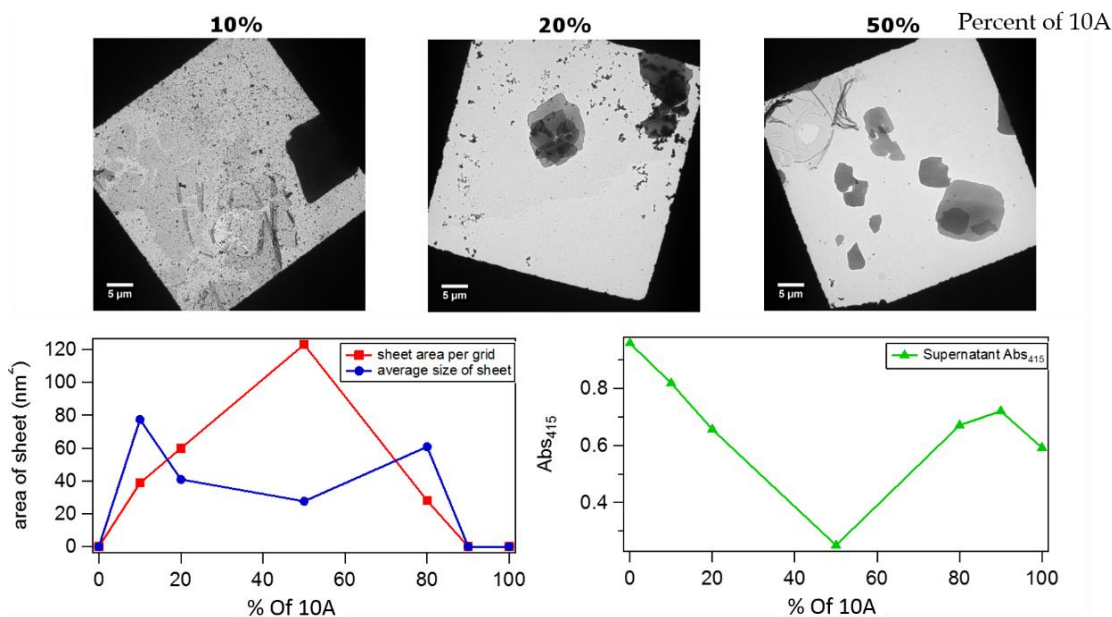


Figure 5.7: Samples were prepared where the ratio of  $^{21}\text{C}$ RIDC3-10A: $^{21}\text{C}$ RIDC3-10B was varied. The samples were analyzed by TEM, and the footprint of sheet coverage was measured for at least 100 grid squares for each sample. The total sheet area was highest at the 1:1 ratio of the DNA sequences, although the average sheet size was smaller, indicating faster nucleation at the 1:1 ratio. The amount of protein in the supernatant was quantified by measuring the absorbance at 415 nm, and the least protein was left in solution at the 1:1 DNA ratio.

contained 0, 5, 10, 25, 40, 45, or 50  $\mu\text{M}$   $^{21}\text{C}$ RIDC3-10A and 50, 45, 40, 25, 10, 5, or 0  $\mu\text{M}$   $^{21}\text{C}$ RIDC3-10B. TEM grids were prepared with each sample, and images were collected at 1700x magnification where entire grid squares could be observed (Figure 5.7, Figure 5.14). The footprint of material was measured for each grid square, and the total amount of ordered material was quantified. It was found that the largest amount of material was observed when the complementary DNA strands were present at a 1:1 ratio; when either strand was absent, no crystals were observed. The average sheet size was smaller when the DNA strands were present in equimolar amounts, indicating that sheet nucleation occurs fastest at these conditions. The absorbance at 415 nm of the supernatant was also measured for each sample to determine the remainder of protein in the supernatant; it is not possible to say whether all of the precipitated protein is present in ordered material, but based on our TEM observations, little non-specific aggregate is observed in the 1:1 sample. Overall, the smallest amount of protein was left in solution in the sample where the DNA strands were present in equimolar amounts, further indicating that sheet formation is dependent on DNA-duplex formation in addition to metal-coordination.

Finally, in order to more directly observe the presence of duplex DNA, ethidium bromide (EtBr), a molecule that fluoresces upon intercalation into double-stranded DNA, was used to stain the hybrid material. EtBr was added to a solution of preformed DNA-protein arrays, and the samples were then imaged by confocal microscopy, obtaining both fluorescence and bright field images. When the images are overlaid, it is apparent that the observed fluorescence overlays with the observed arrays. When the experiment was repeated with RIDC3 sheets, no fluorescence was observed to associate with the arrays (Figure 5.8). The fluorescence emission of the arrays was quantified after incubation with

EtBr using a fluorescent plate reader. As the temperature was raised, the fluorescence signal decreased as the DNA duplex melted, which confirms our earlier observations about heat treatment of the material.

### 5.3.4 Metal-binding interactions

#### 5.3.4.1 Determining the amino acids involved in material formation

Previously, we have confirmed the necessity of  $Zn^{II}$  ions in material formation by observing that no precipitate forms in the absence of  $Zn^{II}$ , and by observing the dissolution

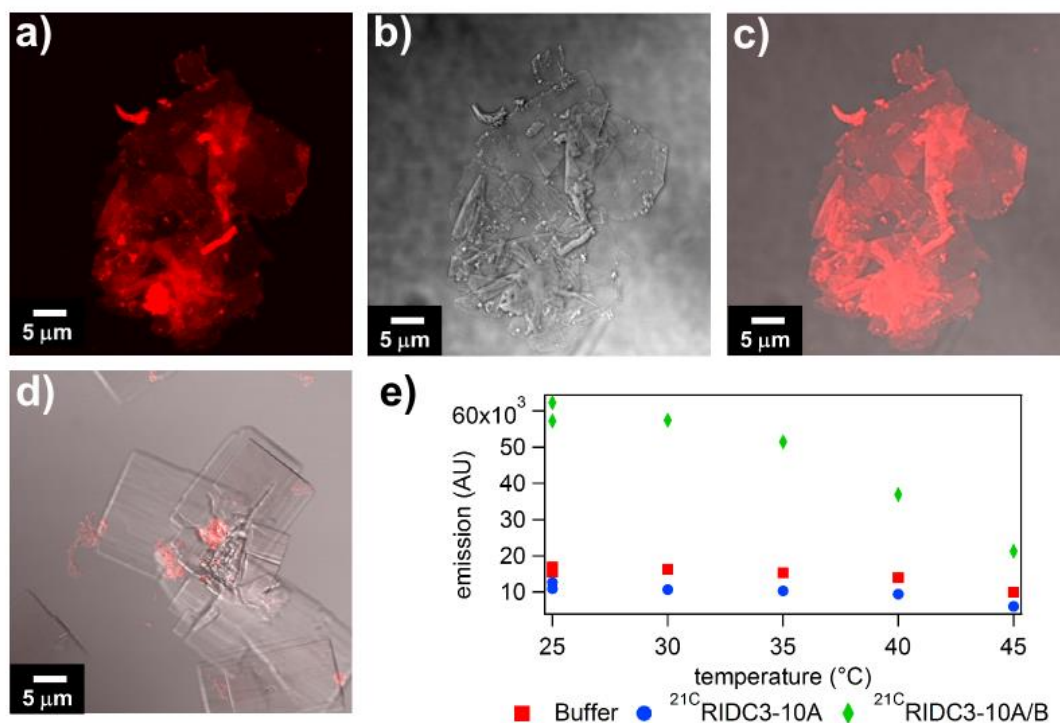


Figure 5.8: Fluorescence analysis of DNA-protein arrays. EtBr was used as a molecule that fluoresces upon intercalation into double stranded DNA. (a) Fluorescence image of DNA-protein material. (b) Bright field image of DNA-protein material. (c) Overlay of fluorescence and bright field images show that the fluorescence overlays with the edges of the sheets. (d) RIDC3 sheets do not show the same fluorescence staining. (e) Bulk fluorescence of <sup>21</sup>C RIDC3-10A/B sheets and <sup>21</sup>C RIDC3-10A. As the temperature is increased, the fluorescence decreases.

of the material upon the addition of the chelator EDTA. In order to determine the stoichiometry of metal binding, we used 4-(2-Pyridylazo)resorcinol (PAR), a fluorescent molecule that can be used to quantify  $Zn^{II}$  in solution. After confirming the formation of ordered materials by TEM, the solution was centrifuged, the supernatant was removed, and the protein assemblies were washed. The assemblies were then dissolved in 20 mM 3-(N-morpholine)propanesulfonic acid (MOPs) buffer and the protein concentration was determined by measuring the absorbance at 415 nm ( $\epsilon_{415} = 148,000$ ). The concentration of  $Zn^{II}$  ions in solution was then measured using PAR (see Materials and Methods), and it was determined that there were between 1 and 1.25 equiv. of  $Zn^{II}$  per monomer.

As discussed above, we believe the metal-binding interactions involved in the formation of the protein-DNA materials to be distinct from those involved in the RIDC3 assemblies, and that the high affinity metal-binding his motifs that form the dimeric interface in RIDC3 are not involved in the DNA-protein hybrid material formation. In order to confirm this hypothesis, we mutated the His residues at positions 73 and 77, which form a bis-his clamp in the stable dimeric interface of RIDC3. As suspected, the same materials were obtained with  $^{21C73A}$ RIDC3-10A/B and  $^{21C77A}$ RIDC3-10A/B (or combinations thereof), confirming our hypothesis that the bis-his clamps are not relevant in the formation of the DNA-protein material (Figure 5.9). At pH values above 5, the deprotonation and tight metal binding of the his binding motifs likely prohibit formation of the metal binding interactions necessary for crystalline material formation, leading to the formation of disordered aggregate. Surprisingly, the protein variant  $^{21C63A}$ RIDC3-10A/B was unable to form ordered materials at any conditions, indicating that H63 may be



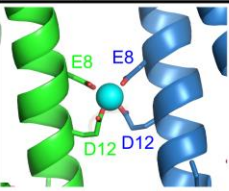
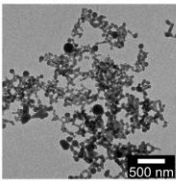
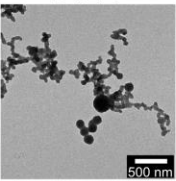
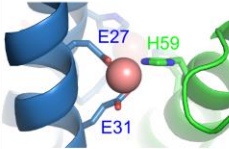
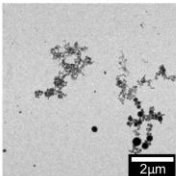
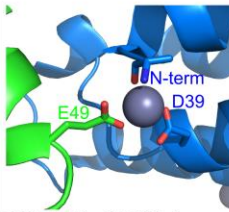
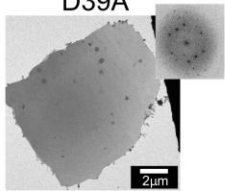
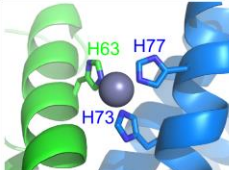
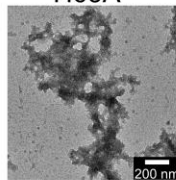
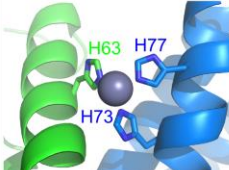
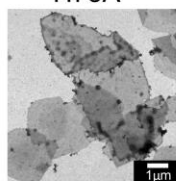
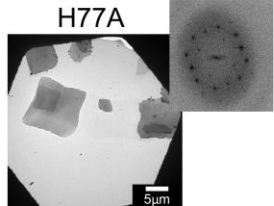
Residue	Binding motif	TEM Results
Glu8 Asp12	 PDB ID: 5BU7	E8A      D12A  500 nm  500 nm
Glu27 Glu31	 PDB ID: 5BU7	E27A  2µm
Asp39	 PDB ID: 3TOM	D39A  2µm
His63	 PDB ID: 3TOM	H63A  200 nm
His73 His77	 PDB ID: 3TOM	H73A      H77A  1µm  5µm

Figure 5.9: Analysis of the ability to form hybrid, ordered materials with protein mutants.

involved in directing array formation, although it is not yet possible to determine if this is a metal-binding interaction.

Crystal structures that had previously been obtained of material-forming RIDC3 variants were examined to determine which amino acids were often found to form metal

contacts, in addition to the his residues that are consistently found at the dimeric interface. At pH 4.75, the side chains of acidic amino acid side chains (i.e., glutamic or aspartic acid) are most likely to be involved in metal binding due to their low pKa values. We therefore made  $^{21}\text{C}$ RIDC3 variants containing the following mutations: E8A, D12A, E27A, and D39A. We found that  $^{8\text{A}21}\text{C}$ RIDC3-10A/B,  $^{12\text{A}21}\text{C}$ RIDC3-10A/B, and  $^{27\text{A}21}\text{C}$ RIDC3-10A/B were all unable to form ordered materials, and only nonspecific aggregates were observed.  $^{21}\text{C}^{39\text{A}}$ RIDC3-10A/B formed crystalline materials with the same lattice parameters as  $^{21}\text{C}$ RIDC3-10A/B, leading us to conclude that residues D39, H73, and H77 are not involved in interactions that stabilize the formation of ordered DNA-protein arrays, but that E8, D12, E27, and H63 may be involved in material formation, either through direct metal-binding, or by stabilizing protein-protein interactions.

### 5.3.5 Structural studies and modeling the protein-assembly

The assembly process of DNA-protein hybrid materials must be cooperative—when any single interaction outcompetes the others, i.e. the pH is raised and the metal-binding affinity of the protein is higher, or DNA sequences with a more stable melting temperature are incorporated, the formation of ordered materials is not observed. This material is able to mimic nature in that it forms due to contributions from a combination of fairly weak interactions. This combination of weak interactions may enable the material to organize into crystalline materials without being stuck in kinetic traps.

The protein crystal structure of metal-free  $^{21}\text{C}^{73\text{A}}$ RIDC3 was recently determined (Figure 5.10). Surprisingly, the same helices were observed to be forming a metal-free dimeric interface, and H73 and H77 were not in a position to make metal-binding contacts with other proteins to form an extended material. We believe it is likely that the same, or a

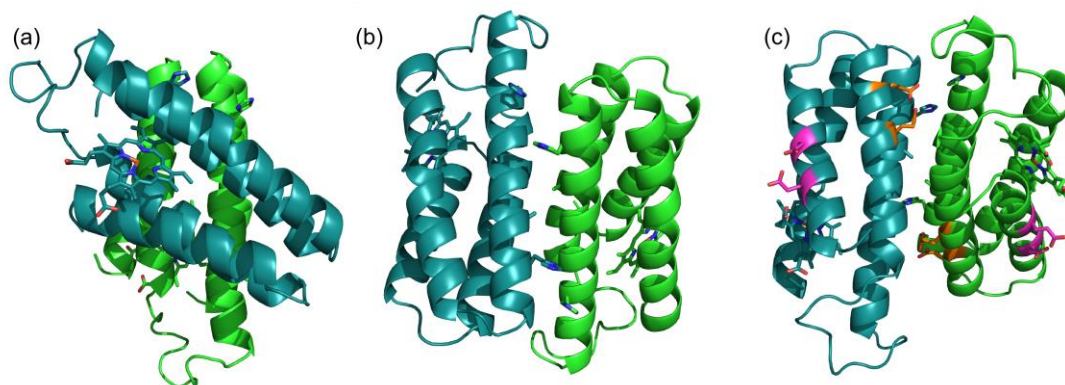


Figure 5.10: Crystal structure of metal free  $^{21C73A}$ RIDC3. (a) and (b) show alternate views of the metal-free dimeric interface which may be similar to what is underlying the structure of the  $^{21C}$ RIDC3-10A/B materials. (c) Amino acids which may be involved in metal binding for the formation of  $^{21C}$ RIDC3-10A/B are highlighted—E8 and D12 are in purple, and E27 and E31 are in orange.

similar, dimer underlies the structure of the DNA-protein conjugate material, as we have concluded that H73 and H77 have no bound metal atoms. We have also previously noted that the dimeric interface of RIDC3 was designed with small, hydrophobic residues in the center of the interface to help stabilize the dimer formation, in addition to promoting specific dimer formation through the incorporation of polar residues at the periphery. Based on the work previously discussed, it is likely that interactions to extend the protein material are forming through either a bidentate E8/D12 metal-binding motif, and/or a bidentate E27/E31 metal-binding motif. These residues have previously been observed to be important in 2D material formation of RIDC3 variants. Further, our solution conditions are compatible with metal-binding primarily by acidic amino acid residues, and mutagenesis experiments indicate that these amino acids may form essential interactions during crystal formation. In order to further explore the structural basis for material formation, we obtained images using cryoEM conditions at the highest possible resolution in addition to

electron diffraction patterns from glucose embedded arrays. The cryoEM images were processed using 2dx and, at best, have a resolution of approximately 8 Å. The electron diffraction patterns exhibit lattice spots are observed to approximately 3 Å; images were obtained at 0 and 50° tilt, but data processing is still ongoing (Figure 5.11).

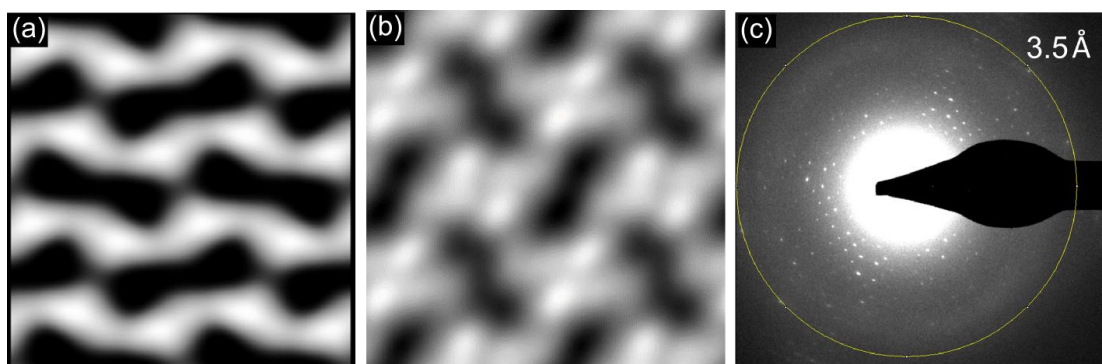


Figure 5.11: (a) Electron density map of negatively stained  $^{21}\text{C}$ RIDC3-10A/B materials. (b) Electron density map of  $^{21}\text{C}$ RIDC3-10A/B materials obtained using cryoEM conditions. The protein density is shown in white in both maps. We attribute the addition density observed in (b) to the presence of DNA, which is not observed by negative stain. (c) Electron diffraction of  $^{21}\text{C}$ RIDC3-10A/B.

#### 5.4 Conclusions

In this study, we have described the design and formation of a DNA-protein hybrid where the DNA-DNA, protein-protein, and protein-metal interactions all contribute to the formation of crystalline, 2D arrays. We have also described how all of these interactions must work in a concerted manner to form ordered materials, and that disordered aggregate forms if any one interaction is too strong, prohibiting the formation of the others in an ordered manner. The formation of this type of material is reminiscent of the elegant natural assemblies where protein and nucleic acids interactions combine to produce large molecular machines, such as the ribosome.<sup>59, 60</sup> Moving forward, we believe that this

strategy of metal-directed assembly allows for the design of hybrid-materials comprised of multiple functionalities without intensive computational redesign.

## **5.5 Materials and Methods**

### **5.5.1 General considerations**

Unless otherwise stated, reagents and solvents were purchased from Fisher Scientific and used without further purification. Oligomers were ordered from Integrated DNA Technologies or Eurofins Genomics with a 5' six carbon amino linker and used without further purification.

### **5.5.2 Site-directed mutagenesis and protein expression/purification**

The D8A, D12A, E27A, D39A, H63A, H73A, and H77A amino acid substitutions were introduced into the pET-RIDC3 expression vector using QuikChange (Stratagene) site-directed mutagenesis and primers synthesized by Integrated DNA technologies. The D21C mutation had previously been introduced into the pET-RIDC3 expression vector, and all of these plasmids were transformed into chemically competent *E. coli* cells and expressed as previously reported. (Salgado, JACS 2007)

### **5.5.3 Conjugation of DNA to protein**

DNA was ordered from Integrated DNA Technology or Eurofins Genomics with a 6-carbon, 5' linker with a 5' amide, and used without further purification. The DNA was dissolved in water to a final concentration of 1 mM. 7.5 mg sulfosuccinimidyl-4-[N-maleimidomethyl]cyclohexane-1-carboxylate (sulfo-SMCC, 172 mM) was dissolved in 100  $\mu$ L dimethylformamide (DMF). 400  $\mu$ L of the DNA stock solution was combined with the sulfo-SMCC solution and 500  $\mu$ L of conjugation buffer (CB, 16.7 mM potassium phosphate monobasic, 83.3 mM potassium phosphate dibasic, 150 mM sodium chloride at pH

7.3) was added and the solution was mixed by vortexing. The solution was incubated at 35 °C in the dark for 1.5-2 hr. The maleimide-functionalized DNA was purified by HPLC (Buffer A: 5 mM sodium acetate, pH 5.0; Buffer B: acetonitrile) and eluted from the column in 30% buffer B. The desired fraction was collected, frozen, and lyophilized to dryness overnight.

Approximately 20 equiv. of dithiothreitol (DTT) were added to 1.5 mL of 0.7 mM <sup>21</sup>C-RIDC3 (or variant) and incubated at room temperature for 30 min to fully reduce the protein. An Econo-Pac 10DG column (BioRad) was used to remove excess DTT and the protein was eluted in 2 mL CB. The lyophilized, dry DNA was re-dissolved in 1 mL CB and added to the protein, which was present in large excess. The conjugation reaction proceeded for 12 hr at 4 °C in the dark.

The reaction mixture was loaded onto an Econo-Pac 10DG column (BioRad) and eluted in 10 mM sodium phosphate buffer, pH 8.0. The protein-DNA conjugate was purified on a BioRad Biologic Duo Flow FPLC with a Bio-Scale Mini Macro-Prep High Q Cartridge (BioRad). 10 mM sodium phosphate, pH 8.0 was used as buffer A, and 10 mM sodium phosphate with 1 M sodium chloride, pH 8.0 was used as buffer B. Unlabeled protein eluted at approximately 20% buffer B, protein-DNA conjugate eluted at approximately 50% buffer B, and free DNA eluted at approximately 65% buffer B. Fractions of DNA-protein conjugate were combined, concentrated, and stored in deionized water at -80 °C.

### 5.5.4 Characterization of DNA-protein conjugates

Electrospray ionization mass spectrometry to verify the mass of the protein-DNA conjugate was performed at the Molecular Mass Spectrometry Facility at UC San Diego.

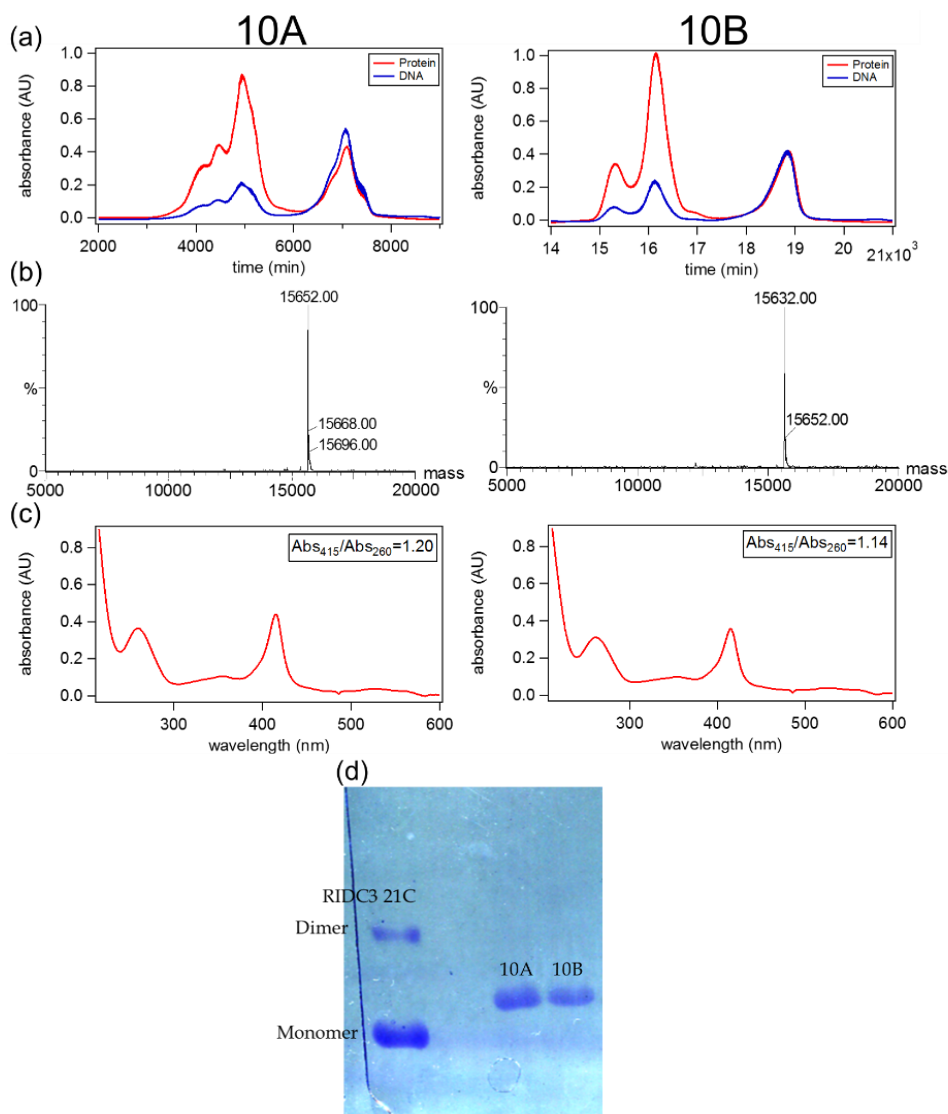


Figure 5.12: Analysis of DNA-protein conjugate. (a) FPLC trace of DNA-protein conjugate. (b) ESI-MS of DNA-protein conjugate. <sup>21</sup>C RIDC3-10A: Expected 15655, observed 15652. <sup>21</sup>C RIDC3-10B: Expected: 15637, observed: 15632. (c) UV-vis spectra showing the absorbance at 415 nm corresponding to the protein and 260 nm corresponding to the DNA. (d) SDS-PAGE gel showing the increase in protein mass upon DNA conjugation to protein.

Samples were diluted to a concentration of 0.1-1.0 mg/mL using a solution of 50% methanol in water. Gel electrophoresis was used to observe the shift in mass upon DNA-conjugation, and ensure the purity of each sample. (Figure 5.12)

The Soret band of the protein heme is at 415 nm with an extinction coefficient of  $\epsilon_{415} = 148,000$ . The ratio of the protein absorbance at 415 nm to the DNA absorbance at 260 nm was determined to be approximately 1.15 for pure DNA-conjugate.

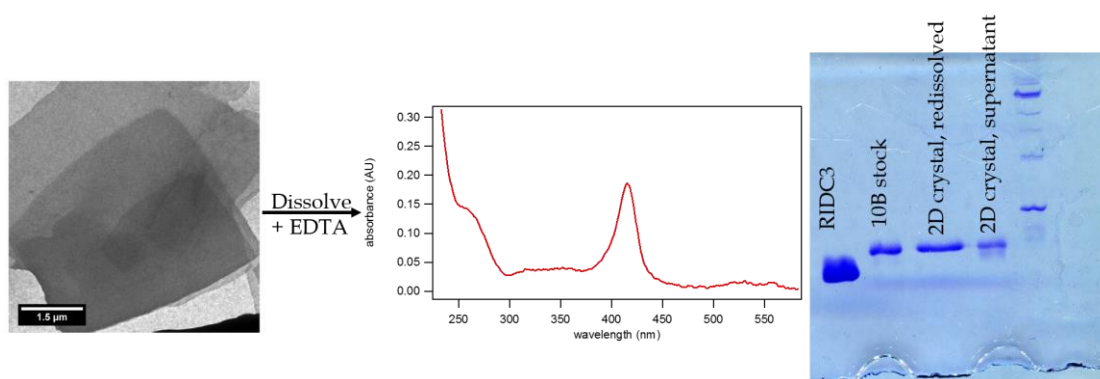


Figure 5.13: Analysis of a dissolved crystal. The UV-vis ratio of  $Abs_{415}:Abs_{260}$  was as expected, and SDS-PAGE gel electrophoresis confirmed the presence of only DNA-protein conjugate.

### 5.5.5 Preparation of $^{21}C$ RIDC3-DNA nanostructures

Samples were prepared with  $25 \mu M$   $^{21}C$ RIDC3-10A and  $25 \mu M$   $^{21}C$ RIDC3-10B (or the desired protein-DNA combination) in 20 mM 2-(N-morpholine)ethanesulfonic acid (MES) buffer at pH 4.75, for a total protein concentration of  $50 \mu M$ . A 5 mM  $ZnCl_2$  stock was used to add 4 equiv. of  $Zn^{II}$  to the solution. The samples were prepared at room temperature, and immediately moved to storage at  $4 \text{ }^\circ C$ , and the solution became opaque



within 10 min. When using the 12A/B DNA sequences, the procedures were identical but the solution was left to incubate at room temperature. Over an incubation period of 12 hr, protein material settled to the bottom of the solution, but could be easily re-suspended by shaking or pipetting.

## **5.5.6 Imaging of nanostructures**

### **5.5.6.1 Negatively stained samples for transmission electron microscopy (TEM)**

A 3  $\mu\text{L}$  solution of sample was pipetted onto carbon-coated Cu grids (Electron Microscopy Sciences, Carbon Film on 400 square mesh Copper Grids) that had been glow discharged within 30 min of sample addition. The grids were blotted with filter paper to remove excess liquid, washed by submerging in a 250  $\mu\text{L}$  drop of water, blotted to again remove excess liquid, and stained by the addition of 5  $\mu\text{L}$  of 1% uranyl acetate (UA) in water to the grid. After a 5 min incubation, the grid was blotted to remove excess UA solution, and a second aliquot of UA was added. After the second 5 min incubation, the grid was blotted dry using filter paper. Grids were imaged in a 200 keV FEI Sphera transmission electron microscope equipped with a  $\text{LaB}_6$  filament. Images were recorded on a Gatan 2K<sup>2</sup> CCD camera. Objective lens underfocus settings ranged from 250 nm to 2  $\mu\text{m}$ .

### **5.5.6.2 CryoEM**

A 3  $\mu\text{L}$  sample of protein solution was deposited onto either a freshly glow-discharged, homemade lacey carbon grid or Quantifoil grid (Electron Microscopy Sciences, Quantifoil R2/4 Holey Carbon on 200 Mesh Copper). The grid was blotted from behind for 8 s using filter paper, and was then plunged into liquid ethane slush. The grids

were stored in liquid nitrogen until transfer into a precooled FEI Polara multispecimen holder. The grids were analyzed in a 300 keV FEI Polara electron microscope and images were recorded on a Gatan direct detection device with a pixel field size of 3696 x 3838 pixels at a nominal magnification of 95,000x for a calibrated pixel size of 2.2 Å. Low dose settings were used with a spot size of 8 and a dose rate of 3.983 e<sup>-</sup>/Å<sup>2</sup>\*s with dose fractionation settings and a total exposure time of 4s. Objective-lens underfocus settings ranged from 0.5 μm to 3 μm.

### **5.5.6.3 Electron Diffraction of Glucose-Embedded Crystals**

2-dimensional arrays were prepared for electron diffraction analysis by mixing 3 μL of protein solution with 3 μL of 10% glucose. This mixture was added to a recently glow discharged, carbon-coated Cu grid (Electron Microscopy Sciences, Carbon Film on 400 square mesh Copper Grids) and incubated for 10 min. The grid was then blotted to dryness, loaded into a cryotransfer holder, and cooled to -180 °C. Electron diffraction analysis was performed in a 200 keV FEI Sphera microscope using low dose conditions with a spot size of 10 and a 20 s exposure time. Images were collected on a Gatan 4K<sup>2</sup> CCD camera.

### **5.5.6.4 Scanning Electron Microscopy (SEM)**

To prepare samples for SEM, protein-DNA arrays were pelleted by centrifuging at 13,300 rpm for 10 min. The buffer was removed, and the sheets were re-suspended in water. The samples were coated using an Emitech Iridium Sputter Coater. Analysis was performed using an FEI UHR SFEG SEM with an accelerating voltage of 5 kV and a spot size of 2.

### **5.5.6.5 Atomic Force Microscopy (AFM)**

To prepare samples for analysis by AFM, 10  $\mu\text{L}$  of a sheet-containing solution was centrifuged, the supernatant was removed, and the sheets were re-suspended in 10  $\mu\text{L}$  water. The sample was then deposited on freshly cleaved mica (Ted Pella), and incubated for 10 min. At that time, it was dried using a stream of nitrogen without washing.

Analysis was performed using a Veeco Scanning Probe Microscope using Silicon AFM probes with aluminum reflex coating and a resonance frequency of 300 kHz (Ted Pella, Tap300Al-G). Images were obtained at a field size consisting of 512 x 512 pixels. Image analysis was done using WSxM 5.0.<sup>61</sup>

### **5.5.7 Testing for DNA-hybridization**

#### **5.5.7.1 Changing the ratio of DNA strands**

In order to determine the necessity of the presence of complementary DNA-strands conjugated to proteins, a series of samples were set-up where the ratio of  $^{21}\text{C}$ RIDC3-10A: $^{21}\text{C}$ RIDC3-10B was varied. Although the total protein concentration was maintained at 50  $\mu\text{M}$ , the ratio of conjugated DNA strands was varied by the following amounts: 1:0, 9:1, 4:1, 1:1, 1:2, 1:4, 1:9, 0:1. After a 12 hr incubation period at 4  $^{\circ}\text{C}$ , grids were prepared for each sample as described above. Images were collected at a nominal magnification of 1700x with a pixel size of 60.8  $\text{\AA}$ . The footprint of the sheets was measured using ImageJ, and the average area of sheet coverage/grid was calculated. Additionally, the absorbance of the supernatant was measured for each sample to determine the amount of protein left in solution and therefore not incorporated into protein-DNA arrays.

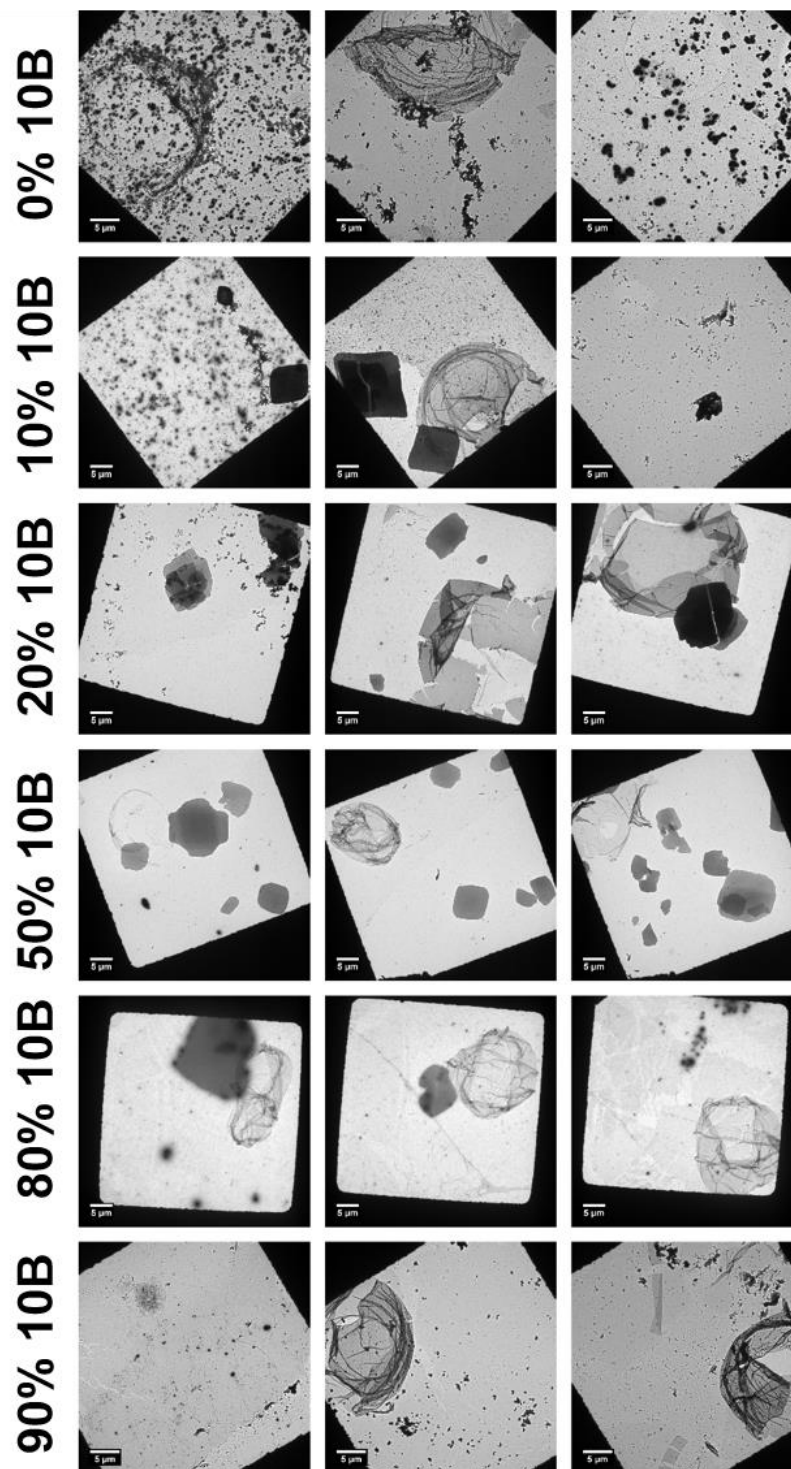


Figure 5.14: TEM images of grid squares set up with  $^{21}\text{C}$ RIDC3-10A and  $^{21}\text{C}$ RIDC3-10B at varying ratios.

### 5.5.7.2 Confocal microscopy

0.5  $\mu\text{L}$  of 10  $\mu\text{g}/\text{mL}$  ethidium bromide (EtBr) solution was added to 5  $\mu\text{L}$  samples of DNA-protein materials, nominally at 50  $\mu\text{M}$  total protein concentration. After 5 min, 2.5  $\mu\text{L}$  of the solution was pipetted onto a glass slide and was immediately covered with a cover slip and the edges were sealed with clear nail polish.

Samples were analyzed using an Olympus FV1000 Confocal microscope in the Microscopy Core in the UC San Diego School of Medicine using an excitation wavelength of 488 nm and 100x magnification. Bright field images were also obtained, and overlaid with the fluorescence images.

### 5.5.7.3 Fluorescence experiments using DNA intercalating molecules

Samples were analyzed using a fluorescence plate reader after the addition of either EtBr to a final concentration of 1  $\mu\text{g}/\text{mL}$  or SybrSafe (ThermoFisher) to a final concentration of 1x. 50  $\mu\text{L}$  samples were added to a 24-well, black-walled plate. Fluorescence emission was measured using an excitation wavelength at 485 nm and measuring emission at 535 nm for SybrSafe, or using an excitation wavelength at 535 nm and measuring emission at 595 for EtBr. Measurements were taken in triplicate with 400 ms integration with a 5 min wait time between measurements.

### 5.5.8 Quantification of $\text{Zn}^{\text{II}}$ in assembled arrays

A standard curve to quantify  $\text{Zn}^{\text{II}}$  concentration was generated using 4-(2-Pyridylazo)resorcinol (PAR) absorbance on an Agilent 8453 UV-vis spectrometer and fit to the equation  $y = mx + b$  (Figure 5.15). For solutions of DNA-protein materials, the sample was centrifuged for 1 min at 13,300 rpm, washed with 20 mM MES buffer at pH

4.75, and the material was dissolved in 300  $\mu\text{L}$  of 20 mM 3-(N-morpholine)propanesulfonic acid (MOPs) buffer with 150 mM NaCl at pH 7.0. 100  $\mu\text{L}$  aliquots of protein solution were removed, and the protein concentration was calculated using the measured absorbance at 415 nm as described above. 100  $\mu\text{L}$  of 20 mM MOPs buffer at pH 7 with 150 mM NaCl and 5 M guanidium HCl was then added to the protein solution, and after a 5 min incubation at room temperature, PAR was added at the same concentration as the standard curve was generated to quantify the amount of  $\text{Zn}^{\text{II}}$  in solution. Finally, EDTA was added to chelate  $\text{Zn}^{\text{II}}$  ions and obtain the PAR background absorbance.

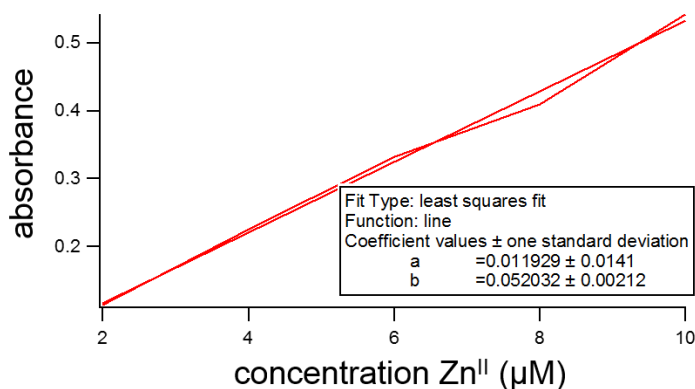


Figure 5.15: PAR calibration curve to detect  $\text{Zn}^{\text{II}}$  concentration in solution.

### 5.5.9 Macromolecular crystallography

All crystals were obtained by sitting-drop vapor diffusion consisting of 2  $\mu\text{L}$  of protein solution and 1  $\mu\text{L}$  precipitant solution. Crystals were obtained at room temperature over a period of a few weeks. X-ray diffraction data were collected at 100 K at beamline

of the Stanford Synchrotron Radiation Lightsource (SSRL) using 0.98-Å radiation. X-ray diffraction data were collected at 100 K at SSRL BL12-2 and subsequently integrated using MOSFLM and scaled with SCALA.<sup>62</sup> Structures were then determined by molecular replacement using PHASER<sup>63</sup> and subjected to rigid-body, positional and thermal refinement in REFMAC,<sup>64</sup> along with manual rebuilding in COOT.<sup>65</sup> Crystallographic data collection and refinement statistics are listed in Table S1. All figures of the resulting structures were produced using PYMOL.<sup>66</sup>

Table 5.2: X-ray data collection and refinement statistics for <sup>21</sup>C<sup>73</sup>A<sub>RIDC3</sub>  
\*denotes highest resolution shell

Data collection location	SSRL BL 12-2
Unit cell dimensions (Å)	54.9 × 49.2 × 64.9 $\alpha=\beta=\gamma=90^\circ$
Space group	<i>P2</i> <sub>1</sub>
Resolution (Å)	19.26 – 2.5
X-ray Energy (keV)	12,657
Number unique reflections	51812
Redundancy	2.7
Completeness (%)*	89.9 (90.2)
$\langle I/\sigma I \rangle$ *	8.3 (3.0)
$R_{\text{sym}}$ (%)*	6.2 (27.5)
$R_{\text{work}}/R_{\text{free}}$ (%)	21.3/28.8
R.m.s. deviations	
Bond lengths (Å)	0.012
Bond angles (°)	1.59
Ramachandran plot (%)	
Most favored	100
Allowed	0
Disallowed	0.0

### 5.5.10 Image analysis

The dm2mrc function of IMOD<sup>67</sup> was used to convert image files to .mrc. Gain normalization was applied using a reference obtained through SerialEM.<sup>68</sup> Etomo was then used to align the image stacks and create an aligned stack for each set of dose fractionated images and a single image was projected from each stack. Analysis of TEM images was performed using 2dx<sup>69</sup> to generate electron density maps. Chimera<sup>70</sup> was used to analyze electron density maps and protein structures, and Pymol<sup>66,71</sup> was used to generate figures.

### 5.6 Acknowledgements

Chapter 5 is reproduced in part from a manuscript currently being prepared for submission. Smith, S.J.; Cardone, G.; Suominen, L.; Baker, T.S.; Tezcan, F.A. Two-dimensional crystals assembled through three different types of biological interactions.2016.

### 5.7 References

- (1) Flynn, C. E.; Lee, S.-W.; Peelle, B. R.; Belcher, A. M. *Acta Mater.* **2003**, *51*, 5867.
- (2) Dominguez, R.; Holmes, K. C. *Annu. Rev. Biophys.* **2011**, *40*, 169.
- (3) Wade, R. H.; Chretien, D.; Job, D. *J. Mol. Biol.* **1990**, *212*, 775.
- (4) Pum, D.; Toca-Herrera, J. L.; Sleytr, U. B. *Int. J. Mol. Sci.* **2013**, *14*, 2484.
- (5) Sára, M.; Sleytr, U. B. *J. Bacteriol.* **2000**, *182*, 859.
- (6) Pashuck, E. T.; Cui, H.; Stupp, S. I. *J. Am. Chem. Soc.* **2010**, *132*, 6041.
- (7) Przybyla, D. E.; Chmielewski, J. *J. Am. Chem. Soc.* **2008**, *130*, 12610.
- (8) Mark, S. S.; Bergkvist, M.; Yang, X.; Teixeira, L. M.; Bhatnagar, P.; Angert, E. R.; Batt, C. A. *Langmuir* **2006**, *22*, 3763.
- (9) Dieluweit, S.; Pum, D.; Sleytr, U. B. *Supramol. Sci.* **1998**, *5*, 15.



- (10) Baneyx, F.; Matthaei, J. F. *Curr. Opin. Biotechnol.* **2014**, *28*, 39.
- (11) Ilk, N.; Egelseer, E. M.; Sleytr, U. B. *Curr. Opin. Biotechnol.* **2011**, *22*, 824.
- (12) Shenton, W.; Pum, D.; Sleytr, U. B.; Mann, S. *Nature* **1997**, *389*, 585.
- (13) Sinclair, J. C. *Curr. Opin. Cell Biol.* **2013**, *17*, 946.
- (14) Seeman, N. C. *Nature* **2003**, *421*, 427.
- (15) Seeman, N. C. *Annu. Rev. Biochem.* **2010**, *79*, 65.
- (16) Rothmund, P. W. K. *Nature* **2006**, *440*, 297.
- (17) Douglas, S. M.; Dietz, H.; Liedl, T.; Hogberg, B.; Graf, F.; Shih, W. M. *Nature* **2009**, *459*, 414.
- (18) Sharp, T. H.; Bruning, M.; Mantell, J.; Sessions, R. B.; Thomson, A. R.; Zaccai, N. R.; Brady, R. L.; Verkade, P.; Woolfson, D. N. *Proc. Natl. Acad. Sci. U.S.A.* **2012**, *109*, 13266.
- (19) Hartgerink, J. D.; Granja, J. R.; Milligan, R. A.; Ghadiri, M. R. *J. Am. Chem. Soc.* **1996**, *118*, 43.
- (20) Zhang, S.; Holmes, T.; Lockshin, C.; Rich, A. *Proc. Natl. Acad. Sci. U.S.A.* **1993**, *90*, 3334.
- (21) Papapostolou, D.; Smith, A. M.; Atkins, E. D. T.; Oliver, S. J.; Ryadnov, M. G.; Serpell, L. C.; Woolfson, D. N. *Proc. Natl. Acad. Sci. U.S.A.* **2007**, *104*, 10853.
- (22) Jiang, T.; Xu, C.; Liu, Y.; Liu, Z.; Wall, J. S.; Zuo, X.; Lian, T.; Salaita, K.; Ni, C.; Pochan, D.; Conticello, V. P. *J. Am. Chem. Soc.* **2014**, *136*, 4300.
- (23) Fletcher, J. M.; Harniman, R. L.; Barnes, F. R. H.; Boyle, A. L.; Collins, A.; Mantell, J.; Sharp, T. H.; Antognozzi, M.; Booth, P. J.; Linden, N.; Miles, M. J.; Sessions, R. B.; Verkade, P.; Woolfson, D. N. *Science* **2013**, *340*, 595.
- (24) Valery, C.; Artzner, F.; Paternostre, M. *Soft Matter* **2011**, *7*, 9583.
- (25) Egelman, E. H.; Xu, C.; DiMaio, F.; Magnotti, E.; Modlin, C.; Yu, X.; Wright, E.; Baker, D.; Conticello, V. P. *Structure* **2015**, *23*, 280.
- (26) Sinclair, J. C.; Davies, K. M.; Venien-Bryan, C.; Noble, M. E. M. *Nat. Nanotech.* **2011**, *6*, 558.

- (27) Padilla, J. E.; Colovos, C.; Yeates, T. O. *Proc. Nat. Acad. Sci. U.S.A.* **2001**, *98*, 2217.
- (28) Lai, Y.-T.; King, N. P.; Yeates, T. O. *Trends Cell Biol.* **2012**, *22*, 653.
- (29) Dotan, N.; Arad, D.; Frolow, F.; Freeman, A. *Angew. Chem. Int Ed.* **1999**, *38*, 2363.
- (30) Lai, Y.-T.; Cascio, D.; Yeates, T. O. *Science* **2012**, *336*, 1129.
- (31) Ringler, P.; Schulz, G. E. *Science* **2003**, *302*, 106.
- (32) Kitagishi, H.; Kakikura, Y.; Yamaguchi, H.; Oohora, K.; Harada, A.; Hayashi, T. *Angew. Chem. Int. Ed.* **2009**, *48*, 1271.
- (33) Oohora, K.; Onoda, A.; Hayashi, T. *Chem. Commun.* **2012**, *48*, 11714.
- (34) King, N. P.; Bale, J. B.; Sheffler, W.; McNamara, D. E.; Gonen, S.; Gonen, T.; Yeates, T. O.; Baker, D. *Nature* **2014**, *510*, 103.
- (35) King, N. P.; Sheffler, W.; Sawaya, M. R.; Vollmar, B. S.; Sumida, J. P.; André, I.; Gonen, T.; Yeates, T. O.; Baker, D. *Science* **2012**, *336*, 1171.
- (36) Gonen, S.; DiMaio, F.; Gonen, T.; Baker, D. *Science* **2015**, *348*, 1365.
- (37) Niemeyer, C. M.; Sano, T.; Smith, C. L.; Cantor, C. R. *Nucleic Acids Res.* **1994**, *22*, 5530.
- (38) Niemeyer, C. M. *Curr. Opin. Chem. Biol.* **2000**, *4*, 609.
- (39) Aldaye, F. A.; Palmer, A. L.; Sleiman, H. F. *Science* **2008**, *321*, 1795.
- (40) Wilner, O. I.; Weizmann, Y.; Gill, R.; Lioubashevski, O.; Freeman, R.; Willner, I. *Nat. Nano.* **2009**, *4*, 249.
- (41) Wilner, O. I.; Shimron, S.; Weizmann, Y.; Wang, Z.-G.; Willner, I. *Nano Lett.* **2009**, *9*, 2040.
- (42) Delebecque, C. J.; Lindner, A. B.; Silver, P. A.; Aldaye, F. A. *Science* **2011**, *333*, 470.
- (43) Niemeyer, C. M.; Koehler, J.; Wuerdemann, C. *ChemBioChem* **2002**, *3*, 242.
- (44) Malo, J.; Mitchell, J. C.; Vénien-Bryan, C.; Harris, J. R.; Wille, H.; Sherratt, D. J.; Turberfield, A. J. *Angew. Chem. Int. Ed.* **2005**, *44*, 3057.

- (45) Cohen, J. D.; Sadowski, J. P.; Dervan, P. B. *J. Am. Chem. Soc.* **2008**, *130*, 402.
- (46) Mou, Y.; Huang, P. S.; Hsu, F. C.; Huang, S. J.; Mayo, S. L. *Proc. Natl. Acad. Sci. U.S.A.* **2015**, *112*,
- (47) Mou, Y.; Yu, J.-Y.; Wannier, T. M.; Guo, C.-L.; Mayo, S. L. *Nature* **2015**, *525*, 230.
- (48) Sanghamitra, N. J. M.; Ueno, T. *Chem. Commun.* **2013**, *49*, 4114.
- (49) Tabbasum, K.; Rao, C. P. *RSC Adv.* **2015**, *5*, 16828.
- (50) Bai, Y.; Luo, Q.; Zhang, W.; Miao, L.; Xu, J.; Li, H.; Liu, J. *J. Am. Chem. Soc.* **2013**, *135*, 10966.
- (51) Qiao, S. P.; Lang, C.; Wang, R. D.; Li, X. M.; Yan, T. F.; Pan, T. Z.; Zhao, L. L.; Fan, X. T.; Zhang, X.; Hou, C. X.; Luo, Q.; Xu, J. Y.; Liu, J. Q. *Nanoscale* **2016**, *8*, 333.
- (52) Song, W. J.; Sontz, P. A.; Ambroggio, X. I.; Tezcan, F. A. *Annu. Rev. Biophys.* **2014**, *43*, 409.
- (53) Radford, R. J.; Brodin, J. D.; Salgado, E. N.; Tezcan, F. A. *Coord. Chem. Rev.* **2011**, *255*, 790.
- (54) Salgado, E. N.; Radford, R. J.; Tezcan, F. A. *Acc. Chem. Res.* **2010**, *43*, 661.
- (55) Brodin, J. D.; Smith, S. J.; Carr, J. R.; Tezcan, F. A. *J. Am. Chem. Soc.* **2015**, *137*, 10468.
- (56) Brodin, J. D.; Carr, J. R.; Sontz, P. A.; Tezcan, F. A. *Proc. Nat. Acad. Soc. U.S.A.* **2014**, *111*, 2897.
- (57) Brodin, J. D.; Ambroggio, X. I.; Tang, C.; Parent, K. N.; Baker, T. S.; Tezcan, F. A. *Nat. Chem.* **2012**, *4*, 375.
- (58) Kukolka, F.; Niemeyer, C. M. *Org. Biomol. Chem.* **2004**, *2*, 2203.
- (59) Wimberly, B. T.; Brodersen, D. E.; Clemons, W. M.; Morgan-Warren, R. J.; Carter, A. P.; Vonnrhein, C.; Hartsch, T.; Ramakrishnan, V. *Nature* **2000**, *407*, 327.
- (60) Ban, N.; Nissen, P.; Hansen, J.; Moore, P. B.; Steitz, T. A. *Science* **2000**, *289*, 905.

- (61) Horcas, I.; Fernández, R.; Gómez-Rodríguez, J. M.; Colchero, J.; Gómez-Herrero, J.; Baro, A. M. *Rev. Sci. Instrum.* **2007**, *78*, 013705.
- (62) Winn, M. D.; Ballard, C. C.; Cowtan, K. D.; Dodson, E. J.; Emsley, P.; Evans, P. R.; Keegan, R. M.; Krissinel, E. B.; Leslie, A. G. W.; McCoy, A.; McNicholas, S. J.; Murshudov, G. N.; Pannu, N. S.; Potterton, E. A.; Powell, H. R.; Read, R. J.; Vagin, A.; Wilson, K. S. *Acta Cryst. D.* **2011**, *67*, 235.
- (63) McCoy, A. J.; Grosse-Kunstleve, R. W.; Adams, P. D.; Winn, M. D.; Storoni, L. C.; Read, R. J. *J Appl Crystallogr* **2007**, *40*, 658.
- (64) Murshudov, G.; Vagin, A.; Dodson, E. *Acta Cryst.* **1996**, *D53*, 240.
- (65) Emsley, P.; Cowtan, K. *Acta Cryst.* **2004**, *D60*, 2126.
- (66) DeLano, W. L. *The PYMOL Molecular Graphics System* (<http://www.pymol.org>); 2003.
- (67) Kremer, J. R.; Mastronarde, D. N.; McIntosh, J. R. *J. Struct. Biol.* **1996**, *116*, 71.
- (68) Mastronarde, D. *Microsc. Microanal.* **2003**, *9*, 1182.
- (69) Gipson, B.; Zeng, X.; Zhang, Z. Y.; Stahlberg, H. *J. Struct. Biol.* **2007**, *157*, 64.
- (70) Pettersen, E. F.; Goddard Td Fau - Huang, C. C.; Huang Cc Fau - Couch, G. S.; Couch Gs Fau - Greenblatt, D. M.; Greenblatt Dm Fau - Meng, E. C.; Meng Ec Fau - Ferrin, T. E.; Ferrin, T. E. *J. Comput. Chem.* **2004**, *25*, 1605.
- (71) Schrodinger, LLC The PyMOL Molecular Graphics System, Version 1.8

## **6. Conclusions and Future Directions**

### **6.1 Introduction**

A variety of strategies have been used to engineer protein-protein interactions<sup>1-3</sup> and protein assemblies.<sup>4-6</sup> Here, we have discussed a method of metal-directed protein self-assembly, inspired by the use of metal ions at protein interfaces in nature,<sup>7</sup> to control interactions between individual biological molecules<sup>8,9</sup> or throughout extended micrometer-scale arrays.<sup>10,11</sup> The use of directed metal-interactions allows for the formation of highly versatile materials, with large morphological changes observed with minimal surface redesign.

### **6.2 Peptide-HCM based mimics of protein-protein interactions**

We have introduced a new method of inducing  $\alpha$ -helicity in short, unstructured peptides, and demonstrated its versatility in several systems.<sup>12</sup> Many research groups have proposed peptide therapeutics as solutions for disease targets previously assumed to be “undruggable.”<sup>13</sup> As discussed in chapters 2 and 3, the system that we have developed is robust in its ability to fold helical peptides and protects against protease degradation. Additionally, the use of metal ions instead of covalent cross-links offers the advantage to incorporate metal-based functionality, which was demonstrated by the use of  $\text{Re}^{\text{I}}$  to create a luminescent peptide-HCM in addition to imparting structure to the peptide backbone. Our ability to bind DNA by peptides based on the GCN4 sequence further demonstrates the utility of metal ions in both structuring and orientating the peptides in biologically relevant structures.

Moving forward, by carefully selecting targets of interest, we believe the peptide-HCM system could have many applications in targeting biological interactions using structured peptides. We envision high impact in the development of a peptide-based HCM that could be used for targeted drug delivery of metallotherapeutics. Specifically, we believe that the use of substitution-inert metal ions could create stable,  $\alpha$ -helical peptides that could be targeted to specific biological targets through peptide recognition at a protein interface. The inherent properties of the substitution-inert metal—whether for fluorescence imaging or therapeutic use—could then be utilized at these specific locations.

### **6.3 Designing protein assemblies**

#### **6.3.1 Assembly of variable diameter protein nanotubes**

The assembly of 1- and 2D, ordered protein materials has previously been demonstrated using MDPSA.<sup>10,11</sup> Through a slight redesign of the protein building block, we have now introduced the assembly of variable diameter protein nanotubes.<sup>14</sup> The anisotropic assembly of these tubes stems from the incorporation of high- and low-affinity Zn<sup>II</sup> binding sites. The relative differences in the metal-binding affinity between binding sites allows us to control the relative assembly rate of the material along the longitudinal and transverse coordinates, ultimately manifesting macroscopically as a tube with controllable diameter. Importantly, unlike other designed materials, we believe these assemblies to be kinetically directed and are able to respond to environmental conditions, making them reminiscent of biological materials that respond to external stimuli to modify their structure or assembly state.

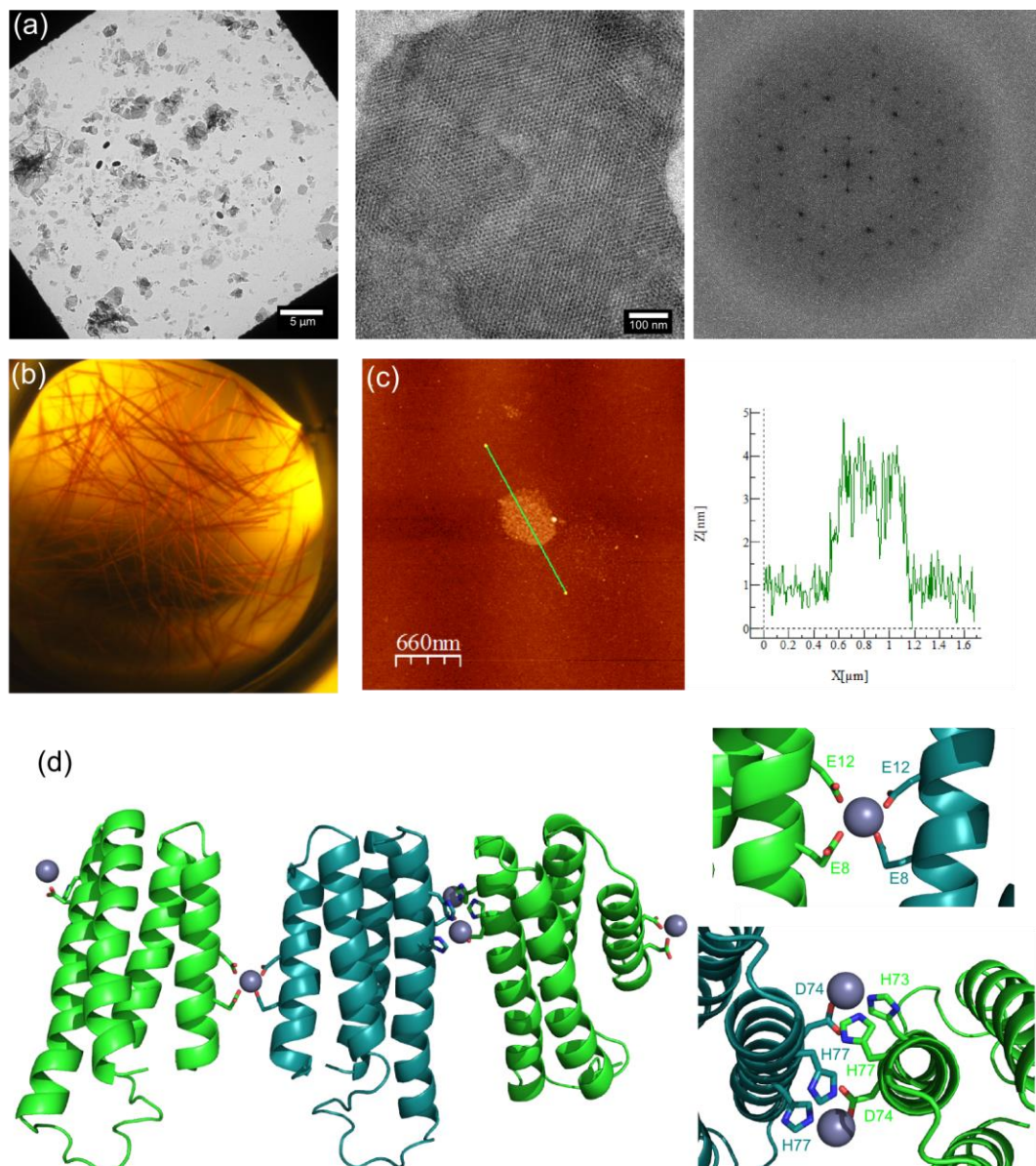


Figure 6.1: Analysis of  $^{21}\text{C}^{63}\text{A}$  RIDC3 materials. (a) TEM images at low and high magnification and the FFT of a 2D sheet showing the lattice with calculated unit cell parameters of  $a = b = 130 \text{ \AA}$ ,  $\alpha = 120^\circ$ . (b) 3D crystal grown for x-ray analysis. (c) AFM data showing the height of the sheets to be approximately 3 nm, corresponding to single layer protein arrays. (d) Crystal structure obtained from  $^{21}\text{C}^{63}\text{S}$  RIDC3 3-dimensional crystals.  $\text{Zn}^{\text{II}}$  ions were bound at two distinct dimeric interfaces and the metal-protein interactions are shown on the right.

### 6.3.2 Single point mutations cause large morphological changes

As in the design of the protein nanotubes, we have discovered that small changes in the protein structure can lead to large morphological changes in the material that is formed. For instance, in chapter 5, we discussed the synthesis of  $^{21}\text{C}$ RIDC3 variants where the his residues normally found at the dimeric protein interface were mutated to ala residues ( $^{21}\text{C}^{63\text{A}}$ RIDC3,  $^{21}\text{C}^{73\text{A}}$ RIDC3, and  $^{21}\text{C}^{77\text{A}}$ RIDC3). Surprisingly, we discovered that  $^{21}\text{C}^{63\text{A}}$ RIDC3 and  $^{21}\text{C}^{73\text{A}}$ RIDC3 were able to form 2D crystals upon the addition of  $\text{Zn}^{\text{II}}$  ions. This was unexpected in part because  $^{21}\text{C}$ RIDC3 had never been observed to form ordered arrays. The  $^{21}\text{C}^{63\text{A}}$ RIDC3 materials have been more fully characterized, and a crystal structure obtained. As shown in Figure 6.1, these materials are single-layered based on AFM measurements, and have approximate lattice parameters of  $a=b=130 \text{ \AA}$ ,  $\alpha = 120^\circ$ . Two distinct metal binding interactions are present in the crystal structure—two H73, H77, and D74 (from a second monomer) binding motifs are observed at the expected dimeric interface, while a second E8-D12-E8-D12 motif extends the structure in a linear fashion. There is a twist across the protein monomers as the material extends, which may account for the observed hexagonal diffraction pattern in the TEM images, but further structural analysis is ongoing. Compared to our previously obtained structures, these materials appear to be much less stiff, as the nanomaterials appear very thin with a much larger number of folds and material deformations than we have previously observed.

$^{21}\text{C}^{73\text{A}}$ RIDC3 materials, conversely, appear to pack into multilayer, stiff, narrow sheets that appear to bundle. Based on limited data from fft of TEM images, these materials appear to be flat, 2D sheets as opposed to 1D nanotubes, but additional structural analysis



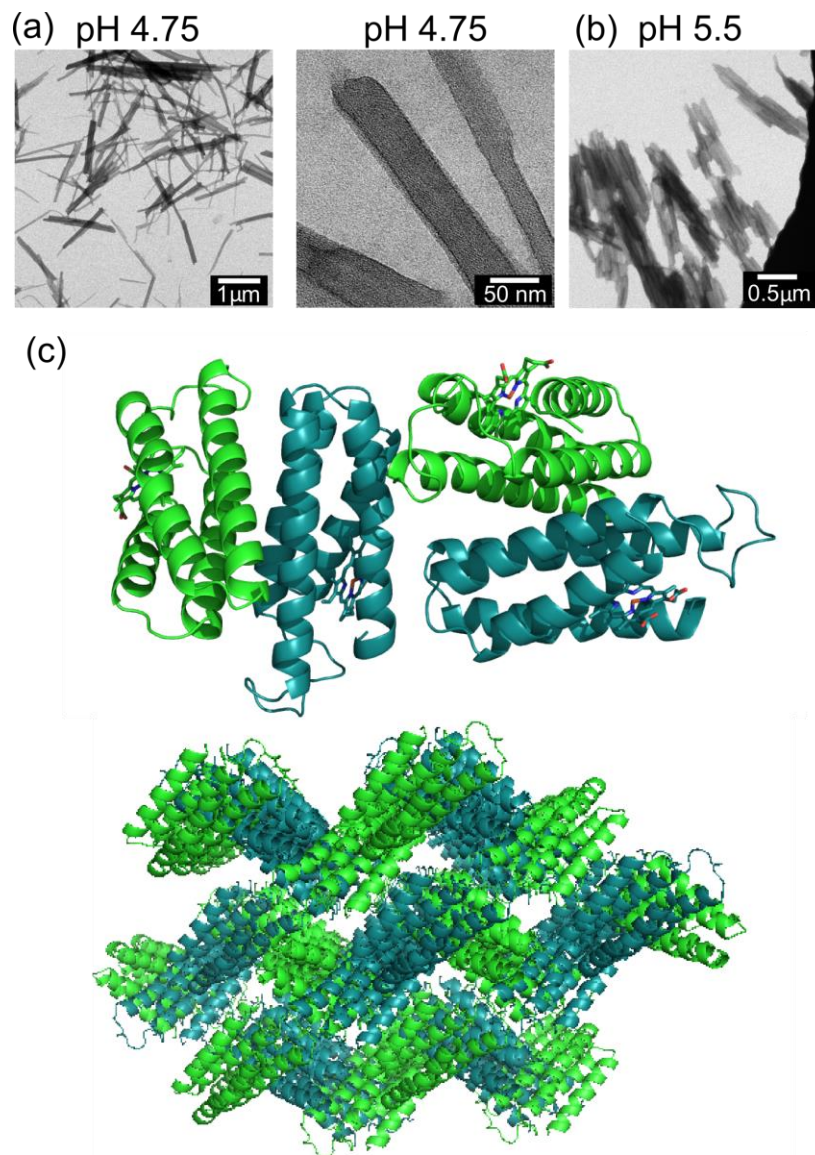


Figure 6.2: Analysis of  $^{21C73A}$ RIDC3 materials. TEM images were obtained at pH 4.75 (a) and pH 5.5 (b). (c) 3D crystals were grown and found to be metal free. The top image shows the packing of two dimers, where the dimeric interface is along the same helices as observed in RIDC3. The bottom image shows the 3D packing of 2D sheets, which may be relevant to the protein packing in the crystals observed via TEM.

is necessary to better characterize the structures. A crystal structure was obtained and was found to be metal free. The expected dimeric interface was still present, and we attribute this to the hydrophobic interactions that have been engineered at that dimeric interface.

The TEM images and crystal structure are shown in Figure 6.2, and work is ongoing to determine whether the metal-free crystal structure arrangement correlates with the observed 2D materials.

The observation of these structures highlights both the potential and the difficulties of treating proteins as ligands for MDPSA. As we have demonstrated with these two examples, and by the protein tubes discussed in Chapter 4, a single building block can be used to create discrete assemblies with highly divergent properties.  $^{59}\text{H}^{96}\text{C}$ RIDC3 assembles exclusively into nanotubes, and moderating solution conditions changes the width of the nanotubes that form, and thereby their mechanical properties. Here, we have presented two additional mutants whose assembly and eventual morphological properties appear to be different from any protein-based materials we have previously obtained. This diversity within our system provides the potential to design materials for a number of applications, but also demonstrates the difficulty in treating proteins as simple ligands. Unlike designed organic molecules for metal binding, proteins have a large number of amino acid residues that can bind metal, and it can be difficult to predict which binding sites will be most favorable upon the addition of metal ions. In all the engineered materials discussed here,  $\text{Zn}^{\text{II}}$  has been used to coordinate proteins and direct structure formation. The incorporation of metal ions with different binding geometries may be a second route towards creating materials with diverse properties.

### **6.3.3 Applications of protein and hybrid DNA-protein materials**

There is considerable interest in the design of bionanomaterials consisting of multiple components, as this would allow for the incorporation of multiple functionalities into a single material. We have now presented an example of a hybrid DNA-protein

material whose assembly is dependent on both protein-protein and DNA-DNA interactions, in addition to metal-directed assembly. Unlike many multiple component arrays where assembly is dependent only on a single set of interactions, this material forms due to cooperative interactions of all three components. It will be important to further explore the incorporation of diverse DNA-sequences to better understand and control assembly pathways. Protein assemblies have been discussed as having potential applications in therapeutics; it has previously been demonstrated that the use of viral nanoparticles for multivalent protein display can enhance vaccine response or direct therapeutics to specific locations.<sup>15</sup> We believe that the facile assembly of ordered, DNA-protein materials could exploit the recognition properties of both DNA and protein in addition to protein functionalities.

#### **6.4 Conclusions**

Overall, we have demonstrated the expansion of MDPSA to induce structure in small peptides to target protein-protein and protein-DNA, protect against proteolytic cleavage, and incorporate metal-functionality on peptide platforms. On larger scales, we have expanded the properties of materials accessible using the RIDC3 building block with MDPSA. Although there are considerable challenges to be overcome in the design and applications of these materials, we believe we have a generalizable system that can be utilized for a number of protein engineering applications.

## **6.5 Materials and Methods**

### **6.5.1 Negatively stained samples for transmission electron microscopy (TEM)**

A 3  $\mu\text{L}$  solution of sample was pipetted onto carbon-coated Cu grids (Electron Microscopy Sciences, Carbon Film on 400 square mesh Copper Grids) that had been glow discharged within 30 min of sample addition. The grids were blotted with filter paper to remove excess liquid, washed by submerging in a 250  $\mu\text{L}$  drop of water, blotted to again remove excess liquid, and stained by the addition of 5  $\mu\text{L}$  of 1% uranyl acetate (UA) in water to the grid. After a 5 min incubation, the grid was blotted to remove excess UA solution, and a second aliquot of UA was added. After the second 5 min incubation, the grid was blotted dry using filter paper. Grids were imaged in a 200 keV FEI Sphera transmission electron microscope equipped with a LaB<sub>6</sub> filament. Images were recorded on a Gatan 2K<sup>2</sup> CCD camera. Objective lens underfocus settings ranged from 250 nm to 2  $\mu\text{m}$ .

### **6.5.2 Atomic Force Microscopy (AFM)**

To prepare samples for analysis by AFM, 10  $\mu\text{L}$  of a sheet-containing solution was centrifuged, the supernatant was removed, and the sheets were re-suspended in 10  $\mu\text{L}$  water. The sample was then deposited on freshly cleaved mica (Ted Pella), and incubated for 10 min. At that time, it was dried using a stream of nitrogen without washing.

Analysis was performed using a Veeco Scanning Probe Microscope using Silicon AFM probes with aluminum reflex coating and a resonance frequency of 300 kHz (Ted Pella, Tap300Al-G). Images were obtained at a field size consisting of 512 x 512 pixels. Image analysis was done using WSxM 5.0 (cite Horcas et al Review of Scientific Instruments 78 (2007)).<sup>16</sup>

### 6.5.3 Macromolecular crystallography

All crystals were obtained by sitting-drop vapor diffusion consisting of 2  $\mu\text{L}$  of protein solution and 1  $\mu\text{L}$  precipitant solution. Crystals were obtained at room temperature over a period of a few weeks. X-ray diffraction data were collected at 100 K at beamline of the Stanford Synchrotron Radiation Lightsource (SSRL) using 0.98- $\text{\AA}$  radiation. The CCP4 suite of programs was used to process diffraction data,<sup>17</sup> and molecular replacement was used to solve the structure with MOLREP using RIDC3 as a search model.<sup>17</sup> Structures were then determined by molecular replacement using PHASER<sup>18</sup> and subjected to rigid-body, positional and thermal refinement in REFMAC,<sup>19</sup> along with manual rebuilding in COOT.<sup>20</sup>

Table 6.1: X-ray data collection and refinement statistics for <sup>21</sup>C<sup>63</sup>S-RIDC3.  
\*denotes highest resolution shell

Data collection location	SSRL BL 12-2
Unit cell dimensions ( $\text{\AA}$ )	69.8 $\times$ 69.8 $\times$ 146.3 $\alpha=\gamma=90^\circ$ , $\beta=120^\circ$
Space group	$P6_222$
Resolution ( $\text{\AA}$ )	37.95 – 3.5
X-ray Energy (keV)	12,657
Number unique reflections	3272
Redundancy	25.8
Completeness (%)*	99.8 (100)
$\langle I/\sigma I \rangle$ *	14.9 (11.2)
$R_{\text{symm}}$ (%)*	19.1 (48.4)
$R_{\text{work}}/R_{\text{free}}$ (%)	26.9/33.1
R.m.s. deviations	
Bond lengths ( $\text{\AA}$ )	0.012
Bond angles ( $^\circ$ )	1.725
Ramachandran plot (%)	
Most favored	99
Allowed	4
Disallowed	1

## 6.6 References

- (1) Baek, S.; Kutchukian, P. S.; Verdine, G. L.; Huber, R.; Holak, T. A.; Lee, K. W.; Popowicz, G. M. *J. Am. Chem. Soc.* **2012**, *134*, 103.
- (2) Walensky, L. D.; Kung, A. L.; Escher, I.; Malia, T. J.; Barbuto, S.; Wright, R. D.; Wagner, G.; Verdine, G. L.; Korsmeyer, S. J. *Science* **2004**, *305*, 1466.
- (3) Wang, D.; Chen, K.; Kulp, J. L.; Arora, P. S. *J. Am. Chem. Soc.* **2006**, *128*, 9248.
- (4) Lai, Y.-T.; Cascio, D.; Yeates, T. O. *Science* **2012**, *336*, 1129.
- (5) Gonen, S.; DiMaio, F.; Gonen, T.; Baker, D. *Science* **2015**, *348*, 1365.
- (6) Sinclair, J. C.; Davies, K. M.; Venien-Bryan, C.; Noble, M. E. M. *Nat. Nanotech.* **2011**, *6*, 558.
- (7) Song, W. J.; Sontz, P. A.; Ambroggio, X. I.; Tezcan, F. A. *Annual Review of Biophysics* **2014**, *43*, 409.
- (8) Salgado, E. N.; Radford, R. J.; Tezcan, F. A. *Acc. Chem. Res.* **2010**, *43*, 661.
- (9) Radford, R. J.; Brodin, J. D.; Salgado, E. N.; Tezcan, F. A. *Coord. Chem. Rev.* **2011**, *255*, 790.
- (10) Brodin, J. D.; Carr, J. R.; Sontz, P. A.; Tezcan, F. A. *Proc. Natl. Acad. Sci. U.S.A.* **2014**, *111*, 2897.
- (11) Brodin, J. D.; Ambroggio, X. I.; Tang, C.; Parent, K. N.; Baker, T. S.; Tezcan, F. A. *Nat. Chem.* **2012**, *4*, 375.
- (12) Smith, S. J.; Du, K.; Radford, R. J.; Tezcan, F. A. *Chem. Sci.* **2013**, *4*, 3740.
- (13) Verdine, G. L.; Walensky, L. D. *Clin. Cancer Res.* **2007**, *13*, 7264.
- (14) Brodin, J. D.; Smith, S. J.; Carr, J. R.; Tezcan, F. A. *J. Am. Chem. Soc.* **2015**, *137*, 10468.
- (15) Venter, P. A.; Dirksen, A.; Thomas, D.; Manchester, M.; Dawson, P. E.; Schneemann, A. *Biomacromolecules* **2011**, *12*, 2293.
- (16) Horcas, I.; Fernández, R.; Gómez-Rodríguez, J. M.; Colchero, J.; Gómez-Herrero, J.; Baro, A. M. *Review of Scientific Instruments* **2007**, *78*, 013705.
- (17) Winn, M. D.; Ballard, C. C.; Cowtan, K. D.; Dodson, E. J.; Emsley, P.; Evans, P. R.; Keegan, R. M.; Krissinel, E. B.; Leslie, A. G. W.; McCoy, A.;

McNicholas, S. J.; Murshudov, G. N.; Pannu, N. S.; Potterton, E. A.; Powell, H. R.; Read, R. J.; Vagin, A.; Wilson, K. S. *Acta Cryst. D.* **2011**, *67*, 235.

(18) McCoy, A. J.; Grosse-Kunstleve, R. W.; Adams, P. D.; Winn, M. D.; Storoni, L. C.; Read, R. J. *J. Appl. Crystallogr.* **2007**, *40*, 658.

(19) Murshudov, G.; Vagin, A.; Dodson, E. *Acta Cryst.* **1996**, *D53*, 240.

(20) Emsley, P.; Cowtan, K. *Acta Crystallogr. Sect. D-Biol. Crystallogr.* **2004**, *D60*, 2126.